Nidovirus Papain-Like Proteases: Structural Insight Into Substrate Recognition and Innate Immune Suppression

By

Ben A. Bailey-Elkin

A Thesis submitted to the Faculty of Graduate Studies of
The University of Manitoba
in partial fulfillment of the requirements for the degree of

Doctor of Philosophy

Department of Microbiology
University of Manitoba
Winnipeg, Manitoba, Canada

Abstract

Nidoviruses are an order of positive-sense RNA viruses, which include the families Arteriviridae and Coronaviridae. Nidoviruses express their complement of non-structural proteins (nsps) as a single polyprotein, which is cleaved into functional domains by proteases encoded within. The equine arterivirus (EAV) and Middle East respiratory syndrome coronavirus (MERS-CoV) encode for papain-like protease domains within nsp2 and nsp3, respectively, which serve a replicative role through their polyprotein processing activities.

During infection, the host innate immune response is triggered by incoming pathogens, and engages multiple signalling pathways which are in-part dependent on the post-translational modification by ubiquitin (Ub). These signalling processes are tightly regulated by deubiquitinases (DUBs), which remove Ub from their cellular targets in order to reverse their effects.

The EAV papain-like protease 2 (PLP2) and the MERS-CoV papain-like protease (PL^{pro}), in addition to their replicative functions, were proposed to interfere with the induction of the cellular innate immune response to infection by acting as deubiquitinating enzymes. The fact that these enzymes rely on a single active site in order to carry out both DUB and polyprotein processing activities complicates our ability to assess the role of these functions independently. Here, the crystal structures of EAV PLP2, and the MERS-CoV PL^{pro} in covalent complex with their Ub substrates were determined, and structure-guided mutagenesis was used to selectively remove DUB activity permitting the independent study of their DUB activities. Specific mutations targeting the Ub-binding interface of these enzymes inhibited DUB activity while permitting replicative polyprotein processing. Studies using these DUB-deficient enzymes

demonstrated directly their role in the down regulation of cellular innate immune responses. In an effort to further define the molecular basis for substrate recognition by these viral DUBs, their structures were determined in complex with the antiviral Ub-like molecule ISG15, permitting further structural characterization of substrate recognition.

In addition to the structural characterization of PL^{pro} in complex with cellular substrates, the structures of PL^{pro} in complex with novel, selective Ub-based inhibitors of the enzyme were determined. These inhibitors bound with high affinity mediated by a combination of hydrophobic and hydrogen-bonding interactions, inhibiting polyprotein cleavage, innate immune suppression and viral replication in cell culture.

Acknowledgements

I would first like to thank my supervisor, Dr. Brian Mark for his guidance, and encouragement throughout the course of my graduate training. I will always be grateful for the insight, knowledge and support you have provided over all of these years. I would also like to extend my gratitude to my committee members, Dr. Joe O'Neil and Dr. Silvia Cardona, for their thoughtful insight and discussions had over many committee meetings.

I would like to recognize the funding sources that have provided financial support throughout the course of this research – the Natural Sciences and Engineering Research Council, Research Manitoba and the University of Manitoba. Many thanks as well to all of the beamline staff at the Canadian Light Source.

I would also like to recognize the many wonderful collaborators I have had the pleasure of working with throughout my studies. Dr. Mazdak Khajehpour at the University of Manitoba, Dr. Puck van Kasteren, Robert Knaap, Dr. Marjolein Kikkert and Prof. Eric Snijder at the Leiden University Medical Centre, and Dr. Wei Zhang and Dr. Sachdev Sidhu at the University of Toronto.

I would like to thank the entire faculty in the department of Microbiology for their support and guidance. Within the Mark lab I would like to thank the fantastic undergraduate students I've had the privilege of working with - Garrett Johnson, Wen He, Kate Parkinson, Robin Nurse and Nick Ferens. I am also very grateful for the many friendships that have evolved over the last few years. Thank you Grishma for your always positive outlook, Ankoor for the coffee, Matt for the company at the beamlines, Barney for being a great squash student, Justin for the ball hockey snipes and to Damien for your friendship both on and off the ice.

Finally, I would like to thank my friends and family for always being there.

Dedication

This thesis is dedicated to my parents, Ian and Norma, to my brother Will and to my partner Leigh. I love you all.

Thank you Mom and Pops for your unwavering support, and to Will for being the best brother a brother could ask for.

Finally, thank you Leigh, for everything.

Table of Contents

List of Figures

List of Tables

List of Copyrighted Materials

List of Abbreviations

HEPES	4-(2-hydroxyethyl)-1-piperazineethanesulfonic acid
AdV	Adenovirus
Å	Angstrom
BLI	Biolayer interferometry
Bis-Tris	Bis(2-hydroxyethyl)amino-tris(hydroxymethyl)methane
BL2	Blocking-loop 2
CLS	Canadian Light Source
CV	Column volume
CoV	Coronavirus
CCHFV	Crimean-Congo hemorrhagic fever virus
CRL	Cullin-RING ubiquitin ligase
cGAMP	Cyclic-GMP-AMP
cGAS	Cyclic-GMP-AMP synthase
°C	Degrees celcius
DUB	Deubiquitinase
DTT	Dithiothreitol
dsDNA	Double-stranded deoxyribonucleic acid
DUGV	Dugbe virus
DMEM	Dulbecco's modified Eagle medium
EMEM	Eagle's minimum essential medium
ER	Endoplasmic reticulum
EVG	Enterovirus species G
EBV	Epstein–Barr virus
EAV	Equine arterivirus
ELF	Equine lung fibroblast
ERVV	Erve virus
EDTA	Ethylenediaminetetraacetic acid
eIF4G	Eukaryotic translation initiation factor 4 G
FBS	Fetal bovine serum
FCS	Fetal calf serum
FMDV	Foot-and-mouth disease virus
GST	Glutathione S-transferase
GAPDH	Glyceraldehyde 3-phosphate dehydrogenase
GFP	Green fluorescent protein
HA	Hemagglutinin
HSV1	Herpes simplex virus 1
htUSP	Herpesvirus tegument ubiquitin-specific protease
HRP	Horseradish peroxidase
hrs	Hours

h.p.i.	Hours post-infection
HCoV	Human coronavirus
HCMV	Human cytomegalovirus
IgG	Immuniglobulin G
IKK	Inhibitor of NF-κB kinase
IFN	Interferon
IRF	Interferon-regulatory factor
ISG15	Interferon-stimulated gene 15
IRAK1	Interleukin-1 receptor-associated kinase 1
IPTG	Isopropyl β-D-1-thiogalactopyranoside
ITC	Isothermal titration calorimetry
KSV	Kaposi's sarcoma-associated herpesvirus
K	Kelvin
kDa	Kilodaltons
LDV	Lactate dehydrogenase elevating virus
LSB	Laemmli sample buffer
LUMC	Leiden University Medical Centre
LN_2	Liquid nitrogen
LB	Lysogeny broth
MJD	Machado-Joseph disease proteases
MDV	Marek's disease virus
MDA5	Melanoma Differentiation-Associated protein 5
mRNA	Messenger ribonucleic acid
µL	Microliter
µM	Micromolar
MERS-CoV	Middle East respiratory syndrom coronavirus
mL	Milliliter
mM	Millimolar
min	Minutes
MAVS	Mitochondrial antiviral-signaling protein
MLVs	Modified-live virus
M	Molar
MR	Molecular replacement
MHV	Mouse hepatitis virus
m.o.i	Multiplicity of infection
MAD	Multi-wavelength anomalous dispersion
MCMV	Murine Cytomegalovirus
NSDV	Nairobi sheep disease virus
nL	Nanoliter
NEM	N-ethylmaleimide
Ni-NTA	Nickel-nitrilotriacetic acid

Nsp	Non-structural protein
OD_{600}	Optical density at 600 nm
OTU	Ovarian tumour domain
PLP	Papain-like protease
PL^{pro}	Papain-like protease
PFA	Paraformaldehyde
PRR	Pattern recognition receptor
PBS	Phosphate-buffered saline
PEG	Polyethylene glycol
PEI	Polyethylenimine
PEDV	Porcine Epidemic Diarrhea Virus
PRRSV	Porcine reproductive and respiratory syndrome virus
p.i.	Post-infection
PKR	Protein kinase R
PrV	Pseudorabies virus
qRT-PCR	Quantitative real-time PCR
RIP1	Receptor-interacting protein 1
rpm	Revolutions per minute
RLR	RIG-I-Like Receptor
RT	Room temperature
RMSD	Root-mean-square deviation
SHFV	Simian hemorrhagic fever virus
ssRNA	Single-stranded ribonucleic acid
SAD	Single-wavelength anomalous dispersion
SDS	Sodium dodecyl sulfate
SDS-PAGE	Sodium dodecyl sulfate polyacrylamide gel electrophoresis
STING	Stimulator of interferon genes
TBK1	TANK-binding kinase 1
TCAG	The Centre for Applied Genomics
TRIF	TIR-domain-containing adapter-inducing interferon-β
TLR	Toll-like receptor
TGEV	Transmissible gastroenteritis coronavirus
Tris	Tris(hydroxymethyl)aminomethane
TYMV	Turnip yellow mosaic virus
Ub	Ubiquitin
UCH	Ubiquitin carboxyl-terminal hydrolase
UbV	Ubiquitin variant
UbVME	Ubiquitin vinyl methyl ester
Ub-3Br	Ubiquitin-3-bromopropylamine
Ub-AFC	Ubiquitin-7-amino-4-trifluoromethylcoumarin
Ub-AMC	Ubiquitin-amino-methyl-coumarin

UBL	Ubiquitin-like domain
USP	Ubiquitin-specific protease
UM	University of Manitoba
UT	University of Toronto

Chapter 1
Literature review: Structure and function of viral deubiquitinating enzymes

Adapted from: Bailey-Elkin, B.A., Knaap, R.C.M., Kikkert, M., Mark, B.L. (2017) Structure and function of viral deubiquitinating enzymes. *J Mol Biol.* **429**, 3441-3470

Contributions statement:

The following chapter was written as an invited review article in collaboration with Robert Knaap and Marjolein Kikkert (Leiden University Medical Centre; LUMC). I wrote sections 1.2, 1.3, 1.4, 1.6, 1.7, 1.8 and 1.9. All of the listed authors took part in editing the final manuscript.

1.1 Introduction

1.1.1 Viruses and the ubiquitin system

Viruses have had a significant impact on society throughout history, and it is only since we have started to understand how they establish infection and how they interact with their hosts that we have been able to develop the means to control the diseases they cause. Although viruses depend on the molecular machineries of their host cells for replication, they also express their own specialized replication enzymes to support the production of new virus particles and the spread of infection. Not only do they have to find ways to exploit the cellular machinery they need to establish infection (while often competing with the interests of the cell), they also have to deal with elaborate antiviral mechanisms that are triggered immediately upon entry of viral material into the cell. Many of these challenges are met by specialized viral enzymes that hijack or manipulate critical cellular systems, and it is therefore not surprising that the study of viruses has repeatedly led to insights into the biology of the cell itself, since viruses have had to "learn" how the cell works in order to survive.

One of the important cellular machineries that is manipulated by viruses is the ubiquitin (Ub) system. Ubiquitination involves the covalent attachment of the C-terminal Gly76 residue of Ub via an isopeptide bond to the ε-amino group of a Lys residue or the α-amino group of the N-terminal residue of a protein substrate (1). Ub is a small, 76 amino acid protein that is highly conserved, stable, structured and ubiquitously expressed in virtually all cell types. It adopts a β-grasp fold, consisting of a mixed β-sheet structured around a central α-helix, and harbours a C-terminal diGly motif (**Figure 1.1 A**). An exposed hydrophobic patch is centralized around residue Ile44 (frequently referred to as the Ile44 patch) and often facilitates recognition by Ub-binding domains **(Figure 1.1 A**) (2,3). The process of Ub conjugation to substrates is regulated

by the E1, E2 and E3 enzymatic cascade leading to (multi)monoubiquitination, or formation of polyUb chains upon the modification of a substrate-attached Ub at Met1, Lys6, Lys11, Lys27, Lys29, Lys33, Lys48, Lys63 residues on Ub (1,4,5). PolyUb chains can be homogeneous when Ub is attached to the same lysine residue on each Ub in the chain, however mixed-linkage polyUb chains and branched Ub chains can also be formed (6). Classically, Lys48-linked chains adopt compact conformations (**Figure 1.1 B**) and play an important role in proteasomal degradation whereas Lys63-linked chains adopt an extended conformation **(Figure 1.1 C**), and have been implicated in positively mediating signal transduction (1). Both types of ubiquitination are involved in regulating the signaling that directs the antiviral innate immune response (7,8). Additional Ub-like proteins (UBLs) such as SUMO or NEDD8 are structured around a β-grasp fold and possess a C-terminal diGly motif similar to Ub, which allows for covalent conjugation to substrates by their respective E1, E2 and E3 enzymes (9-11). In contrast, the UBL protein Interferon-stimulated gene 15 (ISG15) is comprised of two tandem Ub-like folds that are connected by a short linker, however it retains the distinctive diGly motif at its C-terminus for attachment to target proteins (**Figure 1.1 D**). While ISG15 conjugation has been shown to mediate protection from a number of viruses in mice (reviewed in (12) and (13)), its role in antiviral immunity remains poorly understood. Interetsingly, human ISG15 deficiencies do not appear to alter susceptibility to viral infections (14), and curiously, soluble ISG15 in fact appears to downregulate IFN signaling (15).

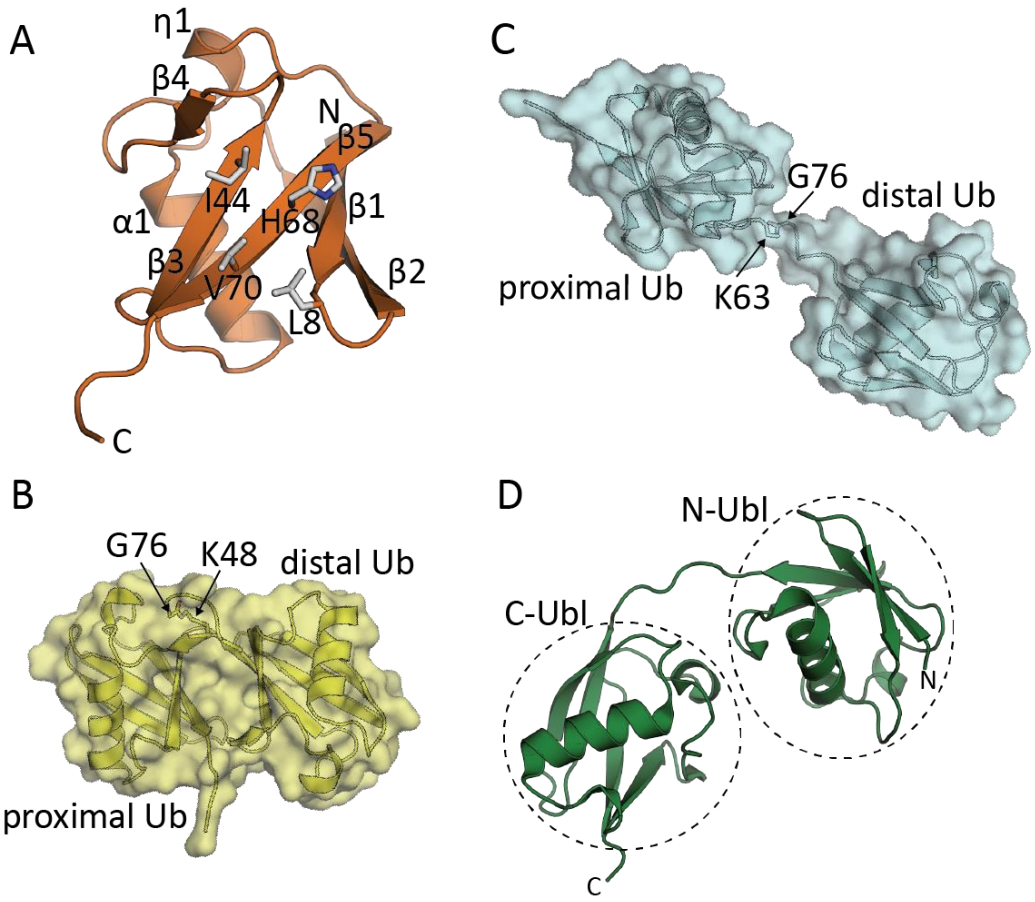

Figure 1.1 Structure of Ub and ISG15.
(A) Ubiquitin (PDB ID: 1UBQ) is shown in cartoon representation, with the residues forming the Ile44 patch shown as sticks. (B) Crystal structure of the compact, Lys48-linked diUb (PDB ID: 1AAR) is shown as a cartoon with transparent surface, with the isopeptide bond between Lys48 and Gly76 indicated**. (**C) Crystal structure of the extended, Lys63-linked diUb (PDB ID: 2JF5) is shown as a cartoon with transparent surface, with the isopeptide bond between Lys63 and Gly76 indicated. The proximal (that which is closer to the substrate) and distal (that which is further from the substrate) Ub moietys in the diUb molecule are also indicated. (D) crystal structure of ISG15 (PDB ID: 1Z2M) is shown as cartoon, with the N- and C-terminal Ub-like domains indicated. All structural images were generated using PyMOL (16).

The ubiquitination process is highly dynamic and reversible, allowing cells to regulate signal transduction pathways as a response to different stimuli such as virus infections. Deubiquitinating enzymes (DUBs) catalyze the removal of Ub or UBLs from cellular substrates, resulting in either complete deubiquitination or editing/trimming of Ub chains (17). Around 100 human DUBs can be classified into five major families based on their catalytic mechanism and structural features (17,18). The majority of DUBs are cysteine proteases, which contain an active site catalytic dyad comprised of a Cys nucleophile and a His base arranged in close proximity. The His appears to activate the Cys nucleophile by lowering the pKa of the sidechain and stabilizing the negatively charged thiolate (17). Often a third polar residue is present, which likely helps orient the His residue appropriately to facilitate activation of the nucleophile (17). The Cys protease DUB families include Ub-specific proteases (USPs), ovarian tumour proteases (OTUs), Ub C-terminal hydrolases (UCHs) and Machado-Joseph disease proteases (MJDs); whereas, the fifth family of DUBs consisting of JAB1/MPN/MOV34 (JAMM) are metalloproteases. More than half of the human DUBs belong to the USP family, and generally cleave all Ub linkage types without a clear preference (19). This is in contrast to the sixteen human OTU DUBs that hydrolyse defined subsets of Ub linkage types (20).

Almost all important cellular processes are regulated (in part) by ubiquitination. Whether it is, for example, gene expression, protein trafficking, protein degradation, autophagy, cell cycle progression, programmed cell death, cell survival, or innate immune response, all are regulated by Ub and/or UBLs, either positively or negatively, or both. As viruses are extensively using or dealing with some, if not all, of these processes during infection, it is not surprising that several interactions between viruses and the Ub(-like) system in the context of these kinds of cellular processes have been identified. These interactions have been reviewed from several different

perspectives by others (21-30). In particular, however, from all these data it has become apparent that Ub-mediated regulation of the antiviral innate immune response may be one of the most important targets of viral manipulation.

1.1.2 Antiviral innate immune response and its regulation by ubiquitin

The innate immune system of host cells is triggered upon infections with pathogens such as parasites, bacteria and viruses. In the case of viruses, sensing of viral proteins or specific forms of viral nucleic acid will initiate activation of the innate immune response leading to expression of antiviral molecules, including interferons (IFNs), pro-inflammatory cytokines and chemokines (31). Type-I interferons (IFN-α/β) will induce an antiviral state by upregulating the expression of hundreds of interferon stimulated genes (ISGSs) in infected and neighbouring cells to limit virus replication and spread (32). Furthermore, the adaptive immune system becomes activated, promoting antigen presentation and developing effective T and B cell responses that may ultimately result in clearance of the virus. Excessive activation of the innate immune system can, however, cause chronic inflammation and autoimmune disorders (33), and antiviral signaling pathways are therefore strictly regulated. Key mechanisms that trigger and fine-tune these immune responses in eukaryotes are the post-translational phosphorylation and ubiquitination of cellular immune factors, which can alter their interaction, localization, stability or activity (**Figure 1.2**)(7,8,34-36).

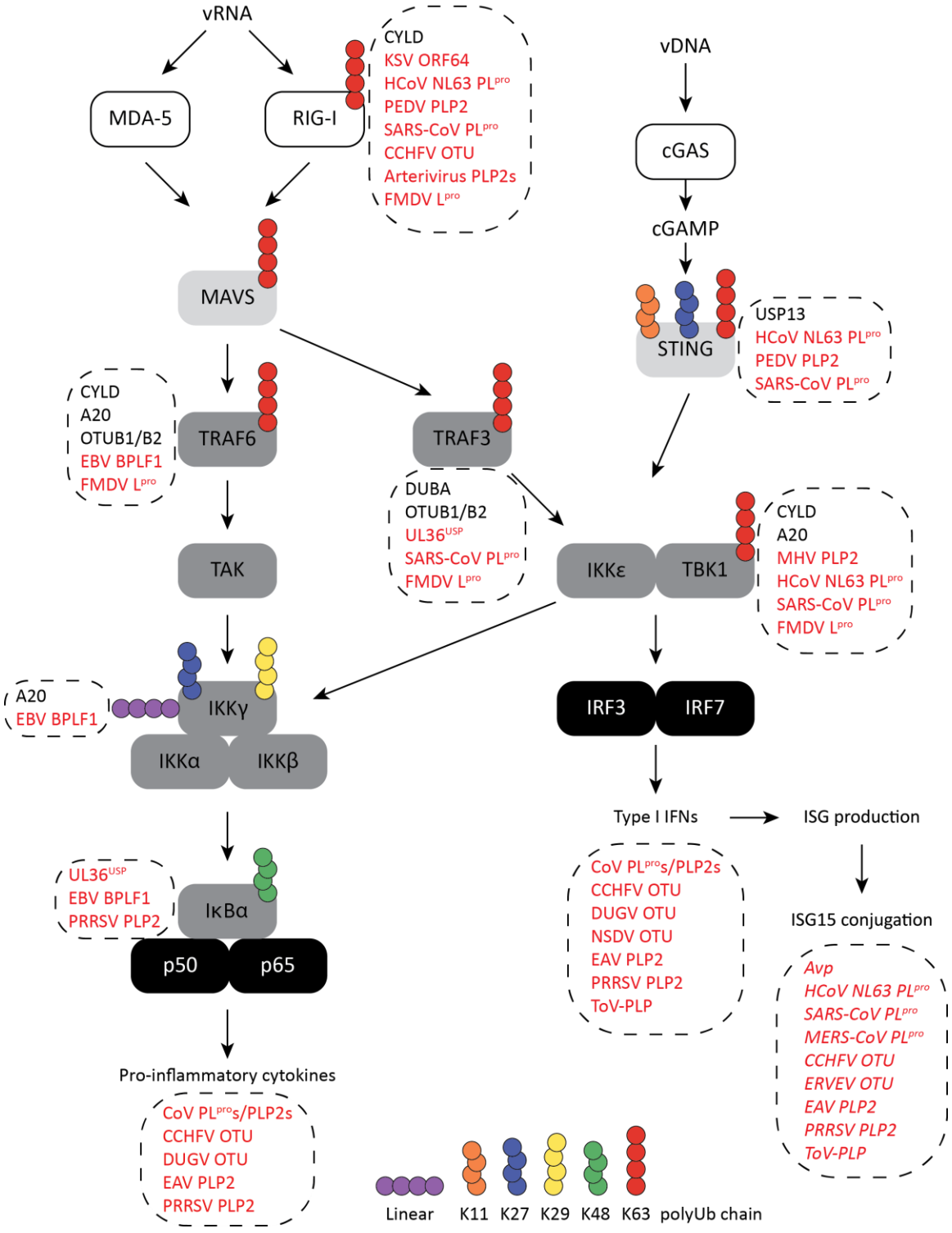

Figure 1.2 Illustration of the activation of the innate immune response and its manipulation by human or viral DUBs.

White boxes highlight the cytoplasmic receptors RIG-I, MDA5 and cGAS that can sense viral RNA or DNA via adaptor proteins MAVS or STING, in light grey, which in turn activate kinase complexes (partly depicted in dark grey). Ultimately, transcription factors IRF3, IRF7, p50 and p65 (black boxes) are activated and translocate to the nucleus to induce the transcription of type I IFNs and pro-inflammatory cytokines. Differently linked polyUb chains involved in the activation of the innate immune response are shown by the different colored polyUb chains. Dashed boxes placed next to innate immune signaling factors contain human or viral DUBs that remove Ub chains from these specific targets. DUBs placed below the type I IFN or NF-κB pathway (inducing the expressing of pro-inflammatory cytokines) interfere with these pathways without knowing their exact substrate(s). Human DUBs are shown in black, vDUBs in red and vDUBs having deISGylating activity are shown in red italic.

The first step of the innate immune response is the detection of pathogen-associated molecular patterns by a large repertoire of pattern-recognition receptors (PRRs) present on immune and non-immune cells. On the surface, and in endosomal compartments of immune cells, toll-like receptors (TLRs) play an important role as viral PRRs. Subsequent signaling is directed via MyD88, TIR-domain-containing adaptor-inducing IFN-β (TRIF), interleukin-1 receptor-associated kinase 1 (IRAK1) and -4, and receptor-interacting protein 1 (RIP1), ultimately leading to production of type-I IFNs. Intra-cytosolic sensors for the detection of viral nucleic acids in virtually all cells are RIG-I-like receptors (RLRs), NOD-like receptors and viral DNA sensors (cyclic-GMP-AMP synthase (cGAS) and IFI16 are the key sensors) (37,38). RLRs include retinoic acid-inducible gene I (RIG-I) and melanoma differentiation factor 5 (MDA5), which bind different forms of viral RNA leading to their activation and oligomerization that will induce the interaction with mitochondrial antiviral signaling protein (MAVS). MAVS recruits signaling molecules such as E3 ligases of the TNF receptor-associated factor (TRAF) protein family to activate kinase complexes. TRAF6 will recruit the TAK complex that will phosphorylate inhibitor of NF-κB kinase γ (IKKγ) (also known as NF-κB essential modulator (NEMO)) which in turn will form a complex with IKKα/β. This complex will initiate degradation of the NF-κB inhibitor IκBα, which frees NF-κB to promote transcription of pro-inflammatory cytokines. Another protein recruited to MAVS, TRAF3, activates a complex comprised of TANK-binding kinase 1(TBK1)/IKKε to phosphorylate interferon regulatory factor 3 (IRF3) and IRF7. Phosphorylation enables the IRF transcription factors to dimerize and induce the expression of type I IFNs in concert with NF-κB (31,36). Secreted IFN-α/β will bind to IFN receptors and activate the Janus kinase–signal transducer and activator of transcription pathway resulting in the transcription of ISGs. ISG-encoded proteins, including ISG15, have antiviral

activity by interfering with processes like viral replication or translation (32). With respect to the detection of DNA viruses, virus-derived cytosolic DNA binds to sensor cGAS, which stimulates the synthesis of cyclic-GMP-AMP (cGAMP) (39). cGAMP then activates stimulator of interferon genes (STING), a membrane bound protein on the endoplasmic reticulum (ER), which recruits TBK1 and initiates IRF3-mediated transcription of type I IFNs and pro-inflammatory cytokines.

Activation of innate immune signaling is regulated, besides by phosphorylation, through ubiquitination performed by specialized E3 ligases such as the members of the family of TRIM E3 ligases (40). These and several other E3s conjugate Lys63-linked and Lys48-linked Ub chains to RIG-I, MAVS, TBK1 and STING, as well as MyD88, TRIF, IRAK1 and RIP1, while TRAF3 and 6 induce their Lys63-linked auto-ubiquitination, which triggers activation (7,8,36). IκBα is degraded by the proteasome after Lys48-linked Ub chains are conjugated, which enables downstream signaling (41). Atypical Ub chains also play a role in activation of the innate immune response since NEMO is a substrate for conjugation by Lys27, Lys29 and linear polyUb chains, and STING can be modified with Lys11 and Lys27 polyUb chains (42,43). Besides conjugated Ub, unanchored ubiquitin chains (Lys63- or Lys48-linked) also seem to play a role in the regulation of innate immune signaling by providing a multimeric scaffold for activation of RIG-I and MDA-5 complexes (44-46). In addition, ubiquitination of IRF3 has been observed, and implicated in the induction of cellular proapoptotic pathways (47), and in the negative regulation of IFN-β signalling (48).

Negative regulation of the innate immune response is achieved by conjugation of Lys48-linked polyUb to degrade signaling factors and thereby dampen expression of type I IFNs and pro-inflammatory cytokines. Additionally, actions of E3 ligases that attach different Ub linkage

chains can be counteracted by several specific cellular DUBs (7,49). CYLD (USP) is able to cleave linear and Lys63-linked Ub chains and it deubiquitinates RIG-I, TRAFs and TBK1 (50). OTUB2 (an OTU domain containing DUB) removes Lys63-linked Ub chains from TRAF3 and TRAF6, as well as does OTUB1, however *in vitro* this latter enzyme preferentially cleaves Lys48-linked Ub chains (20). Interference with the Lys63-linked autoubiquitination of TRAF3 is performed by DUBA (OTUD5), which interacts with TRAF3 (51). A20 is a complex regulator since it contains an OTU domain at its N-terminus that cleaves Lys63-linked polyUb chains, as well as a C-terminal E3 ligase domain for conjugating Lys48-linked Ub (52,53). Deubiquitination of TRAF6 and NEMO by A20 leads to suppression of NF-κB activation. A20 also disrupts the activation of TBK1 complexes containing TRAF3 however the interference mechanism is unknown (54). Additionally, A20 can also bind to specific E2 enzymes and induce their degradation as a mechanism to prevent ubiquitination of other proteins (55). Several more DUBs that play a role in the regulation of the immune response have been identified such as OTU DUBs Cezanne, OTULIN and UPS DUBs USP3, 13 and 21 (7,56-59). Mutations in genes encoding DUBs involved in negative regulation of innate immune signaling, like CYLD and A20, can lead to the development of diseases including cancer, autoimmune and inflammatory disorders, highlighting the importance of DUB-controlled immune signaling (60,61).

1.1.3 Virus-encoded DUBs

Constant co-evolution of hosts and pathogens both shape the cellular antiviral system in order to efficiently eliminate invading pathogens as well as the pathogens that will evolve and adapt to facilitate efficient replication of their genomes (62). In particular, viruses with an RNA genome have a high mutation frequency, which is triggered by the lack of proof-reading activity in the viral RNA polymerases that drive their replication (63). As a result, virus populations are

genetically diverse, enabling them to rapidly adapt to changing circumstances. This also enables viruses to acquire diverse genes from various sources or evolve viral enzymes to expand their activities (64). Mechanisms to avoid or delay activation of the innate immune system are exploited by viruses to manipulate the host cell environment (65,66). Modifying Ub signaling to evade activation of the innate immune response is used by both DNA and RNA viruses, and methods include for example blocking activity or hijacking host E3 ligases or DUBs (67). Another elaborate viral approach is the expression of virus-encoded E3 ligases or DUBs that can suppress the innate immune response, but also potentially affect many other Ub-dependent signaling pathways in the host (67-69). In this review, we focus on virus-encoded DUBs (listed in **Table 1.1**) that have been identified in DNA viruses (adeno- and herpes-viruses) and RNA viruses (corona-, arteri-, nairo-, picorna- and tymo-viruses), with an emphasis on the structural biology of these viral DUBs (vDUBs) and their (potential) innate immune suppressive mechanisms.

Table 1.1 Viral deubiquitinating enzymes and their characterized structures and substrates

Virus family/genus	Virus	DUB domain	Location	In vitro DUB activity	Cellular targets	PDB ID
Adenoviridae	Human adenovirus	Avp	L3 gene product p23	Lys48 polyUb, ISG15(70)	Histone H2A (70)	1AVP, 1NLN, 4EKF, 4PID, 4PIE, 4PIQ, 4PIS, 5FGY, 4WX4, 4WX6, 4WX7
Herpesviridae / alphaherpesviruses	Human herpes simplex virus 1	$UL36^{USP}$	N-terminus of viral tegument protein	Lys48 polyUb (71,72), Lys63 polyUb (72)	TRAF3 (73), IκBα (74)	
	Marek's disease virus	MDV^{USP}		N/A	Unknown	
	Pseudorabies virus	pUL36		N/A	Unknown	
Herpesviridae / betaherpesviruses	Murine Cytomegalovirus	$M48^{USP}$	N-terminus of viral tegument protein	Lys48/63 diUb (75)	Unknown	2J7Q
	Human Cytomegalovirus	$UL48^{USP}$		Lys48/63 polyUb (72)	Unknown	
Herpesviridae / gammaherpesviruses	Epstein-Barr virus	BPLF1	N-terminus of viral tegument protein	Lys48/63 polyUb (76), NEDD8 (77)	EBV ribonucleotide reductase (76), PCNA (78), Cullin (77), TRAF6 (79,80), NEMO, IκBα (80)	

	Kaposi's sarcoma-associated herpesvirus	KSV Orf64		Lys48/63 polyUb (81)	RIG-I (82)	
	Murine gammaherpes virus 68	ORF64^{USP}		N/A	Unknown	
Coronaviridae / alphacoronaviruses	Human coronavirus NL63	HCoV-NL63 PLP2	Membrane- associated nsp3 that is part of the replication-transcription complex	Lys48/63 polyUb (83,84), ISG15 (85)	RIG-I, TBK1, IRF3, STING (86)	
	Porcine epidemic diarrhea virus	PEDV PLP2		N/A	RIG-I, STING (87)	
	Porcine transmissible gastroenteritis coronavirus	TGEV PL1^{pro}		Lys48/63 polyUb (88)	Unknown	3MP2
Coronaviridae / betacoronaviruses	Severe acute respiratory syndrome coronavirus	SARS-CoV PL^{pro}	Membrane- associated nsp3 that is part of the replication-transcription complex	Lys48 polyUb (89-91), Lys63 polyUb (91), ISG15 (89,91), Lys6/11/27/29/33/48/63 diUb (90)	RIG-I, TRAF3, STING, TBK1, IRF3 (92)	4M0W, 5E6J, 3E9S, 3MJ5, 4MM3, 4OVZ, 4OW0, 2FE8, 5TL6, 5TL7
	Middle East respiratory syndrome coronavirus	MERS-CoV PL^{pro}		Lys6/11/29/33/48/63 diUb (90), Lys48 polyUb (90,91,93), Lys63 polyUb (91,93), ISG15 (91)	Unknown	4P16, 4PT5, 4R3D, 4REZ, 4RF0, 4RF1, 4RNA, 4WUR
	Mouse hepatitis virus	MHV PLP2		Lys11/48/63 diUb (94)	IRF3 (95), TBK1 (96)	4YPT
Coronaviridae / gammacoronaviruses	Avian infectious bronchitis virus	IBV PL^{pro}	Membrane- associated nsp3 that is part of the replication-transcription complex	Lys48/63 polyUb (97,98)	Unknown	4X2Z 5BZ0

Arteriviridae	Equine arteritis virus	EAV PLP2	N-terminal region of membrane-associated nsp2 that is part of the replication-transcription complex	Lys48/63 polyUb (99)	RIG-I (99)	4IUM
	Porcine reproductive and respiratory syndrome virus	PRRSV PLP2		Lys6/11/27/29/33/48/63 diUb, Lys48/63 polyUb (100)	IκBα (101), RIG-I (99)	
	Lactate dehydrogenase-elevating virus	LDV PLP2		N/A	RIG-I (99)	
	Simian hemorrhagic fever virus	SHFV PLP2		N/A	RIG-I (99)	
Bunyaviridae / Nairoviruses	Crimean-Congo hemorrhagic fever virus	CCHFV OTU	N-terminal region of RNA-dependent RNA polymerase-containing L-segment	Lys48/63 polyUb (102-104), ISG15 (102-106), Lys6/11 diUb (104), Lys63 diUb (103,104,106)l Lys48 diUb (103,104)	RIG-I (99)	3PHU, 3PHW, 3PHX, 3PT2, 3PSE, 3PRM, 3PRP
	Dugbe virus	DUGV OTU		Lys48/63 polyUb (102-104), ISG15 (102-106), Lys6/11 diUb (104), Lys63 diUb (103,104,106), Lys48 diUb (103,104)	Unknown	4HXD, 3ZNH
	Erve virus	ERVEV OTU		ISG15 (104)	Unknown	5JZE
	Nairobi sheep disease virus	NSDV OTU		N/A	Unknown	
Picornaviridae	Foot-and-mouth disease virus	FMDV L^{pro}	N-terminus of polyprotein	Lys48/63 polyUb (107)	RIG-I, TBK1, TRAF3, TRAF6 (107)	1QOL, 4QBB, 1QMY

	Enterovirus G	ToV-PLP	2C/3A junction of the Enterovirus G polyprotein	Met1/Lys48/63 polyUb, ISG15 (108)	Unknown	
Tymoviridae	Turnip yellow mosaic virus	TYMV PRO	Non-structural protein p206	Lys48/63 polyUb (104,109)	TYMV p66 (109)	4A5U

1.2 Adenoviridae

Adenoviruses (AdVs) are non-enveloped, double stranded DNA (dsDNA) viruses, with their genomes encapsulated in an icosahedral protein shell. Infection by human AdV generally causes mild respiratory disease, although life-threatening disease can occur in immunocompromised individuals. The ability of AdV infection to efficiently stimulate cellular and humoral immune responses, coupled with the relative ease of genetic manipulation and large genome size has led to their intensive investigation as gene delivery vectors (110).

Following virus entry and the onset of genome replication, adenoviruses AdVs rely on the expression of late genes that are primarily responsible for the production of structural proteins involved in virion assembly (111). Following assembly, capsid proteins are proteolytically processed yielding infectious viral particles, a feat accomplished through the activity of the AdV cysteine protease Avp (112). Initial efforts characterizing Avp determined consensus sequences of (M,L,I)XGX↓G and (M,L,I)XGG↓X (113), and further studies identified two viral co-factors that are required for recombinant Avp activity *in vitro*: AdV DNA, and an 11 amino acid peptide derived from the C-terminus of the Avp substrate precursor protein pVI (pVIc) (114).

During viral infection, antigen presentation via cellular major histocompatibility complex class I (MHC-I) is reliant on the degradation of viral peptides via the Ub-proteasome system, and a number of viruses have been found to interfere with this process. Upon observing a reduction in Ub-conjugated proteins in AdV infected cells, Balakirev and coworkers hypothesized that Ad may employ a vDUB to interfere with cellular Ub-dependent processes (70). Using reversible Ub-based probes, Avp was identified as an AdV deubiquitinating enzyme capable of cleaving Lys48-linked tetra Ub chains as well as ISG15, thus providing the first example of a viral

protease with deubiquitinating activity (70). Indeed the demonstration of Avp DUB activity would be supported by the compatibility of the previously elucidated Avp consensus sequences with the C-terminal LRGG motif of Ub (113). The study also demonstrated a significant reduction in cellular levels of ubiquitinated histone H2A in AdV-infected HeLa cells, suggesting a potential ubiquitinated cellular target for Avp.

Ding and coworkers provided the first structural insights into Avp, crystallized in the presence of pIVc (**Figure 1.3 A**) (115). The structural complex revealed similarities with the archetypal cysteine protease papain, which contains a β-sheet "right" (R) and α-helical "left" (L) subdomain that pack together to form a cleft that leads toward the active site (**Figure 1.3 B,C**) (116). The Avp active site is comprised of residues His54, Glu71 and Cys122, which superpose closely with the catalytic triad of papain (**Figure 1.3 D**). A fourth residue, Gln115 is also present and proposed to participate in the formation of the oxyanion hole, which stabilizes the negatively charged tetrahedral intermediates that form during peptide bond hydrolysis. Later studies describing the structure of Avp in the absence of pVIc concluded that pVIc repositions a loop carrying active-site residue His54 to orient the residue towards an optimal geometry for catalysis (**Figure 1.3 A**) (117). The activating peptide pIVc binds Avp by forming a disulfide bridge with the β-sheet lobe of Avp and forming the sixth strand of the core β-sheet structure **(Figure 1.3 A**).

Despite the similarities between Avp and papain, their primary structures differ significantly, with the catalytic triad residues appearing in the order His-Glu-Cys in the case of Avp, compared to Cys-His-Asn in the case of papain. This prompted the establishment of a novel cysteine protease group (currently categorized as a clan CE protease within the MEROPS database) with Avp proposed as an exemplary case of convergent evolution (115). It has been noted however, that proteins with rearranged amino acid sequences, yet similar three-

dimensional structure may be related by circular permutation, which would suggest a common origin (118).

Currently, there is no direct structural evidence for the activation of Avp by DNA, although attempts at modeling these interactions have been made (119). Further structural work may be able to shed light on these questions. The implications of pVIc binding and Avp activation; however, are clearer, and it has been suggested that rational, structure-based efforts could guide the development of novel peptide-based inhibitors of Avp as a treatment for AdV infection (115).

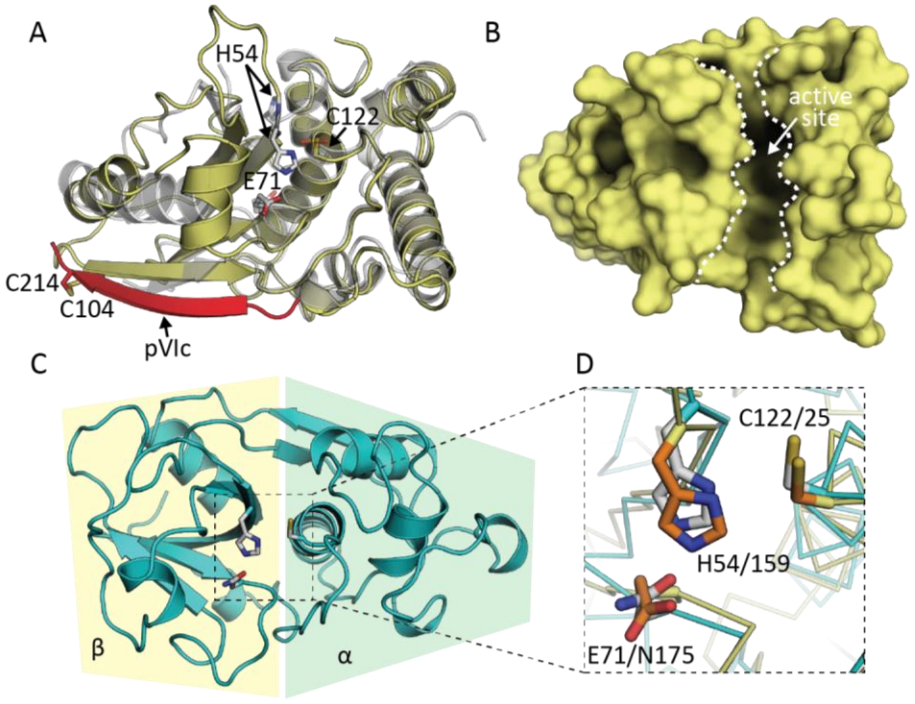

Figure 1.3 Crystal structure of adenovirus Avp.
(A) Superposition of Avp bound to activating peptide pVIc (PDB ID: 1AVP; yellow and red, respectively) and Avp in the absence of pVIc (PDB ID: 4EKF; transparent gray). Active site residues are shown as sticks in both structures, and the disulphide bridge between Avp and pVIc is indicated. (B) Surface representation of Avp (PDB ID: 1AVP). Dashed white lines highlight the active site cleft. (C) Crystal structure of papain (PDB ID: 1PPN). The left (L) α-helical domain and right (R) β-sheet domain are indicated by green and yellow boxes, respectively. (D) Superposition of the active site residues of Avp (yellow) and papain (cyan). Active site residues of papain are shown as gray sticks, and those of Avp are shown as orange sticks. Avp residues are indicated, followed by the equivalent residues of papain. Papain and Avp structures were aligned using the SPalign-NS server (120).

1.3 Herpesviridae

Herpesviruses are large DNA viruses, with dsDNA genomes ranging from 124 to 295 kb (111). The *herpesviridae* family consists of a subset of viruses within the order *Herpesvirales* that infect mammals, birds and reptiles (111). The *herpesviridae* family is further divided into subfamilies, namely the *alpha- beta-* and *gammaherpesvirinae,* on the basis of shared biological characteristics. The herpesvirus virion structure is composed of an icosahedral nucleocapsid hosting the viral genome, which is surrounded by the viral matrix, or tegument, and contained within the viral envelope. All herpesviruses can establish life-long infections in their respective hosts, remaining latent until periods of reactivation.

A number of herpesviruses are important human pathogens. Primary infection by Herpes simplex virus 1 (HSV-1) causes cold sores, which is followed by a period of latency where the virus remains dormant within sensory neurons awaiting reactivation. Reactivation can be provoked via a number of external stimuli, allowing for viral replication and transmission to resume (121). Epstein-Barr virus (EBV) was the first recognized tumor-causing virus to infect humans, and has been associated with a number of diseases affecting B-cells, including Burkitt's Lymphoma, as well as Hodgkins and non-Hodgkins lymphomas (122).

Several examples of herpesviral DUBs are described below, which are all homologues of each other. Herpesviruses have large genomes, and some may code for up to three different deubiquitinating enzymes (123), which emphasizes the apparent importance of DUB activity to these viruses (21).

1.3.1 Herpes simplex virus 1 UL36^{USP}

Seminal work by Borodovsky and coworkers provided a means to rapidly identify deubiquitinating enzymes from cellular extracts (124). Using intein-mediated chemical ligation,

Ub-derivative substrates were fashioned to contain a thiol-reactive group in place of the C-terminal Gly76 residue, which when exposed to a catalytically competent DUB formed a covalent linkage between the Ub-based probe and the active site thiol of the target enzyme (124). The resulting adducts could then be immunoprecipitated and identified by mass spectrometry (124,125). Using their probes, a Ub-reactive ~47 kDa product was identified in lysates of cells infected with HSV-1 (71). The product mapped to the N-terminus of the HSV-1 gene product expressed from the UL36 open reading frame and was subsequently termed UL36^{USP} on the basis of its reactivity with Ub (71). Interestingly, the UL36 ORF encodes for a 3164 amino acid tegument protein, and the identification of a 47 kDa HSV-1 gene product clearly indicated the occurrence of a post-translation cleavage event, although the enzyme responsible for this cleavage remains unknown. UL36^{USP} was found to be active toward both Lys48- and Lys63-linked polyUb chains, with a preference for Lys63 linkages (71,72).

Infection by herpesviruses is detected by different PRRs; however, herpesviruses are able to evade detection by the innate immune system to establish persistent infections (126). Wang *et al.* demonstrated that ectopic expression of UL36^{USP} decreased Sendai virus-mediated production of IFN-β, indicating that UL36^{USP} is involved in modulation of cellular innate immune signaling pathways (73). To probe the role of UL36^{USP} during an infection, the authors used an HSV-1 bacterial artificial chromosome (BAC) system to generate recombinant HSV-1 with a catalytically inactive UL36^{USP} (Cys40Ala). Infections with the UL36^{USP} knockout virus resulted in increased production of IFN-β, while virus containing wild-type UL36^{USP} impaired cellular IFN-β production, demonstrating that UL36^{USP} is an IFN antagonist (73). To further elucidate the role of UL36^{USP}, reporter assays confirmed that UL36^{USP} interfered with IFN-β promoter activation at a level between MAVS and TBK1, possibly via deubiquitination of TRAF3, and

inhibited activity of both IRF- and NF-κB-responsive promoters (73). Later work demonstrated that UL36^{USP} also inhibits NF-κB signaling at a level between IKK and p65 (74). Consistent with this observation, expression of UL36^{USP} resulted in a reduction in the levels of Ub-conjugated IκBα (74).

UL36^{USP} also demonstrated a role in interfering with the STING pathway involved in detection of cytoplasmic viral DNA. UL36^{USP} inhibited cGAS/STING mediated activation of IFN-β and NF-κB-responsive promoters, and reduced production of IFN-β and IL-6 mRNA transcripts (74), presumably through deubiquitination of IκBα.

1.3.2 Murine cytomegalovirus M48^{USP}

Homologues of UL36^{USP} are predicted to exist among all members of the herpesviridae family on the basis of sequence similarity and the absolute conservation of putative catalytic Cys and His residues (127). Indeed, Schlieker *et al.* confirmed the DUB activity of the homologues murine cytomegalovirus (MCMV) M48^{USP} domain using a fluorogenic Ub substrate (127) and later Lys48- and Lys63-linked diUb and cellular Ub conjugates (75). Subsequent determination of the crystal structure of the enzyme bound to Ub vinylmethylester (UbVME) offered the first insights into the structure of a herpesvirus DUB (**Figure 1.4**) (75). M48^{USP} shares little overall structural similarity to other cysteine proteases of known structure. It consists of a central β-sheet sandwiched between two α-helical domains, and the authors proposed M48^{USP} to be a member of a novel class of DUBs, termed herpesvirus tegument USPs (htUSPs). Importantly, the M48^{USP}-Ub structure revealed how the vDUB recognises Ub. The C-terminal extension of Ub binds into a cleft formed between the β-sheet and an α-helical subdomain of M48^{USP}, and recognition of

the hydrophobic Ile44 patch of Ub is facilitated by a unique β-hairpin extending from an 8-stranded β-sheet of the $M48^{USP}$ core (**Figure 1.4**).

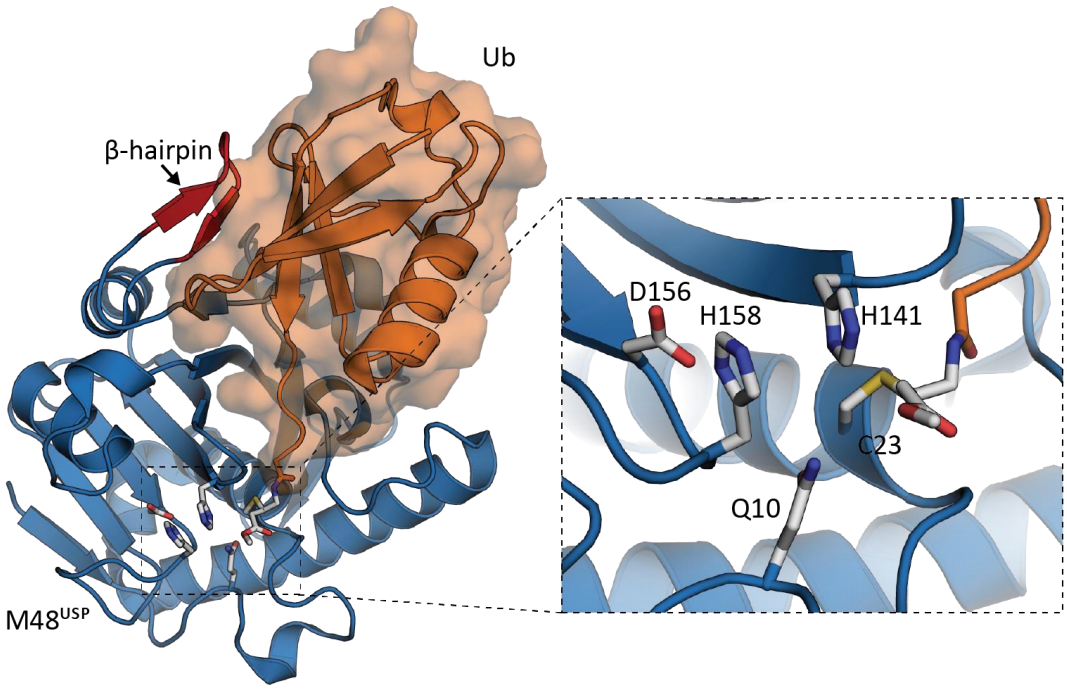

Figure 1.4 Crystal structure of MCMV M48^{USP} in complex with Ub.
MCMV M48^{USP} (PDB ID: 2J7Q; blue cartoon) shown in covalent complex with Ub (orange cartoon with transparent surface representation). The unique β-hairpin of M48^{USP} interacting with the Ile44 patch of Ub is coloured in red. Dashed box contains a close-up of the M48^{USP} active site, with catalytic residues shown as sticks, including the two catalytic bases His158 and His141. Also shown is Gln10 suggested to take part in the formation of the oxyanion hole.

Perhaps the most striking feature of M48^{USP} is the organisation of its catalytic triad. While residue His141, the predicted general base, is spatially conserved with respect to the active site of most papain-like proteases, mutational analysis suggested that His158, also positioned near the Cys nucleophile, could act as a catalytic base, although the authors cautioned that both His residues might participate in catalysis (**Figure 1.4**) (75). In addition, a glutamine (Gln10) residue near the active site was suggested to contribute to the formation of the oxyanion hole, due to its position and strict conservation throughout homologous herpesvirus proteases.

Investigations into the role of M48^{USP} *in vivo* have shown that abrogating the catalytic activity of the vDUB results in significantly attenuated MCMV replication in mice (128). This replication deficiency *in vivo* was attributed in part to increased levels of MCK2, an MCMV encoded pro-inflammatory chemokine (128). M48^{USP} was postulated to be responsible for the careful regulation of MCK2 production and secretion in a mechanism at least partially dependent on proteolytic activity, as evidenced by the accumulation of unglycosylated MCK2 in infected cells but not with M48^{USP} mutant virus, further emphasizing the critical role of vDUBs in regulating inflammatory processes, and the requirement that these processes be carefully controlled to facilitate productive infection (128). While these efforts have provided valuable insight toward the role of M48^{USP} during infection, the specific targets of the vDUB remain to be determined.

1.3.3 Epstein-Barr virus BPLF1

Concomitant with the discovery of MCMV and HSV-1 DUBs, a bona fide deubiquitinase was identified in EBV, a representative of the gammaherpesvirus subfamily (127). Earlier studies using yeast two-hybrid screens identified the interaction of BPLF1, a UL36^{USP} homologue, with the EBV ribonucleotide reductase (RR) (129). EBV RR is composed of a large (RR1) and small

(RR2) subunit, and BPLF1 was shown to reduce cellular levels of ubiquitinated RR1 and thereby inhibit EBV RR activity in a protease-dependent manner. The activity of BPLF1 toward Lys63- and Lys48-linked polyUb partially explained the ability of BPLF1 to inhibit host enzymatic activity via Lys63-linked Ub deconjugation (76).

Interestingly, using GFP-based fluorescence cell culture assays, Gastaldello *et al.* identified BPLF1 as a potent deneddylase that could efficiently remove the Ub-like protein NEDD8 from Cullin, a scaffold protein involved in the formation of Cullin-RING Ub ligases (CRLs) (77). Cullins are well characterized NEDD8 substrates, and CRL activity can be dependent on neddylation (130). BPLF1-mediated deneddylation stabilized CRL substrates, likely via inhibition of CRL-mediated ubiquitination. Of these stabilized substrates, CDT1, a cellular licencing factor required for DNA replication and entrance into S-phase was found to be required for EBV replication (77). EBV BPLF1 was thus found to stabilize host factors critical for the establishment of a cellular environment permissive to EBV replication. Subsequent characterization of an EBV ΔBPLF1 virus revealed it to have severely reduced infectivity and delayed transformation of B-cells (131).

In addition to a role in cell cycle regulation, expression of BPLF1 has been shown to reduce monoubiquitination of proliferating cell nuclear antigen (PCNA) and prevent polymerase recruitment during DNA damage repair (78). Further, BPLF1 has been implicated in the inhibition of the host innate immune response to viral infection. Saito and coworkers demonstrated that over-expression of BPLF1 reduced cellular levels of ubiquitinated TRAF6, inhibiting NF-κB activation and promoting viral replication (79), while others have shown BPLF1 to inhibit TLR signaling likely via deubiquitination of downstream signaling components

(80). Besides BPLF1, EBV may express two other proteins with DUB activity, BSLF1 and BXLF1, but further investigation into their relevance is necessary (123).

1.3.4 Additional deubiquitinating enzymes in the Herpesviridae family

Homologues of UL36^{USP} with confirmed deubiquitinating activity have been identified in human cytomegalovirus (HCMV), murine gammaherpes virus 68 (MHV-68), Marek's disease virus (MDV) and Kaposi's sarcoma virus (KSV) (81,132-134). UL48^{USP} and ORF64^{USP} from HCMV and KSV, respectively, were both found to process Lys48- and Lys63-linked polyUb chains *in vitro* (72,81), and KSV ORF64^{USP} was found to target RIG-I, thereby inhibiting IFN-β and NF-κB promoter activity (82). Recombinant viruses harbouring active site mutations within their respective DUB domains have shed light on the role of herpesvirus DUBs *in vivo*. KSV virus with an active-site mutation in ORF64^{USP} implicated its DUB activity in the lytic replication cycle (81), while recombinant MDV with a catalytically inactive MDV^{USP} implicated DUB activity in the maintenance of cellular transformation *in vivo* (134). Further, an HCMV UL48^{USP} active site mutant decreased the production of infectious viral progeny during infection (132). Finally, while the DUB activity of the pseudorabies virus (PrV) pUL36 domain has yet to be confirmed *in vitro*, infection with a recombinant virus containing a Cys-Ser mutation at the catalytic nucleophile of pUL36 demonstrated delayed neuroinvasion in mice (135). Further investigation into the role of pUL36 *in vivo* using quantitative mass spectrometry identified Lys442 as a conserved, critical ubiquitination site on pUL36, with increased modification observed during infection with the catalytically inactive mutant virus (136). pUL36 was proposed to act as a Ub switch, with ubiquitination/deubiquitination at Lys442 controlling invasive states of PrV, and pUL36 DUB activity, and Lys442 ubiquitination acting as critical factors for neuroinvasion and retrograde axonal transport, respectively (136).

1.4 Coronaviridae

Coronaviruses (CoVs) are enveloped viruses within the order Nidovirales with the largest known positive-sense single-stranded RNA (ssRNA) genomes (26-34 kb). They are grouped further into *alpha-* *beta-* and *gammacoronavirus* lineages based on sequence similarity (111). A number of CoVs cause respiratory disease in humans. Notably, in November 2002 a case of atypical pneumonia in Guangdong, China (137) led to the identification of the severe acute respiratory syndrome coronavirus (SARS-CoV) (138-140), which rapidly caused a global pandemic. Ultimately, successful infection control measures brought the SARS-CoV pandemic to an end in July 2003. More recently, in June 2012 a novel CoV was isolated from a 60-year-old male from Saudi Arabia following a fatal case of severe pneumonia and renal failure (141). This virus, now referred to as Middle East respiratory syndrome coronavirus (MERS-CoV) has since led to 1917 confirmed cases and 684 deaths as of March 2017 (142). Currently no MERS- or SARS-CoV-specific therapies exist. Both MERS- and SARS-CoV are expected to have emerged into human populations through animal vectors, with camels and palm civets expected as the primary zoonotic sources, respectively (143,144).

The SARS-CoV outbreak prompted deeper investigation into CoVs as respiratory pathogens, and post-SARS, the human coronavirus NL63 (HCoV-NL63) was identified, with retrospective analysis suggesting the virus had been circulating in human populations for some time prior to its discovery (145). HCoV-NL63 is most closely related to HCoV-229E, which is one of two CoVs identified pre-SARS in the 1960s and recognized as a causative agent of the common cold (146). HCoV-NL63 has also been associated with croup in young children (147).

CoVs also cause disease in several animals. The neurotropic mouse hepatitis virus (MHV) strains JHM and A59, which group along with SARS-CoV in the *betacoronavirus* genus,

cause demyelinating encephalomyelitis in mice and have served as disease models for multiple sclerosis (148). The porcine transmissible gastroenteritis (TGEV) and porcine epidemic diarrhoea virus (PEDV) are *alphacoronaviruses* that cause significant financial burdens in the pork industry (149).

The non-structural proteins (nsps) of CoVs are encoded within two open reading frames, ORF1a and ORF1b, with translation yielding polyprotein 1a (pp1a) or pp1ab, the latter arising from a -1 ribosomal frameshift that provides access to ORF1b (150). The CoV polyproteins are post-translationally processed into functional nsps by protease domains encoded within, including a 3C-like cysteine protease ($3CL^{pro}$) which functions as the main protease, and either 1 or 2 additional papain-like proteases (PLPs), which are numbered sequentially according to their position within the polyprotein. In cases where only a single PLP is present, it is referred to simply as PL^{pro}.

1.4.1 Severe acute respiratory syndrome coronavirus PL^{pro}

Full-length genomic sequences from a number of clinical isolates of SARS-CoV became available shortly after the pandemic (151-153) and their analysis predicted the presence of a single papain-like protease (PL^{pro}) encoded within nsp3 (154). The absence of a second paralogous PLP domain, combined with an analysis of putative cleavage sites, suggested that PL^{pro} was responsible for cleaving 3 sites within the SARS-CoV polyprotein, and releasing nsp1, nsp2 and nsp3 from the viral polyprotein (154). This activity was soon confirmed experimentally, with PL^{pro} recognising the consensus site LXGG (155,156). Structural modelling of SARS-CoV PL^{pro} based on the crystal structure of the cellular deubiquitinating enzyme herpesvirus-associated ubiquitin-specific protease (HAUSP) suggested that the viral enzyme adopts a papain-like fold with a circularly permutated C4 zinc finger domain (157). The

structural similarity between PL^{pro} and a cellular DUB, along with the compatibility of the PL^{pro} consensus cleavage sequence with the C-terminal RLRGG motif of Ub, led to the hypothesis that PL^{pro} may possess DUB and possibly ISG15 deconjugating (deISGylating) activity (157) .

The *in vitro* DUB (89,158) and deISGylating (89) activities of PL^{pro} were confirmed in parallel by independent groups, demonstrating activity toward Lys48-linked Ub chains. This DUB activity has been implicated in the downregulation of cellular innate immune responses (159), consistent with the observation that SARS-CoV infection prevents IFN-β induction in infected cells (160). Devaraj and co-workers demonstrated that PL^{pro} inhibited RIG-I, MDA5 and TLR3-mediated IFN-β promoter activity, and interfered with signaling components specific to IRF3 activation (159). Interestingly, while their studies showed no effect on NF-κB-dependent transcripts, others found marked reduction in the activity of an NF-κB-responsive promoter in the presence of PL^{pro} (161). The role of PL^{pro} in the inhibition of IRF3 activation has been further investigated, and it has been suggested to deubiquitinate and inhibit the ability of constitutively active IRF3 to induce IFN-β promoter activity (162).

A crystal structure of SARS CoV PL^{pro} confirmed it to have domain organisation similar to HAUSP, which consists of a "thumb", "palm" and "fingers" subdomains that organise together to resemble an extended right hand (**Figure 1.5 A**) (163,164). The α-helical thumb and β-sheet palm domains pack together and host a Cys-His-Asp catalytic triad at their interface, with residues adopting a similar geometry to that found in papain, while the fingers domain harbours a circularly permutated C4 zinc finger as had been predicted (**Figure 1.5 A**) (157). Additionally, a tryptophan residue (Trp107) near the active site was found to be oriented such that the indole ring hydrogen was believed to form part of the oxyanion hole (**Figure 1.5 A**). Also situated near the active site was a six amino acid loop flanked by glycine residues. This

loop is also present in the cellular HAUSP and USP14, where it is termed blocking-loop 2 (BL2) (**Figure 1.5 A**), as it occludes the active site of USP14 in the absence of Ub, and is thus proposed to serve a regulatory function. In PL^{pro}, this loop is found to be in an "open" state, although molecular dynamic simulations predict that the loop samples both "open" and "closed" conformations (165). Intriguingly, the N-terminal domain of PL^{pro} adopts a Ub-like β-grasp fold, which packs against the thumb domain **(Figure 1.5 A)**. While little is known regarding the function of this domain, conflicting data have been reported showing either that this domain is required (161) or dispensable (84) for the immunomodulatory activity of PL^{pro}, although the Ub-like domain does not appear to be necessary with respect to DUB activity (90,161).

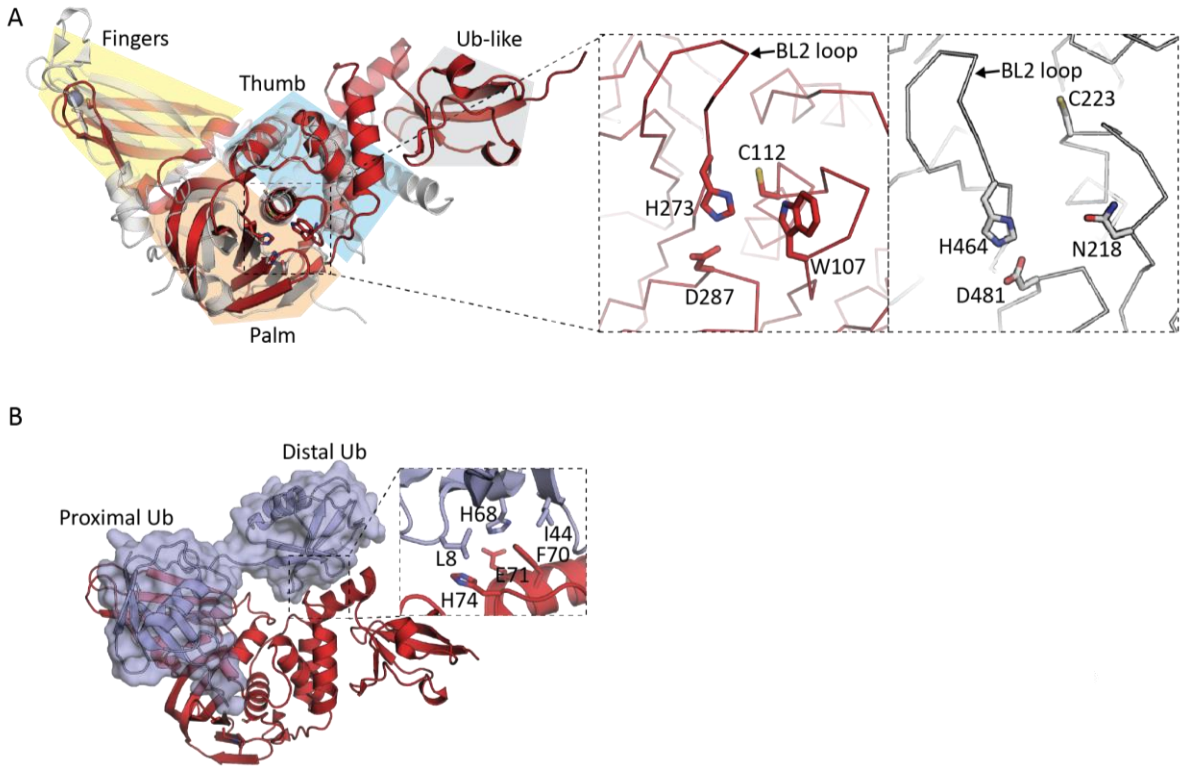

Figure 1.5 Crystal structures of zoonotic SARS- and MERS-CoV PL^{pro} domains.
(A) Superposition of SARS-CoV PL^{pro} (PDB ID: 2FE8; red) with HAUSP (PDB ID: 1NB8; transparent gray). Thumb, fingers, palm and Ub-like domain are indicated with blue, yellow, orange and gray shading, respectively. Inset is a close up of the SARS-CoV PL^{pro} (left panel) and HAUSP (right panel) active sites. Backbone atoms are shown as ribbons, and active site residues are shown as sticks. The BL2 loop is indicated with an arrow. (B) Crystal structure of the SARS-CoV Lys48-linked diUb complex (PDB ID: 5E6J). SARS-CoV PL^{pro} is shown in red, bound to Lys48-linked diUb, shown as a slate cartoon with transparent surface. Inset is a close up on the hydrophobic interactions occurring between PL^{pro} and the distal domain of Lys48-linked diUb, with relevant residues shown as sticks.

A crystal structure of a non-covalent SARS-CoV PL^{pro}-Ub complex showed that the C-terminal linear RLRGG peptide extending from the Ub substrate was bound at the interface between the α and β domains in cleft leading toward the active site (166), as previous modeling had predicted (163), with the BL2 loop undergoing significant conformational changes toward the C-terminus of Ub (166). Crystal structures of PL^{pro} bound to the C-terminal domain of human and mouse ISG15 (mISG15) have also now been reported, demonstrating that species-specific recognition of ISG15 molecules is mediated by unique interactions between PLpro and the respective ISG15s (167). Whether or not PL^{pro} also recognises the N-terminal domain of ISG15(s) remains to be investigated. Recently, the structural basis for Lys48-linked polyUb-binding of SARS-CoV PLpro was elucidated by the determination of the crystal structure of PL^{pro} in covalent complex with Lys48-diUb (168). The Lys48 diUb probe was fashioned with a cysteine-reactive alkyne at the C-terminus of the proximal Ub moiety, enabling covalent binding of the molecule to PL^{pro} and interaction of its individual Ub domains associated with S1 and S2 binding sites on the vDUB domain (**Figure 1.5 B**) (see (169) for nomenclature). Consistent with earlier predictions (170), the Lys48 diUb probe bound PLpro in an extended conformation, as opposed to the canonical compact conformation observed with most Lys48-linked Ub chains. Binding of the distal Ub moiety at the S2 site was governed by a number of solvent-exposed hydrophobic residues at the surface of an α-helix within the thumb domain, which associated with the Ile44 patch of Ub (**Figure 1.5 B**) (168,170). These studies supported earlier observations that Lys48-linked polyUb chains were processed into diUb moieties, and PLpro may recognize Lys48 diUb preferentially (90).

The involvement of PLpro in the maturation of the viral polyprotein, as well as its role in counteracting cellular antiviral signaling pathways have contributed to its recognition as a

promising target for therapeutic intervention, and the availability of X-ray crystallographic data (163,166), along with work describing the substrate specificity of PLpro at its cognate subsites (171,172) has contributed to such efforts. High-throughput screening of small-molecule libraries and rational structure-guided design have led to the identification and development of several lead compounds capable of inhibiting the proteolytic activities of SARS-CoV PLpro (173-180).

1.4.2 Middle East respiratory syndrome coronavirus PL^{pro}

Sequencing of the MERS-CoV genome and phylogenetic analysis indicated that the virus shares most recent common ancestry with bat CoVs HKU4 and HKU5, and led to the identification of a single PL^{pro} domain encoded within nsp3 (181). The polyprotein cleavage sites were initially predicted based on sequence alignment with other CoV polyproteins (181), and PL^{pro} was later confirmed to process sites at the nsp1-2, nsp2-3 and nsp3-4 junctions (91,182,183). The *in vitro* DUB activity of PL^{pro} was subsequently confirmed, displaying activity toward mono Ub (90,184-186), Lys48- and Lys63-linked polyUb (90,91,93), Lys6-, Lys11-, Lys29-, Lys33-linked diUb (90) and ISG15 (91). PL^{pro} was also found to globally deconjugate Ub and ISG15 from cellular targets in cell culture (91,93,183,187).

A crystal structure of the MERS-CoV PL^{pro} domain revealed that the protease adopted a similar fold to SARS-CoV PL^{pro}, with thumb, palm and fingers subdomains, including the presence of a circularly permutated 4C zinc finger and an N-terminal Ub-like domain (93,184). As expected, the active site is comprised of a Cys-His-Asp catalytic triad, although interestingly, the oxyanion hole of MERS-CoV PL^{pro} appears deficient. The tryptophan residue proposed to form part of the oxyanion hole in SARS-CoV PL^{pro} is replaced with a leucine, which is unable to participate in stabilizing the oxyanion since its side chain is entirely non-polar. Consistent with this observation, a tryptophan substitution aimed at restoring the MERS-CoV oxyanion hole

increased the catalytic activity of PL^{pro} (184,185). Differences have also been noted in the BL2 loop, which in the case of SARS-CoV PL^{pro} was found to interact with small molecule inhibitors of the enzyme (174,179). These SARS-CoV-specific compounds are ineffective toward MERS-CoV PL^{pro}, likely due to structural differences in the BL2 loop, and the inability of MERS-CoV PL^{pro} BL2 residues to complete analogous hydrogen bonding and hydrophobic interactions with these compounds (188).

The fact that CoV PL^{pro} domains possess two distinct functions, which comprise both DUB and polyprotein cleavage activities, complicates the ability to study these respective functions exclusively, as both activities depend on the same active site. Studying the role of PL^{pro} DUB activity independent of viral polyprotein processing thus necessitates its selective disruption. We explored the possibility disrupting specifically, the DUB activity of PL^{pro} as a means to determine the effect this activity has on the innate immune response of the host cell. These results were published in the *Journal of Biological Chemistry* (93), and are described in detail in Chapter 5.

Not surprisingly, MERS-CoV PL^{pro} has been identified as a target for small molecule drug design (184,189,190), but development of MERS-CoV-specific antiviral compounds remains in its early stages. Phage display methods have been successful in identifying inhibitors of Ub-binding proteins through the generation Ub variants (UbVs) with significantly enhanced affinity toward their cognate Ub-binding partners, providing a novel and promising platform for the development of Ub-based therapeutics (191-194). We recently described the use of MERS-CoV-specific UbVs as potent inhibitors of viral replication (195). These results are described in detail in Chapter 6.

1.4.3 Human coronavirus NL63 PLP2

HCoV-NL63 possesses two PLP domains, PLP1 and PLP2. PLP2 cleaves the viral polyprotein to release nsp2 and nsp3, although it does not cleave following a diGly motif as found for other CoV PLPs, instead it has been reported to recognise FTKLAG↓GK and VAKQGA↓GF sites within the viral polyprotein (83). Nevertheless, NL63 PLP2 also possesses DUB activity, cleaving Lys48-linked (83) and Lys63-linked polyUb chains (84), as well as ISG15 (85). Initial work demonstrated that HCoV-NL63 infection resulted in impaired IFN-β secretion in cell culture (84), and subsequent studies investigated the role of PLP2 in downregulating the cellular innate immune response. PLP2 down regulated Sendai virus- and RIG-I-mediated IFN-β promoter activity (161), as well as PolyI:C-induced, TLR3-dependent IFN-β promoter activity (84). Consistent with these observations, PLP2 deubiquitinated RIG-I, TBK1, IRF3 and STING in overexpression experiments (86). Its role in downregulating TNF-α-induced NF-κB-dependent signaling pathways was also suggested (161). Interestingly, PLP2 also appears to downregulate RIG-I-mediated IFN-β production irrespective of its catalytic activity (84).

1.4.4 Mouse hepatitis virus PLP2

Sequencing ORF1a and ORF1b of MHV strain JHM identified, besides the main protease, two putative cysteine protease domains, PLP1 and PLP2, which shared homology with cellular papain-like proteases around the putative catalytic Cys and His residues (196). The autoproteolytic activity of PLP2 toward the MHV polyprotein was later demonstrated (197), and the cleavage site within the viral polyprotein recognized by PLP2 was determined to be FSLKGG↓AV. DUB activity of MHV PLP2 was predicted based on the conservation of its

active site residues with the SARS-CoV PL^{pro} domain, and later confirmed *in vitro*, displaying efficient activity toward Lys11, Lys48 and Lys63 diUb and human ISG15 (94). MHV PLP2 was found to inhibit cellular transcription of IFN-β via RIG-I, MAVS-, TBK1- and IRF3-mediated induction pathways (96,161), as well as inhibition of IRF3 phosphorylation and nuclear translocation (95). Further investigation into the mechanism of IRF3-specific inhibition of IFN-β production suggested that TBK1 and, curiously, IRF3 were directly deubiquitinated by PLP2 (95,96). The crystal structure of MHV PLP2 was eventually determined and revealed a Cys-His-Asp catalytic triad, with a Gln residue as a putative contributor to the oxyanion hole, in contrast to the Trp residue found in SARS-CoV PL^{pro} (163). Significant structural similarity was observed with respect to other CoV PLP2/PL^{pro} domains, with MHV PLP2 adopting the thumb, palm and fingers domain architecture common to USP DUBs. Interestingly, mutations in the Ub-like domain adjacent to MHV PLP2 impaired DUB activity, and reduced the thermostability of PLP2 (198).

1.4.5 Additional CoV PLPs

TGEV and PEDV both encode two papain-like protease domains, named $PL1^{pro}$/$PL2^{pro}$ and PLP1/PLP2, respectively. TGEV $PL1^{pro}$ resides in nsp3, cleaving the viral polyprotein at a single site at the nsp2-3 junction following a diGly motif (199), and it was shown to possess DUB activity toward Lys48- and Lys63-linked polyUb chains *in vitro* (88). A crystal structure of TGEV PL1pro revealed that it possesses the palm, thumb and fingers subdomain typical of other viral PL^{pro} and eukaryotic USP domains (88). In terms of the active site construction of the enzyme, a Cys-His-Asp catalytic triad observed at the interface between the thumb and palm, and a glutamine was found to be a likely contributor to the oxyanion hole, occupying a spatially homologous position to that of Trp107 found in the SARS-CoV PL^{pro} domain. A notable

difference from other PLPs was the absence of an N-terminal Ub-like domain, which is only conserved in the region preceding the second PLP domain in CoVs.

The PLP2 domain from PEDV has also been confirmed to deubiquitinate cellular proteins in cell culture, as well as interfere with host innate immune signaling pathways, although its role in polyprotein processing remains to be characterized (87). PEDV PLP2 inhibited RIG-I-mediated IFN-β expression, and NF-κB-responsive promoter activity, although to a lesser extent than HCoV-NL63 PLP2 (87). Inhibition of STING-mediated IFN-β expression was also observed (87).

The avian infectious bronchitis virus (IBV), a prototypical member of the CoV family, had a single PLP (PL^{pro}) identified at the 5' end of its genome, based on the conservation of catalytic Cys and His residues with cellular PLPs, and two MHV PLPs (196). IBV PL^{pro} was found to cleave the polyprotein between Gly-Gly residues at two sites, releasing nsp2 and nsp3 (200-203). It adopts a fold common to USP DUBs, and possesses an N-terminal Ub-like domain seen in most other CoV PL^{pro} domains (98) and it cleaves Lys48- Lys63-linked poly-Ub chains (97), with an apparent preference for Lys63 linkages (98). While DUB activity of IBV PL^{pro} has been demonstrated the importance of this function has not been established.

1.5 Arteriviridae

In addition to CoV, the Nidovirales order includes the Roniviridae, Mesoniviridae and Arteriviridae families that contain viruses with smaller positive-sense, ssRNA genomes relative to the CoV, with sizes of roughly 26, 20 and 15 kb, respectively (204). The arterivirus family currently consists of four virus species that each infect a specific non-human mammal causing persistent infection or acute disease associated with abortions, respiratory disease or lethal haemorrhagic fever (205). Equine arteritis virus (EAV) and especially porcine reproductive and

respiratory syndrome virus (PRRSV) have a tremendous economic impact on the veterinary industry worldwide (206,207). The two other arteriviruses are simian haemorrhagic fever virus (SHFV) and lactate dehydrogenase-elevating virus (LDV), the latter infecting mice. Arteriviruses have a number of features that are similar to CoVs such as virion composition, genome structure, some of the replicase polyprotein functions and their replication strategy. The expression of nsps from large polyproteins is also similar to what was described for CoVs (see former paragraph). The arterivirus polyproteins are cleaved into individual nsps by internally encoded PLPs. PLPs within nsp1 and nsp2 release their respective nsps, and a 3CLpro in nsp4 cleaves all remaining junctions downstream of nsp3. While EAV nsp1 contains a single active protease named PLP1, PRRSV and LDV nsp1 contain two protease domains each; PLP1α and PLP1β. In the case of SHFV there are three functional PLPs in nsp1 to release nsp1α, β and γ (205,208). The PLP2 protease in nsp2 of arteriviruses was shown to cleave the nsp2-3 junction (209). Similar to EAV and PRRSV PLP2, as further elaborated below, SHFV and LDV PLP2 were shown to additionally possess DUB activity and limit innate immune activation by removing Ub from overexpressed RIG-I (99).

1.5.1 Equine arteritis virus PLP2

The nsp2 protease has been suggested to belong to a novel OTU-like superfamily of cysteine proteases (210) strengthened by the evidence that conserved Cys and His residues are required for its protease activity (209). After several human OTU-domain proteins were identified and shown to have DUB activity the Ub-deconjugation activity of a number of viral OTU domains, including EAV PLP2, were examined (102). Ectopic expression of the PLP2 domain alone, or full-length EAV nsp2 indeed resulted in decreased global levels of both Ub and ISG15 conjugates in cultured cells. Genuine DUB activity of EAV PLP2 on both Lys48 and

Lys63-linked polyUb chains was further confirmed by *in vitro* assays using purified protein (99). EAV PLP2 therefore was concluded to have dual activity towards the viral replicase polyproteins and Ub(-like) conjugates. Interestingly, cellular OTU domain containing DUBs generally seem much less promiscuous, as they do not cleave ISG15 conjugates (102) and are usually at least partly specific for certain Ub linkages (20). NF-κB activation by TNF-α was suppressed upon the expression of EAV PLP2 (102), hinting at an innate immune suppressive function of the vDUB. EAV PLP2 also inhibits RIG-I-mediated innate immune signaling upon overexpression, and is able to deubiquitinate RIG-I (99).

We determined the crystal structure of EAV PLP2, and demonstrated that the DUB and polyprotein cleavage activities could be selectively decoupled (211). These results are described in detail in Chapter 2. A vaccination-challenge trial in horses comparing wild-type and DUB negative EAV resulted in slightly decreased replication of the DUB negative virus but comparable clinical disease, antibody response and innate immune response (212). It should be noted that under the experimental conditions no difference was measured between the two viruses, which might be explained by the already high level of protection induced by the wild-type virus (212).

Interestingly, despite the fact that arteriviruses and CoVs are members of the same order of Nidoviridae, suggesting a relatively close evolutionary connection, arteriviruses encode an OTU-like DUB, while CoVs encode a USP DUB. This suggests that the virus families each independently acquired DUBs into their genomes, again emphasizing the apparent importance of such activity for these viruses.

1.5.2 Porcine reproductive and respiratory syndrome virus PLP2

PRRSV PLP2 possesses both in *trans* and *in cis* cleavage activities and mutations disrupting only trans-cleavage activity were lethal for the virus (213). Probing the nsp2/3 cleavage site revealed that the cleavage site is at the Gly1198+1199 dipeptide (213). Besides full-length nps2, many different isoforms of nsp2 having the same N-terminus were detected during infection in cell-culture (214). These likely at least partly account for cleavage products of nsp2 when other conserved Gly dipeptide sites are processed by PLP2. More recently, two nsp2 products were identified as a result of -2 and -1 ribosomal frameshifting in the nsp2 region of the polyprotein gene, yielding nsp2 trans frame (TF) and nsp2N products, respectively (215). Nsp2TF contains a different C-terminal transmembrane domain compared to nsp2 and localized to different intracellular compartments. Removal of nsp2TF attenuated the virus as it replicated slower than wild-type virus and reached lower peak titers (215). For this frameshift event the frameshift site, a frameshift-stimulatory element and, uniquely, a protein factor, nsp1β, are required (216). Some of the nsp2 isoforms were found to be present in or on virus particles and might participate in entry, early steps of virus replication or suppression of host immune responses (217).

PRRSV PLP2 was shown to possess DUB activity towards Ub and ISG15 conjugates (102,218). PLP2 inhibited NF-κB activation in overexpression experiments by interfering with the Lys48-linked polyubiquitination of IκBα and thereby preventing its degradation (101). RIG-I was also deubiquitinated upon overexpression of PRRSV PLP2, suggesting that the DUB activity of PLP2 is responsible for evading RIG-I induced innate immune responses (99). PLP2 of JXwn06, a highly pathogenic PRRSV strain, and that of a modified live virus (MLV) vaccine strain, were shown to cleave all di-Ub chains linked through the different Lys in Ub, but not

linear diUb *in vitro* (100). The greatest difference between these PLP2s was that JXwn06 was more active towards Lys63-linked diUb than MLV. *In vitro*, neither PLP2 cleaved human ISG15-AMC nor the pro-forms of human ISG15 or porcine ISG15, which contradicts the earlier observation of ISG15 conjugate cleavage upon ectopic expression of PLP2 (100,102,218). With respect to the different isoforms of PPRSV nsp2 that include PLP2, no studies have been carried out to assess the specific DUB activities of these variants and their functional contribution during infection.

1.6 Nairoviruses

Nairoviruses are enveloped, negative-sense ssRNA viruses within the family *Bunyaviridae*, which can be further subdivided into serogroups based on antibody cross-reactivities. The serogroups discussed here include the Crimean-Congo haemorhaggic fever serogroup, which includes the Crimean-Congo haemorrhagic fever virus (CCHFV); the Nairobi sheep disease serogroup, which include the Nairobi sheep disease virus (NSDV) and Dugbe virus (DUGV); and the Thiafora serogroup, which includes the Erve virus (ERVV). Nairovirus genomes share a similar structure, and are comprised of three ssRNA segments, small (S), medium (M) and large (L), named as such for their respective nucleotide lengths.

CCHFV is a widespread tick-born virus that is transmitted to humans primarily by members of the *Hyalomma* genus (219). Infection with CCHFV can lead to haemorrhaging and multi organ failure, with a case fatality rate ranging from 10-40%. Currently, there is no protective vaccine and treatment involves only basic management of CCHF symptoms. Contrary to CCHFV, DUGV infection does not lead to serious disease in humans, and is instead associated with mild febrile illness. In contrast, ERVV infections have been postulated to cause

‘thunderclap headaches’ in humans (220), with mice and shrews suspected as potential reservoirs for the virus (221).

1.6.1 Crimean-Congo haemorrhagic fever virus OTU

In 2000, Makarova and coworkers published the discovery of a novel cysteine protease superfamily, based on sequence homology with the *Drosophila* Ovarian Tumour (OTU) gene product (210). While initially an OTU domain was identified at the N-terminus of the Dugbe virus L protein, sequence determination of the CCHFV L-segment later uncovered the presence of a homologous nairovirus OTU domain (222,223).

Following the discovery that A20, a cellular protein with an OTU domain that negatively regulates NF-κB signaling via deubiquitination (224,225), Frias-Staheli and coworkers investigated the role of viral OTU domains *in vivo* and demonstrated that the CCHFV OTU domain indeed possessed DUB activity, actively processing Lys48 and Lys63 polyUb chains, as well as ISG15 *in vitro*, and globally deconjugating Ub and ISG15 from cellular proteins during ectopic expression (102). Expression of the CCHFV OTU domain diminished activity at an NF-κB-responsive promoter during TNF-α stimulation, and established the CCHFV OTU domain as a viral protease involved in the evasion of the cellular innate immune response. The work culminated with the description of a chimeric Sindbis virus expressing the CCHFV OTU domain along with ISG15, which was found to increase lethality in IFN-αβ receptor$^{-/-}$ background mice, effectively preventing ISG15-mediated protection of Sindbis virus lethality. Following work demonstrated that the CCHFV OTU domain mitigates RIG-I-mediated IFN-β expression, suggesting that the enzyme inhibits both antiviral and pro-inflammatory branches of the innate immune response during infection (99).

Crystal structures of the CCHFV OTU domain were subsequently reported bound to Ub (103,105,106), full-length ISG15 (105) or the C-terminal β-grasp domain of ISG15 (106), as well as in its *apo* form (106), and together provided the first structural insights into a viral OTU protease. The CCHFV OTU domain was found to contain α-helical and β-sheet lobes (105,106), and closely resembled the structure of the eukaryotic OTU domain-containing protein from yeast (yOTU1) (Fig. 7A) (226). The active site of CCHFV OTU was comprised of a Cys-His-Asp catalytic triad, arranged in catalytically competent geometry in all reported structures (105,106), and while no side chains were suitably oriented to participate in the formation of the oxyanion hole, the backbone amide of the catalytic Cys40 and a nearby Asp37 were proposed to serve this function (105).

Interestingly, while Ub and ISG15 bound to CCHFV OTU in similar orientations (Fig. 7A, B), the β-grasp domains of these substrates were rotated ~75 degrees with respect to the orientation that Ub binds to a representative eukaryotic OTU DUB from yeast, yOTU1 (Fig. 7A). Interestingly, the alternate binding orientation of Ub and ISG15 to the CCHFV OTU was due, in-part, to the presence of a unique β-hairpin that forms a substantial part of the substrate binding surface on the viral enzyme (Fig. 7A). The β-hairpin structure was thus proposed to facilitate a rotated binding orientation for Ub that also accommodated basic residues within the C-terminal β-grasp domain of ISG15, which appear to prevent its interaction with the yOTU1 (105). Using structure-guided mutagenesis, the DUB and deISGylating activities of CCHFV OTU could be decoupled by exploiting unique interactions between the OTU domain and its cognate substrates, targeting a helical arm structure conserved in most OTU domains in order to disrupt deISGylating activity, and a unique hydrogen bonding interaction occurring at the interface of Ub and the novel β-hairpin structure of CCHFV OTU (106).

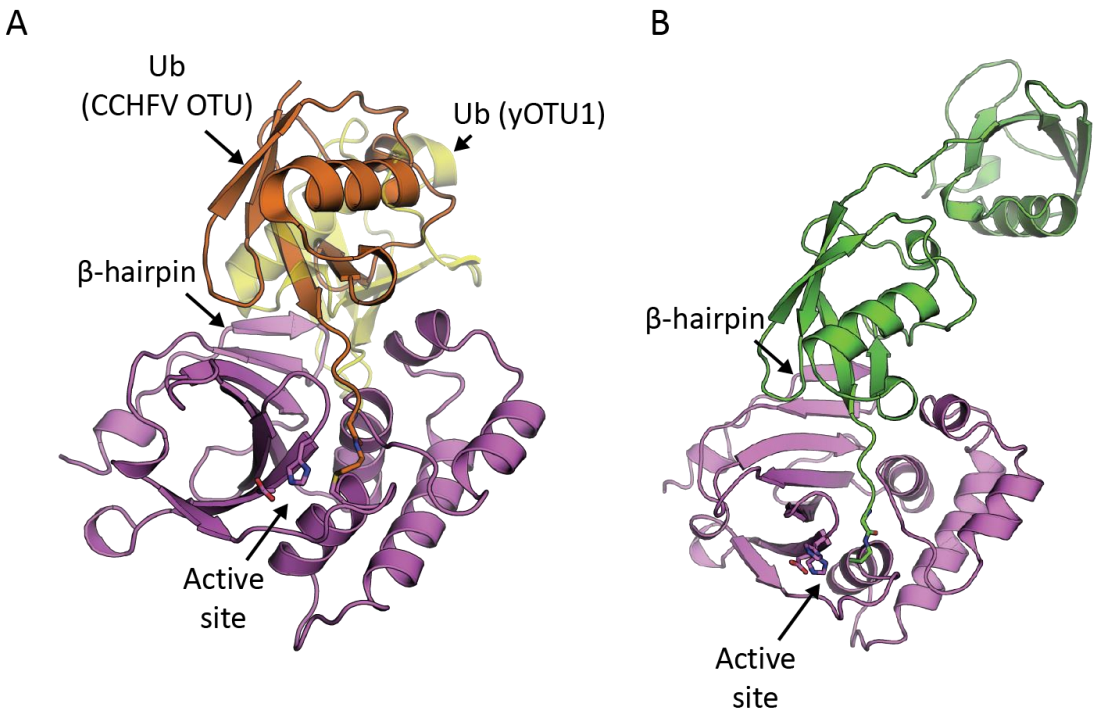

Figure 1.6 CCHFV OTU interacts with Ub and ISG15 in a rotated orientation with respect to yOTU1.
(A) Comparison of the Ub binding orientations of the CCHFV OTU and yeast OTU1 OTU (yOTU1) domains. CCHFV OTU (PDB ID: 3PT2; violet) is shown bound to Ub (PDB ID: 3PT2; orange), and the β-hairpin is indicated with an arrow. yOTU1 in complex with Ub (PDB ID: 3BY4) was superposed onto the CCHFV OTU structure, and yOTU1 was removed for clarity. The yOTU1-bound Ub domain is shown in transparent yellow. (B) Crystal structure of CCHFV OTU (PDB ID: 3PSE; purple) in complex with ISG15 (PDB ID: 3PSE; green). CCHFV OTU binds ISG15 in a comparable orientation to Ub.

In vitro work by multiple groups have shown that CCHFV OTU is active toward Lys6-, Lys11, Lys48 and Lys63 Ub chains (104,106). It was also demonstrated that CCHFV OTU cleaves fluorogenic Ub-AMC and ISG15-AMC substrates, with some groups observing a preference for the Ub substrate (103,104,106), and others demonstrating similar activities toward both substrates (105). Further, Akutsu and coworkers saw a marked increase in activity toward a fluorescent Lys63-linked diUb substrate compared to Lys48-linked diUb, providing kinetic evidence for CCHFV OTU linkage specificity (106). While this demonstrates that CCHFV OTU may be somewhat capable of discriminating between Ub linkage types, structural evidence is necessary to confirm the molecular basis for the observed specificities. Recent advancements in CCHFV reverse genetics systems (227) may also soon enable studies that directly reveal the role of the DUB and deISGylating activities of the OTU domain during CCHFV infection.

1.6.2 Dugbe virus OTU

Similar to the CCHFV OTU domain, the DUGV OTU domain was found to be an effective DUB and deISGylase removing Ub and mISG15 in cell culture (102,228), and a potent DUB *in vitro* cleaving Lys6-, Lys11-, Lys48- and Lys63-linked diUb, and Lys6-linkages with particular efficiency (104). It was also demonstrated that the DUGV OTU was ineffective at processing ISG15, and a description of the DUGV OTU crystal structure in complex with Ub, and a comparison with CCHFV OTU suggested the inability of DUGV OTU to process ISG15 was centralized around residue Thr128, which was unable to form a hydrogen bonding network with ISG15 comparable to the CCHFV OTU residue Glu128. The introduction of Glu128 to DUGV OTU indeed increased reactivity toward a fluorogenic ISG15 substrate by 2000% (104). Additional similarities with the CCHFV OTU domain were found in its ability to down regulate

cellular immune response pathways, where both NF-κB- and IFN-responsive promoter activity were disabled upon stimulation in the presence of DUGV OTU (228).

1.6.3 Erve virus OTU

In contrast to CCHFV and DUGV OTU domains, the ERVV OTU domain is essentially absent of DUB activity, processing activity against ISG15 only, with a particularly high affinity for human ISG15 as determined by isothermal titration calorimetry (ITC) (104,229). Analysis of a crystal structure of ERVV OTU in complex with mISG15 attributed the inability of ERVV OTU to bind Ub to the presence of an electrophilic region (Arg21, Ser132, Asn134) at the interface that binds ISG15, which appears able to accommodate ISG15 residue Glu87, but not the spatially conserved hydrophobic Ub residue Leu8 (229).

1.6.4 Nairobi sheep disease virus OTU

Transfection of Vero cells with NSDV OTU was found to reduce activity at the IFN-β, and IFN-responsive promoters in a protease-dependent fashion, demonstrating that NSDV OTU interferes with both the production and activity of IFN (230). Further, NSDV OTU was shown to deubiquitinate and deISGylate cellular proteins during expression, thus establishing it as a deubiquitinating enzyme capable of interfering with the production and activity of IFN (230).

1.7 Picornaviridae

Picornaviruses are small, non-enveloped positive-sense ssRNA viruses. Within the family *Picornaviridae,* several viruses are known to cause disease in livestock, and indeed the Foot-and-mouth disease virus (FMDV) was the first discovered animal virus (111). A member of the *Aphthovirus* genus, FMDV remains an economically significant pathogen in the livestock industry. FMDV infection is characterized by the formation of vesicles on the feet and mouths of

infected animals, and can lead to substantial economic losses annually due to decreased animal productivity and trade restrictions imposed on infected livestock. Certain members of the Enterovirus genus within the family *Picornaviridae* also cause disease in livestock, and recently an isolate of porcine Enterovirus species G (EVG) was identified that contained a Torovirus PLP domain that appears to have been acquired through cross-order recombination (108).

1.7.1 Foot-and-mouth disease virus L^{pro}

Early research on FMDV identified a cleavage product originating from the N-terminus of the viral polyprotein (231). The cleavage was initially proposed to result from a host protease, but was later found to be carried out autoproteolytically by a FMDV-encoded leader protease (L^{pro}) located within the N-terminus of the nascent polyprotein (232). Translation of L^{pro} can initiate at one of two in-frame start codons, leading to the production of Lab^{pro} and Lb^{pro} isoforms, the former having an additional 28 amino acids at the N-terminus.

Prior studies identified L^{pro} as a potential virulence factor, with L^{pro} cleaving the host eukaryotic translation initiation factor 4 gamma (eIF4G) that is involved in translation of cellular capped mRNA transcripts, thereby prioritizing the translation of viral transcripts (233). Experiments using an FMDV mutant lacking the L^{pro} domain also implicated the protease in the circumvention of cellular innate immune responses by inhibition of cellular IFN-α/β production and associated ISGs, specifically protein kinase R (PKR), a cytoplasmic sensor of viral RNA (234-238). In an attempt to disrupt this activity, de Los Santos *et al.* generated an FMDV virus with point mutations Ile83Ala and Leu86Ala within L^{pro}, and as predicted, these mutations attenuated viral replication, with infection resulting in an increased in cellular IFN-β expression (239). Notably the autoprocessing activity of the FMDV L^{pro} mutant was unaffected, as was its ability to cleave eIF4G (239).

Early bioinformatics results predicted L^{pro} to be a papain-like protease (240,241), sharing sequence similarity with MHV PLPs near the putative catalytic Cys (242). This was later confirmed upon determination of the Lb^{pro} crystal structure, which also provided insight into the autocatalytic mechanism of Lb^{pro} (241), and, in fact, represents the first structural characterization of a viral papain-like cysteine protease (241). The C-terminal polyprotein cleavage site recognized by Lb^{pro} was present in the crystallized construct, and found to occupy the active site of an adjacent Lb^{pro} monomer, mimicking a product-bound complex **(Figure 1.7**). While this *trans* interaction may suggest that Lb^{pro} removal also occurs in *trans* within the context of polyprotein maturation, the authors proposed that removal of Lb^{pro} may also occur in *cis*, due in part to the relatively weak intermolecular contacts between Lb^{pro} monomers, and the propensity for the residues within extended C-terminus of Lb^{pro} turn over the protease and into the active site cleft. NMR results however, show that Lb^{pro} exists as a homodimer in solution (243).

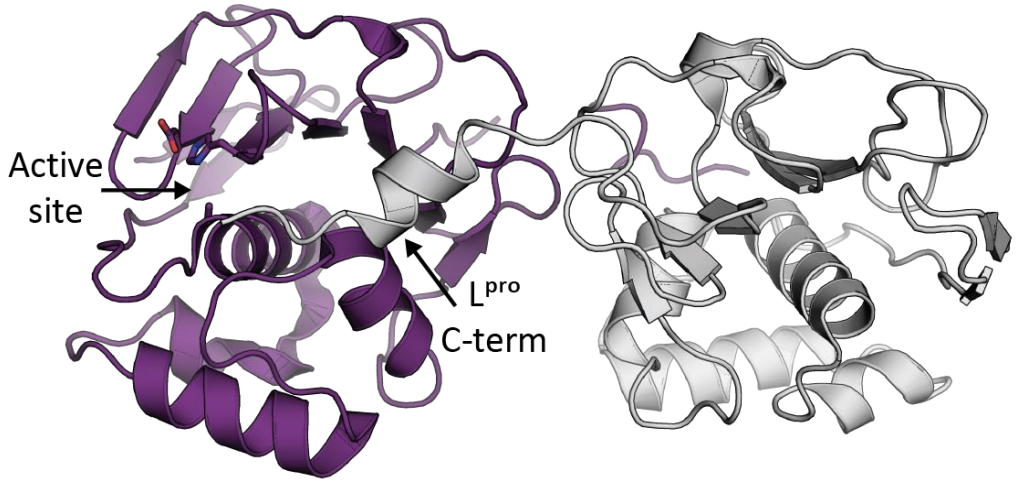

Figure 1.7 Crystal structure of FMDV Lb^{pro}.
FMDV Lb^{pro} (PDB ID: 1QOL) is shown in cartoon, and an adjacent monomer in the asymmetric unit is depicted in gray, with the C-terminus leading toward the active site of the adjacent Lb^{pro} monomer.

Wang *et al.* further investigated the structure of Lb^{pro}, and using secondary-structure matching discovered that it shared structural homology with SARS-CoV PL^{pro} and the eukaryotic USP14, two previously characterized DUBs, which led to the hypothesis that L^{pro} may also possess DUB activity (107). This was confirmed *in vitro*, where L^{pro} cleaved Lys48 and Lys63-linked polyUb chains and globally deubiquitinated cellular proteins during ectopic expression (107). Based on previous findings that the IFN-antagonist and eIF4G processing functions of L^{pro} were apparently independent (239), Wang and coworkers sought to determine if the DUB and eIF4G processing activities were similarly uncoupled. Indeed, the previously characterized Ile83Ala/Leu86Ala L^{pro} mutant was deficient in DUB and IFN-supressing activities, yet retained the ability to hydrolyze eIFG4, effectively linking the DUB and immunosuppressive properties of L^{pro} (107). Further, overexpression of L^{pro} resulted in a reduction of Ub-conjugated RIG-I, TBK1, TRAF3, and TRAF6, providing evidence for the role of L^{pro} in supressing host Ub-dependent innate immune signaling pathways via deubiquitination of cellular signaling components (107).

While a considerable amount of work has gone into the structural and functional characterization of L^{pro}, a number of questions remain. While the autocatalytic activity and substrate specificity of L^{pro} have been characterized, which have led to the development of peptidomimetic compounds as potential inhibitors of L^{pro} (244-246), the molecular basis for Ub recognition by L^{pro} remains to be elucidated. Mutagenesis has been able to discriminate between the DUB activity and polyprotein/eIFG4 processing activities of Lpro, however it is still unclear how these mutations exert their selective effect. It is interesting to note that Ile83Ala/Leu86Ala mutations targeted the SAF-A/B, Acinus, and PIAS (SAP) domain within L^{pro} (239), and while these mutations selectively abrogate DUB activity (107) and delay nuclear translocation (239),

they do not appear to target the likely Ub-binding interface of L^{pro}, which has been demonstrated to be an effective means to inhibit the DUB activity of other vDUBs (93,211). Further adding to the complexity of its role in innate immune suppression, L^{pro} has been implicated in the degradation of NF-κB, although this activity has not been demonstrated directly (238). The structural characterization of L^{pro} in complex with Ub should shed light on some of these questions.

1.7.2 Enterovirus G ToV-PLP

Recently, an EVG isolate was identified containing a previously unseen insertion between non-structural proteins 2C and 3A, flanked by $3C^{pro}$ cleavage sites (108). Further analysis determined that the inserted sequence shared significant similarity with the Torovirus (a member of the order *Nidovirales*) nsp3-like PLP at the amino acid level, which was subsequently termed ToV-PLP. Homology modelling predicted structural similarities between ToV-PLP and the FMDV L^{pro}, leading to the hypothesis that ToV-PLP may possess DUB/deISGylating activities. These suspicions were confirmed, with ToV-PLP showing global DUB and deISGylating activity in cell culture, and *in vitro* analysis demonstrating that ToV-PLP processed ISG15, Lys48- and Lys63-linked polyUb chains, and curiously, showed activity toward Met1 linear Ub chains (108). Infection of swine testicular cells with recombinant EVG lacking ToV-PLP increased cellular type I and type II IFN production, as well as ISG15 transcription, and displayed impaired growth kinetics compared to its ToV-PLP-containing counterpart (108). Although Enteroviruses are known to have high rates of genetic recombination, the cross-order acquisition of a novel DUB by EVG is likely a rare event (108), and the apparent increase in viral fitness with respect to DUB negative EVG further demonstrates the importance of vDUBs in supressing the innate immune response of their hosts.

1.8 Tymoviridae

The turnip yellow mosaic virus (TYMV) is the type species of the family *Tymoviridae*, a group of positive-sense, ssRNA viruses infecting plants. Their non-structural proteins are expressed from two overlapping open reading frames, ORF-206 and ORF-69 (247), which encode for p206 and p69, respectively. The TYMV papain-like protease (PRO) domain is encoded within ORF-206, and cleaves the translation product, p206, at two sites releasing p98, p42 and p66 (248-251). During infection by the virus, the host actively supresses accumulation of the TYMV RNA-dependent RNA-polymerase domain (POL), located in p66, by tagging it with Lys48-linked polyUb, targeting it to the Ub-proteasome system (252). Appreciating that the TYMV PRO consensus site (K/R)LX(G/A/S)(G/A/S) (251) was compatible with the C-terminus of Ub, Chenon *et al.* suggested that PRO may counter this cellular defence mechanism by stabilizing the POL domain during infection via removal of the Lys48-Ub chains (109). Indeed, PRO is able to process Lys48- and Lys63-polyUb chains *in vitro*, and pulse-chase analysis determined that expression of PRO stabilized p66 in a protease-dependent manner (109).

Hidden Markov Model comparison predicted that TYMV PRO shared secondary structure elements with a number of eukaryotic and viral OTU domains, and sequence similarities were identified surrounding the catalytic Cys and His residues, in agreement with the characterized OTU domain (109,210). The crystal structure of the TYMV PRO domain revealed a compact protease domain, composed of α-helical and β-sheet lobes which hosted the catalytic Cys and His residues, respectively, as well as a unique N-terminal lobe (Fig. 9) (253). A structural comparison using the DALI alignment server also detected significant structural similarities with previously reported viral and eukaryotic OTU domains, placing the TYMV PRO domain within the OTU superfamily (254). In general, the active site of PLPs are canopied

by a loop structure. The active site of PRO possesses no such loop, making its active site entirely solvent exposed (253). Also absent was the third residue thought to align the histidine imidazole ring for proper catalysis. Taken together, the pared-down, solvent exposed active site of PRO was thought to account for its relatively poor DUB activity in comparison to other OTU DUBs, and the relaxed specificity of the enzyme at the P1 site (253). Structural evidence for the in *trans* cleavage activity of PRO was also revealed, with the C-terminus of one PRO domain bound into the cleft leading toward the active site of a nearby symmetry mate (Fig. 9) (253). Based on this structure, the strict requirements at P5 and P4 were rationalized by the presence of complementary acidic and hydrophobic pockets, respectively on the surface of PRO (253). Further *in silico* docking studies predicted that the N-terminal lobe of PRO interacts with the hydrophobic Ile44 patch of Ub (253).

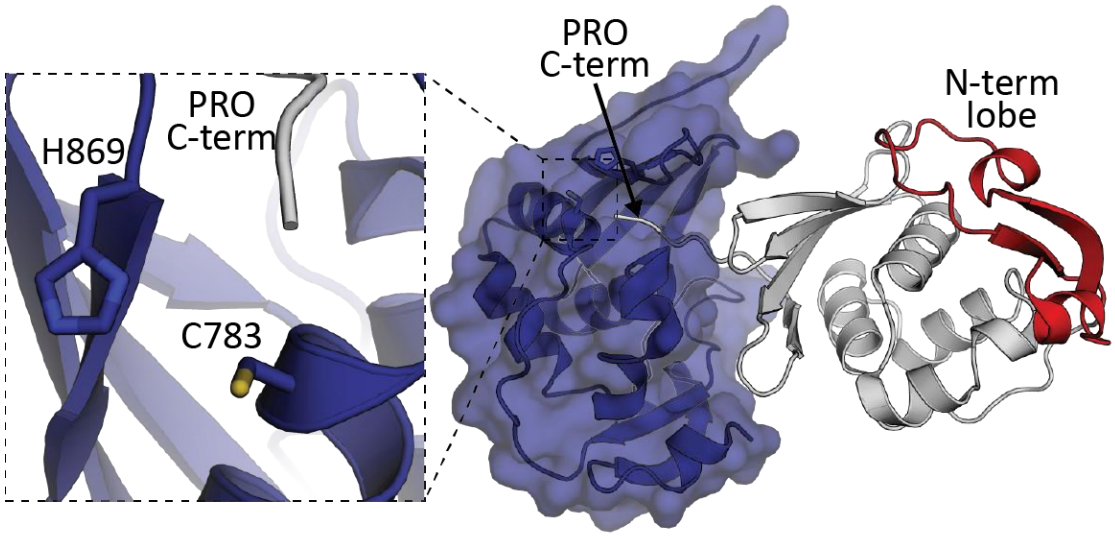

Figure 1.8 Crystal structure of TYMV PRO.
The TYMV PRO domain (PDB ID: 4A5U; deep blue, transparent surface) is shown in cartoon. A symmetry mate (gray) is also shown, with the C-terminus bound in the active site of the adjacent PRO monomer. The N-terminal lobe is coloured red in the adjacent symmetry mate. Dotted box shows a close up of the pared-down PRO active site, with catalytic residues shown as sticks.

1.9 Concluding remarks

Significant effort has been dedicated to uncovering the cellular substrates and structural biology of vDUBs, and the role of these enzymes during infection is now beginning to emerge. However, more work is needed to clarify the picture, since many experiments used to ascertain the cellular targets of vDUBs have relied on overexpression experiments, and thus may not accurately reflect the circumstances of an actual viral infection. Both the cellular ubiquitination system, and viral protein expression are dynamic processes, with the temporal and spatial regulation of these events likely playing a significant role in determining which substrates are accessible to a given vDUB. To complicate matters further, vDUB domains often exist within larger, multi-domain proteins, some of which are membrane bound, yet they are often studied in isolation as soluble cytoplasmic proteins in cell culture, likely unable to exhibit subcellular localization patterns which would be found under biologically relevant conditions. Moreover, additional viral factors present during infection may influence the substrate specificity of a vDUB in question. Indeed, emerging technologies are addressing some of the challenges in accurately analyzing Ub-dependent signaling pathways, with powerful mass spectrometry and proteomics methods targeted at probing the dynamics of these systems, including the stoichiometry and kinetics of Ub conjugation, and the specific linkage types populating cellular substrates of interest (reviewed in (255)). These technologies could now be directed towards revealing the cellular targets and linkage specificities of vDUBs during the course of live virus infection. Further, it is pertinent to recognize that in cases where a viral protease depends on a single active site for both DUB and proteolytic (*i.e.* non-isopeptide bond cleavage) activity, a complete understanding of their genuine cellular targets necessitates the selective inhibition of DUB activity, as described for a select number of multifunctional vDUBs (93,107,211).

Protein X-ray crystallography has provided remarkable insights into the molecular basis for how vDUBs recognize and bind monoUb, yet significant questions remain regarding their ability to recognize a particular Ub linkage type. To date, a single example of a vDUB in complex with a diUb substrate has been described (168); however, exciting new approaches to generate polyUb probes of varying linkage types (256,257) will now undoubtedly enable rapid advances in understanding the structural basis for the recognition of specific linkage types by vDUBs. The recent characterization of several bacterial DUBs has also advanced our understanding of the interplay between the cellular ubiquitination pathways and pathogenic bacteria at a structural level, and highlighted key variable regions within bacterial clan CE proteases permitting adaptation to Ub/Ubl domains and specific Ub linkage types (258).

It is now clear that interfering with Ub-dependent cellular processes through deubiquitination is a powerful strategy used by viruses to promote their survival, as evidenced by the large number of DUBs found in diverse virus lineages. While we have made every effort to include all vDUBs that have been described to date, many more undoubtedly remain to be discovered and characterized. Given the growing body of evidence demonstrating the importance of vDUB activity in viral replication and pathogenesis, vDUBs are now recognized as attractive targets for the design of antiviral therapeutics. Small molecule inhibitors of vDUBs, and novel, selective protein-based approaches to disrupting the proteolytic activity of vDUBs are under active investigation, alongside the development of novel live attenuated virus vaccine candidates with impaired DUB activity. Selective targeting of vDUBs by therapeutic intervention, or through genetic-based disruption thus holds promising potential for the design of future antivirals and vaccines.

1.10 Thesis objectives

Prior to this research, the role of the DUB activity of EAV and MERS-CoV papain-like proteases had not been directly established, although they had been implicated in the inhibition of the cellular innate immune response to infection. The fact that the proteolytic activity of these proteases serves a crucial role in polyprotein processing (and thus viral replication), studying the DUB activity directly poses challenges, due to the fact that both of these activities rely on a single active site. We thus predict that using X-ray crystallography, we will be able to reveal the specific molecular interactions occurring between these viral papain-like proteases and their cognate substrates. Further, we expect that these interactions will be sufficiently distant from the active site that they can be specifically targeted in order to prevent DUB activity while preserving polyprotein processing activities. In addition, we expect that X-ray crystallography will reveal the molecular basis governing the increased affinity of novel Ub variants towards MERS-CoV PL^{pro}, and allow us to structurally characterize these novel Ub-based therapeutics. To this end, the thesis objectives are as follows:

1. To characterize the crystal structures of the papain-like proteases PL^{pro} and PLP2 of MERS-CoV and EAV, respectively, and to elucidate the structural basis for their recognition of the substrates Ub and ISG15 through the study of substrate-bound crystal structures.

2. To employ a rational, structure-guided approach towards the deconvolution of the polyprotein processing and DUB functions of these Nidovirus papain-like protease domains in

order to directly assess the role of papain-like protease DUB activity on the cellular innate immune response.

3. To structurally characterize novel MERS-CoV PL^{pro}-specific Ub-based therapeutics, and demonstrate their ability to inhibit the DUB activity of MERS-CoV PL^{pro}.

Chapter 2
The deubiquitinase function of arterivirus papain-like protease 2 suppresses the innate immune response in infected host cells

Adapted from: van Kasteren, P. B., Bailey-Elkin, B. A.[1], James, T. W.[1], Ninaber, D. K., Beugeling, C., Khajehpour, M., Snijder, E. J., Mark, B. L.[2], and Kikkert, M.[2] (2013) Deubiquitinase function of arterivirus papain-like protease 2 suppresses the innate immune response in infected host cells. *Proc. Natl. Acad. Sci. U. S. A.* **110**, E838-847

[1] Authors contributed equally to this work

[2] Authors contributed equally to this work

Contributions statement:

The project investigating the possibility of selectively disrupting the DUB activity of EAV PLP2 via structure-guided mutagenesis was conceived prior to my arrival in the lab. The crystallization of EAV PLP2 in complex with Ub, as well as the X-ray data collection was accomplished by Terrence James. My contribution included the processing of X-ray diffraction images, model building and refinement of the EAV PLP2-Ub complex, as well as the kinetic analysis of the EAV PLP2 mutants as described in sections 2.2.2, 2.2.3 and 2.2.4 in collaboration with Mazdak Khajehpour at the University of Manitoba (UM). I also wrote sections of the manuscript pertaining to the structural analysis of the PLP2-Ub complex described in sections 2.3.1, 2.3.2 and 2.3.3. The cell culture and virus experiments were carried out by Puck van Kasteren (LUMC).

2.1 Introduction

The synthesis and post-translational cleavage of polyproteins is a common genome expression strategy employed by positive-stranded (+) RNA viruses of eukaryotes. It is used to cope with the consequences of cytoplasmic replication and the limitations of the eukaryotic translation machinery, which essentially preclude the use of (nuclear) RNA splicing and polycistronic mRNAs, respectively (259). The critical cleavage of these viral polyproteins into their functional subunits is mediated by internal virus-encoded proteases (240,260-262), many of which have been found to also target cellular substrates in order to promote virus replication or subvert host antiviral responses. Well-known examples of such dual-specificity proteases are the poliovirus 2A and hepatitis C virus NS3/4A enzymes that, in addition to the viral polyprotein, target host cell proteins involved in translation and innate immune signaling, respectively (263-267).

Arterivirus PLP2 and a protease domain found in the unrelated nairovirus CCHFV, were first identified as potential members of the OTU superfamily of DUBs on the basis of comparative sequence analysis (210). Several laboratories, including our own, subsequently confirmed that arterivirus PLP2s indeed have DUB activity that may be employed to remove Ub from innate immune signaling factors to suppress the induction of an antiviral state (99,101,102). The potential benefits of this strategy are highlighted by the fact that proteases from virus groups as diverse as arteri-, corona-, nairo-, picorna-, hepadna-, and herpesviruses have all been implicated in DUB-based innate immune evasion (see Chapter 1). Thus far, however, direct evidence linking DUB activity to the suppression of innate immune responses in virus-infected cells has not been reported for any of these proteases.

Since the DUB activity of arterivirus PLP2 depends on the same active site mediating the critical nsp2|nsp3 cleavage, it has not been possible to independently study the role of PLP2 in

polyprotein processing and immune evasion in the context of virus infection. Here we present the crystal structure of EAV PLP2 in complex with Ub at 1.45 Å resolution. The complex reveals a distinctly compact conformation compared to other OTU superfamily members and the incorporation of a unique zinc finger within the OTU-fold. Given these features, arterivirus PLP2 represents a novel subclass of zinc-dependent OTU DUBs. Importantly, the PLP2 active site is distant from its Ub-binding surface, allowing for the introduction of mutations in this region that dramatically reduced DUB activity, yet did not affect nsp2|nsp3 cleavage. Compared to wild-type EAV, viruses carrying these mutations elicited a significantly enhanced innate immune response in primary equine cells, while displaying wild-type replication kinetics. Taken together, our results demonstrate that PLP2 DUB activity indeed mediates innate immune suppression during arterivirus infection. The ability to selectively inactivate the PLP2 DUB function may thus contribute to the engineering of improved live attenuated vaccines against arteriviruses and other virus families encoding proteases with similar dual specificities.

2.2 Methods

2.2.1 PLP2 plasmids

For bacterial expression of EAV PLP2, a cDNA fragment encoding residues 261-392 of EAV pp1a and an in-frame C-terminal His_6 purification tag was inserted downstream of a Ub fusion partner in the pASK3 vector (268), yielding plasmid pASK3-ePLP2. A mammalian expression construct encoding an EAV nsp2-3 polyprotein was made by cloning residues 261-1064 of EAV pp1a in-frame with an N-terminal HA tag in the pcDNA3.1 vector (Invitrogen). All mutants were engineered by site-directed mutagenesis using *Pfu* DNA polymerase (Fermentas). All constructs were verified by sequence analysis.

2.2.2 Purification and crystallization of EAV PLP2 bound to Ub

E. coli BL21-Gold(DE3) cells were transformed with pASK3-ePLP2 and cultured to an optical density (OD_{600}) of 0.7 in LB medium at 37°C. The culture was then supplemented with 200 ng/ml of anhydrous tetracycline and incubated for 3 h at 28°C with shaking to induce expression of the Ub-PLP2-His_6 fusion protein. The cells were pelleted and resuspended in ice-cold 20 mM 2-(*N*-morpholino)ethanesulfonic acid (MES) pH 7, 500 mM NaCl, 10% glycerol, 5 mM imidazole pH 7.4, 0.5 mM TCEP and lysed using a French pressure cell (AMINCO). The lysate was clarified by centrifugation and loaded onto a Ni-Nitrilotriacetic acid (NTA) column (Qiagen) pre-equilibrated with lysis buffer. After washing with lysis buffer supplemented with 15 mM imidazole, recombinant PLP2 was eluted from the column using an equilibration buffer supplemented with 150 mM imidazole and exchanged into 50 mM Tris, pH 8.0, 300 mM NaCl and 5 mM dithiothreitol (DTT) before storing at 4 °C. The endogenous DUB activity of PLP2 resulted in the efficient removal of the N-terminal Ub-tag from the fusion protein during expression in *E. coli*; therefore, affinity chromatography yielded highly pure PLP2 carrying a C-terminal His_6 purification tag only.

The mechanism-based suicide inhibitor $Ub_{(1–75)}$–3–bromopropylamine (Ub–3Br) was prepared according to Messick *et al* (226) and Borodovsky *et al* (124), as described by James *et al* (105). Ub-3Br was covalently bound to purified PLP2 by gently mixing the proteins in a 3:2 molar ratio for one hour at 37°C. The resulting PLP2-Ub complex was purified by gel filtration (Superdex 75) followed by anion exchange (Source 15Q) chromatography and then exchanged into 20 mM Tris, pH 8.0, 50 mM NaCl before concentrating to 10 mg/ml and storing at 4°C.

The PLP2-Ub complex was crystallized by hanging-drop vapor diffusion at 10 mg/ml in mother liquor consisting of 100 mM MES pH 6.2, 18% polyethylene glycol (PEG) 20,000.

Crystals were flash-cooled and stored in liquid nitrogen (LN_2) after sweeping them through mother liquor supplemented with 20% glycerol.

2.2.3 X-ray data collection and crystal structure determination

X-ray diffraction data for a multiwavelength anomalous dispersion (MAD) experiment were collected at the Canadian Light Source (beam line 08ID-1). Data were collected at three different wavelengths over the absorption edge of zinc from a single crystal of the PLP2-Ub complex held at 100K in a N_2 (g) stream. The data were processed using MOSFLM and SCALA (269) and structure factor phases were determined using phenix.autosol (270). Initial phases generated by SOLVE were improved by density modification using RESOLVE within the PHENIX package. After reserving a random subset of reflections for cross-validation using the free R-factor (271), a model was built using phenix.autobuild (270) and manually completed and refined using Coot (272) and phenix.refine (270). Crystallographic data and model refinement statistics are summarized in **Table 2.1**.

Table 2.1 Crystallographic data and model refinement statistics for the EAV PLP2-Ub complex

Crystal	EAV PLP2-Ub		
Crystal geometry			
Space group	$P2_1\ 2_1\ 2_1$		
Unit cell (Å)	$a = 38.32, b = 62.23, c = 84.28$ $\alpha = \beta = \gamma = 90°$		
Crystallographic data			
Dataset	Edge (Zinc)	Peak (Zinc)	Remote (Zinc)
Wavelength (Å)	1.2829	1.2824	1.2735
Resolution range (Å)	31.10-1.45 (1.53-1.45)*	31.11-1.45 (1.53-1.45)	31.02-1.45 (1.53-1.45)
Total observations	316923 (34142)	317730 (34806)	317984 (36992)
Unique reflections	36316 (5023)	36344 (5029)	36278 (5075)
Multiplicity	8.7 (6.8)	8.7 (6.9)	8.8 (7.3)
Completeness (%)	99.4 (95.9)	99.4 (96.2)	99.6 (97.1)
Anomalous completeness	99.1 (94.0)	99.2 (94.4)	99.4 (95.8)
R_{merge}	0.054 (0.253)	0.049 (0.205)	0.079 (0.596)
I/σI	19.5 (6.0)	21.3 (7.1)	14.7 (4.2)
Phasing statistics			
FOM	0.61		
FOM after RESOLVE	0.72		
Refinement Statistics			
Reflections in test set	1994		
Protein atoms	3138		
Zinc atoms	1		
Solvent molecules	262		
R_{work} (R_{free})	0.16 (0.18)		
RMSDs			
Bond lengths (Å)/angles (°)	0.012/1.4		
Ramachandran plot			
Most favored/allowed (%)	98/2		
Average B factor (Å^2)			
Macromolecules	20.51		
Solvent	32.25		

* Values in parentheses refer to the highest resolution shell.

2.2.4 In vitro enzymatic assays

The *in vitro* PLP2 DUB assays were carried out in collaboration with Mazdak Khajehpour (UM). The DUB activity of PLP2 (wild type and mutants) was assayed using 7-amino-4-methylcoumarin (AMC) labelled versions of Ub (Ub-AMC) (Boston Biochem) and the C-terminal peptide motif of Ub, RLRGG-AMC (Enzo Life Sciences). The enzymes cleave the AMC label causing a significant increase in the fluorescence quantum yield of the dye. All reactions were performed in 20 mM tris-HCl buffer at pH 8 and 100 mM NaCl. Time-dependent fluorescence traces were collected by a Fluorolog-3 Horiba Jobin Yvon fluorimeter. The monochromators were set to 360 nm (excitation) and to 460 nm (emission). The slits were set between 1-3 nm bandpass depending on substrate concentration. Enzyme activities in all mutants were characterized by the specificity constant $\frac{k_{cat}}{K_m}$. At substrate concentrations significantly smaller than K_m the formation of product follows pseudo-first-order kinetics, therefore the temporal evolution of product fluorescence F follows the equation:

$$F = F_{\infty}\left(1 - \exp\left(-\frac{k_{cat}[\mathrm{E}]}{K_m}t\right)\right) + F_0 \qquad (1)$$

Where F_{∞} is the fluorescence when all AMC is liberated, F_0 is the background fluorescence, $[E]$ is the total enzyme concentration and t is the time elapsed. From fitting the fluorescence time traces to equation 1, all parameters including the specificity constant $\frac{k_{cat}}{K_m}$ are obtained. Our assays indicate that PLP2 exhibits pseudo-first-order kinetics for Ub-AMC at concentrations less than 0.2 μM and for RLRGG-AMC at concentrations less than 150 μM.

2.2.5 Reverse genetics

Mutations in the EAV PLP2-coding sequence were engineered in an appropriate shuttle vector and subsequently transferred to pEAN551/AB, a derivative of EAV full-length cDNA

clone pEAN551 carrying additional (translationally silent) *Afl*II and *Bsp*EI restriction sites (273,274). The virus derived from pEAN551/AB was used as wild-type control in all experiments. All constructs were verified by sequence analysis.

In vitro RNA transcription from *Xho*I-linearized wild-type or mutant EAV full-length cDNA clones was performed using the mMESSAGE mMACHINE T7 Kit (Ambion). Five µg of full-length EAV RNA was electroporated into $5.0*10^6$ BHK-21 cells using the Amaxa Cell Line Nucleofector Kit T and the program T-020 of the Amaxa Nucleofector (Lonza) according to the manufacturer's instructions. Cells were incubated at 39.5°C and virus-containing supernatants were harvested at 24 h post transfection. Titers were determined by plaque assay on primary equine lung fibroblasts (ELFs) essentially as described before (275).

To verify the presence of the correct mutations, RNA was isolated from virus-containing supernatants using the QIAamp Viral RNA Mini Kit (Qiagen) and converted to cDNA using RevertAid H Minus reverse transcriptase (Fermentas) and random hexameric primers. The region of PLP2 encoding the mutations was subsequently PCR amplified using *Pfu* DNA polymerase (Fermentas) and sequenced.

2.2.6 Quantitative real-time PCR

Confluent equine lung fibroblasts (ELFs) were infected with wild-type or mutant EAV at multiplicity of infection (m.o.i.) 5, 0.5, or 0.25 and incubated at 37°C. At the indicated time-points, cell lysates were harvested in TriPure Isolation Reagent (Roche). After the addition of chloroform, the aqueous phase was mixed in a 1:1 ratio with buffer RA1 of the Nucleospin RNA II kit (Macherey-Nagel). RNA was isolated as per manufacturer's instructions and reverse transcribed using RevertAid H Minus RT (Fermentas) and oligo$(dT)_{20}$ primer. Finally, samples were assayed by quantitative real-time PCR (qRT-PCR) on a CFX384 Touch Real-Time PCR

detection system (BioRad) using iTaq SYBR Green Supermix with ROX (BioRad). Primers (see **Table 2.2**) targeting mRNAs encoding equine glyceraldehyde 3-phosphate dehydrogenase (GAPDH), Actin-β, IFN-β, MX1, and the EAV genome were designed using Primer3 (276) or kindly provided by Udeni Balasuriya in the case of IL8. The real-time PCR was followed by a melting-curve analysis, to verify the specificity of the reaction. Results were quantified using the standard curve method and normalized against the geometric mean of the relative quantities of GAPDH and Actin-β mRNA. Data from three independent experiments was analyzed with SPSS Statistics software using a one-sample *t* test or unpaired Student's *t* test, where appropriate. P values <0.05 were considered to be statistically significant.

Table 2.2 Primers used for quantitative real-time PCR

Target (Accession)	Forward primer (5'-3')	Reverse primer (5'-3')
Equine GAPDH (NM_001163856)	TGCCGCCTGGAGAAAGCTGC	GAGGGCAATGCCAGCCCCAG
Equine Actin-β (NM_001081838)	CCACGCCATCCTGCGTCTGG	ACCGCTCGTTGCCGATGGTG
Equine IFN-β (NM_001099440)	AGGTGGATCCTCCCAATGGCCC	GGGGCAACGTTGAGGGGCTC
Equine MX1 (NM_001082492)	CGGCCAGCAGCTGCAGAAGT	GGCCTCCGCTCCCTGGAGAT
Equine IL8 (NM_001083951)	GCCGTCTTCCTGCTTTCTG	CCGAAGCTCTGCAGTAATTCTTGAT
EAV genome (NC_002532)	CCGACCCGGTGTGACCGTTG	AAGGGTCGCGGGTGCCAATG

2.2.7 Deubiquitination during infection

Confluent ELFs were infected with wild-type or mutant EAV at m.o.i. 5 and incubated for 10 hours at 37°C. Cells were then lysed in 500 µl 2xLSB and total ubiquitination was assessed by Western blot analysis as described in section 2.2.9.

Ectopic expression experiments were performed essentially as described before (99), but are described in detail in the supplemental materials and methods together with a description of additional plasmids, cells, and antibodies used.

2.2.8 Plasmids, cells, and antibodies

The following mammalian expression plasmids were described elsewhere: pLuc-IFN-β (277), pRL-TK (Promega), pEBG-RIG-$I_{(2CARD)}$ (278), pcDNA-eGFP (99), pCMV-FLAG-Ub (279), pCAGGS-HA-mUbE1L, pCMV2-FLAG-UbcM8, and pCAGGS-V5-hISG15 (280).

HEK293T cells were cultured in Dulbecco's modified Eagle medium (Lonza) supplemented with 10% fetal bovine serum (FBS), and 2 mM L-glutamine. BHK-21 cells were cultured in Glasgow minimum essential medium (Lonza) supplemented with 5% FBS, 10% tryptose phosphate broth, and 10 mM HEPES (pH 7.4). Primary equine lung fibroblasts (ELF) were cultured in minimum essential medium (Lonza) supplemented with 10% FBS and grown on collagen-coated plastics. All culture media contained 100 U/ml of penicillin and 100 mg/ml of streptomycin.

The following commercially available antibodies were used: α-hemagglutinin (HA) (ab18181; Abcam), α-FLAG (F3165; Sigma-Aldrich), α- glutathione S-transferase (GST) (sc459; Santa Cruz), α-Ub (#3933; Cell Signaling Technology), α-β-actin (A5316; Sigma-Aldrich), donkey-α-mouse-Cy3 (715-165-151; Jackson ImmunoResearch), and goat-α-rabbit-AL488 (A-11008; Invitrogen). The following antibodies were described elsewhere: α-EAV N

protein (clone 3E2) (281) and α-ISG15 (clone 2.1) (282). Rabbit antiserum recognizing the C-terminus of EAV nsp2 was raised using a mix of two peptides (ASTVDPHSFDQKK and GDFLKLNPGFRLIGG) and rabbit antiserum recognizing green fluorescent protein (GFP) was raised using recombinant protein purified from *Escherichia coli*.

2.2.9 Cell-culture based assays

To assess nsp2|3 cleavage by the various PLP2 mutants, HEK293T cells were grown to 80% confluence in 10 cm^2 wells and transfected using calcium phosphate with 4 µg plasmid DNA encoding nsp2-3 containing wild-type or mutant PLP2. After 16 h at 37°C, cells were lysed in 2x Laemmli Sample Buffer (2xLSB; 250 mM Tris, 2% sodium dodecyl sulfate (SDS), 20% glycerol, 0.01% bromophenol blue, 2 mM DTT, pH 6.8). Samples were loaded on SDS-polyacrylamide gels, which were blotted to Hybond-P polyvinylidene difluoride membranes (GE Healthcare) using a semi-dry transfer cell (Bio-Rad). After incubation with the appropriate antibodies, protein bands were visualized using the Amersham ECL Plus detection reagent (GE Healthcare).

To assess the DUB activity of the various PLP2 mutants, HEK293T cells were grown to 80% confluence in 4 cm^2 wells and transfected using calcium phosphate with a combination of plasmids encoding FLAG-Ub (0.25 µg), GFP (0.25 µg), and nsp2-3 containing wild-type or mutant PLP2 (1.5 µg). After 16 h at 37°C, cells were lysed in 2xLSB and analyzed by SDS-PAGE as described above.

To assess the deISGylation activity of the various mutants, HEK293T cells were grown to 80% confluence in 12-well plates and transfected using $CaPO_4$ with a combination of plasmids encoding hISG15 (0.75 µg), HA-mUbE1L (0.25 µg), FLAG-UbcM8 (0.25 µg), GFP (0.25 µg)

and wild-type or mutant nsp2-3 (0.5 µg). After 48 h at 37°C, cells were lysed in 2xLSB and analyzed by SDS-PAGE as described above.

2.2.10 Luciferase-based IFN-β promoter activity assay

HEK293T cells, grown to 80% confluence in 2 cm^2 wells, were transfected in quadruplicate with a combination of plasmids encoding firefly luciferase under control of the IFN-β promoter (50 ng), renilla luciferase (5 ng), RIG-$I_{(2CARD)}$ (25 ng) and nsp2-3 containing wild-type or mutant PLP2 (500 ng) using Lipofectamine2000 (Invitrogen). The total amount of DNA used for transfection was adjusted to 1 µg per well by the addition of the appropriate amount of empty vector. After 12 h at 37°C, three out of four wells were lysed in 100 µl passive lysis buffer (Promega), and samples were assayed for luciferase activity using the Dual-Luciferase reporter assay system (Promega) on a Mithras LB 940 multimode reader (Berthold Technologies). The remaining wells from each of three independent experiments were lysed in 2xLSB, mixed in a 1:1:1 ratio and analyzed by SDS-PAGE as described above. Using SPSS Statistics software, an unpaired two-tailed Student's *t* test was used to determine the statistical significance of the results, which were obtained in three independent experiments. P values <0.05 were considered to be statistically significant.

2.2.11 Immunofluorescence microscopy

Confluent ELFs were infected with wild-type or mutant EAV at a multiplicity of infection (m.o.i.) of 5 and incubated at 37°C. At 3, 6, and 9 h post infection (p.i.), cells were fixed with 3% paraformaldehyde (PFA) in phosphate buffered saline (PBS; pH 7.4). Following permeabilization in 0.2% Triton X-100 in PBS, EAV nsp2 and N protein were visualized by indirect immunofluorescence microscopy using the appropriate antibodies. Specimens were

examined with a Zeiss Axioskop 2 fluorescence microscope with an Axiocam HRc camera and Zeiss Axiovision 4.2 software.

2.3 Results

2.3.1 EAV PLP2 adopts a compact OTU-domain fold with a unique integral zinc finger.

Previously, EAV PLP2 was identified and characterized by a combination of bioinformatics analysis and site-directed mutagenesis, and two residues in particular were implicated in catalysis: Cys270 and His332. Throughout this paper, amino acid numbers refer to the sequence of full-length EAV pp1a (209). The crystal structure of EAV PLP2 (residues 261-392; 13.6 kDa) was determined as a covalent complex with the mechanism-based inhibitor Ub(1−75)–3–bromopropylamine (Ub–3Br) (124,226). Since the conservation of multiple cysteine residues and their demonstrated importance for protease function suggested that PLP2 could bind zinc (209), the crystal structure of the complex was determined by a multi-wavelength anomalous dispersion (MAD) phasing experiment using X-ray diffraction data collected over the zinc absorption edge (Table 2.1). The resulting electron density map revealed residues 261-387 of PLP2 bound to a complete Ub molecule and allowed a model of the complex to be built and refined (Rwork= 0.16, Rfree= 0.18) to 1.45 Å resolution (**Figure 2.1 A-B**).

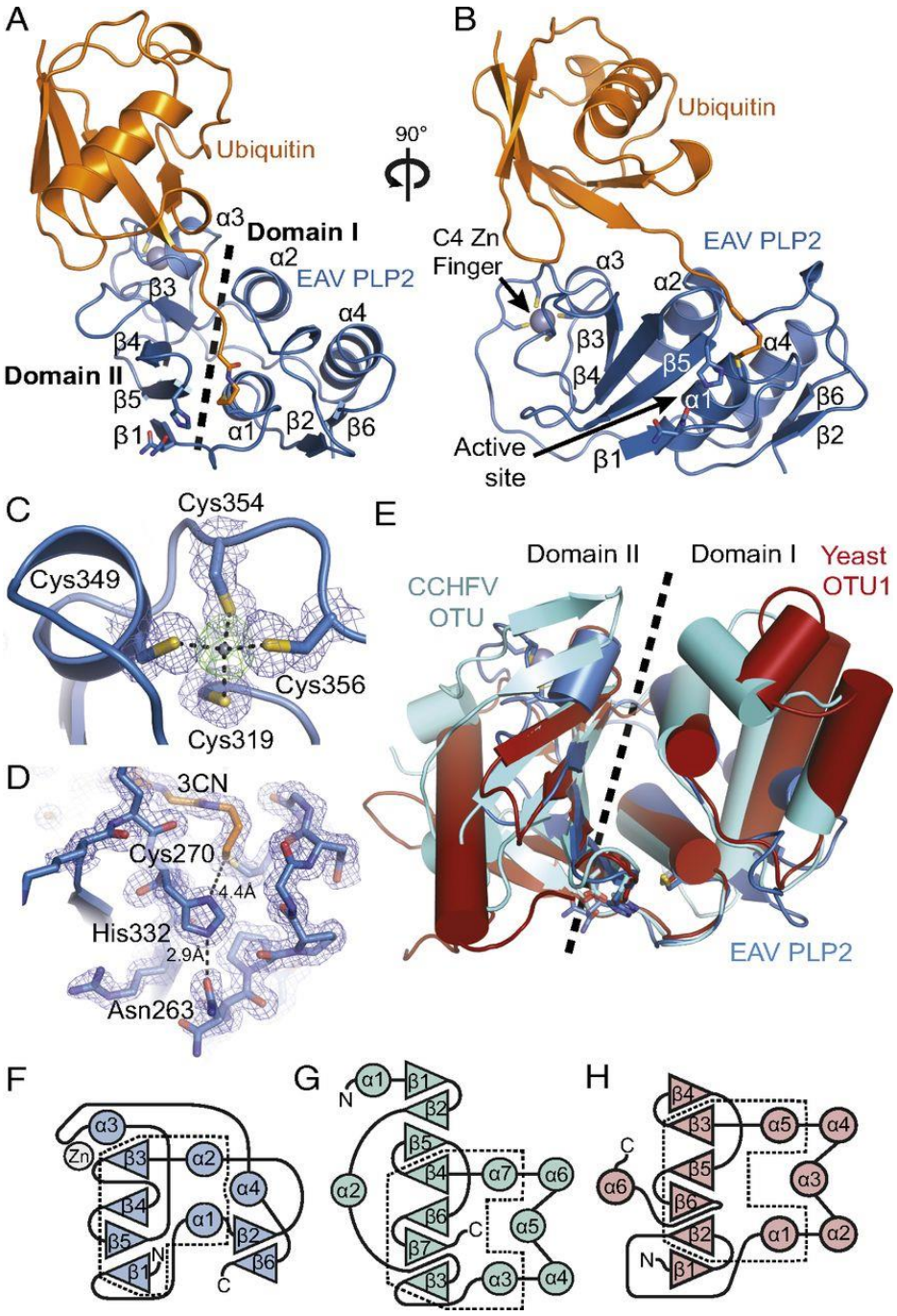

Figure 2.1 Structure of the EAV PLP2-Ub complex and superposition with yeast OTU1 and CCHFV OTU.

(A) Structure of EAV PLP2 (blue) bound to Ub (orange) showing the two-domain fold. (B) 90 degree rotation of complex shown in *panel A*. (C) Electron density for the C4 zinc finger motif. Blue density is a maximum-likelihood weighted $2F_o$-F_c map contoured at 1.0σ. Green density

about the zinc atom (grey) is a F_o-F_c omit map contoured at 5.0σ. (D) The catalytic triad of the EAV PLP2 active site. Blue density is a maximum-likelihood weighted $2F_o$-F_c map contoured at 1.0σ. The cysteine nucleophile (Cys270) is covalently linked to Ub via the 3CN linker, which replaces Gly76 of Ub. Asn263, which orients the imidazole ring of His332, occurs in two alternate conformations. (E) Superposition of EAV PLP2 (blue), CCHFV OTU (cyan) and yeast OTU1 (red). PLP2 shares a conserved core of two central α-helixes and a four-stranded β-sheet with CCHFV OTU and yeast OTU1. Topology diagrams for EAV PLP2, CCHFV OTU and yeast OTU1 are shown in panels F, G, and H, respectively. The region that is conserved amongst the enzymes is outlined (dashed box). Structural images were prepared using PyMOL (283). This figure was originally published in *Proceedings of the National Academy of Sciences USA*. van Kasteren PB, Bailey-Elkin BA, James TW, Ninaber DK, Beugeling C, Khajehpour M, Snijder EJ, Mark BL, Kikkert M (2013) The deubiquitinase function of arterivirus papain-like protease 2 suppresses the innate immune response in infected host cells. Feb 26;110(9):E838-47.

The protease adopts a compact, two-domain fold with a shallow Ub-binding surface that directs the C-terminus of the bound Ub molecule (the 'distal' Ub in an isopeptide-linked diUb molecule) towards a solvent exposed active site that indeed includes Cys270 and His332 (**Figure 2.1 A-B**). Domain I of PLP2 (residues 267-307 and 365-387) consists of a three-helix bundle (α1, α2, α4) packed against a two-stranded antiparallel sheet (β2↑ β6↓). Domain II centers on a four-stranded β-sheet (β1↑ β5↓ β4↑ β3↑) and an α-helix (α3) that together pack against helices α1 and α2 of domain I. Domain II comprises the majority of the Ub-binding surface, which is stabilized by four cysteine residues (Cys 319, 349, 354, 356) that coordinate a zinc ion with tetrahedral geometry (**Figure 2.1 C**). Their arrangement forms a C4 zinc finger that resembles a C-terminal type zinc necklace motif (284). A large insertion between positions C1 (Cys319) and C2 (Cys349), which includes His332, appears to extend the stabilizing effect of the zinc finger throughout much of domain II. A fifth cysteine (Cys344) is located near the zinc ion but does not coordinate with it, consistent with other zinc necklace motifs that have been described (284) and with previous findings showing that a Cys344 to alanine mutation had no effect on catalytic activity of PLP2 (209). Three of the cysteines (Cys 319, 349, and 354) are fully conserved in arteriviruses, and mutational analysis of these residues and Cys356 demonstrated zinc binding to be essential for catalytic activity (209). Given its distance from the active site however (~25 Å) (**Figure 2.1 B**), the zinc finger appears to play a structural role as opposed to participating in catalysis. Expression of PLP2 in *E. coli* grown in the absence of zinc (M9 medium) yielded insoluble protein, supporting the idea that the zinc finger is structural and is likely required for correct folding of the protease.

Consistent with OTU DUBs and papain-like cysteine proteases in general, the PLP2 active site contains a catalytic cysteine nucleophile (Cys270) and histidine (His332) residue,

along with an asparagine (Asn263) that hydrogen bonds with the imidazole ring of His332 (**Figure 2.1 D**). As expected, the side chain of Cys270 is covalently coupled to the C-terminus of Ub via the 3-propylamine (3CN) modification, mimicking the acyl-enzyme intermediate step of the catalytic reaction and confirming the identity of Cys270 as the catalytic nucleophile.

Fold analysis of the PLP2 structure using the DALI server (285) revealed that its closest structural homologues indeed belong to the OTU superfamily of DUBs (17,210). The most significant matches were to yeast Otu1 (226) (Z-score: 5.1) and the viral OTU protease from CCHFV (103,105,106) (Z-score: 4.6) (**Figure 2.1 E**), followed by Otubain1 from human (286) and *Caenorhabditis elegans* (287) (Z-scores: 4.1 and 4.0, respectively), and the OTU-domain of human DUBA (288) (Z-score: 3.9). The sequence identity of the PLP2 regions that aligned with these OTU proteases was low (ranging from 9% for yeast Otu1 to 21% for human Otubain1); however, they accounted for ~60% of the total PLP2 structure and superposed well with the equivalent regions in the above proteins, with an average root-mean-square deviation (rmsd) of ~2.8 Å. The greatest structural similarity between PLP2 and members of the OTU superfamily occurs at the active site and adjoining channel that binds the C-terminal RLRGG-tail of Ub.

2.3.2 The PLP2 zinc finger motif plays a central role in Ub binding

Arterivirus PLP2 and nairovirus OTU enzymes differ from eukaryotic OTU DUBs in that they also remove the Ub-like antiviral protein Interferon Stimulated Gene 15 (ISG15) from target proteins, a process also known as deISGylation (102,218). ISG15 conjugation has been postulated to interfere with proper viral protein function, possibly through steric hindrance, although the exact mechanism underlying its antiviral activity is unknown (289). For CCHFV OTU, cross-reactivity with ISG15 arises primarily from a unique β-hairpin on the Ub-binding surface. The hairpin modifies the surface so that the viral enzyme binds the β-grasp folds of Ub

and the C-terminal Ub-like domain of ISG15 in an orientation that is rotated nearly 75° with respect to that observed for Ub bound to a representative eukaryotic OTU DUB from yeast (Otu1) (105,106) (**Figure 2.2 A**). Surprisingly, the β-hairpin is absent in EAV PLP2 and replaced by helix α3 of the zinc finger motif (**Figure 2.2 A**). However, in keeping with the role of the β-hairpin in CCHFV OTU, residues of helix α3 bind to the hydrophobic 'Ile44 patch' of Ub, a site commonly targeted by Ub-binding proteins (2), and they also assist in positioning Ub in a rotated manner equivalent to that observed for CCHFV OTU (**Figure 2.2 B, C**).

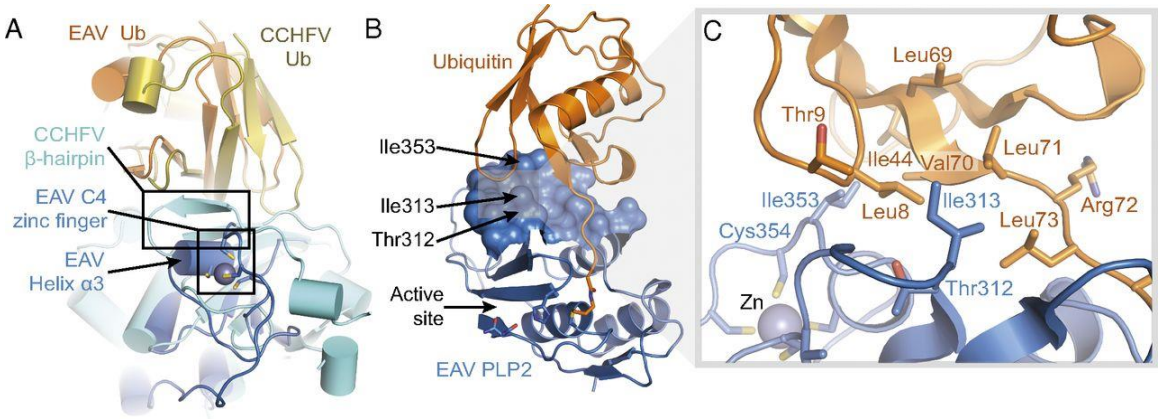

Figure 2.2 Ub-binding surface of EAV PLP2.
(A) Superposition of EAV PLP2 (blue) and CCHFV OTU (cyan) in complex with Ub. Both enzymes grasp Ub in a similar orientation, with the C4 zinc finger motif of EAV PLP2 replacing the β-hairpin of CCHFV OTU. (B) EAV PLP2 (blue) bound to Ub (orange), showing the 612 $Å^2$ Ub-binding surface. Residues targeted for mutational analysis to disrupt DUB activity are indicated by arrows. (C) Close-up of the EAV PLP2-Ub binding surface. EAV PLP2 residue Ile353 forms van der Waals interactions with Ile44, Leu8, and Val70 of Ub, whereas residues Thr312 and Ile313 interact with a hydrophobic patch on Ub (formed by residues Leu8, Val70, Leu71, and Ile73) closer to the active site of PLP2. This figure was originally published in *Proceedings of the National Academy of Sciences USA*. van Kasteren PB, Bailey-Elkin BA, James TW[1], Ninaber DK, Beugeling C, Khajehpour M, Snijder EJ, Mark BL, Kikkert M (2013) The deubiquitinase function of arterivirus papain-like protease 2 suppresses the innate immune response in infected host cells. Feb 26;110(9):E838-47.

2.3.3 Structure-guided decoupling of PLP2 deubiquitinase and polyprotein cleavage activities

Given the distance of helix α3 from the PLP2 active site (**Figure 2.1 B**), we hypothesized that mutations could be introduced into this region of the Ub-binding surface that would selectively disrupt PLP2 DUB activity without affecting EAV polyprotein cleavage at the putative nsp2|nsp3 junction (RLIGG↓). While this sequence closely resembles the C-terminal tail of Ub (RLRGG↓), we postulated that the nsp2 sequence immediately upstream of the nsp2|nsp3 junction does not adopt a Ub-like fold and that the majority of the PLP2 Ub-binding surface is therefore not required for its cleavage. To test our hypothesis, we used the crystal structure to select three positions within the PLP2 Ub-binding surface, Thr312, Ile313, and Ile353, and engineer a panel of (combined) mutations (**Figure 2.2 B-C**). Ile353 is located at the C-terminal end of helix α3 next to C3 (Cys354) of the zinc finger motif. It projects directly into the Ile44 patch of Ub where it makes extensive van der Waals interactions with Ile44, Val70, and Leu8. Given that Ile353 is located on the Ub-binding surface, we aimed to disrupt Ub binding by introducing various other residues at this position, including large bulky residues such as arginine and tryptophan. Thr312 and Ile313 are located closer to the active site, where they make additional hydrophobic interactions with Leu8, Leu71, and Leu73 of Ub. In an attempt to further disrupt the interaction between PLP2 and Ub, the mutations Thr312Ala and Ile313Val were also combined with changes at position Ile353. Given the close proximity of Ile313 to Leu73 of the RLRGG motif of Ub, mutation to valine was chosen to minimize adverse effects on nsp2|nsp3 cleavage.Before proceeding to infection experiments with mutant viruses, we used ectopic expression of PLP2 and an in vitro enzymatic assay to characterize the effect of various mutations at the positions described above on polyprotein processing and DUB activity. To this end, mutations were introduced into a mammalian expression vector encoding a self-cleaving

nsp2-3 polyprotein carrying an N-terminal HA-tag. Upon expression of nsp2-3 in HEK293T cells, wild-type PLP2 mediated efficient cleavage of the nsp2|nsp3 junction (**Figure 2.3 A**). As expected, a PLP2 active site mutant (Cys270Ala/His332Ala) did not display any processing of the nsp2|nsp3 site and only the nsp2-3 precursor was detected. Seven single-site mutants, in which the Ub-binding surface was targeted by replacement of Thr312 or Ile353, displayed wild-type levels of nsp2|nsp3 cleavage, suggesting that their polyprotein processing was not notably affected. In addition, combinations of mutations at positions Thr312, Ile313, and Ile353 were tested, with similar results (**Figure 2.3 A**). Longer exposure times did reveal some nsp2-3 precursor, even in the case of wild-type PLP2, but this amount only marginally increased when two or three mutations were combined (**Figure 2.4 B**).

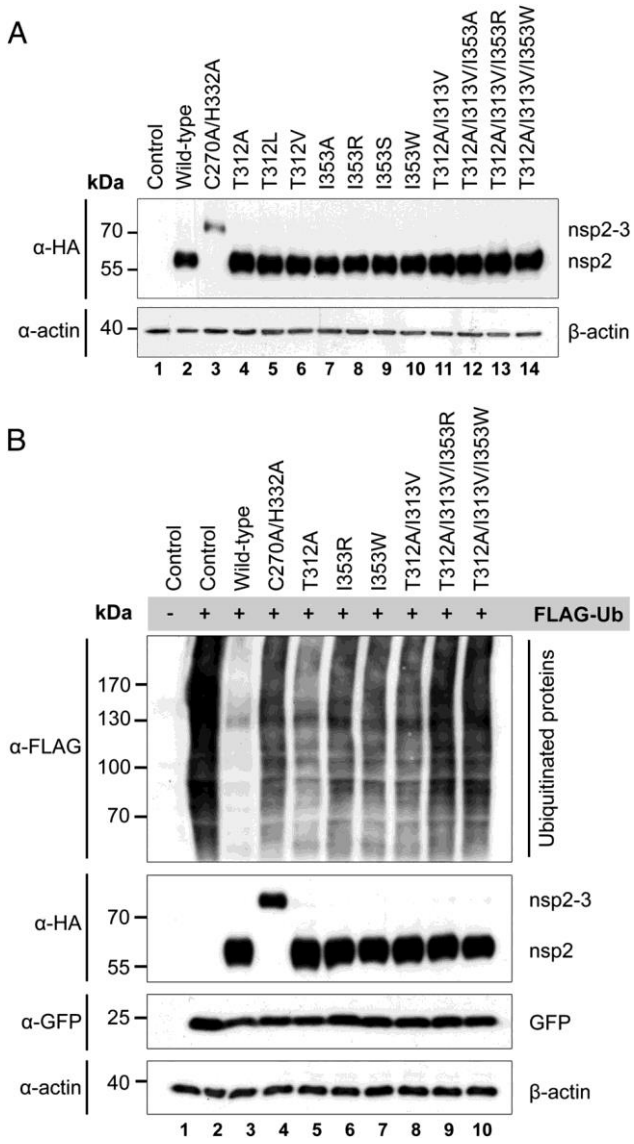

Figure 2.3 Decoupling of the polyprotein processing and DUB activities of EAV PLP2.
(A) HEK293T cells were transfected with plasmids encoding nsp2-3 containing wild-type or mutant PLP2. After 16 h at 37°C, cells were lysed and results were analyzed by Western blot. Proteolytic processing of the nsp2|nsp3 junction by wild-type PLP2 resulted in the release of HA-tagged nsp2 from the nsp2-3 precursor. (B) HEK293T cells were transfected with a combination of plasmids encoding nsp2-3 containing wild-type or mutant PLP2 and FLAG-Ub. Expression of FLAG-Ub leads to FLAG-tagged ubiquitination of a wide range of cellular proteins, which can be visualized on Western blot using an anti-FLAG antibody. Ub, ubiquitin. This figure was originally published in *Proceedings of the National Academy of Sciences USA*. van Kasteren PB, Bailey-Elkin BA, James TW, Ninaber DK, Beugeling C, Khajehpour M, Snijder EJ, Mark BL, Kikkert M (2013) The deubiquitinase function of arterivirus papain-like protease 2 suppresses the innate immune response in infected host cells. Feb 26;110(9):E838-47.

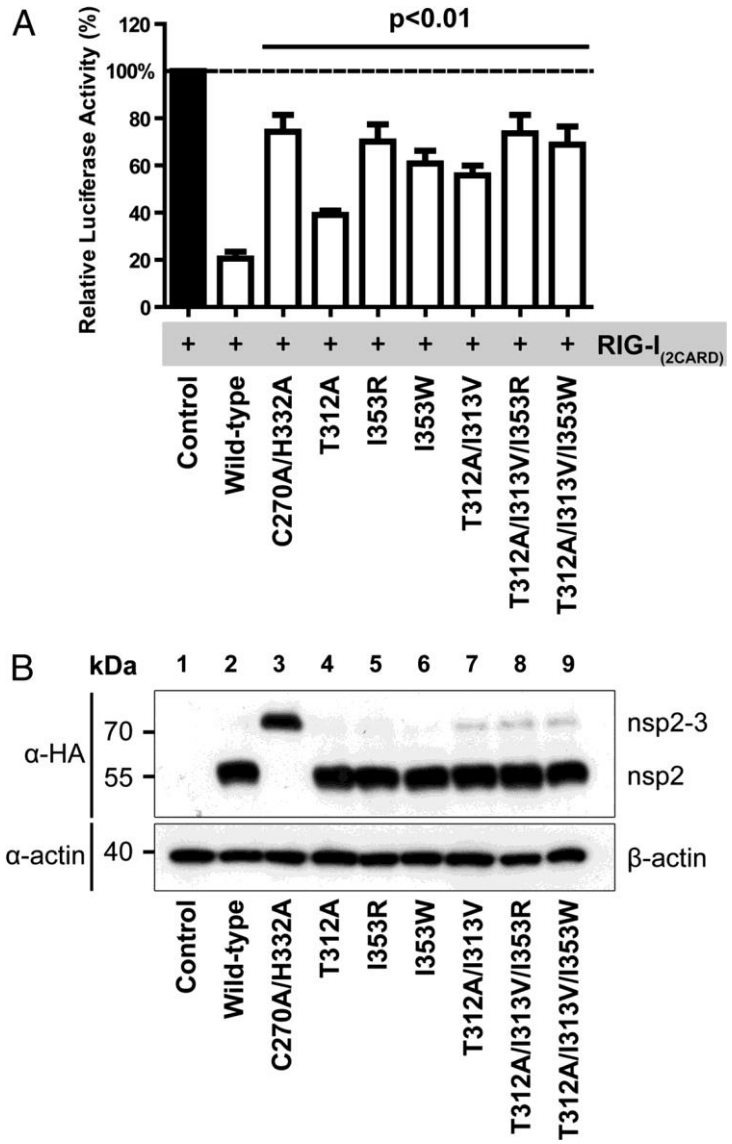

Figure 2.4 PLP2 Ub-binding surface mutations attenuate inhibition of IFN-β promoter activation.

(A) Luciferase-based reporter assay to assess the effect of various Ub-binding surface mutations on the inhibition of IFN-β promoter activity by PLP2. HEK293T cells were transfected with a combination of plasmids encoding firefly luciferase under control of the IFN-β promoter, renilla luciferase, RIG-I$_{(2CARD)}$, and nsp2-3 containing wild-type or mutant PLP2. Results were obtained in three independent experiments. Error bars represent standard deviations and p-values are relative to wild-type. (B) Lysates obtained in each of the three experiments used for panel A were mixed in a 1:1:1 ratio and analyzed by Western blot for the expression of nsp2-3. This figure was originally published in *Proceedings of the National Academy of Sciences USA*. van Kasteren PB, Bailey-Elkin BA, James TW, Ninaber DK, Beugeling C, Khajehpour M, Snijder EJ, Mark BL, Kikkert M (2013) The deubiquitinase function of arterivirus papain-like protease 2 suppresses the innate immune response in infected host cells. Feb 26;110(9):E838-47.

Next, we assayed the effect of these mutations on PLP2 DUB activity by transfecting mammalian cells with plasmids encoding FLAG-tagged Ub and nsp2-3 carrying wild-type or mutant PLP2. FLAG-tagged ubiquitination of a wide range of cellular targets could be visualized by Western blot analysis using an anti-FLAG antibody (**Figure 2.3 B**). As expected, expression of wild-type PLP2 strongly decreased the accumulation of Ub-conjugates, while expression of the active site mutant (Cys270Ala/His332Ala) had a negligible effect. **Figure 2.3 B** presents the results obtained with a selection of PLP2 Ub-binding surface mutants with the most pronounced effect on DUB activity, some of which approached the level of the active site mutant. In contrast, these Ub-binding surface mutations had only minor effects on deISGylating activity of PLP2 (**Figure 2.5**).

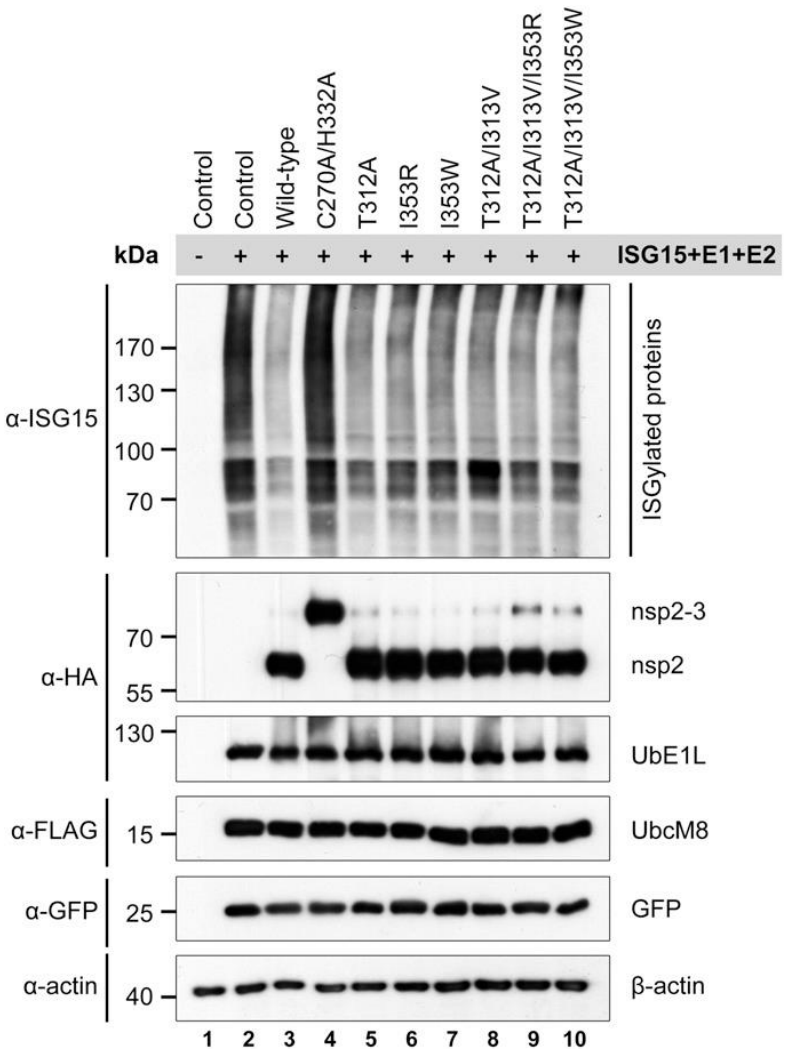

Figure 2.5 The DeISGylating activity of PLP2 is only mildly affected by Ub-binding surface mutations.

HEK293T cells were transfected with a combination of plasmids encoding nsp2-3 containing wild-type or mutant PLP2, GFP, hISG15, and the E1 and E2 enzymes needed for its conjugation: HA-UbE1L and FLAG-UbcM8. ISGylation is visualized on Western blot using an anti-ISG15 antibody. This figure was originally published in *Proceedings of the National Academy of Sciences USA*. van Kasteren PB, Bailey-Elkin BA, James TW, Ninaber DK, Beugeling C, Khajehpour M, Snijder EJ, Mark BL, Kikkert M (2013) The deubiquitinase function of arterivirus papain-like protease 2 suppresses the innate immune response in infected host cells. Feb 26;110(9):E838-47.

To corroborate our findings from the expression system showing that PLP2 DUB activity could be selectively removed without disturbing nsp2|nsp3 cleavage, an *in vitro* activity assay of recombinant PLP2 produced in *E. coli* was performed using the fluorescently labeled substrates Ub-AMC or RLRGG-AMC, representing the C-terminal peptide motif of Ub. By comparing the activity of PLP2 mutants against Ub-AMC (which requires the Ub-binding surface) versus their activity against RLRGG-AMC (which binds to the active site region only), PLP2 mutants with a selective reduction in DUB activity could be identified. Indeed, compared to wild-type enzyme, mutants I353W and I353R exhibited ~10- and 20-fold reductions in specificity (k_{cat}/K_m) toward Ub, respectively; in contrast, their activity towards RLRGG-AMC was unaltered (**Table 2.3**). Expression of PLP2 containing additional mutations at Thr312 and Ile313 yielded insoluble protein in *E. coli*, preventing analysis of these mutants. Nevertheless, the results of the *in vitro* activity assay further confirmed the successful decoupling of the polyprotein processing and DUB activities of EAV PLP2 by specifically targeting key residues of the Ub-binding surface.

Table 2.3 Effect of Ub-binding surface mutations on the substrate specificity of PLP2

	Substrate	
PLP2 enzyme	RLRGG-AMC (k_{cat}/K_m)($M^{-1}s^{-1}$)	Ub-AMC (k_{cat}/K_m)($M^{-1}s^{-1}$)
Wt	45 ± 11	17000 ± 4000
I353R	65 ± 7	413 ± 177
I353W	155 ± 12	1741 ± 850

2.3.4 The ability of PLP2 to suppress innate immune signaling depends on its DUB activity

The effect of the various PLP2 Ub-binding surface mutations on innate immune signaling was initially assessed in the context of ectopic nsp2-3 expression using a luciferase-based IFN-β promoter activity assay. For this, HEK293T cells were transfected with a combination of plasmids encoding firefly luciferase under control of the IFN-β promoter, renilla luciferase as an endogenous control, constitutively active RIG-$I_{(2CARD)}$ to induce innate immune signaling (278), and EAV nsp2-3 containing either wild-type or mutant PLP2. In this assay, reporter gene expression was reduced to approximately 20% upon co-expression of wild-type PLP2, while 80% of the level of the untreated control was retained upon expression of the PLP2 active site mutant (Cys270Ala/His332Ala) (**Figure 2.4 A**). Compared to wild-type PLP2, all mutants included in **Figure 2.4** were significantly impaired in their inhibitory activity ($p<0.01$), with mutants I353R, I353W, Thr312Ala/Ile313Val/Ile353Arg, and Thr312Ala/Ile313Val/Ile353Trp displaying inhibition levels similar to that of the active site mutant ($p>0.05$). Western blot analysis confirmed equal expression of wild-type and mutant nsp2-3 (**Figure 2.4 B**). These results demonstrated that, at least in the context of the nsp2-3 expression system, the selective removal of PLP2 DUB activity significantly disrupted its ability to suppress IFN-β promoter activity.

2.3.5 Arteriviruses lacking PLP2 DUB activity elicit an enhanced host innate immune response

Having identified mutations in PLP2 that reduce its ability to suppress Ub-mediated innate immune signaling (**Figure 2.4** A) without adversely affecting nsp2|nsp3 cleavage (**Figure 2.3 A**), we were in a position to directly evaluate the importance of PLP2 DUB activity for immune evasion during arterivirus infection. The six (combinations of) mutations used in **Figure 2.3 B** and **Figure 2.4** were introduced into an EAV full-length cDNA clone and mutant viruses

were launched by electroporation of *in vitro* transcribed RNA into BHK-21 cells. Immunofluorescence microscopy subsequently confirmed expression of both nsp2 and the structural nucleocapsid (N) protein, followed by virus spread to initially untransfected cells. This indicated that viruses carrying these (combinations of) mutations were replication competent.

We next focused on the two mutants showing the greatest decrease in inhibitory activity in the IFN-β promoter activity assay: Ile353Arg and Thr312Ala/Ile313Val/Ile353Arg (**Figure 2.4 A**). We first characterized the replication kinetics of these mutants in a time-course experiment in primary equine lung fibroblasts (ELFs), which are derived from the natural host species of EAV and are likely to maintain an intact innate immune response. ELFs were infected with wild-type or mutant EAV at a multiplicity of infection (m.o.i.) of 0.5 or 5. The first-cycle replication kinetics as determined by quantitative real-time PCR (qRT-PCR) measurement of viral genome RNA levels did not notably differ between wild-type and mutant EAV **(Figure 2.6 A-B**). In addition, viral titers in cell-culture supernatants harvested from infected ELFs at 24 h p.i. revealed no significant difference between wild-type and mutant EAV (**Figure 2.6 C**). Finally, immunofluorescence microscopy of ELFs infected with m.o.i. 5 revealed expression of nsp2 from 6 hours post-infection (h p.i). onward, and by 9 h p.i. also expression of N protein could be seen in all cells for both wild-type and mutant EAV (**Figure 2.7**). These results demonstrated that the replication kinetics of the PLP2 Ub-binding surface mutants and wild-type control were essentially the same, in line with our previous conclusion that cleavage of the nsp2|nsp3 site is hardly affected by these mutations. At the same time, Western blot analysis showed that, compared to wild-type EAV, the DUB activity of both mutants was severely impaired during infection (**Figure 2.6 D**).

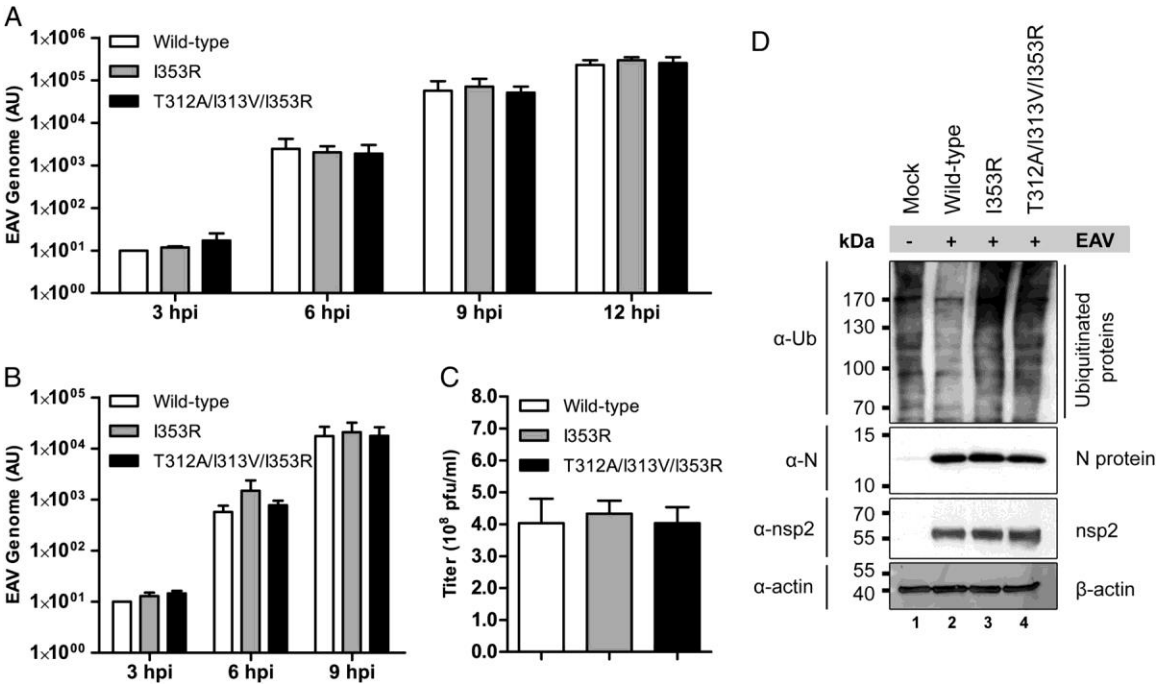

Figure 2.6 EAV PLP2 mutants display similar replication kinetics as wild-type virus.
Equine lung fibroblasts were infected with wild-type or mutant EAV at m.o.i. 0.5 (A) or 5 (B, C, D). (A) and (B) At the indicated time-points, total RNA was isolated for qRT-PCR measurement of EAV genomic RNA levels. Results, which were obtained in three independent experiments, were analyzed using the standard curve method and normalized against the relative quantities of GAPDH and β-actin mRNA. Error bars represent standard deviations. **(**C) At 24 h p.i., cell-culture supernatants were harvested and virus titers were determined by plaque assay on ELFs. Results were obtained in three independent experiments and error bars represent standard deviations. (D) Cells were lysed at 10 h p.i. and total ubiquitination was assessed by Western blot analysis. This figure was originally published in *Proceedings of the National Academy of Sciences USA*. van Kasteren PB, Bailey-Elkin BA, James TW, Ninaber DK, Beugeling C, Khajehpour M, Snijder EJ, Mark BL, Kikkert M (2013) The deubiquitinase function of arterivirus papain-like protease 2 suppresses the innate immune response in infected host cells. Feb 26;110(9):E838-47.

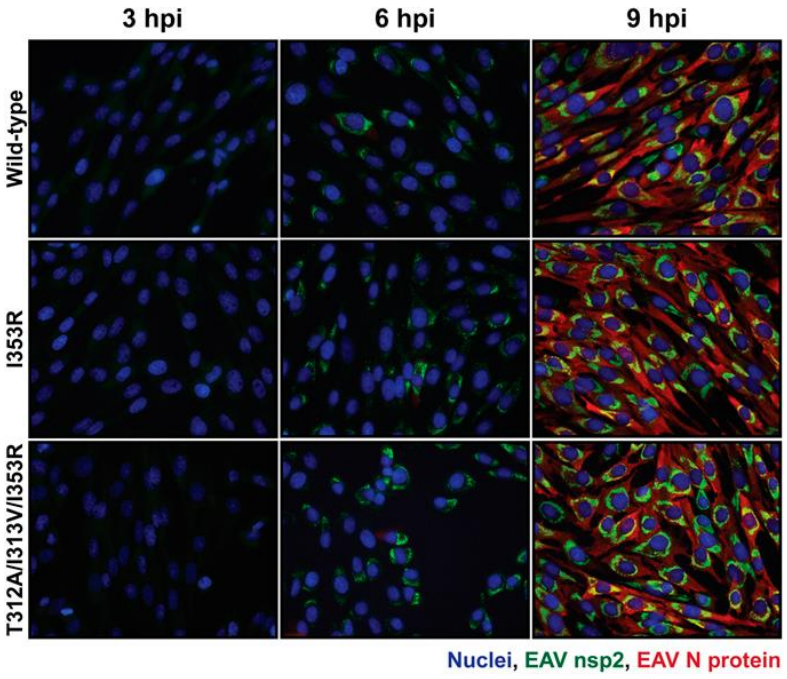

Figure 2.7 Immunofluorescence microscopy reveals similar replication kinetics for WT and PLP2 mutant viruses.
ELFs were infected with wild-type or mutant EAV at m.o.i. 5. At 3, 6, and 9 hpi, cells were fixed for immunofluorescence microscopy, and EAV nsp2 (green), N protein (red), and nuclei (blue) were visualized using the appropriate antibodies or Hoechst dye, respectively. This figure was originally published in *Proceedings of the National Academy of Sciences USA*. van Kasteren PB, Bailey-Elkin BA, James TW, Ninaber DK, Beugeling C, Khajehpour M, Snijder EJ, Mark BL, Kikkert M (2013) The deubiquitinase function of arterivirus papain-like protease 2 suppresses the innate immune response in infected host cells. Feb 26;110(9):E838-47.

Subsequently, we used qRT-PCR to measure the levels of mRNAs encoding IFN-β, the IFN-stimulated protein MX1, and the pro-inflammatory cytokine IL8 and investigated the effect of mutations Ile353Arg and Thr312Ala/Ile313Val/Ile353Arg on innate immune signaling during infection of ELFs. Initially, we infected ELFs with wild-type or mutant EAV at m.o.i. 5, but in this set-up IFN-β mRNA levels remained below the detection limit at all time-points analyzed (from 3 to 12 h p.i.), suggesting that the innate immune response triggered by EAV upon initial infection is very limited. Therefore, we next infected ELFs with wild-type or mutant EAV at m.o.i. 0.25, resulting in infection of about 20% of cells. We hypothesized that this would allow for IFN-β-mediated priming of uninfected cells as a result of paracrine signaling from cells infected during the first round. The expression of IFN-stimulated genes would then result in a more potent response during the second cycle of infection. Indeed, following such a low m.o.i. infection with wild-type EAV, low but detectable levels of IFN-β mRNA were induced by 20 h p.i. (**Figure 2.8 A**). Interestingly, at both 20 and 24 h p.i., cells infected with either mutant showed significantly increased levels of IFN-β mRNA compared to wild-type virus-infected cells ($p<0.05$), with mutant Thr312Ala/Ile313Val/Ile353Arg showing the most pronounced difference. In addition, the levels of MX1 mRNA differed significantly between wild-type and mutant EAV-infected cells at 24 h p.i. (**Figure 2.8 B**). In contrast, at 20 and 24 h p.i., no significant difference in the levels of IL8 mRNA was observed upon infection with wild-type or mutant EAV (**Figure 2.8 C**). Equally efficient replication of wild-type and mutant EAV was corroborated by comparing viral genome RNA levels, for which no significant differences were measured (**Figure 2.8 D**). In summary, these data show that the PLP2 DUB function is indeed involved in the inhibition of innate immune signaling during EAV infection in primary equine

cells and that it is possible to specifically inactivate this function to suppress immune evasion of otherwise fully replication-competent viruses.

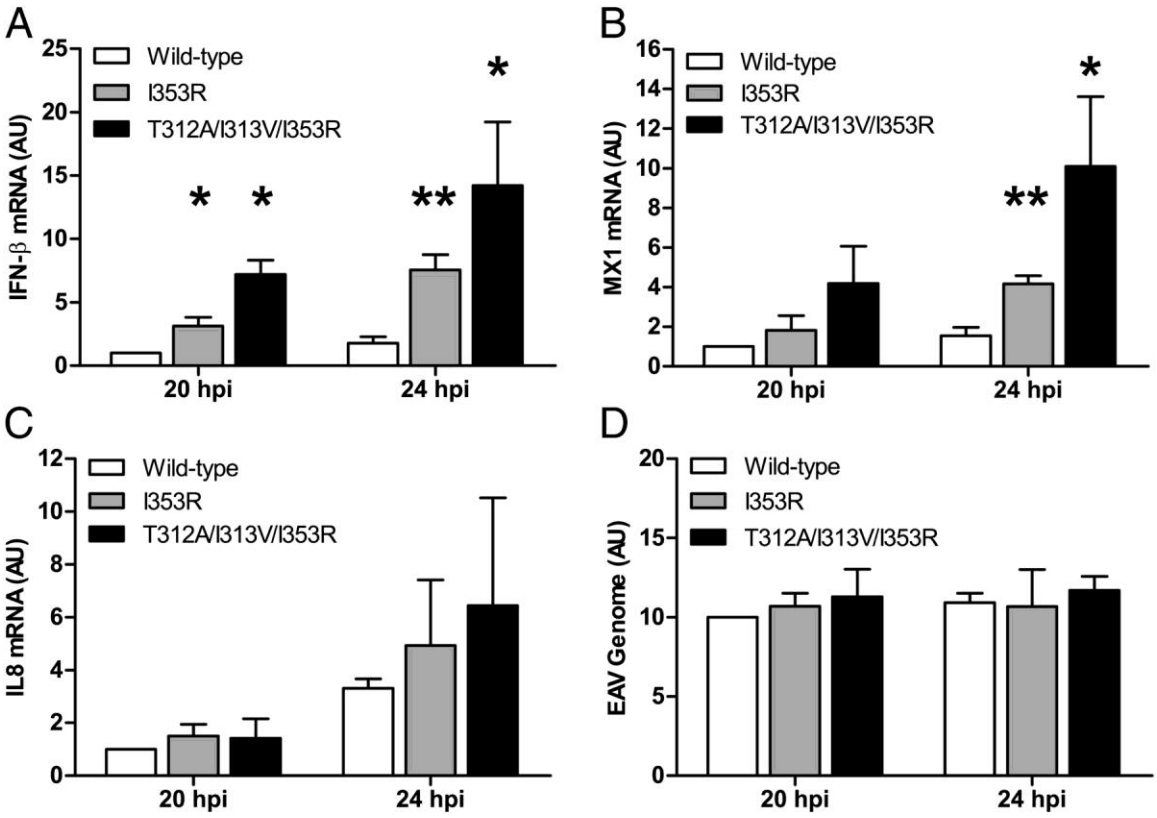

Figure 2.8 EAV lacking PLP2 DUB activity elicits an enhanced innate immune response.
ELFs were infected with EAV encoding wild-type or mutant PLP2 at m.o.i. 0.25 and at 20 and 24 h p.i. RNA was isolated for qRT-PCR measurement of the levels of (A) IFN-β mRNA, (B) MX1 mRNA, (C) IL8 mRNA, or (D) EAV genomic RNA. Results, which were obtained in three independent experiments, were analyzed using the standard curve method and normalized against the relative quantities of GAPDH and β-actin mRNA. Error bars represent standard deviation and asterisks indicate a significant difference relative to wild-type at the same time-point. * $p<0.05$; ** $p<0.01$. This figure was originally published in *Proceedings of the National Academy of Sciences USA*. van Kasteren PB, Bailey-Elkin BA, James TW, Ninaber DK, Beugeling C, Khajehpour M, Snijder EJ, Mark BL, Kikkert M (2013) The deubiquitinase function of arterivirus papain-like protease 2 suppresses the innate immune response in infected host cells. Feb 26;110(9):E838-47.

2.4 Discussion

Due to the widespread adoption of polyprotein synthesis and cleavage as a genome expression strategy in +RNA viruses and retroviruses, proteases have become key regulatory enzymes of the replication of many important human and animal pathogens. Moreover, virus-host co-evolution has offered ample opportunity to develop additional protease functions, which promote virus replication by targeting cellular rather than viral substrates. Since both functions depend on the same protease active site, it has been intrinsically difficult to study them independently during virus infection, mainly because protease inactivation *per se* is generally incompatible with virus viability. The independent assessment of the cleavage of host cell targets requires its decoupling from viral polyprotein processing, which to date has only been achieved for the poliovirus 2A protease (290-292). However, our present work on EAV PLP2 demonstrates how structure-guided mutagenesis can offer a solution to this problem. The identification of a Ub-binding surface that is distant from the PLP2 active site, allowed us to specifically inactivate the DUB function of the enzyme and - ultimately - probe its relevance in the context of the infected cell. Compared to wild-type EAV, viruses that lack PLP2 DUB activity induced a significantly enhanced innate immune response in primary equine cells, while displaying essentially identical replication kinetics, thus demonstrating the importance of this activity in the evasion of innate immune signaling by arteriviruses.

Analysis of the EAV PLP2 fold using the DALI server identified members of the OTU superfamily as its closest structural relatives, supporting its classification as a member of this superfamily. However, the limited sequence similarity between arterivirus PLP2 and other OTU proteases was previously rated as statistically insignificant (210) and our structure reveals topological features that deviate considerably from a typical OTU-fold. Domain I of known

OTU-domain structures contains a pair of solvent exposed α-helices that pack perpendicularly against two internal helices (**Figure 2.1 E, G-H**). While the internal helices are conserved in PLP2 (α1 and α2), the solvent exposed helices have been replaced by a single helix (α4) that packs parallel to helices α1 and α2 to form a three-helix bundle that comprises most of domain I (**Figure 2.1 E-F**). This topology subtly resembles the L domain of papain (116) and markedly reduces the size of domain I and its contribution to Ub binding relative to other OTU DUBs that have been determined in complex with Ub (103,105,106,226,288). The compact fold of arterivirus PLP2 may be required for its function in replicase polyprotein maturation, an activity that is not shared by cellular OTU DUBs or the OTU protease of CCHFV (293).

A more striking deviation from known OTU-domain structures is the presence of the zinc finger in PLP2 domain II (**Figure 2.1 C**) and its critical importance for catalytic activity (209). Ub-binding domains that contain zinc fingers exist within a number of OTU DUBs, but none comprise part of the distal Ub-binding site within the OTU-fold. Instead, they exist as accessory domains that are connected to the OTU-domain through flexible linkers (17), where, in the case of A20, they appear to provide additional polyUb linkage specificity and possibly target the protein to specific signaling complexes (294). For PLP2, the zinc finger is an integral part of the OTU-fold and it plays a central role in binding and positioning the distal Ub molecule on the protease surface (**Figure 2.2 A**). Currently, OTU DUBs are grouped into three subclasses based on their structural characteristics: the Otubains, the A20-like OTU's, and the OTU's (17). Given the unique features of EAV PLP2, we propose that arterivirus PLP2 enzymes represent a new, fourth subclass of zinc-dependent OTU's.

We believe that the structure-guided inactivation of the PLP2 DUB function may contribute to the engineering of improved modified live vaccines (MLVs) for arteriviruses.

Although generally effective strategies for the prevention and control of equine viral arteritis have been developed, several field strains are poorly neutralized by antibodies from horses vaccinated with the ARVAC vaccine strain (295) and EAV outbreaks continue to cause significant disruptions of the horse breeding industry (296). While our current work focuses on EAV PLP2, the corresponding protease of PRRSV has been shown to have very similar immune evasive properties in a variety of experimental settings (99,101,102). Since its discovery in the late 1980s, PRRSV has spread around the globe and now ranks among the most important swine pathogens. PRRSV infection causes annual losses of approximately $664 million in the United States alone (206) and the emergence of highly virulent strains in China is of particular concern (297-299). Moreover, the virus has proven difficult to control and it has been suggested to counteract innate immunity, thus undermining the overall immune response and viral clearance in infected animals. Consequently, inactivation of the PLP2 DUB function may be an important step in the design of improved vaccine candidates. These should induce a more robust innate response and, therefore, also a more potent adaptive immune reaction than that achieved with the currently available MLVs. Multiple studies have suggested that additional arterivirus nsps may contribute to innate immune evasion (300,301) and, consequently, vaccine efficacy may be further bolstered by targeting a combination of such functions. As in this study, detailed insight into the molecular interactions of these other arterivirus proteins and their host ligands will likely be required to achieve this goal without crippling the basic replication capacity of the virus. In cell culture, our most promising EAV PLP2 mutant, carrying mutations Thr312Ala/Ile313Val/Ile353Arg, induced an approximately 8-fold increase in IFN-β mRNA levels compared to wild-type virus. Although we were unable to investigate this effect *in vivo* due to the lack of a small animal model for EAV

infection, the disabling of immune evasion mechanisms can result in significant virus attenuation. One striking example is the modification of the immune evasive influenza virus NS1 protein, which yielded attenuated viruses that are promising vaccine candidates (302).

In addition to opening new possibilities for vaccine development, the mutants described in this paper should provide excellent tools for identifying the cellular targets of PLP2, which to date remain unknown. Although Western blot analysis suggests that PLP2 acts in a very promiscuous fashion, causing a general decrease in the levels of ubiquitinated host proteins (**Figure 2.6 D**), our qRT-PCR results support the idea that there is at least some degree of specificity in the inhibition of innate immune signaling, as evidenced by the PLP2-mediated inhibition of IFN-β mRNA transcription, but not IL8 mRNA transcription (**Figure 2.8 A, C**). Since the expression of IFN-β depends largely on the activation of the transcription factor IRF3 and expression of pro-inflammatory cytokines like IL8 does not (303), our findings suggest that PLP2-mediated inhibition of innate immunity is primarily directed at IRF3-dependent signaling. Future experiments will aim at elucidating the target specificity of arterivirus PLP2.

Arteriviruses are not the only virus family harboring proteases with multiple substrate specificities. Especially interesting in this respect are the distantly related CoVs, which infect a wide variety of species, including livestock, companion animals, bats, and humans. Six CoV species have now been found to infect humans, causing symptoms ranging from mild respiratory illness to acute respiratory syndromes, as in the case of SARS-CoV (150) and the recently emerged HCoV-EMC/2012 (141,181). The replicase polyproteins of coronaviruses harbor one or two papain-like proteases (PL^{pro}s) that participate in polyprotein maturation and presumably promote evasion of innate immunity by means of their DUB activity (84,95,159,161). Although the CoV PL^{pro}s belong to the Ub-specific protease (USP) (88,163) rather than the OTU

superfamily of DUBs, it is likely that also CoV PL^{pro} substrate specificities can be decoupled using a similar structure-guided approach. Here we have illustrated how structure-guided mutagenesis of such a viral protease may be used to enhance the innate immune response to infection, a strategy that may be applied in the design of MLVs targeting arteriviruses and other virus families encoding similar dual-specificity proteases.

Chapter 3
Crystallographic analysis of the equine arterivirus papain-like protease 2 bound to equine ISG15

Contributions statement

This work was performed in collaboration Puck van Kasteren in the group of Marjolein Kikkert (LUMC). Puck van Kasteren visited the University of Manitoba, and under my supervision purified and crystallized the EAV PLP2-eISG15 complex. I later collected the X-ray diffraction data for the complex, determined the crystal structure, and performed the structural analysis described below. This work is to be published.

3.1 Introduction

As discussed in section 1.1, the induction of cellular innate immune responses are dependent, in part, on Ub-mediated signalling cascades, and the post-translational modification by Ub can be actively reversed through the activity of cellular (and viral) DUBs. In the case of EAV, PLP2 has been shown to possess DUB activity, specifically targeting the innate immune receptor RIG-I (99), and I previously completed the crystal structure determination of EAV PLP2 bound to Ub to understand the molecular features it uses to recognize and bind Ub (Chapter 2).

In addition to its DUB activity, EAV PLP2 was shown in cell culture to reduce cellular levels of conjugated ISG15, suggesting that PLP2 is capable of interfering with an additional facet of the innate immune response to viral infection (102,211). While this apparent deISGylating activity has been demonstrated in cell culture, the structural basis for the recognition of ISG15 by PLP2 has not been explored. To investigate the molecular basis for this additional activity, I crystallized PLP2 covalently bound to equine ISG15 (eISG15), the natural substrate found in the EAV host. The PLP2-eISG15 structure revealed the specific interactions occurring between the enzyme and its cognate substrate, and molecular modeling of human ISG15 bound to EAV PLP2 suggests that EAV PLP2 has evolved towards a preference for eISG15, at least within the context of these two substrates. Further, comparing the PLP2-eISG15 with previously determined PLP2-Ub structure indicates that PLP2 likely has a greater affinity for Ub, than for eISG15.

3.2 Materials and methods

3.2.1 Cloning and construction of eISG15 expression plasmid

The codon-optimized nucleotide sequence for equine ISG15 (eISG15) was synthesized by BlueHeron biotech based on the predicted ORF (XM_001496658.2), and included a Cys79Ser mutation, in accordance with the observation that the homologous mutation in human ISG15 prevented aggregation during expression (304). The synthetic ORF was provided in plasmid pUCminusMCS (pUC-eISG15; Blue Heron Biotech) and included NdeI and BspQI restriction sites at the 5' and 3' ends, respectively, to allow for directional insertion into plasmid pTXB1 (New England Biolabs), which places eISG15 in-frame with C-terminal intein domain followed by a chitin-binding domain, and under control of an IPTG-inducible T7 promoter. pUC-eISG15 and pTXB1 were digested with NdeI/BpsQI, PCR cleaned, ligated and transformed into *E. coli* BL21 DE3 (Gold) cells under ampicillin selection. The resulting plasmid pTXB1-eISG15^{C79S} was verified by Sanger sequencing (TCAG, Toronto).

3.2.2 Protein expression, purification and crystallization

eISG15 was expressed, purified, and derivatized to eISG15-3-bromopropylamine (eISG15-3Br) using the same methods as described for Ub-3Br (see section 2.2.2). EAV PLP2 was expressed and purified as described in section 2.2.2. In order to form the EAV PLP2-eISG15 complex, PLP2 and eISG15-3Br were mixed together at room temperature for 0.5 hrs at final concentrations of 0.2 and 0.6 mg/mL, respectively. The resulting complex was dialyzed against 50 mM BisTris pH 7.0, 125 mM NaCl, 2 mM DTT (buffer A). To separate PLP2 and eISG15 from the eISG15-PLP2 complex, the sample was loaded onto a 6 mL Source 15S cation exchange column (GE Healthcare) at 2 mL/min, and eluted over a linear gradient from 0-100%

buffer B (50 mM BisTris pH 7.0, 350 mM NaCl, 2 mM DTT) at 2.5 mL/min over 200 mL. The peak corresponding to the PLP2-eISG15 complex was further purified by size exclusion chromatography on a Superdex 75 gel filtration column (GE Healthcare) equilibrated in 20 mM BisTris pH 7.0, 150 mM NaCl, 2 mM DTT. The resulting purified PLP2-eISG15 complex was concentrated to 7.5 mg/mL and screened for conditions that promote crystallization. Sitting-drop vapour diffusion experiments were setup using a Crystal Gryphon robotic drop setter (Art Robbins Instruments) using 300 nL of protein and 300 nL of crystallization solution, with a well volume of 50 μL and incubated at 21°C. Initial hits for the PLP2-eISG15 complex were found in the PEG II crystallization screen (Qiagen) in well H9 (0.2M $Ca(OAc)_2$, 0.1 M HEPES pH 7.5, 10% (w/v) PEG 8000).

3.2.3 X-ray data collection, processing and structural determination of the PLP2-eISG15 complex

A single crystal was harvested directly from the initial screen, cryoprotected by sweeping through well solution supplemented with a final concentration of 20% glycerol and initial X-ray diffraction data collected in house on a Rigaku 007HF MicroFocus X-ray generator and R-AXIS IV++ detector. Preliminary analysis of X-ray diffraction images diffracting to ~4.5 Å determined an orthorhombic unit cell with dimensions a = 30.90 Å, b = 71.25 Å, c = 122.46 Å; $\alpha = \beta = \gamma = 90°$. Additional crystals from well H9 were harvested, cryoprotected in well solution supplemented with 20% glycerol and stored in LN_2 until data collection at the Canadian Light Source (Saskatoon) on beamline 08B1-1. X-ray images collected at the CLS were integrated and scaled using XDS (305) and merged using Aimless (306). Initial phases estimates were obtained from a molecular replacement experiment within phenix.phaser (307) using EAV PLP2 (4IUM),

and polyalanine models of the C-terminal and N-terminal UBL domains of ISG15 (1Z2M) as independent search models. The domains were placed in the following order: 1) PLP2, 2) C-terminal UBL, 3) N-terminal UBL. An initial model was built using phenix.autobuild (308), and subsequent model building and refinement was carried out in Coot (309) and phenix.refine (310), respectively. Data reduction and model refinement statistics are reported in **Table 3.1**

Table 3.1 Crystallographic and refinement statistics for the EAV PLP2-eISG15 complex

Crystal	EAV PLP2-eISG15
Crystal geometry	
Space group	$P2_12_12_1$
Unit cell (Å)	*a*=30.67 *b*=71.20 *c*=121.88; α=β=γ=90°
Crystallographic statistics	
Wavelength (Å)	1.2828
Resolution range (Å)	35.60-2.60 (2.72-2.60)*
Total observations	31769 (3850)
Unique reflections	8652 (1029)
Multiplicity	3.7 (3.7)
Completeness (%)	99.2 (99.6)
R_{merge}	0.048 (0.572)
CC1/2	99.0 (68.4)
I/σI	14.3 (2.2)
Wilson B-factor (Å^2)	69.8
Refinement statistics	
Reflections in test set	863
Protein atoms	2040
Zinc atoms	1
Solvent molecules	13
R_{work}/R_{free}	0.2113/0.2685
RMSDs	
Bond lengths/angles (Å/°)	0.003/0.65
Ramachandran plot	
Favored/allowed (%)	93.8/5.9
Average B factor (Å^2)	
Macromolecules	76.16
Solvent	71.15

*Values in parentheses refer to the highest resolution shell

3.3 Results

3.3.1 Comparison of equine and human ISG15 structures

Although the primary sequence of ISG15 is poorly conserved across species (229), all crystal structures of ISG15 molecules to date - which include murine, human and now equine - adopt a familiar tertiary structure which is composed of two β-grasp domains interconnected by a short linker region (**Figure 1.1 D**). Equine ISG15 (eISG15) shares 72% sequence identity with human ISG15 (**Figure 3.1 A**), and independently, both N-terminal and C-terminal UBL domains of eISG15 align well with human ISG15, with RMSD values of 1.27 Å and 0.35 Å, respectively. It is worth noting that while the fold of the two β-grasp domains is consistent for all ISG15 molecules, the orientation of the β-grasp domains with respect to one another is quite variable, not only between ISG15s of different species, but between different crystal forms of the same ISG15, and even between asymmetric unit members within a single crystal. This indicates that there is considerable flexibility within the region linking the two UBL domains of ISG15. A superposition of all of the human ISG15 crystal structures and the eISG15 structure determined here emphasizes the flexibility of ISG15 (**Figure 3.1B**).

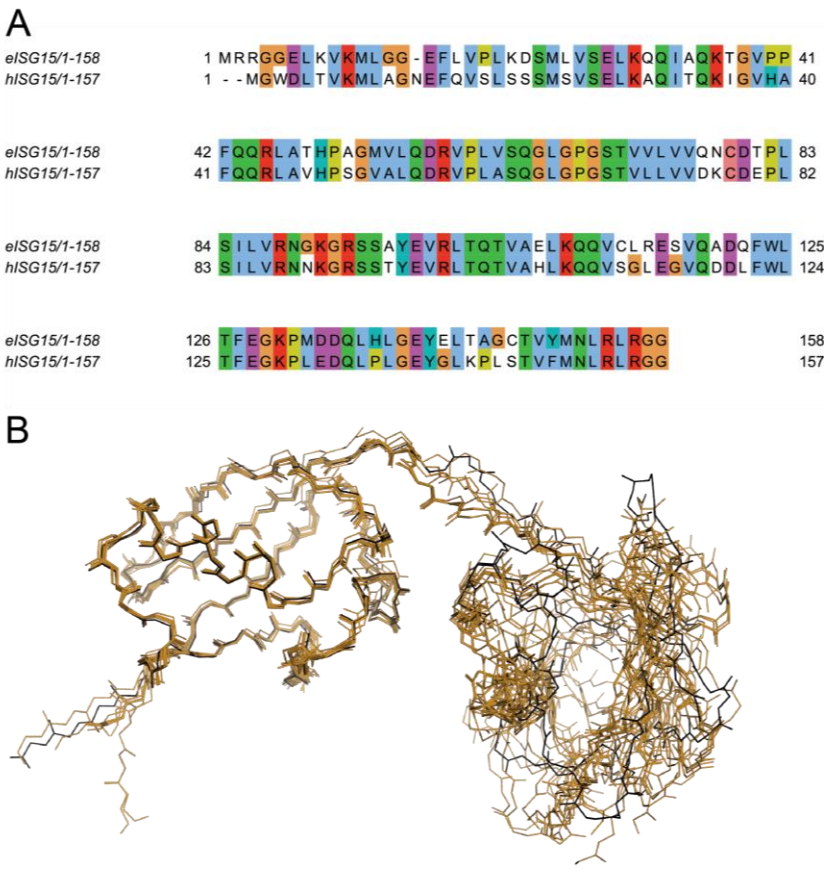

Figure 3.1 Structure and sequence alignment of equine and human ISG15.
(A) Amino acid sequence alignment of the predicted eISG15 sequence with human ISG15. Alignment and image generated using Jalview using the Clustal sequence alignment algorithm (311). Alignment colours depict chemical properties of aligned residues. (B) Crystal structures of human ISG15 and the eISG15 structure solved here were aligned within PyMOL (16), with the N-terminal domains of ISG15 excluded from the alignment. Human ISG15 structures are depicted as backbone atoms in orange, and eISG15 is shown in black.

3.3.2 Molecular basis for eISG15 recognition by EAV PLP2

eISG15 bound to PLP2 in a similar orientation to Ub (**Figure 3.2 A**), with the C-terminal RLRGG motif extending toward the active site, and forming the same network of hydrogen bonds observed in the previously determined PLP-Ub structure (**Figure 3.2 B**). Interestingly, all eISG15 residues found to interface with PLP2 were localized to the C-terminal UBL domain, with the N-terminal UBL domain extending out toward the solvent without contacting PLP2. This suggests that the specificity of PLP2 toward eISG15 is determined solely by a single UBL domain, as has been previously shown for the CCHFV OTU DUB (105), and the eukaryotic deISGylase USP18 (312). Further, interactions between eISG15 and PLP2 are minimal, and outside of the linear RLRGG peptide bound in the active site, consist solely of hydrophobic interactions. As was seen in the PLP2-Ub complex, interaction with the C-terminal UBL domain of eISG15 is centralized around PLP2 residue Ile353, which forms hydrophobic interactions with Tyr150 and Thr126 of eISG15 (**Figure 3.2 C**). Additionally, PLP2 residue Ile313 packs against the hydrophobic side chains of eISG15 residues Gly90, Leu153 and Leu155 (**Figure 3.2 D**).

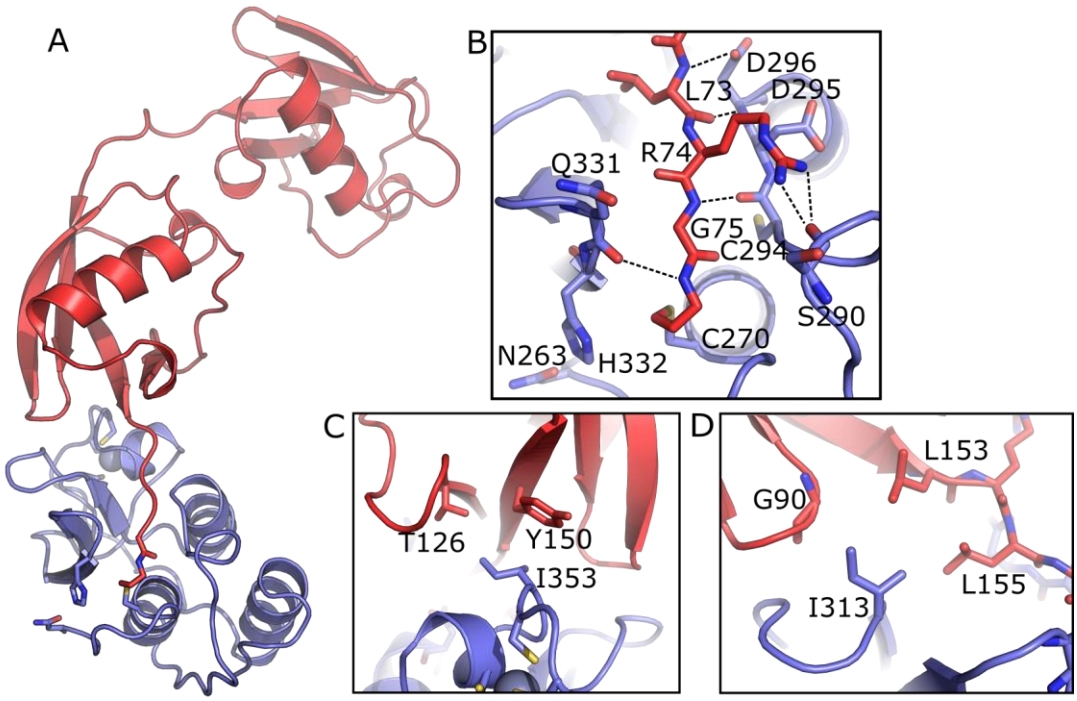

Figure 3.2 Crystal structure of EAV PLP2 in complex eISG15.
(A) Crystal structure of EAV PLP2 (slate) in complex with eISG15 (red). (B) Close up of the C-terminus of eISG15 covalently bound in the active site of EAV PLP2. Relevant side chains are labelled and shown as sticks, and hydrogen bonds are indicated by dashed lines. (C) Hydrophobic interactions between PLP2 residue Ile353 and eISG15 residues Thr126 and Tyr150. D) Hydrophobic interactions between PLP2 residue Ile313 and eISG15 residues Gly90, Leu153 and Leu155.

Multiple reports have demonstrated the activity of EAV PLP2 toward Ub in both *in vitro* (99,211) and ectopic cell culture systems (99,102,211). Data supporting the activity of EAV PLP2 toward ISG15 however is sparse, and consists only of cell culture data demonstrating global deISGylating activity, and further, relied on the use of human ISG15, as opposed to eISG15.

In the absence of *in vitro* data to support the bona fide deISGylating activity of PLP2, structural analysis of the enzyme in complex with eISG15, and a comparison of the substrate binding interface with respect to human ISG15 can provide insight into the potential substrate specificity of PLP2. Amino acid side chains on eISG15 that appear to favour PLP2 binding over ISG15s from other species could provide support for the hypothesis that EAV PLP2 preferentially recognizes ISG15 originating from its natural host, which in turn would suggest that EAV PLP2 genuinely recognizes eISG15 *in vivo*. To this end, a molecular model of PLP2 in complex with human ISG15 was generated based on the EAV-eISG15 structure.

While the majority of amino acid differences that occur between eISG15 and human ISG15 localize outside of the PLP2 binding interface (**Figure 3.3**), a single residue in human ISG15 – Asn89, appears to clash with PLP2 residue Ile313, suggesting that human ISG15 is a suboptimal substrate for EAV PLP2 (**Figure 3.3**). In contrast eISG15 residue Gly90, which is spatially equivalent to human ISG15 residue Asn89, does not clash with EAV PLP2. Taken together, it is possible that EAV PLP2 has evolved to recognize specifically the ISG15 originating from its natural host, and this apparent selectivity suggests that eISG15 may be a genuine substrate for EAV PLP2.

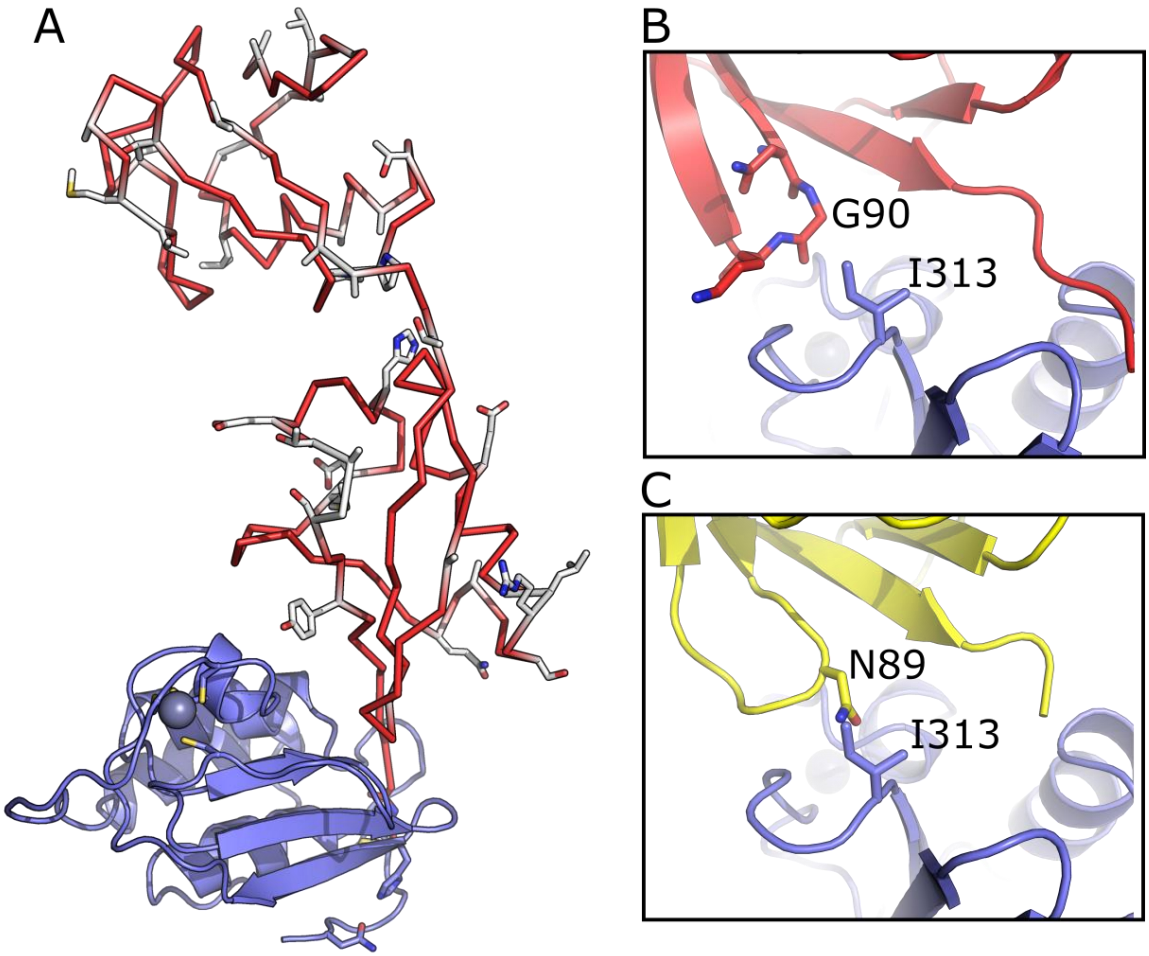

Figure 3.3 Amino acid differences between equine and human ISG15
(A) EAV PLP2 (slate) is shown as a cartoon bound to eISG15 (red), displayed as a ribbon. Residues in eISG15 that differ from the homologous residues with respect to human ISG15 are shown as sticks in white. (B) Close up of the hydrophobic interaction between PLP2 residue Ile313 and eISG15 residue Gly90. (C) Structural model of human ISG15 (yellow; 1Z2M) bound to EAV PLP2 highlighting steric clash between ISG15 residue Asn89 and PLP2 residue I313. The C-terminal UBL of human ISG15 was superposed to the C-terminal UBL of eISG15, and eISG15 was removed for clarity.

3.3.3 Comparison of the EAV PLP2-Ub and EAV PLP2-eISG15 structures

A superposition of the EAV PLP2-eISG15 complex with the previously determined EAV PLP2-Ub complex (211) shows that the PLP2 domains in either complex retain essentially identical folds, with no significant structural changes occurring during eISG15 binding with respect to Ub binding. Interestingly, fewer interactions are present between eISG15 and PLP2 compared to Ub, suggesting that PLP2 may have evolved to preferentially process Ub over eISG15. Notably, salt-bridge interactions occurring between PLP2 residues Asp296 and Glu297 and Ub residue Arg42 are not present during eISG15 binding due to the substitution of Arg42 with the structurally equivalent eISG15 residue Trp124, which is uncharged and too short to extend toward PLP2 (**Figure 3.4 A-D**).

Additional differences in Ub versus eISG15 binding by PLP2 might be attributed to slight variations in the position of a structurally conserved β-hairpin present in both substrates. In Ub, the hairpin formed by strands β1 and β2 is positioned outwards and away from the core of Ub. This positioning appears to be driven by the satisfaction of a hydrophobic interaction between residues Leu8 (positioned on the β-hairpin), and Val70, two residues which contribute to the formation of the Ub hydrophobic patch (**Figure 1.1**). The surface exposed Leu8 forms a hydrogen bond *via* its main-chain carbonyl group with the main-chain amide of PLP2 residue Arg317. In eISG15, residue Gly90 is structurally homologues to Ub residue Leu8, and resides on a β-hairpin formed by strands β5 and β6, while Asn152 occupies the homologues position to Ub residue Val70. The absence of a hydrophobic interaction between Gly90 and Asn152 places the hairpin toward the cavity of eISG15, and away from the main-chain amide of PLP2 residue Asn152, and is thus unable to form an analogous hydrogen bond to that seen in the case of Ub

binding. In contrast, the larger sidechain of Ub residue Leu8 precludes its positioning away from PLP2, and allows the formation of a main-chain hydrogen bond.

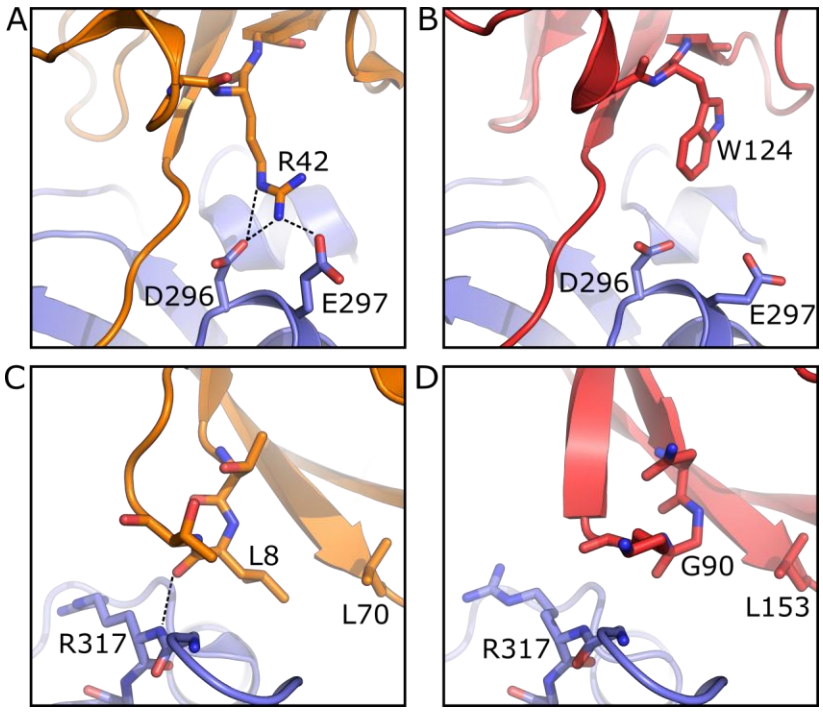

Figure 3.4 Structural comparison of PLP2 when bound to equine ISG15 and Ub.
(A) Ub (orange; 4IUM) bound to EAV PLP2 (slate; 4IUM), highlighting the hydrogen bonding interactions (dashed lines) occurring between PLP2 residues Asp296 and Glu297 with Ub residue Arg42. The homologous residue Trp124 in eISG15 (red) (B) is unable to form these interactions. (C) Mainchain hydrogen bonding interaction between the backbone carbonyl of Ub residue Leu8, and the backbone amide of PLP2 residue Arg317. This interaction is not seen in the PLP2-eISG15 complex with the homologous residue Gly90 (D).

3.4 Discussion

The crystal structure of the EAV PLP2-eISG15 complex reported herein gives the first look at a previously undetermined ISG15 molecule, which adopts a fold common to other ISG15 molecules containing two UBL folds connected by a short linker. As is seen with other DUB-ISG15 complexes, PLP2 engages only a single UBL. This manner of substrate recognition is similar to that of CCHFV OTU and the eukaryotic deISGylase USP18, which interact solely with the C-terminal UBL of ISG15 (105,312). In fact to date, there are no crystal structures providing evidence that the N-terminal domain of ISG15 is recognized by any cognate protease.

Currently, the importance of ISG15 during viral infection is poorly understood, and unsurprisingly, the role of ISG15 during viral infections in equine hosts remains essentially unexplored, although increased ISG15 mRNA levels have been detected in West Nile virus-infected equine PBMCs, suggesting that it does serve a role (313). Interestingly, differences in the primary sequence of ISG15, especially in the C-terminal domain where interactions with viral proteases are known to occur, may play an important role in host tropism of viruses that depend on deISGylating enzymes to evade host immune responses. The structural determination of PLP2 in complex with eISG15 opens the possibility to selectively deconvolute the deISGylating and deubiquitinating activities of EAV PLP2, in order to distinguish the effects of these separate functions individually during infection. As has been previously demonstrated, recombinant DUB-deficient EAV strains remain viable (211), the generation of EAV strains capable of processing Ub, but not eISG15 could act as an essential tool with which to assess the role of eISG15 specifically during infection in an *in vivo* system. Specific disruption of DUB activity has indeed been performed in the case of the CCHFV OTU domain (106), and the effect of these mutations in recombinant CCHFV has recently been assessed (314), demonstrating that

the removal of deISGylating activity, but not the DUB activity of CCHFV OTU results in reduced levels of viral L protein. As mentioned previously, there have been no *in vitro* studies assessing the deISGylating activity of EAV PLP2, in part due to the absence of commercially available fluorogenic eISG15 substrates. However pro-forms of ISG15 proteins from several species have recently been used to assess the activity of viral deISGylases toward ISG15 substrates from different species (100), and isothermal titration calorimetry has been used to assess the affinities of deISGylases towards ISG15(s) (167). Further *in vitro* experiments, either through use of fluorogenic or pro-ISG15 substrates will help characterize the deISGylating activity of EAV PLP2 and its preference for eISG15 over ISG15 molecules from other organisms. The structural studies described here provide insight into this question, as it appears EAV PLP2 is structurally optimized to recognize eISG15 as opposed to human ISG15, and provides further support for EAV PLP2 having bona fide deISGylating activity.

Chapter 4
Viral OTU Deubiquitinases: A Structural and Functional Comparison

Adapted from: Bailey-Elkin, B. A.[1], van Kasteren, P. B.[1], Snijder, E. J., Kikkert, M.[2], and Mark, B. L[2]. (2014) Viral OTU deubiquitinases: a structural and functional comparison. *PLoS Pathog.* **10**, e1003894

[1] Authors contributed equally to this work
[2] Authors contributed equally to this work

Contributions Statement

This opinion article was written following the publication of an article describing the crystal structure of the TYMV PRO domain (253). This publication appeared shortly after our manuscript describing the EAV PLP2 domain (211). Presumably due to the close succession of these publications, the authors did not cite our work on the EAV enzyme and the structural similarities and differences between these vDUBs. Thus, we took this opportunity to provide a brief review and structural comparison that brought together the current knowledge of viral ovarian tumor domain proteases. The opinion was written by me and Puck van Kasteren, and editing of the document was undertaken by all of the listed authors.

4.1 Introduction

The covalent attachment of Ub to protein substrates, i.e. ubiquitination, plays a pivotal regulatory role in numerous cellular processes (1,35,315-317). Ubiquitination can be reversed by DUBs (318) and, not surprisingly, various virus groups encode such DUBs to influence Ub-mediated host cell processes (71,78,81,83,84,95,99,101,102,107,109,123,132,135,319). Some of these viral DUBs resemble proteases belonging to the OTU superfamily (103-106,211,253,320). Makarova *et al*. previously identified OTU proteases as a novel superfamily of cysteine proteases from different organisms (210), and their bioinformatics-based analysis included several of the viral enzymes discussed here. Recently reported structures of these viral DUBs include the OTU domains of the nairoviruses CCHFV (103,105,106) and DUGV (104), the PLP2 domain of EAV (211), and the PRO domain of the TYMV (253,320) (**Figure 4.1 A-D**). These viruses are strikingly diverse, considering that nairoviruses are mammalian negative-strand RNA viruses, while the mammalian arteriviruses and plant tymoviruses belong to separate orders of positive-strand RNA viruses**.**

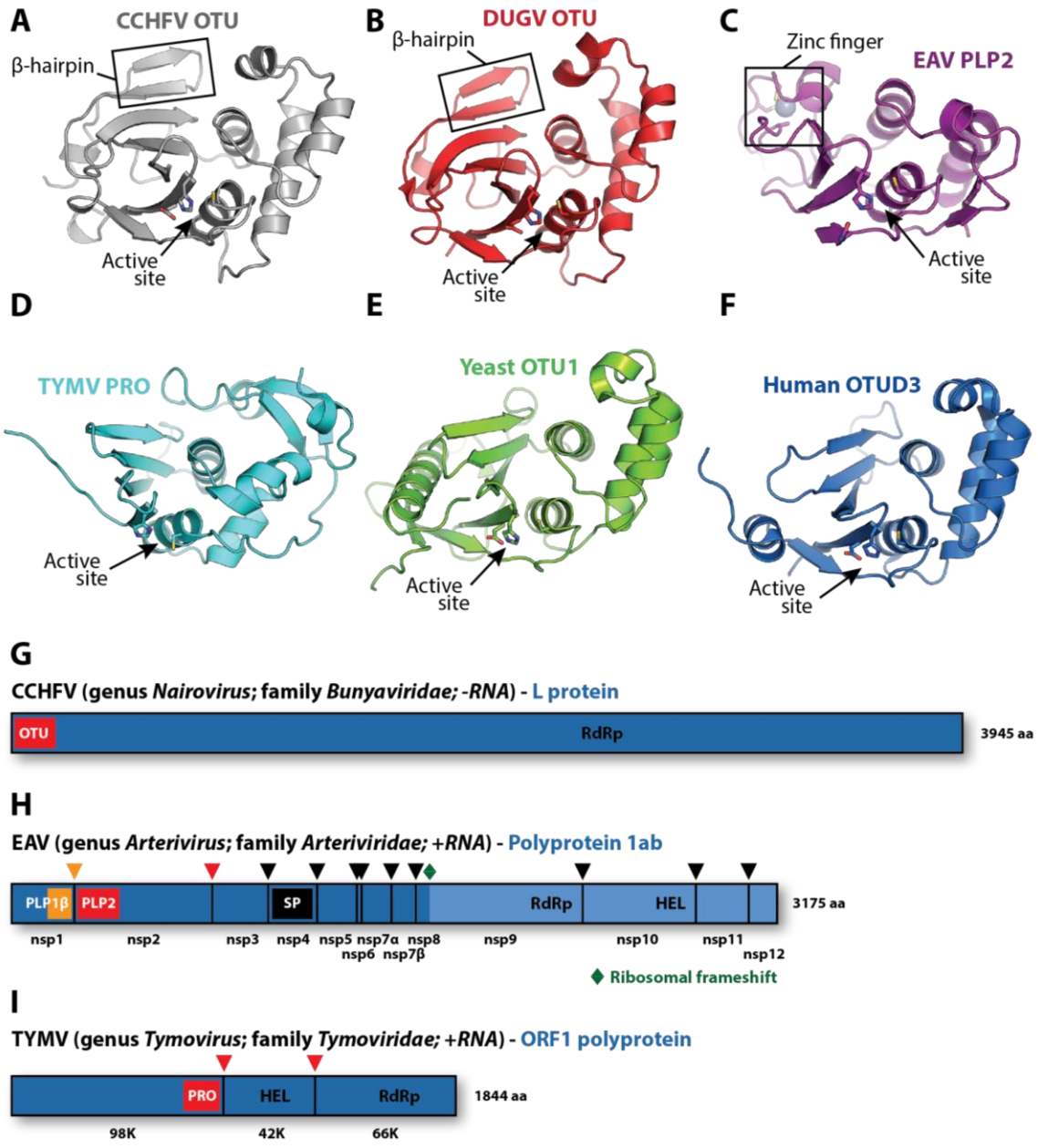

Figure 4.1 Viral and eukaryotic OTU domain structures and viral protein context.
Crystal structures of (A) CCHFV OTU (3PT2) (105), (B) DUGV OTU (4HXD) (104), (C) EAV PLP2 (4IUM) (211), (D) TYMV PRO (4A5U) (253,320), (E) yeast OTU1 (3BY4) (226), and (F) human OTUD3 (4BOU) (20). The β-hairpin motifs of CCHFV OTU and DUGV OTU are indicated in boxes in panels A and B, respectively, and the zinc-finger motif of EAV PLP2 is boxed in panel C. Active sites are indicated with arrows. The CCHFV OTU, DUGV OTU, EAV PLP2 and yeast OTU1 domains were crystallized in complex with Ub, which has been removed for clarity. Structure images were generated using PyMol (321). (G) Schematic representation of the CCHFV large (L) protein (222,223). A similar organization is found in the DUGV L protein, but is not depicted. The OTU domain resides in the N-terminal region of this protein and is not

involved in autoproteolytic cleavage events (293). (H) Schematic representation of the EAV polyprotein 1ab (205). PLP2 resides in nsp2 and is responsible for the cleavage between nsp2 and nsp3 (209). (I) Schematic representation of the TYMV ORF1 polyprotein (251). PRO resides in the N-terminal product of this polyprotein and is responsible for two internal cleavages (248,251). Key replicative enzymes are indicated in G, H, and I. Coloured arrowheads denote cleavage sites for the indicated protease domains.

The proteasomal degradation pathway is an important cellular route to dispose of viral proteins, as exemplified by the turnover of the TYMV polymerase (252). Moreover, the degradation of this protein is specifically counteracted by the DUB activity of TYMV PRO, which thus promotes virus replication (109). The functional characterization of viral OTU DUBs remains incomplete and future studies will likely reveal additional roles in replication and virus-host interplay.

4.2 Results and discussion

4.2.1 Structural comparison of viral OTU deubiquitinases

It is important to note that many positive-strand RNA viruses, including arteriviruses and tymoviruses, encode polyproteins that are post-translationally cleaved by internal protease domains (262). Thus, while CCHFV OTU is not involved in viral protein cleavage and its activity seems dispensable for replication (293) (**Figure 4.1 G**), both arterivirus PLP2 and tymovirus PRO are critically required for viral replication due to their primary role in polyprotein maturation (209,248,251,273,322) (**Figure 4.1 H,I**). Interestingly, while both EAV PLP2 and TYMV PRO can process peptide bonds *in cis* and *in trans* (209,251), PRO does not cleave peptide bonds in linear polyUb chains *in vitro* (104). To date, activity of EAV PLP2 towards linear polyUb chains has not been reported.

Based on mutagenesis of putative catalytic residues, arterivirus PLP2 and tymovirus PRO were initially generally classified as papain-like cysteine proteases (209,249,323). Now that crystal structures of these proteases are available, it is possible to search the DALI server (285) in order to identify structurally similar domains. Using the 3-dimensional coordinates of TYMV

PRO, the most recently solved structure of a viral OTU protease, such a query identifies structural similarity with eukaryotic OTU DUBs as well as the nairovirus OTU domains and EAV PLP2 (**Table 4.1**). A superposition of these viral protease structures with yeast OTU1 (226) further highlights their similarities (**Figure 4.2 A-C**), and these comparisons together clearly position them within the OTU DUB superfamily. Sequence comparisons alone were insufficient to demonstrate this conclusively, as the similarity of viral OTU domains with each other and with eukaryotic OTU proteases is very limited and mostly restricted to the areas surrounding the active site residues (210).

Structural characterization of nairovirus (CCHFV and DUGV) OTU domains and EAV PLP2 in complex with Ub revealed that while these viral proteases adopt a fold that is consistent with eukaryotic OTU DUBs, they possess additional structural motifs in their S1 binding site that rotate the distal Ub relative to the binding orientation observed in eukaryotic OTU enzymes (**Figure 4.2 D,E**) (103-106,211). In the case of CCHFV OTU, this alternative binding mode was shown to expand its substrate repertoire by allowing the enzyme to also accommodate ISG15. Since TYMV PRO was crystallized in its apo form (253,320), it remains to be determined whether its S1 site binds Ub in an orientation similar to EAV PLP2 and nairovirus OTU or eukaryotic OTU DUBs.

Table 4.1 Three-dimensional structural alignment of viral OTU domains against selected structures in the Protein Data Bank using the DALI server.

DALI Query:	**CCHFV OTU**	**DUGV OTU**	**TYMV PRO**	**EAV PLP2**
	3PT2 (105)	4HXD (104)	4A5U (253,320)	4IUM (211)
Human OTUD3	14.5; 12%*	14.4; 15%	7.6; 12%	4.2; 13%
4BOU (20)	2.1 Å (123)**	2.1 Å (123)	1.9 Å (85)	2.4 Å (69)
Yeast OTU1	11.8; 16%	11.6; 20%	7.3; 12%	5.1; 9%
3BY4 (226)	2.9 Å (126)	2.5 Å (123)	2.3 Å (91)	3.3 Å (81)
CCHFV OTU		28.1; 55%	6.8; 15%	4.6; 19%
3PT2 (105)		0.9 Å (157)	3.0 Å (91)	2.6 Å (74)
DUGV OTU			6.9; 12%	4.5; 19%
4HXD (104)			2.8 Å (90)	2.6 Å (74)
TYMV PRO				3.2; 13%
4A5U (253,320)				2.8 Å (64)

*z-score >2 indicates significant structural similarity (324)); % sequence identity.
**Root-mean-square deviation (RMSD) values are indicated, followed by the number of residues used for RMSD calculation in brackets. Value represents the average distance (Å) between alpha carbons used for comparison.

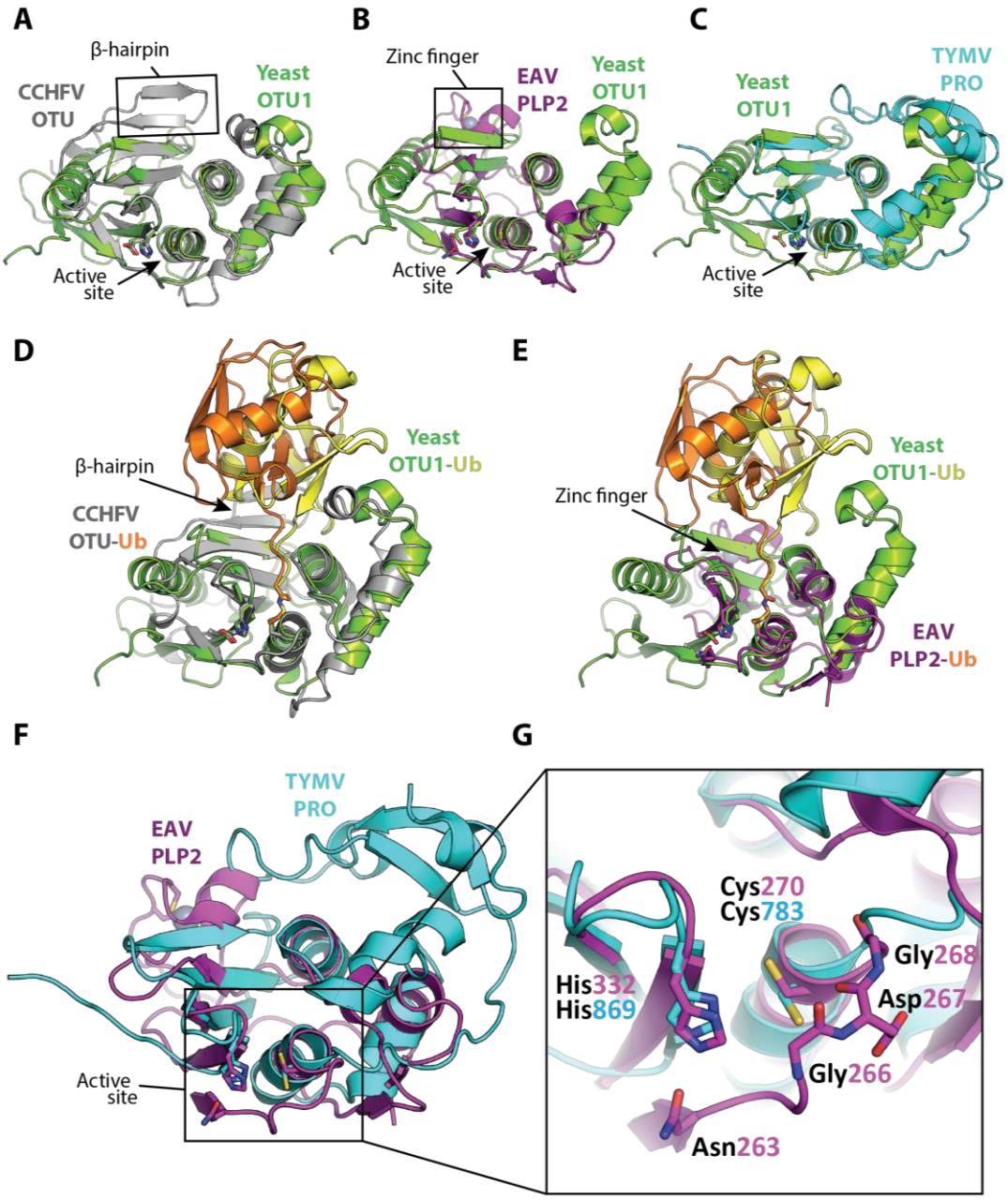

Figure 4.2 Superpositions of the viral OTU proteases with yeast OTU1 and one another. Superpositions of yeast OTU1 (3BY4) (226) with (A) CCHFV OTU (3PT2) (105), RMSD: 1.8Å over 112 residues, (B) EAV PLP2 (4IUM) (211), RMSD: 2.8Å over 69 residues, and (C) TYMV PRO (4A5U) (253,320), RMSD: 1.4Å over 76 residues. Superpositions of the yeast OTU1-Ub complex with (D) the CCHFV OTU-Ub complex and (E) the EAV PLP2-Ub complex, highlighting the difference in the orientation of Ub between the two viral OTU domains versus the eukaryotic yeast OTU1 domain. The Ub that is complexed with yeast OTU1 is depicted in yellow, while the Ub complexed with CCHFV OTU or EAV PLP2 is depicted in orange. (F) Superposition of EAV PLP2 and TYMV PRO, RMSD: 2.5Å over 53 residues. (G) Close-up of

the active site region (boxed) of the superposition depicted in F. Side chains of the catalytic cysteine (Cys270 and Cys783 for EAV PLP2 and TYMV PRO, respectively) and histidine (His332 and His869 for EAV PLP2 and TYMV PRO, respectively) residues are shown as sticks, as well as the active site Asn263 for EAV PLP2. The backbone amide group of Asp267 likely contributes to the formation of the oxyanion hole in the active site of EAV PLP2, yet a functionally equivalent residue is absent in TYMV PRO. The Gly266 and Gly268 residues flanking Asp267 in EAV PLP2 are depicted as sticks as well for clarity. Note the alternative orientation of the active site cysteine residue of TYMV PRO which, unlike EAV PLP2, was not determined in covalent complex with a Ub suicide substrate. All alignments were generated using the PDBeFOLD server (325), and thus the reported RMSD values differ from those reported in **Table 4.1** where the DALI server was used. The yeast OTU1, CCHFV OTU and EAV PLP2 domains were all crystallized in complex with Ub, which has been removed in panels A, B, C, F, and G for clarity. All images were generated using PyMol (321).

A remarkable feature of EAV PLP2 is the incorporation within the OTU-fold of a zinc finger that is involved in the interaction with Ub (**Figure 4.1 C** and **Figure 4.2 E**). The absence of similar internal zinc-finger motifs in other OTU superfamily members prompted us to propose that PLP2 prototypes a novel subclass of zinc-dependent OTU DUBs (211).Finally, an interesting structural difference between TYMV PRO and other OTU proteases of known structure is the absence of a loop that generally covers the active site (**Figure 4.2 F,G**). Because of this, TYMV PRO lacks a complete oxyanion hole. It also lacks a third catalytic residue that would otherwise form the catalytic triad that has been observed in other OTU proteases (**Figure 4.2 G**). Lombardi *et al.* suggested that the resulting solvent exposure of the active site may contribute to the broad substrate specificity of TYMV PRO (253). Interestingly, EAV PLP2 also has broad substrate specificity, cleaving Ub, ISG15 and the viral polyprotein, even though it does possess an intact oxyanion hole and an active site that is not solvent exposed. Future work may uncover additional aspects relating to the unusual architecture of the TYMV PRO active site. The presence of structurally similar proteases, each displaying unique features, in these highly diverse virus groups suggests that their ancestors have independently acquired their respective OTU enzymes. Although their origins remain elusive, one possible scenario is the scavenging of an OTU DUB-encoding gene that directly enabled the ancestral virus to interact with the cellular ubiquitin landscape (210). The absence of an OTU homologue in other lineages of the bunyavirus family strongly suggests that a nairoviral ancestor acquired an OTU DUB through heterologous recombination. In this scenario, the current differences between the nairoviral and eukaryotic OTU domains would reflect divergent evolution. In the case of arteriviruses however, it is also conceivable that a preexisting papain-like protease that was initially only involved in polyprotein maturation acquired OTU-like features through a process of convergent evolution.

Although rare, such a scenario would account for the limited structural similarity between eukaryotic OTU domains and EAV PLP2, which contrasts with that observed for nairovirus OTU (**Table 4.1, Figure 4.2 A,B**). For tymoviruses, which encode one (OTU) protease, the existence of related viruses that do not encode a protease domain, or that encode one (papain-like) or two (OTU combined with a second papain-like) protease domains, complicates the development of a straightforward scenario describing PRO acquisition and evolution (326). These and other intriguing unsolved questions should be addressed through structural and functional studies of additional OTU-like proteases, be it viral or cellular, the results of which may shed more light on the various scenarios explaining the evolution of viral OTU domains.

Chapter 5
Crystal structure of the MERS coronavirus papain-like protease bound to ubiquitin facilitates targeted disruption of deubiquitinating activity to demonstrate its role in innate immune suppression

Adapted from: Bailey-Elkin, B. A.[1], Knaap, R. C.[1], Johnson, G. G., Dalebout, T. J., Ninaber, D. K., van Kasteren, P. B., Bredenbeek, P. J., Snijder, E. J., Kikkert, M.[2], and Mark, B. L.[2] (2014) Crystal structure of the Middle East respiratory syndrome coronavirus (MERS-CoV) papain-like protease bound to ubiquitin facilitates targeted disruption of deubiquitinating activity to demonstrate its role in innate immune suppression. *J. Biol. Chem.* **289**, 34667-34682

[1] Authors contributed equally to this work

[2] Authors contributed equally to this work

Contributions statement

The work characterizing the MERS-CoV PL^{pro} domain was carried out in collaboration with the group of Eric Snijder at the LUMC. I generated the MERS-CoV PL^{pro} expression constructs and developed purification protocols, as well as crystallized and determined the structure of PL^{pro} in its apo form and covalently bound to Ub, and designed mutations for the selective disruption of PL^{pro} DUB activity as described in sections 5.2.2, 5.2.3, 5.2.4, 5.2.5, 5.2.6 and 5.2.7. The cell culture DUB and polyprotein cleavage assays, as well as the *in vitro* Ub linkage analysis was performed by Robert Knaap at the LUMC. The manuscript was prepared by myself and Robert Knaap, and was edited my myself, Robert Knaap, Brian Mark, Marjolein Kikkert and Eric Snijder. A European provisional patent application has been filed describing the use of UbVs as viral polypeptide inhibitors. (05134196)

5.1 Introduction

As outlined in section 1.4, the DUB activities of MERS- and SARS-CoV PL^{pro} have been implicated in the suppression of host antiviral pathways since these proteases can suppress IFN-β induction upon their ectopic expression (84,159,161,183,187,327). Previous work has shown that during infection, SARS-CoV indeed suppresses the host's antiviral responses by preventing the induction of IFN-β expression in cell culture (160,328,329). Similarly, MERS-CoV infection has been found to elicit a poor type-1 IFN response in cultured monocyte-derived dendritic cells (330) and alveolar epithelial A549 cells (331), as well as *ex vivo* in bronchial and lung tissue samples (331). Furthermore, delayed induction of pro-inflammatory cytokines in human airway epithelial cells infected with MERS-CoV has been reported (332).

Although the above observations suggest that MERS- and SARS-CoV actively suppress antiviral responses such as IFN-β production and inflammation, they do not directly implicate the DUB activity of PL^{pro} as being responsible for (part of) this suppression. Due to the dependence of MERS-CoV replication on the ability of PL^{pro} to cleave the nsp1-nsp3 region of the replicase polyproteins, studying the role of PL^{pro} DUB activity, specifically in the suppression of the cellular innate immune response, is difficult since both activities depend on the same enzyme active site. Selective inactivation of only the DUB activity of PL^{pro} would enable the study of how this activity alone affects cellular signalling; however, achieving this requires detailed information on the structural basis of Ub recognition and deconjugation by PL^{pro}. To this end, we determined the crystal structure of MERS-CoV PL^{pro} bound to Ub to elucidate the molecular determinants of Ub recognition. Based on the structure of this complex, mutations were introduced that selectively disrupted Ub recognition by targeting regions of the Ub-binding site on PL^{pro} that were sufficiently distant from the active site of the protease. Using

this approach, we were able to remove the DUB activity from PL^{pro} without affecting its ability to cleave the nsp3|4 cleavage site *in trans*. This enabled us, for the first time, to demonstrate that the DUB activity of MERS-CoV PL^{pro} can suppress the MAVS-mediated induction of IFN-β expression.

5.2 Methods

5.2.1 Cells, antibodies and plasmids

HEK293T cells were cultured in Dulbecco's modified Eagle's medium (DMEM) supplemented with 10% fetal calf serum (FCS; Bodinco BV), 100 U/mL penicillin, 100 U/mL streptomycin and 2 mM L-glutamine (cell culture medium and supplementals were obtained from Lonza).

Primary antibodies used were mouse anti-HA (ab18181; Abcam), mouse anti-V5 (37-7500; Invitrogen), mouse anti-β-actin (A5316; Sigma-Aldrich), mouse anti-FLAG (F3165; Sigma-Aldrich), and rabbit anti-GFP (99). As secondary antibodies horseradish peroxidase (HRP)-conjugated antibodies were used (P0447 and P0217; Dako).

The following plasmids were described elsewhere: pASK3 (333), pcDNA-eGFP (99), pCMV-FLAG-ubiquitin (Ub) (279), pLuc-IFN-β (277), pEBG-RIG-$I_{(2CARD)}$ (278), pcDNA-FLAG-MAVS (334) and pEGFP-C1-$IRF3_{(5D)}$ (335).

5.2.2 Construction of MERS-CoV PL^{pro} expression plasmids

A cDNA fragment encoding the PL^{pro} domain (amino acids 1479–1803 of the MERS-CoV pp1a/pp1ab polyprotein (NCBI ID: JX869059); pp1a/pp1ab amino acid numbering is used throughout the rest of the article) was cloned into bacterial expression vector pASK3 in-frame with N-terminal Ub and a C-terminal His_6 purification tag to produce pASK-MERS-CoV-PL^{pro}.

Using standard methodologies the sequence encoding amino acids 1480-1803 of MERS-CoV pp1a/pp1ab was PCR amplified, cloned downstream of the T7 promoter of expression vector pE-SUMO (LifeSensors), and used to transform *E. coli* BL21 (DE3) GOLD cells (Stratagene) grown under kanamycin selection (35 μg/mL). Recombinant expression plasmid (pE-SUMO-PL^{pro}) was isolated from a single colony and DNA sequencing confirmed the expected sequence of the PL^{pro} domain, and the in-frame fusion of the 5'-end to a sequence encoding a His_6-SUMO purification tag, which facilitated purification of the product by Ni-NTA affinity chromatography as described below.

To obtain high expression in eukaryotic cells, the sequence of MERS-CoV nsp3-4 (amino acids 854-3246) flanked by an N-terminal HA tag and a C-terminal V5 tag was optimized based on the human codon usage frequency, and potential splice sites and polyadenylation signals were removed. This sequence was synthesized (Invitrogen), and subsequently cloned into the pCAGGS vector (Addgene) using standard methodologies. The following expression constructs were generated: pCAGGS-HA-nsp3-4-V5 (amino acids 854-3246), pCAGGS-HA-nsp3C-4-V5 (amino acids 1820-3246, which does not include the PL^{pro} domain), and pCAGGS-HA-nsp3-Myc (amino acids 854-2739). The sequence encoding MERS-CoV PL^{pro} (amino acids 1479-1803) was PCR amplified using synthetic plasmid DNA as a template and cloned in frame with a C-terminal V5 tag in the pcDNA3.1(-) vector (Invitrogen). The pASK-MERS-CoV-PL^{pro} and pcDNA3.1-MERS-CoV-PL^{pro} expression constructs served as templates for site-directed mutagenesis using the QuickChange strategy with Pfu DNA polymerase (Agilent). All constructs were verified by sequencing. The sequences of the constructs and primers used in this study are available on request.

5.2.3 *Purification of MERS-CoV PL^{pro} and* in vitro *DUB activity assay*

In vitro DUB activity assays were performed with recombinant MERS-CoV PL^{pro} batch-purified from lysates of *E. coli* strain C2523. Cells transformed with pASK-MERS-CoV-PL^{pro} were cultured to an optical density (OD_{600}) of 0.6 in lysogeny broth (LB) at 37°C. Protein expression was then induced with 200 ng/mL anhydrotetracycline for 16 h at 20°C. The cells were pelleted, resuspended in lysis buffer (20 mM HEPES, pH 7.0, 200 mM NaCl, 10% (vol/vol) glycerol and 0.1 mg/mL lysozyme) and lysed for 1 h at 4°C followed by sonication. The lysate was clarified by centrifugation at 20000 x g for 20 min at 4°C and the soluble fraction was applied to talon resin (GE Healthcare) pre-equilibrated with lysis buffer. After a 2 h rolling incubation at 4°C the beads were washed four times with wash buffer (20 mM HEPES, pH 7.0, 200 mM NaCl, 10% (vol/vol) glycerol and 20 mM imidazole) followed by the elution of the protein with elution buffer (20 mM HEPES, pH 7.0, 200 mM NaCl, 10% (vol/vol) glycerol and 250 mM imidazole). Eluted protein was dialysed against storage buffer (20 mM HEPES, pH 7.0, 100 mM NaCl, 50% (vol/vol) glycerol, 2mM DTT) and stored at −80°C. N-terminal Ub is cleaved from the Ub-PL^{pro}-His_6 fusion protein by the PL^{pro} domain itself during expression. To achieve removal of the Ub from mutated and/or inactive PL^{pro}, *E. coli* strain C2523 containing pCG1, expressing Ubp1, was used (268).

In vitro DUB activity assays were performed as described by van Kasteren *et al*. (99). Briefly, indicated amounts of purified MERS-CoV PL^{pro} wild-type or active site mutant (Cys1592Ala) were incubated with 2.5 µg of either Lys48-linked polyUb chains or Lys63-linked polyUb chains (Boston Biochem) in a final volume of 10 µL. Isopeptidase T (Boston Biochem) served as a positive control. After a 2 h incubation at 37°C the reaction was stopped by addition of 4×LSB (500 mM Tris, 4% SDS, 40% glycerol, 0.02% bromophenol blue, 2 mM DTT, pH

6.8). SDS-PAGE gels were stained with Coomassie brilliant blue (Sigma-Aldrich) and scanned using a GS-800 calibrated densitometer (Bio-Rad).

5.2.4 Expression and purification of MERS-CoV PL^{pro} for crystallization

E. coli BL21(DE3) GOLD cells harbouring pE-SUMO-PL^{pro} were grown at 37ºC with aeration in 500 ml of LB containing kanamycin (35 μg/mL) to an OD_{600} of 0.6-0.8. Expression of the His_6-SUMO-PL^{pro} fusion protein was then induced by the addition 1 mM Isopropyl β-D-1-thiogalactopyranoside (IPTG) for 18 h at 16ºC with aeration. Cells were pelleted by centrifugation and stored at -80ºC.

Cell pellets were resuspended in ice-cold lysis buffer (150 mM Tri pH 8.5, 1 M NaCl, 0.1 mM phenylmethanesulfonylfluoride (PMSF), 2 mM DTT) and lysed using a French pressure cell (AMINCO). Cell lysate was clarified by centrifugation (17211 x g at 4ºC) and the supernatant containing the His_6-SUMO-PL^{pro} fusion was applied to a column containing Ni-NTA affinity resin (Qiagen). The column was washed with 10 column volumes of lysis buffer supplemented with 25 mM imidazole, followed by elution of the fusion protein with lysis buffer containing 250 mM imidazole. The His_6-SUMO tag was then removed from PL^{pro} by adding His_6-tagged Ulp1 SUMO protease to the eluted SUMO-PL^{pro} fusion followed by dialysis of the protein mixture overnight against 2 L cleavage buffer (150 mM NaCl, 50 mM Tris pH 8.0, 1 mM DTT) at 4ºC. Tag-free PL^{pro} was separated from His_6-SUMO and the His_6-Ulp1 SUMO protease by passing the dialyzed protein mix through a Ni-NTA gravity column. The flow-through contained purified PL^{pro} that was subsequently dialyzed against 20 mM Tris pH 8.5, 150 mM NaCl, 2 mM DTT and further purified by gel filtration using a Superdex 75 (GE Healthcare) gel-filtration column.

5.2.5 Covalent coupling of Ub to PL^{pro}

$Ub_{(1–75)}$-3-bromopropylamine (Ub-3Br) is a modified form of Ub with a reactive C-terminus that forms an irreversible covalent linkage to the active site cysteine of DUB enzymes and was prepared according to Messick *et al*. (226) and Borodovsky *et al*. (124). Purified PL^{pro} was incubated with a 2-fold molar excess of Ub-3Br and incubated for 1 h at room temperature with end-over-end mixing. The resulting PL^{pro}-Ub complex was dialyzed into 20 mM Tris pH 8.5, 150 mM NaCl, 2 mM DTT and excess Ub-3Br was removed by gel filtration using a Superdex 75 column.

5.2.6 Crystallization of PL^{pro} and PL^{pro}-Ub complexes

The purified PL^{pro}-Ub complex was concentrated and crystallized at 20°C in two different conditions using the vapour diffusion method: 1) 20% PEG 4000, 0.1 M trisodium citrate pH 5.4, 20% isopropanol at 10 mg/mL, which yielded the structure of open PL^{pro}-Ub (see section 5.3.2.2), and 2) 1.80 M ammonium sulphate ($AmSO_4$) at 20 mg/mL, which yielded the structure of closed PL^{pro}-Ub (see section 5.3.2.2). Crystals of unliganded PL^{pro} were also grown using the vapour diffusion method in 18% PEG 4000, 0.1 M trisodium citrate pH 5.6, 16% isopropanol after concentrating the protein to 12 mg/ml. Immediately prior to crystallization 1 M DTT was added to the protein to a final concentration of 5 mM, which was found to improve crystallization.

In preparation for X-ray data collection, single crystals of open PL^{pro}-Ub from condition 1 above were briefly swept through a droplet of cryoprotectant composed of 22% PEG 4000, 0.1M trisodium citrate pH 5.6, 20% 1,2-propanediol before flash cooling in liquid nitrogen. Similarly, single crystals of closed PL^{pro}-Ub from condition 2 above and unbound PL^{pro} were cryoprotected in 1.85 M ammonium sulfate ($AmSO_4$), 15% glycerol and 22% PEG 4000, 0.1 M

trisodium citrate pH 5.6, 10% 1,2-propanediol, respectively, before flash-cooling in liquid nitrogen.

5.2.7 Data collection and structure determination

X-ray diffraction data were collected from all crystals at the Zn-K absorption edge at beamline 08B1-1 of the Canadian Light Source and integrated using XDS (305). Integrated data were then scaled using Scala (306). Initial phase estimates for reflections collected from unliganded and Ub-bound PL^{pro} were determined via a single wavelength anomalous dispersion (SAD) experiment. The position of the Zn anomalous scatterer was identified using HySS (336), and density modification was performed with RESOLVE (337) within the phenix.autosol pipeline (338). Initial models were constructed using phenix.autobuild, and further model building and refinement was carried out using Coot (309) and phenix.refine (310). Crystallographic statistics for all structures are found in **Table 5.1**.

Table 5.1 Crystallographic statistics for MERS-CoV PL^{pro} and PL^{pro}-Ub structures

Crystal	PL^{pro}	Open PL^{pro}-Ub	Closed PL^{pro}-Ub
Crystal geometry			
Space group	$P6_3$	$P6_3$	$P6_522$
Unit cell (Å)	*a*=*b*=137.94 *c*=57.70; α=β=90° γ=120°	*a*=*b*=136.77 *c*=57.99; α=β=90° γ=120°	*a*=*b*=176.92 *c*=84.55; α=β=90° γ=120°
Crystallographic data			
Wavelength (Å)	1.28294	1.28280	1.28219
Resolution range (Å)	45.15-2.80 (2.90-2.80)*	44.23-2.15 (2.22-2.15)	44.24-2.80 (2.90-2.80)
Total observations	137170 (13780)	124058 (12315)	283649 (28118)
Unique reflections	15683 (1566)	33472 (3291)	19694 (1918)
Multiplicity	8.7 (8.8)	3.7 (3.7)	14.4 (14.7)
Completeness (%)	100.00 (100.00)	98.73 (98.12)	99.97 (100)
Anomalous completeness	99.4 (98.5)	92.4 (92.6)	100 (100)
R_{merge}	0.085 (0.76)	0.041 (0.79)	0.061 (0.78)
CC1/2	0.99 (0.83)	0.99 (0.54)	1 (0.93)
CC*	0.99 (0.95)	1 (0.84)	1 (0.98)
I/σI	17.13 (3.42)	20.52 (1.97)	34.01 (3.69)
Wilson B-factor ($Å^2$)	75.15	46.79	74.96
Phasing statistics			
Figure of merit (FOM)	0.12	0.18	0.23
FOM after RESOLVE	0.64	0.63	0.67
Refinement statistics			
Reflections in test set	1570	1996	1609
Protein atoms	2384	3020	3020
Zinc atoms	1	1	1
Solvent molecules	26	205	65
R_{work} (R_{free})	0.23 (0.27)	0.20 (0.23)	0.24 (0.28)
RMSDs			
Bond lengths/angles (Å/°)	0.002/0.60	0.002/0.52	0.002/0.54
Ramachandran plot			
Favored/allowed (%)	95/5	95/5	93/7
Average B factor ($Å^2$)	76.70	66.80	86.50
Macromolecules	76.70	69.20	86.60
Solvent	76.65	65.40	84.20

*Values in parentheses refer to the highest resolution shell

5.2.8 Protease activity assays in cell culture

HEK293T cells, grown to 80% confluence in 12-well plates, were transfected using the calcium phosphate transfection method (339). To determine the DUB activity of MERS-CoV PL^{pro}, plasmids encoding FLAG-tagged Ub (0.25 μg), GFP (0.25 μg) and MERS-CoV-PL^{pro}-V5 (0.2 μg) were co-transfected. A combination of plasmids encoding GFP (0.25 μg), HA-nsp3C-4-V5 (0.2 μg) and MERS-CoV-PL^{pro}-V5 (0.15 μg) were transfected to assess the *in trans* cleavage activity of MERS-CoV-PL^{pro}. Total amounts of transfected DNA were equalized to 2 μg by the addition of empty pcDNA vector. At 18 h post-transfection, cells were lysed in 2× LSB. Proteins were separated in a SDS-polyacrylamide gel and blotted onto Hybond-P (GE Healthcare) using the Trans-blot turbo transfer system (Bio-Rad). Aspecific binding to the membrane was blocked with dried milk powder solution and after antibody incubation, protein bands were visualized using Pierce ECL 2 Western blotting substrate (Thermo Scientific).

5.2.9 *Luciferase-based IFN-β reporter assay*

Using the calcium phosphate method, 80% confluent HEK293T cells in 24-well plates were transfected with 5 ng *Renilla* luciferase encoding plasmid pRL-TK (Promega), IFN-β-Luc firefly reporter plasmid (25 ng), innate immune response inducer plasmids encoding $RIG\text{-}I_{(2CARD)}$, MAVS or $IRF3_{(5D)}$ (25 ng) and indicated quantities of MERS-CoV PL^{pro} or MERS-CoV nsp3 encoding expression plasmids. Total amounts of transfected DNA were equalized to 1 μg by the addition of empty pcDNA vector. At 16 h post-transfection, cells were lysed in 1x passive lysis buffer (Promega). Firefly and *Renilla* luciferase activity was measured using the Dual-Luciferase reporter assay system (Promega) on a Mithras LB 940 multimode reader (Berthold Technologies). Experiments were performed in triplicate and independently repeated at least four times. Firefly luciferase activity was normalized to *Renilla* luciferase and statistical significance

was determined using an unpaired two-tailed Student's *t* test. Values <0.05 were considered statistically significant. 4× LSB was added to the remaining lysates and these samples were analyzed by Western blotting as described above.

5.3 Results

5.3.1 DUB activity of recombinant MERS-CoV PL^{pro}

It was shown in cell culture experiments that ectopic expression of MERS-CoV PL^{pro} resulted in deconjugation of polyUb and ISG15 from cellular targets (183,187). DUB activity of purified recombinant MERS-CoV PL^{pro} was also demonstrated using Ub-7-amino-4-trifluoro-methylcoumarin (Ub-AFC) (185) or Ub-AMC (184) as a substrate. To characterize the direct activity of recombinant MERS-CoV PL^{pro} towards polyUb, we purified the enzyme from *E. coli* and incubated it with either Lys48- or Lys63-linked polyUb chains. Wild-type PL^{pro} degraded both Lys48- and Lys63-linked chains in a concentration-dependent manner, while mutating the active site nucleophile (Cys1592Ala) severely reduced the activity of the enzyme towards both Ub linkage types (**Figure 5.1**). No clear preference of the enzyme for cleaving either the Lys63 or the Lys48 Ub linkage was observed under the conditions used in this *in vitro* DUB assay (compare **Figure 5.1 A** and **B**). This assay clearly demonstrated that the protease domain used throughout this study for ectopic expression and crystallisation experiments possesses DUB activity towards Lys48- and Lys63-linked Ub chains, and that this activity does not require other viral or cellular proteins. During the preparation of this manuscript, an article by Báez-Santos and co-workers was published in which similar results were presented (91).

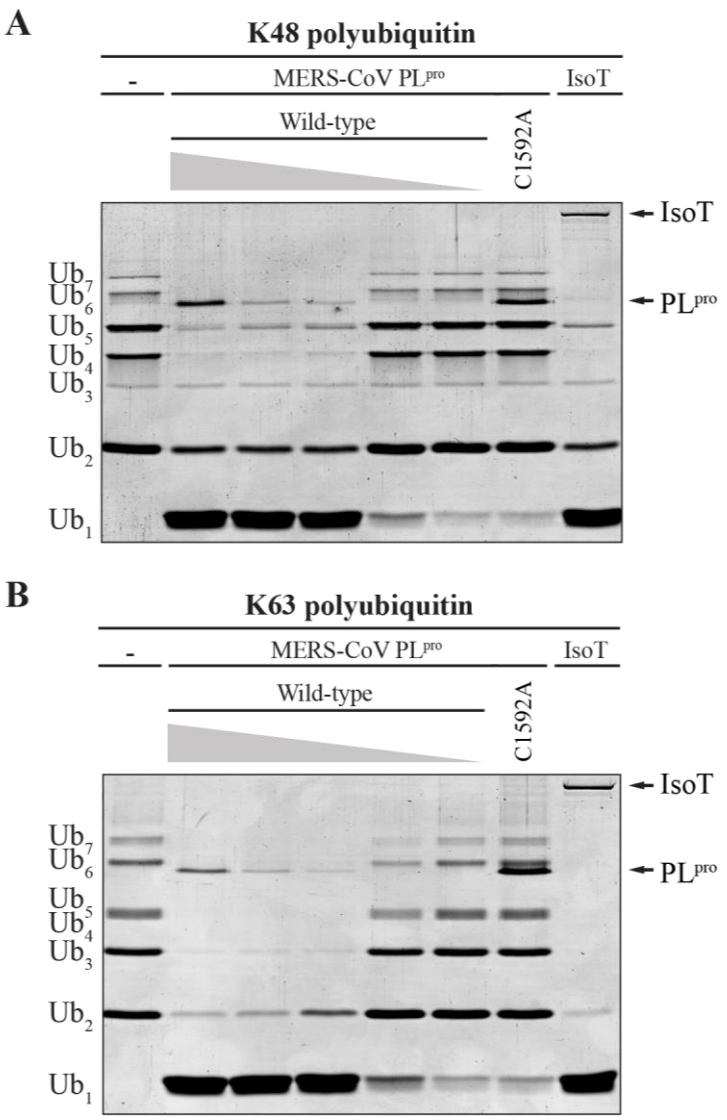

Figure 5.1 *In vitro* cleavage of Lys48- and Lys63-linked polyubiquitin chains by recombinant MERS-CoV PL^{pro}.

Purified recombinant MERS-CoV PL^{pro} was incubated with 2.5 µg Lys48-linked (A) or Lys63-linked (B) polyUb chains of different length in each reaction for 2hr at 37°C in a final volume of 10 µL. A range of 2-fold dilutions starting at 2 µM MERS-CoV wild-type PL^{pro} per reaction was used. Activity of the PL^{pro} active site mutant (Cys1592 was replaced by Ala) was assessed at a concentration of 2 µM. Isopeptidase T (IsoT, 0.5 µg per reaction) served as a positive control (340). This figure was originally published in the *Journal of Biological Chemistry*. Bailey-Elkin BA, Knaap RCM, Johnson GG, Dalebout TJ, Ninaber DK, van Kasteren PB, Bredenbeek PJ, Snijder EJ, Kikkert M, Mark BL. Crystal structure of the MERS coronavirus papain-like protease bound to ubiquitin facilitates targeted disruption of deubiquitinating activity to demonstrate its role in innate immune suppression. 2014; 289:34667-82. © the American Society for Biochemistry and Molecular Biology.

5.3.2 Crystal structures of MERS-CoV PL^{pro} and PL^{pro}-Ub complexes

5.3.2.1 MERS-CoV PL^{pro}

The crystal structure of PL^{pro} was determined both on its own and as a covalent complex with Ub (PL^{pro}-Ub). The PL^{pro} domain crystallized in space group $P6_3$, and consistent with another recently determined crystal structure of MERS-CoV PL^{pro} (184), we found the protease to adopt a fold consistent with DUBs of the USP family. The structure includes a C-terminal catalytic domain containing a right-handed fingers, palm and thumb domain organization, as well as an N-terminal Ubl domain found in many USPs, including that of SARS-CoV (163,341) (**Figure 5.2 A**). The packing of the palm and thumb domains forms a cleft leading into the active site in a manner consistent with the domain organization prototyped by the Clan CA group of cysteine proteases (342). The Ubl domain packs against the thumb domain composed of helices α2-7, which in turn packs against the palm domain comprised of strands β6, β7 and β14-19. Extending from the palm, the fingers domain is composed of strands β10, β11, β13, β14, β19 and contains a C_4 Zn-ribbon motif (343) coordinating a Zn atom via residues Cys1672, Cys1675, Cys1707 and Cys1709 in tetrahedral geometry, similar to that of SARS PL^{pro}, transmissible gastroenteritis coronavirus (TGEV) PL1^{pro}, and cellular USP2 and USP21 (88,163,344,345).

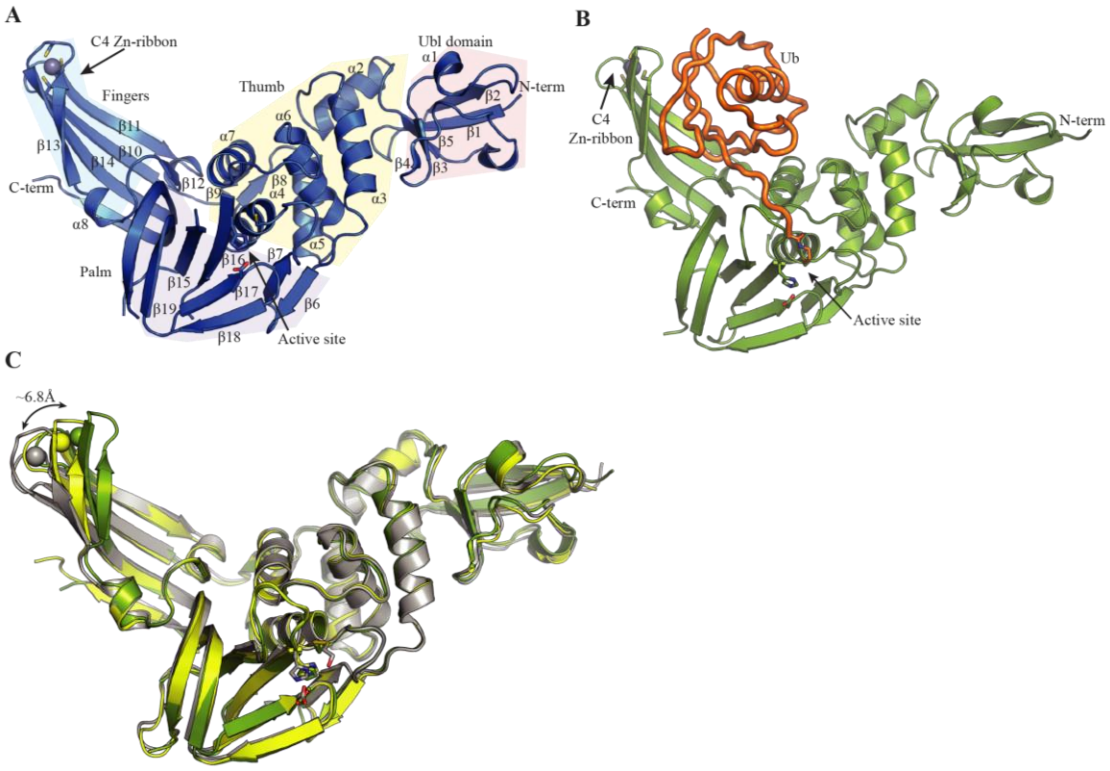

Figure 5.2 MERS-CoV PL^{pro} and PL^{pro}-Ub structures.
(A) Structure of the MERS-CoV PL^{pro} domain (2.15Å resolution). The palm, thumb, fingers and N-terminal ubiquitin-like (Ubl) domains are indicated by coloured panels, and arrows indicate the active site and C_4 Zn-ribbon motif. The active site residues are depicted as sticks. (B) Structure of the MERS-CoV PL^{pro} bound to Ub (2.8Å resolution). PL^{pro} is shown in green, and the covalently bound Ub molecule is orange and shown as tubes. Active site residues are shown as sticks with Gly75 and the 3CN linker of Ub covalently linked to Cys1592 of PL^{pro}. (C) Superposition showing a ~6.8Å movement of the Zn-ribbon motif between the open (yellow) and closed (green) PL^{pro}-Ub structures and a previously reported PL^{pro} structure (grey) (PDB ID: 4P16; (184)). Our PL^{pro} structure is not shown since it is highly similar to the open PL^{pro}-Ub structure. Movement of the Zn-ribbon motif was determined by measuring the distance between the Zn atom of the respective structures. Superpositions were performed in Coot (309). Ub was removed from the closed and open PL^{pro}-Ub structures for clarity. Figures were created using PyMOL (321). This figure was originally published in the *Journal of Biological Chemistry*. Bailey-Elkin BA, Knaap RCM, Johnson GG, Dalebout TJ, Ninaber DK, van Kasteren PB, Bredenbeek PJ, Snijder EJ, Kikkert M, Mark BL. Crystal structure of the MERS coronavirus papain-like protease bound to ubiquitin facilitates targeted disruption of deubiquitinating activity to demonstrate its role in innate immune suppression. 2014; 289:34667-82. © the American Society for Biochemistry and Molecular Biology.

5.3.2.2 PL^{pro} covalently bound to Ub

The MERS-CoV PL^{pro}-Ub complex crystallized in two different space groups ($P6_3$ and $P6_522$), which revealed a considerable level of conformational flexibility in the protein. Electron density maps calculated using diffraction data collected from PL^{pro}-Ub complex that crystallized in space group $P6_3$ revealed weak density for the covalently bound Ub molecule. Although the entire bound Ub molecule could be modeled within its binding site on PL^{pro} in this crystal form, high temperature factors for atoms comprising the modeled Ub molecule suggested it was not rigidly bound to the protease despite being covalently linked to the active site cysteine. Further analysis of the crystal packing revealed that the Ub molecule was fully exposed to solvent and not involved in crystal contacts, which provided a degree of mobility to Ub when bound to PL^{pro} (**Figure 5.3 A**). This result encouraged us to pursue additional crystallization conditions, which yielded crystals of PL^{pro}-Ub in space group $P6_522$ (**Figure 5.3 B** and **Figure 5.2 B**). The crystal packing in this space group allowed for multiple crystal contacts between the bound Ub monomer and surrounding symmetry mates, and resulted in clear, well-defined density for the Ub molecule (**Figure 5.3 B**). Interestingly, relative to the $P6_3$ crystal forms of PL^{pro}, the fingers domain in this crystal form was moved toward Ub (**Figure 5.2 C**). In light of these movements, the PL^{pro}-Ub structure with the fingers domain positioned away from Ub (space group $P6_3$) will hereafter be referred to as 'open' PL^{pro}-Ub, whereas the structure with the fingers domain shifted towards Ub (space group $P6_522$) will be referred to as 'closed' PL^{pro}-Ub. An overlay of the different PL^{pro} crystal structures that have been determined reveals that these structures vary in the position of the Zn-ribbon motif, further suggesting a high degree of mobility for this region (**Figure 5.2 C**). In line with this observation, movement of the fingers domain toward bound Ub was also reported for the SARS-CoV PL^{pro} domain, which displayed a 3.8Å movement of the Zn

atom when comparing the Ub-bound and unbound structures (166). Further comparison of the closed MERS-CoV PL^{pro}-Ub structure with the recently determined SARS-CoV PL^{pro}-Ub structure (166) revealed differences in the relative orientation of the fingers domain of the two proteases. The MERS-CoV PL^{pro} fingers domain was found to be shifted approximately 26° away from the palm domain compared to that of SARS-CoV PL^{pro}, resulting in a slight difference in the Ub binding orientation, with the MERS-CoV PL^{pro}-bound Ub being positioned closer towards helix α7 of the palm domain (**Figure 5.4**).

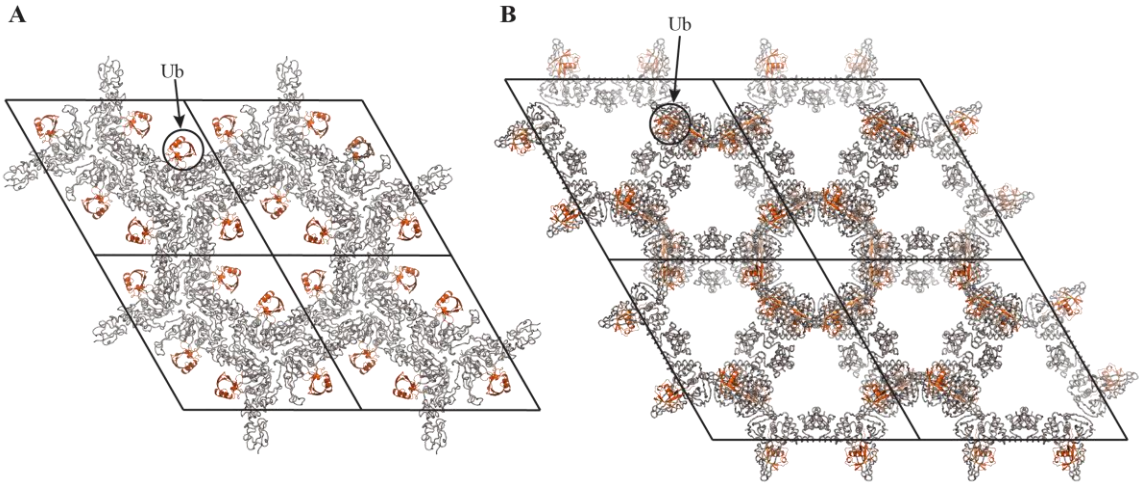

Figure 5.3 Crystal packing arrangement of the open and closed MERS-CoV PL^{pro}-Ub structures. The contents of 4 unit cells are shown, with PL^{pro} and Ub depicted in grey and orange, respectively. (A) The open PL^{pro}-Ub structure crystallized in space group $P6_3$, where Ub was found to face the solvent, uninvolved in crystal contacts. (B) The closed PL^{pro}-Ub structure crystallized in space group $P6_522$, where Ub no longer faces the solvent, and is involved in crystal contacts. Figures were created using PyMOL (73). This figure was originally published in the *Journal of Biological Chemistry*. Bailey-Elkin BA, Knaap RCM, Johnson GG, Dalebout TJ, Ninaber DK, van Kasteren PB, Bredenbeek PJ, Snijder EJ, Kikkert M, Mark BL. Crystal structure of the MERS coronavirus papain-like protease bound to ubiquitin facilitates targeted disruption of deubiquitinating activity to demonstrate its role in innate immune suppression. 2014; 289:34667-82.

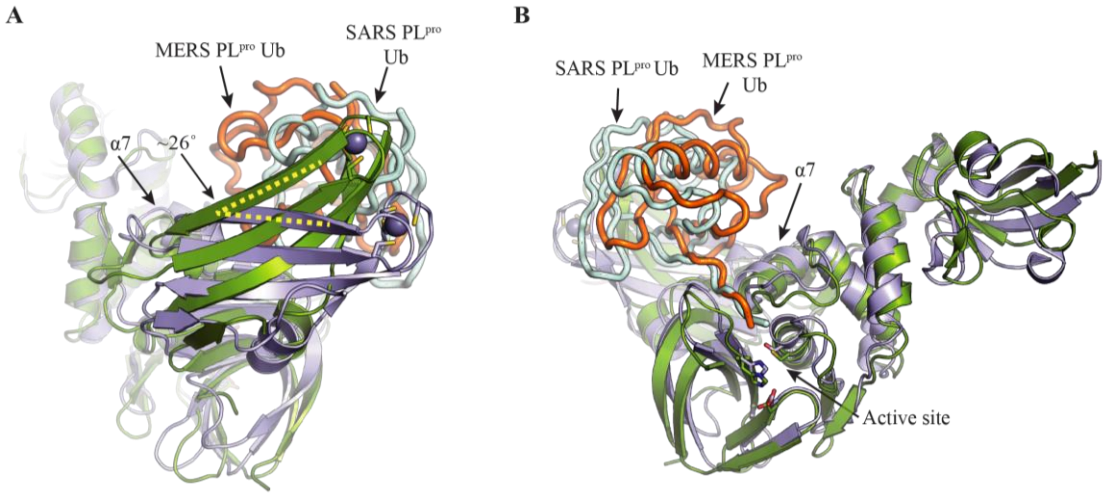

Figure 5.4 Structural comparison of the SARS-CoV PL^{pro}-Ub and MERS-CoV PL^{pro}-Ub complexes.
(A) Superposition of the closed MERS-CoV PL^{pro}-Ub complex (green) and the SARS-CoV PL^{pro}-Ub complex (purple, PDB ID: 4M0W) using SSM superpose in Coot (309) (bound Ub molecules were ignored during the superposition). The Ub molecules bound to the MERS-CoV PL^{pro} domain and SARS-CoV PL^{pro} domain are depicted as tubes in orange and pale cyan, respectively. The ~26° shift in the fingers domain between the two respective structures is indicated. (B) Alternate orientation of the SARS-CoV PL^{pro}-Ub and MERS-CoV PL^{pro}-Ub superpositions highlighting the difference in Ub binding. In the MERS-CoV PL^{pro}-Ub complex, Ub is found shifted towards helix α7 compared to the SARS PL^{pro}-Ub complex. Helix α7 of MERS-CoV PL^{pro} is indicated with an arrow. Figures were created using PyMOL (321). This figure was originally published in the *Journal of Biological Chemistry*. Bailey-Elkin BA, Knaap RCM, Johnson GG, Dalebout TJ, Ninaber DK, van Kasteren PB, Bredenbeek PJ, Snijder EJ, Kikkert M, Mark BL. Crystal structure of the MERS coronavirus papain-like protease bound to ubiquitin facilitates targeted disruption of deubiquitinating activity to demonstrate its role in innate immune suppression. 2014; 289:34667-82. © the American Society for Biochemistry and Molecular Biology.

5.3.2.3 PL^{pro} active site organization and interaction with the C-terminal RLRGG motif of Ub

The cleft formed between the palm and thumb domains of PL^{pro} guides the C-terminal $_{72}$RLRGG$_{76}$ motif of Ub towards the protease active site, and the interactions between the C-terminal motif of Ub and the active site cleft are depicted in **Figure 5.5** (panels **A** and **B**). The PL^{pro} active site is composed of a Cys1592-His1759-Asp1774 catalytic triad, which adopts a catalytically competent arrangement in both the unliganded and Ub-bound structures of PL^{pro} (**Figure 5.5 C**). The oxyanion hole of the PL^{pro} active site appears to be comprised of backbone amides from residues Asn1590, Asn1591 and Cys1592, which appear suitably arranged to stabilize the negative charge that develops on the carbonyl oxygen of the scissile bond during catalysis (**Figure 5.5 C**). Interestingly, as noted by Lei *et al.*, the MERS-CoV PL^{pro} active site appears incomplete. In SARS-CoV PL^{pro}, Trp107 (amino acid numbering according to structure PDB ID: 2FE8) is positioned within the enzyme's active site with the indole nitrogen of its side chain oriented such that it likely is involved in forming part of the oxyanion hole (163). In the case of MERS-CoV PL^{pro}, we and others (184,185) have found the structurally equivalent residue in MERS-CoV PL^{pro} to be Leu1587, which would be unable to participate in stabilizing the oxyanion during catalysis. Furthermore, it was recently shown that MERS-CoV PL^{pro} Leu1587Trp mutants show greater catalytic efficiency than wild-type PL^{pro} (184,185). Given the effect this residue has on the catalytic rate of PL^{pro}, it will be very interesting to understand how this residue influences MERS-CoV replication kinetics. It has been proposed that the decreased catalytic efficiency may influence maturation of the MERS-CoV polyprotein (185), and could be involved in the recognition of residues downstream of the scissile bond of the polyprotein cleavage sites or in the modulation of PL^{pro} DUB activity.

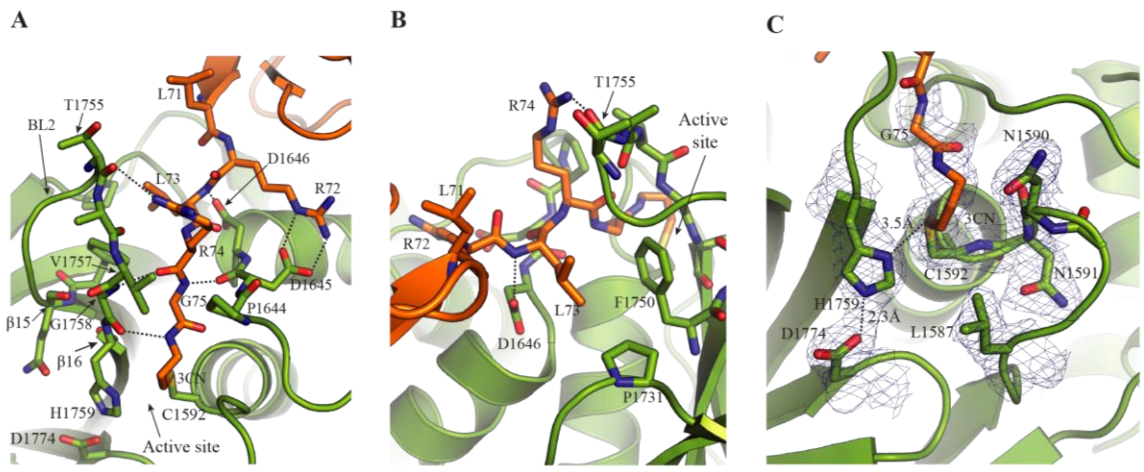

Figure 5.5 Active site of MERS-CoV PL^{pro} and interactions with the C-terminal RLRGG motif of Ub.

Interactions between open PL^{pro} (green) and the C-terminal RLRGG motif of Ub (orange) are depicted in panels A and B. (A) The main-chain amide of the 3CN linker, which mimics Gly76 of Ub, forms a hydrogen bond with the main chain carbonyl of PL^{pro} residue Gly1758. The main-chain amide of Gly75 of Ub forms a hydrogen bond with the carbonyl group of PL^{pro} Asp1645, and a hydrogen bonding interaction occurs between the main-chain carbonyl of Arg74 of Ub and the main-chain amide of Gly1758 of PL^{pro}. The side-chain η-amino group of Ub residue Arg74 is hydrogen bonded to the main-chain carbonyl group of PL^{pro} Thr1755. Hydrogen bonds also occur between the side-chain ε- and η-amino groups of Ub Arg72 and the carboxylate of PL^{pro} Asp1645, as well as between the main-chain amide of Ub residue Leu73 and side chain PL^{pro} residue Asp1646. The BL2 loop between strands β15 and β16 is indicated with an arrow. (B) Alternate orientation of the PL^{pro} active site showing a hydrogen bonding interaction between the Ub Lle73 main-chain amide group and the side-chain carboxylate of PL^{pro} residue Asp1646. The side chain of Ub residue Leu63 also undergoes hydrophobic interactions with PL^{pro} residues Phe1750 and Pro1731. (C) The MERS-CoV PL^{pro} Cys1592-His1759-Asp1774 catalytic triad residues are shown, as well as residues Asn1590 and Asn1591, which together with Cys1592 form the oxyanion hole via their backbone amide groups. The covalent 3CN molecule is shown linking the C-terminus of Ub to the active site Cys1592 of PL^{pro}. The active site Leu1587 residue, which is not involved in oxyanion hole formation, is also shown. The electron density is a maximum-likelihood weighted $2F_{obs}$-F_{calc} map contoured at 1.0σ. Figures created using PyMOL (321). This figure was originally published in the *Journal of Biological Chemistry*. Bailey-Elkin BA, Knaap RCM, Johnson GG, Dalebout TJ, Ninaber DK, van Kasteren PB, Bredenbeek PJ, Snijder EJ, Kikkert M, Mark BL. Crystal structure of the MERS coronavirus papain-like protease bound to ubiquitin facilitates targeted disruption of deubiquitinating activity to demonstrate its role in innate immune suppression. 2014; 289:34667-82. © the American Society for Biochemistry and Molecular Biology.

Interestingly, differences were observed in the position of a loop on PL^{pro} connecting strands β15 and β16, which is structurally analogous to the blocking loop (BL2) first described in the structure of USP14 (346). This loop is disordered in our unliganded PL^{pro} structure, and that previously determined by others (184), however in both of our PL^{pro}-Ub structures we found this loop to be fully resolved, supported by the main-chain H-bonding interactions between Arg74 of Ub and Gly1758 of PL^{pro}, as well as a hydrophobic interaction between Val1757 and Pro1644 - two PL^{pro} residues present on opposite sides of the active site cleft (**Figure 5.5 A**). The side-chain η-amino group of the Ub residue Arg74 is also hydrogen bonded to the main-chain carbonyl group of PL^{pro} residue Thr1755, however this interaction is only seen in the open PL^{pro}-Ub structure. The SARS-CoV PL^{pro} domain has also been crystallized both in the presence (163) and absence (166) of Ub, and while the BL2 loop of unbound SARS-CoV PL^{pro} was resolved in two of three monomers of the asymmetric unit, the third showed weak electron density for BL2 and high temperature factors indicating a high degree of mobility. In addition, in the TGEV USP domain $PL1^{pro}$ a structurally analogous BL2 loop was found to be in an open conformation with poorly defined electron density in the absence of substrate (88). It is interesting to note that all three CoV USP DUBs crystallized to date (from MERS-CoV, SARS-CoV and TGEV) demonstrate a significant degree of flexibility within the BL2 loop region in the absence of substrate, and that none of the structures determined in their unbound form demonstrate obstruction of the active site via BL2.

5.3.3 Structure-guided design of PL^{pro} mutants defective in DUB activity

We previously demonstrated that the DUB activity of EAV PLP2, which resembles the OTU-domain containing family of DUBs (254), could be selectively removed without affecting its ability to process the EAV replicase polyprotein. This allowed us to establish that the DUB

activity of PLP2 is directly responsible for suppressing Ub-dependent antiviral pathways during infection of primary host cells (211). Subsequently, Ratia and co-workers have applied a similar strategy to the SARS-CoV PL^{pro} domain in order to selectively remove the DUB activity of PL^{pro} while maintaining the nsp2-3 processing function (71). We now used the crystal structure of the USP-like MERS PL^{pro}-Ub complex to guide the design of mutations targeting the Ub-binding site on PL^{pro} that would disrupt Ub binding without affecting the structural integrity of the active site. PL^{pro} residues interacting directly with Ub were replaced with larger, bulkier residues that would prevent Ub binding by altering both shape and surface electrostatics of the Ub-binding site. Individual mutation of eight different PL^{pro} residues – Arg1649, Thr1653, Ala1656, Asn1673, Val1674, Val1691, Val1706 and Gln1708 – and combinations thereof, were generated (**Figure 5.6 A-D**). Importantly, these residues are located at a distance from the PL^{pro} active site, and thus we hypothesized that they would only participate in DUB activity and not polyprotein processing.

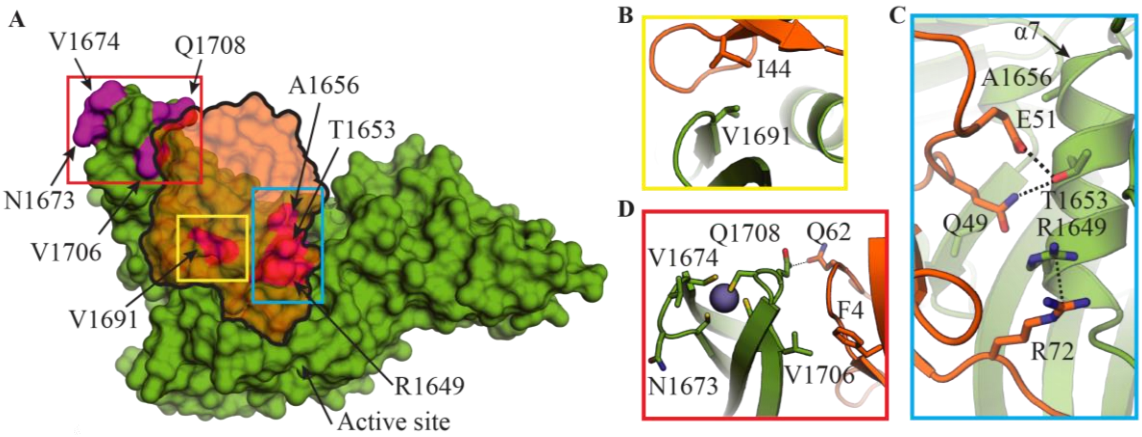

Figure 5.6 Structure-guided mutagenesis of PL^{pro} residues involved in Ub recognition.
(A) Surface representation of the closed MERS-CoV PL^{pro}-Ub complex. PL^{pro} is shown in green, and Ub is shown in transparent orange. Those residues that were mutated in order to disrupt Ub binding are coloured magenta, and are indicated with arrows. Coloured boxes refer to close-up views of the PL^{pro}-Ub interactions, and are shown to the right. (B) Hydrophobic interaction is shown between Val1691 of PL^{pro} and Ile44 of Ub. (C) Thr1653 of PL^{pro} is shown hydrogen bonded to Gln49 and Glu51 of Ub, and Arg1649 of PL^{pro} is shown interacting with Arg72 of Ub. (D) Hydrogen bonding interactions are shown between Gln1708 of PL^{pro} and Gln62 of Ub, and a hydrophobic interaction is shown between Val1706 of PL^{pro} and Phe4 of Ub. Asn1673 and Val1674 of PL^{pro}, which do not interact with Ub, are also displayed. Figures created using PyMOL (321). This figure was originally published in the *Journal of Biological Chemistry*. Bailey-Elkin BA, Knaap RCM, Johnson GG, Dalebout TJ, Ninaber DK, van Kasteren PB, Bredenbeek PJ, Snijder EJ, Kikkert M, Mark BL. Crystal structure of the MERS coronavirus papain-like protease bound to ubiquitin facilitates targeted disruption of deubiquitinating activity to demonstrate its role in innate immune suppression. 2014; 289:34667-82. © the American Society for Biochemistry and Molecular Biology.

Despite significant movement within the fingers domain of PL^{pro}, most interactions between the protease and Ub are consistent between the open and closed Ub-bound complexes. Residue Ile44 of Ub, which forms part of the hydrophobic patch that is commonly recognized by Ub-binding proteins (2), interacts with the hydrophobic side-chain of Val1691 of PL^{pro} (**Figure 5.6 B**). Residues Gln49 and Glu51 of Ub form hydrogen-bonding interactions with Thr1653 that is present on helix α7, which runs through the center of PL^{pro}. Two arginine residues, Arg1649 of PL^{pro} and Arg72 of Ub (the latter of which forms part of the C-terminal tail of Ub that is bound in the PL^{pro} active site cleft) are oriented such that the guanidinium groups of these residues are arranged in a stacked conformation (**Figure 5.6 C**). In addition, due to the inward movement towards Ub of the closed PL^{pro}-Ub fingers domain, a unique hydrogen-bonding interaction between Gln62 of Ub and Gln1708 of PL^{pro}, and a hydrophobic interaction between Phe4 of Ub and Val1706 of PL^{pro} were found to occur in this complex (**Figure 5.6 D**). Residue Ala1656 is positioned near the C-terminus of PL^{pro} helix α7, and while it is not directly involved in Ub binding we believed that it was positioned such that the introduction of larger residues (e.g. arginine or phenylalanine) could disrupt Ub recognition, and thus this residue was targeted for mutation (**Figure 5.6 C**). Two residues on the solvent-facing region of the PL^{pro} Zn-ribbon motif, Asn1673 and Val1674, were also targeted for mutagenesis. Though they do not bind Ub at the S1 binding site (the substrate binding site on PL^{pro} responsible for binding monoUb in our structure – see (169) for nomenclature), we hypothesized that it may inhibit association with the distal Ub on Lys63 polyUb chains based on a superposition of a Lys63-linked diUb model onto the PL^{pro}-bound Ub molecule of the closed PL^{pro}-Ub complex structure determined here (not shown). In addition, the crystal structure of USP21 bound to linear diUb was recently determined and revealed that the tip of the fingers domain of this DUB acts as an S2 recognition site, binding to

the distal Ub of a linear diUb molecule (345). Given the structural similarity between Lys63 diUb and linear diUb, and the clear activity we observed for MERS-CoV PL^{pro} towards Lys63, we hypothesized that mutating residues Asn1673 and Val1674 near the Zn-ribbon may also disrupt Ub processing.

5.3.4 Targeted mutations within the PL^{pro}-Ub binding site disrupt Ub processing but not proteolytic cleavage of the nsp3|4 site

Using a previously described ectopic expression assay (211), we monitored the effects of amino acid substitutions in PL^{pro}, as described above, on overall levels of Ub-conjugated proteins in HEK293T cells, as well as the ability of these PL^{pro} variants to process the MERS-CoV nsp3|4 polyprotein cleavage site *in trans*. V5-tagged PL^{pro} (wild-type and mutants) was co-expressed with N-terminally HA-tagged and C-terminally V5-tagged MERS-CoV nsp3C-4 excluding the PL^{pro} domain, from here on referred to as HA-nsp3C-4-V5. We assume that the successful processing of the nsp3|4 site in HA-nsp3C-4-V5 is indicative of unaltered proteolytic cleavage capability of PL^{pro}, which during infection facilitates the release of nsp1, 2 and 3 from the viral polyproteins. Processing of HA-nsp3C-4-V5 *in trans* by wild-type PL^{pro} and our panel of mutants was visualized *via* Western blotting (**Figure 5.7 A**). Whereas wild-type PL^{pro} was able to cleave HA-nsp3C-4-V5 substrate *in trans*, the PL^{pro} active site mutant Cys1592Ala was unable to cleave the nsp3|4 site (**Figure 5.7 A**, compare lanes 5 and 6; 19 and 20). As expected, each of the substitutions in the Ub-binding site of PL^{pro} only minimally affected nsp3|4 cleavage, with the exception of the Ala1656Arg mutant that displayed a clearly reduced ability to cleave HA-nsp3C-4-V5 compared to wild-type PL^{pro} (**Figure 5.7 A**, compare lanes 5 and 10). This suggests that Ala1656 of PL^{pro} may be involved in recognizing and binding sequences in the vicinity of

the nsp3|4 cleavage site. Most double and triple substitutions tested were also slightly less efficient in cleaving HA-nsp3C-4-V5 compared to the wild-type control.

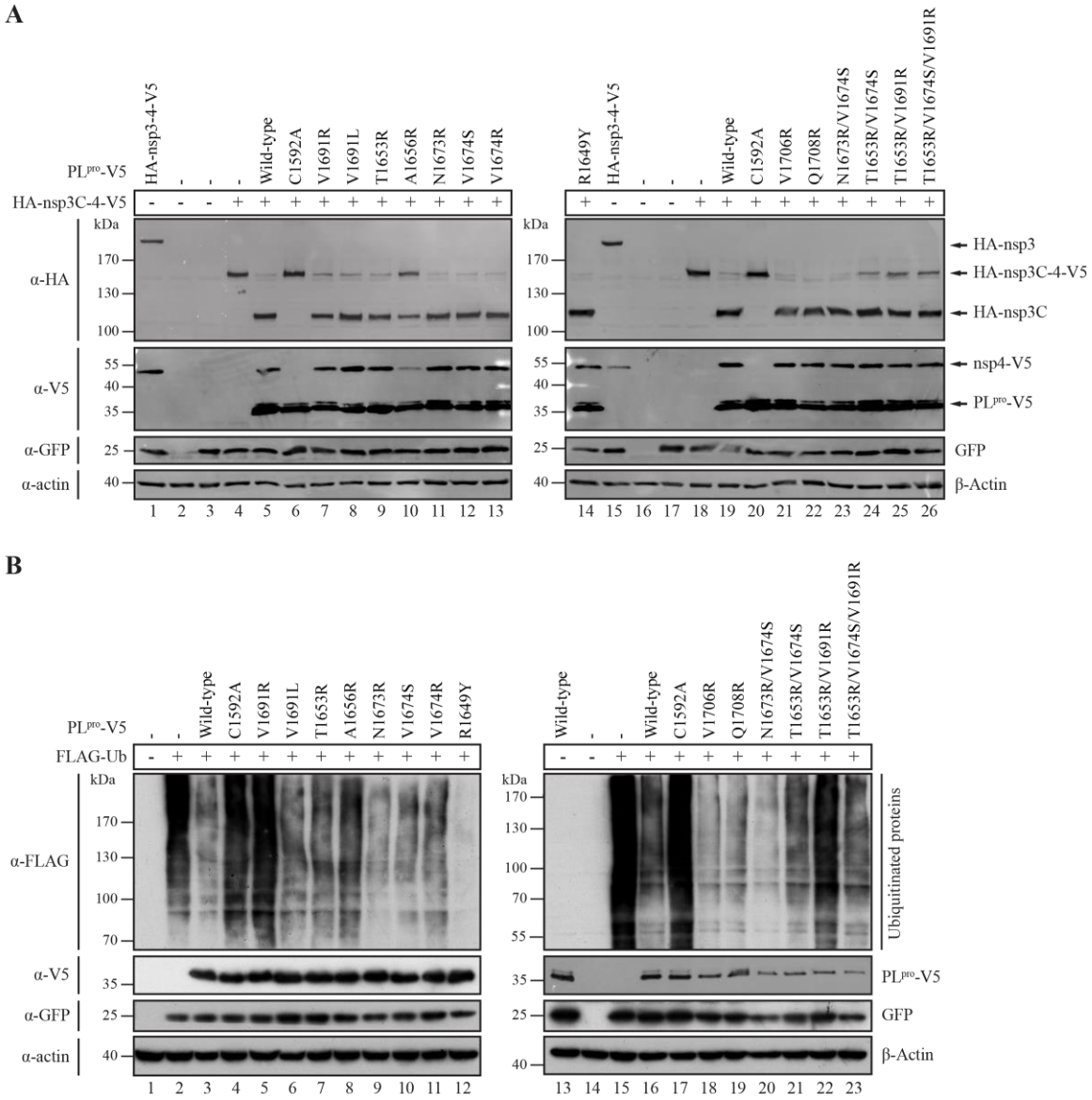

Figure 5.7 Effect of PL^{pro} mutations on *in trans* cleavage of nsp3|4 and on DUB activity.
(A) HEK293T cells were co-transfected with plasmids encoding HA-nsp3C-4-V5 (which does not contain PL^{pro}), PL^{pro}-V5 (wild-type and mutants) and GFP (as a transfection control). As a control, plasmid encoding HA-nsp3-4-V5 which includes the PL^{pro} domain was transfected (lanes 1 and 15), and cleavage resulted in the generation of full-length HA-tagged nsp3 and V5-tagged nsp4. Cells were lysed 18 h post transfection and expressed proteins were analyzed by Western blotting. Proteolytic cleavage was measured from the generation of N-terminal HA-tagged nsp3C and C-terminal V5-tagged nsp4. (B) HEK293T cells were transfected with a combination of plasmids encoding FLAG-Ub, PL^{pro}-V5 (wild-type and mutants) and GFP (as a transfection control). Cells were lysed 18 h post transfection and expressed proteins were analyzed by Western blotting to visualize the deconjugation of FLAG-tagged Ub from a wide range of cellular proteins by MERS-CoV PL^{pro} wild-type and mutants. This figure was originally

published in the *Journal of Biological Chemistry*. Bailey-Elkin BA, Knaap RCM, Johnson GG, Dalebout TJ, Ninaber DK, van Kasteren PB, Bredenbeek PJ, Snijder EJ, Kikkert M, Mark BL. Crystal structure of the MERS coronavirus papain-like protease bound to ubiquitin facilitates targeted disruption of deubiquitinating activity to demonstrate its role in innate immune suppression. 2014; 289:34667-82.

In order to analyse the effect of the mutations on overall DUB activity, PL^{pro}-V5 was co-expressed with FLAG-Ub, and the levels of FLAG-Ub-conjugated cellular proteins were visualized *via* Western blotting (**Figure 5.7 B**). Expression of wild-type PL^{pro} resulted in a strong decrease of the accumulation of FLAG-Ub conjugates whereas a negligible effect was observed upon expression of active site mutant Cys1592Ala (**Figure 5.7 B**, compare lanes 3 and 4; 16 and 17). Substitutions of residue Val1691, positioned on strand β12 of PL^{pro}, and Thr1653 and Ala1656, residues located on helix α7 (**Figure 5.6 B, C**), displayed the clearest reduction of PL^{pro} DUB activity (**Figure 5.7 B**, lanes 5-8). The Val1691Arg mutation had the most pronounced effect, and a PL^{pro} Thr1653Arg/Val1691Arg double mutant also displayed severely reduced DUB activity, comparable to that seen for the active site mutant (**Figure 5.7 B**, compare lanes 4, and 5; 17 and 22). Notably, a more conservative substitution at the same position, Val1691Leu, had a much less pronounced effect on DUB activity (**Figure 5.7 B**, lane 6). Substitution of Val1674 with either Ser or Arg impaired DUB activity, however to a much lesser extent than substitutions targeting Val1691, Thr1653 and Ala1656 (**Figure 5.7 B**, compare lanes 5-8, 10 and 11). The Asn1673R substitution did not negatively affect DUB activity of PL^{pro} at all, whereas the Asn1673Arg/Val1674Ser double substitution resulted in slightly greater DUB activity (**Figure 5.7 B**, lanes 9 and 20). These results do not support our hypothesis based on modeling that Asn1673 and Val1674 might form part of an S2 binding site that recognizes an additional distal Ub within a Lys63-linked chain. Further structural studies are needed to validate the role of these residues in binding Ub chains. It should be noted however that these mutants may still be able to process Lys63-linked polyUb chains by recognizing a single Ub monomer at the end of a polyUb substrate, which may explain the ineffectiveness of these mutations in disrupting DUB activity. Mutations at residues Val1706 and Gln1708 did not influence DUB

activity of PL^{pro} (**Figure 5.7 B**, lanes 18 and 19). Given that these residues were only found to interact with Ub in our closed PL^{pro} structure (**Figure 5.6 A**), their failure to inhibit DUB activity in this cellular DUB assay is not surprising, and indicates that these residues are not essential for Ub recognition. Interestingly and repeatedly observed, the Arg1649Tyr mutant was found to have even greater DUB activity than wild-type PL^{pro} (**Figure 5.7 B**, compare lanes 3 and 12). This residue was found to interact with residue Arg72 of Ub, and while this result was unexpected, it is possible that the Arg1649Tyr mutant retains the ability to interact with Arg72 of Ub *via* a cation-π interaction between the aromatic tyrosine inserted into PL^{pro} and the positively charged arginine of Ub. Together, the findings from our mutagenesis study demonstrate that it is possible to selectively decouple the DUB and polyprotein processing activities of MERS-CoV PL^{pro} through structure-guided site-directed mutagenesis.

5.3.5 PL^{pro} DUB activity suppresses the innate immune response

Conjugation and deconjugation of Ub plays an important role in the regulation of the innate immune response, and not surprisingly, pathogens have evolved mechanisms to subvert these Ub-dependent pathways (reviewed in (35)). For arteriviruses, which are distant relatives of CoVs within the nidovirus order, it has been shown that the DUB activity of their PLP2 is involved in antagonizing IFN-β activation upon ectopic expression, and for EAV this was confirmed during infection in host cells (101,211). Coronavirus papain-like proteases have been suggested to act as IFN-β and NF-κB antagonists as well (84,87,95,159). MERS-CoV PL^{pro} is thought to possess these properties based on its capability to inhibit RIG-I-, MDA5- and MAVS-induced IFN-β promoter stimulation, and to reduce TNF-α-induced NF-κB reporter gene activity (183,187). We therefore designed luciferase-based reporter gene assays to establish whether the DUB activity of MERS-CoV PL^{pro} alone suffices to antagonize the IFN-β pathway. To this end,

we first assessed at which level of this innate immune signal transduction pathway MERS-CoV PL^{pro} is most active as a suppressor.

Innate immune signaling was induced in HEK293T cells by expression of one of three signalling factors: RIG-I, MAVS or IRF3, which stimulate the pathway leading to IFN-β production at different levels. Since RIG-I and IRF3 normally need to be activated through post-translational modification (ubiquitination and phosphorylation respectively), constitutively active variants were used ($RIG\text{-}I_{(2CARD)}$ and $IRF3_{(5D)}$) which efficiently induce downstream signalling independent of these activation steps. Cells were co-transfected with plasmids encoding one of these innate immune signalling proteins and wild-type PL^{pro}, the PL^{pro} active site mutant Cys1592Ala or full-length MERS-CoV nsp3 containing the PL^{pro} domain. The inhibitory effect of the PL^{pro} variants on the activation of the IFN-β promotor by the different stimuli was measured via co-expression of a firefly luciferase reporter gene under control of the IFN-β promoter. Another co-transfected plasmid encoding *Renilla* luciferase was included as an internal control in order to be able to correct for variability in transfection efficiency. At 16 h post-transfection luciferase activities were measured, and activation of the IFN-β promoter induced by expression of $RIG\text{-}I_{(2CARD)}$, MAVS, or $IRF3_{(5D)}$ was set at 100% (**Figure 5.8**). In accordance with Mielech *et al*. (187), we observed that MERS-CoV PL^{pro} significantly reduced the IFN-β promoter activation that could be induced by expression of either $RIG\text{-}I_{(2CARD)}$ or MAVS. This effect was concentration-dependent, while the PL^{pro} active site mutant was unable to block IFN-β promoter activation (**Figure 5.8 A, C**). MERS-CoV nsp3 expression also inhibited RIG-I- and MAVS-mediated IFN-β promoter induction (**Figure 5.8 B, D**), and together this suggested that PL^{pro} inhibits innate immune signalling at least downstream of the MAVS adaptor, and possibly also in the signalling between RIG-I and MAVS. MERS-CoV PL^{pro} also

inhibited activation of the IFN-β promoter after stimulation with $IRF3_{(5D)}$ in a concentration-dependent manner, while the Cys1592Ala mutant did not reduce IFN-β promoter activation (**Figure 5.8 E**). However, expression of full length MERS-CoV nsp3 did not significantly inhibit IFN-β promoter activation after stimulation with $IRF3_{(5D)}$ (**Figure 5.8 F**). This suggests that the subcellular localization of the protease, which in case of full-length nsp3 is membrane anchored and in case of the PL^{pro} domain is presumably cytosolic, may be important in determining its substrate specificity. Taken together, our results suggest that MERS-CoV PL^{pro} primarily interferes with the IFN-β signalling pathway at the level between MAVS and IRF3.

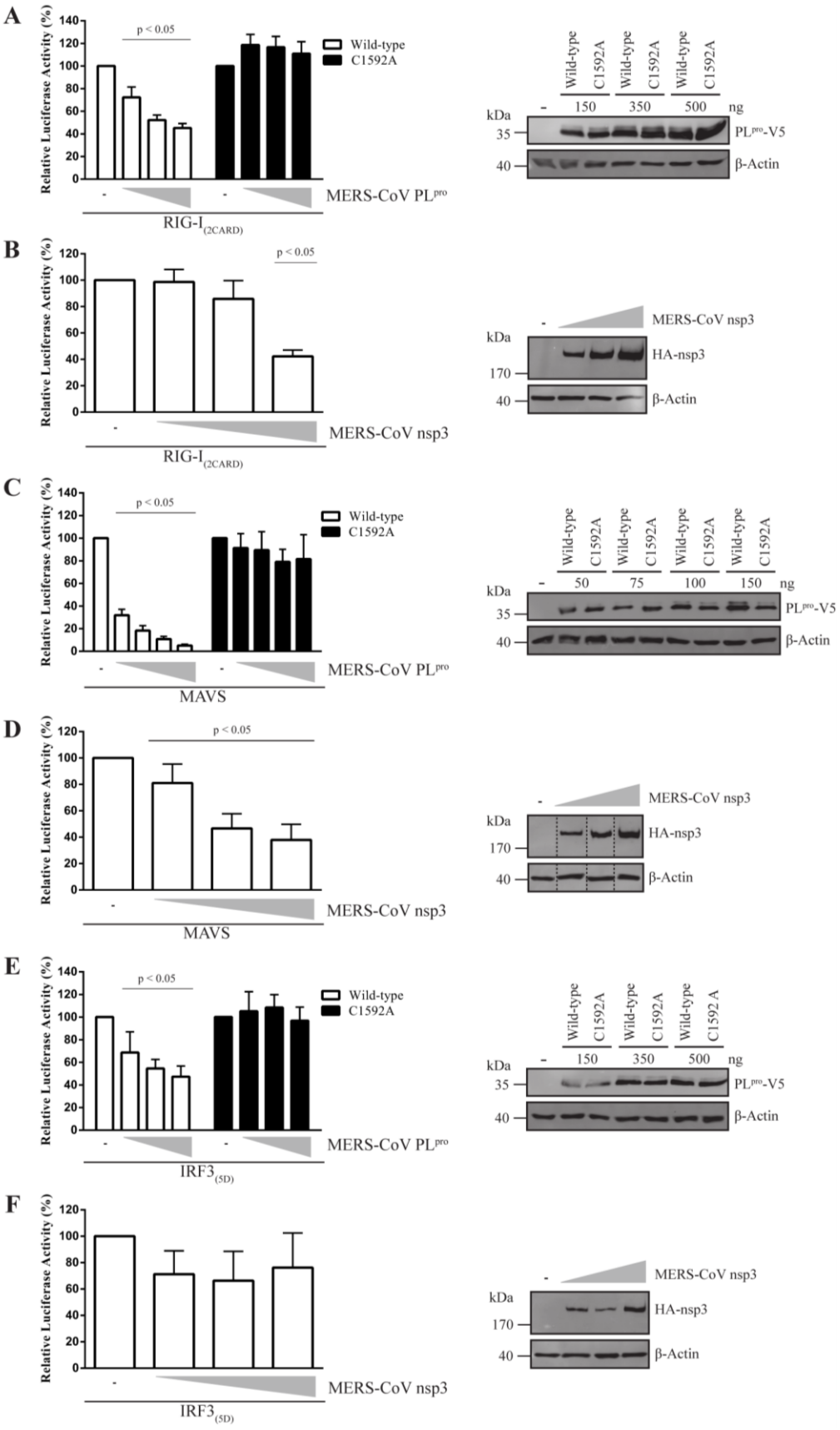
A
Relative Luciferase Activity (%)
p < 0.05
Wild-type
C1592A
MERS-CoV PLpro
RIG-I(2CARD)
Wild-type
C1592A
150
350
500
ng
kDa
35
PLpro-V5
40
β-Actin
B
p < 0.05
MERS-CoV nsp3
RIG-I(2CARD)
170
HA-nsp3
C
p < 0.05
MAVS
50
75
100
150
D
p < 0.05
MAVS
E
p < 0.05
IRF3(5D)
F
IRF3(5D)

Figure 5.8 MERS-CoV PL^{pro} inhibits RIG-I- and MAVS-induced IFN-β promoter activity. HEK293T cells were transfected with a combination of plasmids expressing a firefly luciferase reporter gene under control of the IFN-β promoter, *Renilla* luciferase, innate immune response inducers $RIG\text{-}I_{(2CARD)}$, MAVS or $IRF3_{(5D)}$ and increasing amounts of MERS-CoV PL^{pro} wild-type, active site mutant Cys1592Ala (A, C and E) or full-length MERS-CoV nsp3 (B, D and F). Upon induction of the innate immune response with $RIG\text{-}I_{(2CARD)}$ and $IRF3_{(5D)}$, cells were transfected with the PL^{pro} (0, 150, 350 or 500 ng) or nsp3 (0, 350, 500 of 1000 ng) constructs. Upon induction with MAVS, cells were transfected with 0, 50, 75, 100 or 150 ng PL^{pro} construct or 0, 150, 350, 500 ng of the nsp3 expression vector. At 16 h post transfection, cells were lysed and luciferase activity was measured. All experiments were repeated independently at least four times. Significance was evaluated using an unpaired two-tailed Student's *t* test; p values <0,05 were considered significant. Bars represent mean with error bars indicating the standard deviation. Western blotting was used to verify expression of MERS-CoV PL^{pro} and nsp3. This figure was originally published in the *Journal of Biological Chemistry*. Bailey-Elkin BA, Knaap RCM, Johnson GG, Dalebout TJ, Ninaber DK, van Kasteren PB, Bredenbeek PJ, Snijder EJ, Kikkert M, Mark BL. Crystal structure of the MERS coronavirus papain-like protease bound to ubiquitin facilitates targeted disruption of deubiquitinating activity to demonstrate its role in innate immune suppression. 2014; 289:34667-82. © the American Society for Biochemistry and Molecular Biology.

We therefore chose to use MAVS-mediated induction of IFN-β promoter activation in subsequent experiments. This also resulted in the strongest inhibition by PL^{pro}, providing a maximum window to assess the effects on IFN-β promoter inhibition by the PL^{pro} mutants with specifically inactivated DUB activity. Inhibition of IFN-β promoter activation by wild-type and mutant PL^{pro} was determined by calculating the relative luciferase activity (**Figure 5.9**). Expression of wild-type PL^{pro} reduced MAVS-induced IFN-β promoter activity to ~20% of the control, whereas active site mutant C1592A reduced it by only a few percent compared to the untreated control (**Figure 5.9**). Substitutions Thr1653Arg and Ala1656Arg resulted in greatly impaired DUB activity (**Figure 5.7 B**, lanes 7 and 8), and compared to wild-type PL^{pro}, expression of these mutants resulted in higher IFN-β promoter activity with relative luciferase values of approximately 54% and 58% respectively (**Figure 5.9**). It should however be noted that the Ala1656Arg mutant was also impaired in cleaving the nsp3|4 site and therefore this mutation non-specifically disrupted the two proteolytic functions of PL^{pro}. Strikingly, each mutant containing the Val1691Arg substitution was completely unable to inhibit IFN-β promoter activation resulting in relative luciferase activity levels similar to those seen with the active site mutant (**Figure 5.9** lanes 4, 16 and 17). This strongly suggested that the DUB activity of PL^{pro}, which we found to be severely impaired in Val1691Arg mutants (**Figure 5.7 B**), is responsible for supressing MAVS-induced IFN-β promoter activity in this assay. The level of reduction in DUB activity corresponded to the degree of inhibition of IFN-β promoter activation for all PL^{pro} mutants tested, which strengthens this conclusion. In accordance with its increased DUB activity, mutant Arg1649Tyr suppressed MAVS-induced IFN-β promoter activity more effectively than wild-type PL^{pro}.

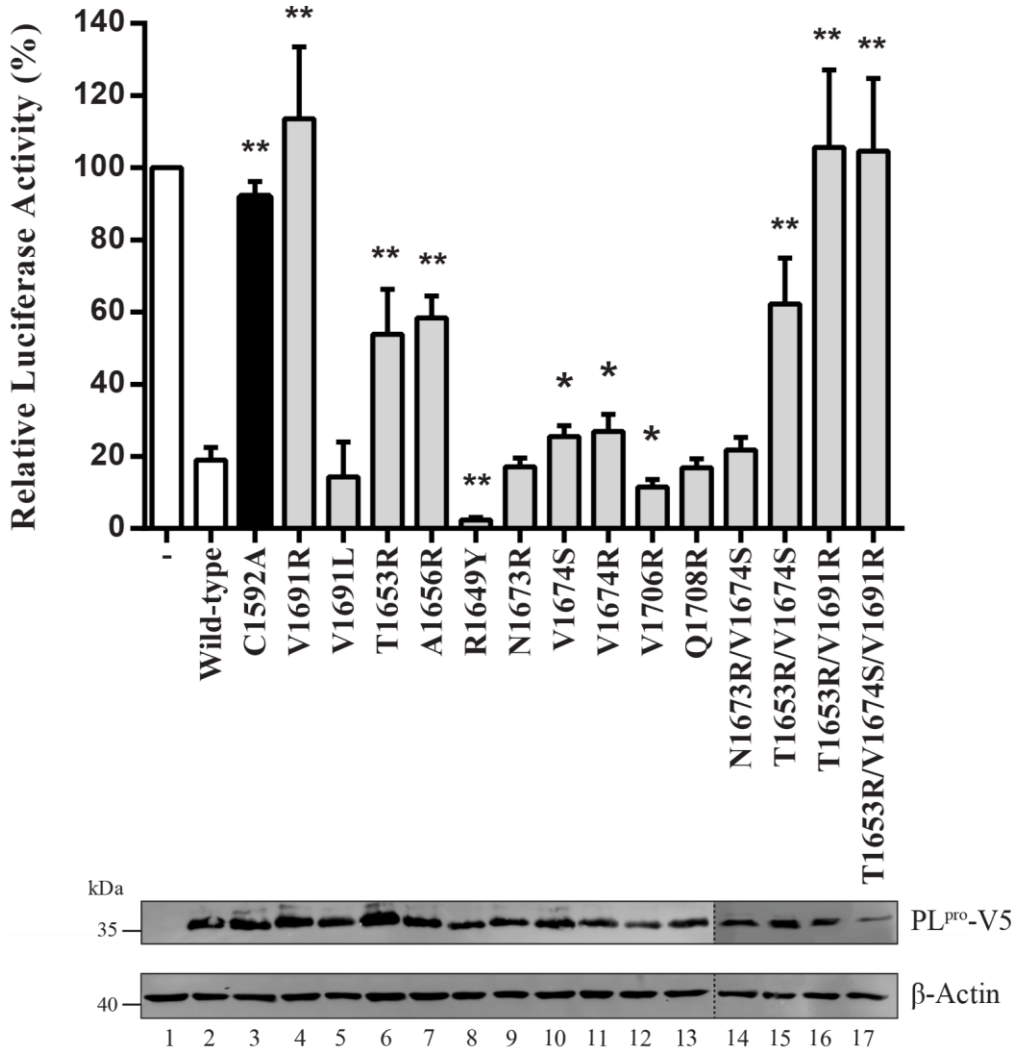

Figure 5.9 DUB activity is required for IFN-β promoter antagonism by MERS-CoV PL^{pro}. HEK293T cells were transfected with plasmids encoding a firefly luciferase reporter gene under control of the IFN-β promoter, *Renilla* luciferase, innate immune response inducer MAVS (25 ng) and MERS-CoV PL^{pro} wild-type and mutants (75 ng). At 16 h post transfection, cells were lysed and luciferase activity was measured. All experiments were repeated independently at least four times. Significance relative to wild-type was evaluated using an unpaired two-tailed Student's *t* test; significant values were indicated with * if $p<0.05$ and ** if $p<0.01$. Bars correspond to the mean with error bars showing the standard deviation. Western blotting was used to verify expression of MERS-CoV PL^{pro}. This figure was originally published in the *Journal of Biological Chemistry*. Bailey-Elkin BA, Knaap RCM, Johnson GG, Dalebout TJ, Ninaber DK, van Kasteren PB, Bredenbeek PJ, Snijder EJ, Kikkert M, Mark BL. Crystal structure

of the MERS coronavirus papain-like protease bound to ubiquitin facilitates targeted disruption of deubiquitinating activity to demonstrate its role in innate immune suppression. 2014; 289:34667-82.

Taken together, our data show that the DUB activity of MERS-CoV PL^{pro} suffices to efficiently suppress MAVS-induced IFN-β promoter activation and that this activity can be selectively disabled, without disrupting protease activity towards the nsp3|4 cleavage site, by targeting the Ub-binding site of the enzyme. This demonstrates for the first time that the DUB activity of MERS-CoV PL^{pro} is specifically responsible for suppressing the innate immune response.

5.4 Discussion

Guided by the MERS PL^{pro}-Ub crystal structures, we here describe how the DUB activity of PL^{pro} can be selectively disabled by introducing mutations into the S1 binding pocket of the protease (**Figure 5.6**). Particularly the substitution of Val1691 with the bulky and charged arginine residue severely impaired DUB activity in our cell culture-based assays. In addition, our results demonstrate that the majority of the mutations within the S1 Ub-binding site of PL^{pro} that were tested do not affect *trans* cleavage of the nsp3|4 junction, with the exception of an Ala1656Arg mutant that did disrupt cleavage of the nsp3|4 site. The latter result indicates that A1656 resides is in a region of PL^{pro} that recognizes both Ub and a region of the nsp3C-4 construct that was used to test cleavage efficiency.

Our results demonstrate that the DUB activity of MERS-CoV PL^{pro} inhibits IFN-β promoter activation when innate immune signalling is induced by co-expression of either RIG-I or MAVS. The fact that suppression of IFN-β promoter activation was completely eliminated for several of our mutants (**Figure 5.9**) strongly suggests that the proteolytic activity still present in those mutant enzymes has no additional role in the suppression of this particular branch of the innate immune response, for example by directly cleaving RIG-I or MAVS. A number of other CoV papain-like proteases with DUB activity have also been implicated in antagonizing the host

innate immune response (84,87,95,159). In agreement with our data, recent studies have demonstrated the ability of MERS-CoV PL^{pro} to inhibit RIG-I-, MDA5- and MAVS-dependent IFN-β promoter activation, as well as to down-regulate the level of IFN-β mRNA transcripts in MDA5-stimulated cells (187). The current data supports the hypothesis that all these activities solely depend on the deubiquitinating capacities of these coronavirus enzymes. Reports regarding the dependence of MERS-CoV PL^{pro}-mediated IFN-β antagonism on the enzyme's protease activity have however varied thus far. Mielech *et al.* (187) recently demonstrated that a MERS-CoV nsp3 fragment containing PL^{pro} but excluding the transmembrane domain can inhibit MAVS-, RIG-I- and MDA5-dependent IFN-β promoter activation, and MDA5 mediated IFN-β mRNA transcription only with a functional PL^{pro} active site. Yang *et al.* (183) on the other hand used a MERS-CoV PL^{pro} expression product extending into the nsp3 transmembrane region to demonstrate that down-regulation of RIG-I-stimulated IFN-β promoter activity is seen even with an active site knock-out mutant. Here we show that inhibition of RIG-I-, MAVS- and IRF3-induced IFN-β promoter activity by the MERS-CoV PL^{pro} domain is clearly dependent on a functional active site, and that it is specifically the DUB activity of the protease that mediates this inhibition. It can however not be ruled out that other parts of nsp3 contain additional innate immune suppressing activities, which may be responsible for the protease-independent effects reported with longer expression products.

Ubiquitination plays an important role in the regulation of pathways involved in detecting and counteracting viral infections, and, not surprisingly, a number of viruses of substantial diversity have been found to deploy DUB enzymes that manipulate these signalling processes by reversing the post-translational modification of cellular proteins by Ub conjugation (68,327). Some of these DUBs, specifically those found in (+)RNA viruses, are also critical for viral

replication by catalyzing the proteolytic cleavage of specific sites in viral polyproteins, thus complicating our ability to study the direct effects of the additional DUB activity of these viral proteases. Ultimately, these effects need to be studied in the context of a viral infection, however a simple inactivation of the protease/DUB would not only fail to prove the specific involvement of the DUB activity, it would also prevent viral replication. The method described here selectively removed the DUB activity of the MERS-CoV PL^{pro} domain while leaving polyprotein processing activity at the nsp3|4 site unhindered, thus paving the way for the application of these mutations to recombinant MERS-CoV and the direct study of the role of DUB activity during infection.

We were able to show that Lys48- and Lys63-linked polyUb chains are processed *in vitro* by MERS-CoV PL^{pro} at similar rates, which is in accordance with a recent report by Baez-Santos and coworkers (91). In contrast, SARS-CoV PL^{pro} rapidly cleaves Lys48-linked polyUb and displays only moderate activity for Lys63 linkages in similar assays (170). It has been suggested that SARS-CoV PL^{pro} may recognize Lys48-linked diUb via its S1 and S2 sites (170), although to date no crystal structures have been reported of SARS-CoV PL^{pro} in complex with a diUb substrate. Similarly, no such structural data has been obtained for MERS-CoV PL^{pro}, and thus future structural studies are necessary to determine precisely how MERS-CoV PL^{pro} recognizes polyUb substrates and whether the preferences observed in expression systems can be confirmed in situations representative of an infection.

In addition to deconjugating Ub, MERS- and SARS-CoV PL^{pro} also recognize the antiviral Ubl molecule ISG15 (89,187), and the structural basis for ISG15 recognition by PL^{pro} is discussed in Chapter 7. Structure-guided mutagenesis of MERS-CoV PL^{pro} to selectively disrupt deISGylation without affecting polyprotein cleavage would further expand our insights into the

role of this additional activity in CoV immune evasion. The specific removal of DUB and potentially deISGylating activity from viral proteases that suppress the host innate immune response may open new avenues to engineer attenuated viruses for use as modified life virus (MLV) vaccines.

Chapter 6
Potent and selective inhibition of pathogenic viruses by engineered ubiquitin variants

Adapted from: Zhang, W.[1], Bailey-Elkin, B. A.[1], Knaap, R. C. M.[1], Khare, B., Dalebout, T. J., Johnson, G. G., van Kasteren, P. B., McLeish, N. J., Gu, J., He, W., Kikkert, M.[2], Mark, B. L.[2], and Sidhu, S. S.[2] (2017) Potent and selective inhibition of pathogenic viruses by engineered ubiquitin variants. *PLoS Pathog.* **13**, e1006372

[1] Authors contributed equally to this work

[2] Authors contributed equally to this work

Contributions statement

This work was carried out in collaboration with the research groups of Marjolein Kikkert, and Sachdev Sidhu, at the LUMC and University of Toronto (UT), respectively. Wei Zhang (UT) identified MERS-CoV- and CCHFV OTU-specific UbVs by phage display, and performed the *in vitro* binding assays to determine UbV specificity and potency. During the progress of this research, I visited the LUMC, and under the supervision of Marjolein Kikkert and with the assistance of Robert Knaap (LUMC) performed the preliminary deubiquitination assays in order to demonstrate the effectiveness of MERS-CoV-specific UbVs in cell culture (see **Figure 6.9** and **Figure 6.10**) using the methods described in sections 6.2.9, 6.2.10, 6.2.12 and 6.2.13. I also performed preliminary reporter assays demonstrating that MERS-CoV-specific UbVs restore IFN-β promoter activity in the presence of MERS-CoV PL^{pro} (see **Figure 6.11**) using the methods described in section 6.2.13. The cell culture assays were subsequently optimized and repeated by Robert Knaap. In addition, the cell culture work showing that UbVs inhibited replication of MERS-CoV were carried out by Robert Knaap.

I performed the expression, purification and crystallization of the MERS-CoV-UbV complexes, as well as the X-ray data collection, processing and structural determination and analysis, described in sections 6.2.6.1, 6.2.6.3, 6.2.7.1 and 6.2.8.1. Crystallization of the CCHFV OTU-UbV complexes was carried out by Baldeep Khare (UM), and structural determination of the complexes was carried out by Baldeep Khare and Brian Mark. Structural analysis of the CCHFV OTU-UbVs was carried out by me, Baldeep Khare and Brian Mark. The manuscript was written by me, Wei Zhang and Robert Knaap, and edited by Sachdev Sidhu, Brian Mark and Marjolein Kikkert.

6.1 Introduction

As discussed in previous chapters, the importance of vDUBs in viral replication and innate immune evasion make them attractive pharmacological targets. Their structural similarity with human DUBs, however, has posed a significant challenge that complicates the successful development of highly selective small molecule vDUB inhibitors (347). Despite intensive efforts, only a handful of inhibitors targeting vDUB proteases have been reported, and none have been approved for clinical use (348). To meet this challenge, we have developed a strategy to target the vDUB activity as an antiviral approach by the rapid identification of virus-specific, protein-based vDUB inhibitors from a phage-displayed library of billions of Ub variants (UbVs). The exquisite specificity of identified UbVs has also enabled us to isolate UbVs that potently inhibit human Ub-binding proteins with equally high specificity (191,193). Here we describe UbVs that selectively block the deubiquitinating and deISGylating activities of MERS-CoV PL^{pro} and CCHFV OTU vDUB domains, respectively. Importantly, UbVs specific for MERS-CoV abolished replicative polyprotein processing activities. Expression of MERS-CoV-specific UbVs during MERS-CoV infection reduced infectious progeny titers by more than four orders of magnitude, demonstrating the remarkable potency of UbVs as antiviral agents.

6.2 Methods

6.2.1 Selection of ubiquitin variants

The phage-displayed UbV library used in this study was re-amplified from Library 2 as previously described (193). Protein immobilization and the following UbV selections were done according to established protocols (191,349). Briefly, purified viral proteases were coated on 96-well MaxiSorp plates (Thermo Scientific 12565135) by adding 100 µL of 1 µM proteins and

incubating overnight at 4ºC. Afterwards, five rounds of selections using the phage-displayed UbV library were performed against immobilized proteins including the following steps: (*a*) Each phage particle in the library pool displays a unique UbV and encapsulates the encoding DNA; (*b*) Binding phages are captured with an immobilized protein; (*c*) Non-binding phages are washed away; and (d) Bound phages are amplified by infection of bacteria. The enriched phage pool is cycled through additional rounds of selection to further enrich for protein-binding UbVs. After the fifth round of binding selections, individual phages with improved binding properties were identified by phage enzyme-linked immunosorbent assay (ELISA) using established techniques and subjected to DNA sequencing of the phagemids to obtain UbV sequences (191,349).

6.2.2 Lentivirus transduction and MERS-CoV infections

To produce lentiviruses, HEK293T cells (Virgin lab, Washington University School of Medicine) grown in a T175 flask were transfected with packaging vectors pMDLg/pRRE and pRSV-REV, envelope protein-expressing vector pCMV-VSVG (350) and the transfer vector (pLenti6.3/TO/V5-DEST containing GFP or FLAG-UbVs) using polyethylenimine (PEI; Polysciences Inc.). Medium was replaced 24 h post transfection and 48 h and 72 h post transfection supernatant was collected, centrifuged (1000 x g for 10 min) and filtered through a 0.45 μm filter before storage at -80°C. Titers of the lentivirus particles were determined by p24 antigen ELISA (ZeptoMetrix). HuH-7 (Bartenschlager lab, Heidelberg University) and MRC5 cells (CCL-171; American Type Culture Collection) grown in a 12-well plate were transduced with lentiviruses encoding GFP or FLAG-ME.1 diluted in DMEM containing 2% FCS and 8 μg/ml Polybrene (Sigma Aldrich). Medium was replaced 24 h post transduction (pt), and 32 h or

48 h pt protein lysates were obtained by adding 250 µl 2xLSB containing 25 mM N-ethylmaleimide (NEM) to each well while cells grown on coverslips were fixed with 3% PFA in PBS.

GFP and FLAG-ME.1 expression were analyzed by Western blotting as described in section 6.2.12. Fixed cells that were grown on coverslips were permeabilized with 0.1% Triton X-100 in PBS and subsequently indirect immunofluorescence assays were carried out. Primary and secondary antibodies were diluted in PBS containing 5% FCS and Hoechst 33258 was added to the secondary antibody dilution to stain nuclear DNA. Coverslips were analyzed with a Zeiss Axioskop 2 fluorescence microscope with an Axiocam HRc camera.

To obtain a cell population in which >90% of the cells expressed GFP, the amount of lentivirus yielding 120 ng of p24 was required to transduce $1x10^5$ HuH-7 cells and 40 ng of p24 for $1x10^5$ MRC5 cells was required. HuH-7 or MRC5 cells ($1x10^5$/12-well) were transduced with lentiviruses encoding GFP, FLAG-Ub.AA, FLAG-ME.1 or FLAG-ME.4. Cells were infected with MERS-CoV with a m.o.i. of 0.01 32 h or 48 h pt. MERS-CoV inocula were prepared in PBS containing 50 µg/ml DEAE-dextran and 2% FCS. Cells were inoculated for 1 h at 37°C and the inoculum was replaced with Eagle's minimum essential medium (EMEM) containing 2% FCS. Supernatants were harvested 32 h post MERS-CoV infection and simultaneously cells were lysed in 4x LSB for Western blotting analysis. MERS-CoV titers were determined by plaque assays on Vero cells (Department of Viroscience, Erasmus Medical Center) as described by van den Worm et al. (351). MERS-CoV infection experiments were performed at least twice and plaque assays were performed in duplicate in order to determine MERS-CoV titers. Work with MERS-CoV was performed inside biosafety cabinets in Biosafety Level 3 facilities at Leiden University Medical Center.

6.2.3 ELISA assays to evaluate binding and specificity

Proteins under study were immobilized on 384-well MaxiSorp plates (Thermo Scientific 12665347) by adding 30 µL of 1 µM proteins for overnight incubation at 4 ºC. Phage and protein ELISA against immobilized proteins was performed as previously described (191,193). Binding of phage was detected using anti-M13-HRP antibody (GE Healthcare 27942101) and binding of FLAG-tagged UbVs was detected using anti-FLAG-HRP antibody (Sigma-Aldrich A8592). To measure the half maximal binding concentration (EC_{50}) of UbVs binding to viral proteases, the concentration of UbVs or wild type Ub was varied from 0 to 4 µM (24 points, 1:2 dilution), while the concentration of target proteins immobilized on the plate remained at 1 µM. EC_{50} values were calculated using the GraphPad Prism software with the built-in equation formula (non-linear regression curve).

6.2.4 Octet Bio-Layer Interferometry (BLI)

Experiments were performed as previously described (191). Concentrated analyte and ligand proteins were diluted into BLI reaction buffer (25 mM HEPES pH 7.0, 150 mM NaCl, 0.1 mg/ml bovine serum albumin and 0.01% tween 20). Experiments of BLI were carried out on Octet RED96 system (ForteBio) using anti-GST antibody biosensors for GST-tagged ligands and His-tagged analytes at 25˚C. 7-9 concentration points of analytes covering a wide titration range were applied for BLI experiments. Sensorgram raw data were processed and extracted by Octet Analysis 9.0. Binding constants K_D were obtained by fitting the response wavelength shifts in the steady-state regions using the single-site binding system equation shown below.

$$R_{eq} = R_{max} \frac{[C]}{K_D + [C]}$$

where R_{eq} is the value of the response shift in the steady-state region in each sensorgram curve, *[C]* is the titrant concentration, R_{max} is the maximal response in the steady-state region, K_D is the binding constant for the single-site binding system. In both equations, R_{max} and K_D values are unknown and the Levenberg–Marquardt algorithm was used to perform iterative non-linear least squares curve fitting in Profit 6.2 (QuantumSoft) to obtain the fitted R_{max} and K_D.

6.2.5 Deconjugation assays

6.2.5.1 Ub/ISG15-AMC

Inhibition assays using Ub-AMC or ISG15-AMC (both Boston Biochem) as deconjugation substrates were performed as described before (193,352). Experiments were performed in assay buffer (50 mM HEPES, pH 7.5, 0.01% Tween 20, 1 mM dithiothreitol (DTT)) containing 1 μM Ub-AMC substrate, 10 nM vDUBs and 12 serial dilutions of UbVs. vDUBs and UbV were mixed in assay buffer as indicated and incubated at room temperature for 2 min prior to the addition of Ub-AMC. All serial dilutions were performed in 96-well plates and subsequently transferred to 384-well black plates (Thermo Scientific) for making measurements. Deconjugation activity was measured by monitoring the increase of AMC fluorescence emission at 460 nm (excitation at 360 nm) for 30 min using a BioTek Synergy2 plate reader (BioTek Instruments, Winooski, VT). IC_{50} values were calculated using the GraphPad Prism software with the built-in equation formula (non-linear regression curve).

6.2.5.2 Lys48/Lys63 tetra-Ub

Inhibition assays using Biotin Tetra-Ub wild-type chains (Lys48- or Lys63-linked, Boston Biochem) as deubiquitination substrates were performed in assay buffer (50 mM HEPES, pH 7.5, 100 mM NaCl, 1 mM DTT) containing 1 μM substrate, 1 μM vDUB and 10 μM UbV as

indicated. After incubation at 37°C for the indicated times, reactions were stopped by the addition of 10 mM EDTA and SDS-PAGE sample buffer and resolved using 4-20% gradient gels (Bio-Rad). The cleavage of Lys48/Lys63 tetra Ub chains was evaluated by Western blotting, probed with ExtrAvidin®-Peroxidase (Sigma).

6.2.6 Protein expression and purification

6.2.6.1 Ubiquitin variants ME.2 and ME.4

Plasmids named pET53-ME.2, and -ME.4 were transformed into $CaCl_2$-competent *Escherichia coli* BL21 (DE3) Gold cells (Agilent) to allow for T7 polymerase-driven expression of N-terminally His_6-tagged UbVs ME.2 and ME.4 respectively. Cells were grown at 37°C in the presence of 150 μg/mL ampicillin to an optical density (OD_{600}) of 0.6 and then induced at 16°C by addition of IPTG (final concentration 1 mM). After overnight incubation, cells were resuspended in lysis buffer (500 mM NaCl, 50 mM Tris pH 8.0) and lysed via French press. The cell lysate was clarified by centrifugation at 17,211 x g at 4°C for 30 min, then incubated with 2 mL Ni-NTA Superflow resin (Qiagen) at 4°C for 30 min, and poured into a gravity column. The column was washed with 50 mL of lysis buffer, followed by 50 mL of lysis buffer containing 50 mM imidazole. Protein was eluted in lysis buffer containing 250 mM imidazole. Following affinity purification, UbVs were further purified using a Superdex 75 size exclusion column (GE Healthcare), eluting in 20 mM Tris pH 8.5, 150 mM NaCl and 2 mM DTT.

6.2.6.2 Ubiquitin variants CC.2 and CC.4

Plasmids encoding UbVs CC.2 and CC.4, named pET53-CC.2 and -CC.4 respectively, were transformed into $CaCl_2$-competent *E. coli* BL21 (DE3) Gold cells, and grown in LB media supplemented with 150 μg/ml Ampicillin at 37˚C with shaking to an OD_{600} of 0.8-1.5. Protein

expression was induced by the addition of a final concentration of 1 mM IPTG for 19-21 hours at 28˚C. Cells were resuspended in lysis buffer (for CC.2: 50 mM Tris pH 7.2, 150 mM NaCl; for CC.4: 50 mM Tris pH 8.0, 150 mM NaCl) and lysed using either French Press or a freeze-thaw cycle that was performed three times. For the latter, cells were frozen at -80˚C after addition of 150 µl of 20 mg/ml lysozyme followed by incubation on ice for 20 min, and thawed at room temperature. Lysis was followed by addition of 100-300 µl of DNase I (10 mg/ml) while mixing on a magnetic stirrer. Lysates from French Press or the freeze-thaw procedure were clarified by centrifugation at 48,298 x g for 30-40 min. Supernatants were loaded onto a gravity column containing Ni-NTA Superflow resin (Qiagen) that had been pre-equilibrated with Buffer A (50 mM Tris pH 8.0, 150 mM NaCl). The column was washed with 2-3 column volumes (CV) of Buffer A supplemented with 20 mM imidazole and eluted in a step-wise manner with Buffer A containing 500 mM imidazole. Fractions of interest, as determined from SDS-PAGE, were pooled and dialyzed twice against Buffer A. The proteins were concentrated and loaded onto the Superdex 75 size exclusion column. CC.2 was eluted in 20 mM Tris pH 7.4, 150 mM NaCl and 1 mM DTT, and CC.4 was eluted in 50 mM Tris pH 8.0, 150 mM NaCl and 2 mM DTT.

6.2.6.3 MERS-CoV PL^{pro}

The MERS-CoV PL^{pro} domain was expressed and purified as described previously (254). Briefly, *E. coli* BL21 (DE3) Gold cells transformed with plasmid pE-SUMO-PL^{pro} were grown to an OD_{600} of 0.6-0.8 at 37˚C in the presence of 35 µg/mL kanamycin. Protein expression was induced by the addition of a final concentration of 1 mM IPTG and overnight incubation at 16˚C. Cells were resuspended in lysis buffer (150 mM Tris, pH 8.5, 1 M NaCl, 2 mM DTT), lysed via French press and clarified via centrifugation at 17,211x g. Clarified lysate was loaded onto a Ni-NTA gravity column and washed with lysis buffer, followed by lysis buffer supplemented with

25 mM imidazole and subsequent elution in lysis buffer supplemented with 250 mM imidazole. The SUMO-PL^{pro} fusion was cleaved overnight in 150 mM NaCl, 50 mM Tris, pH 8.0, 1 mM DTT in the presence of Ulp1 SUMO protease. Cleaved, tagless MERS-CoV PL^{pro} was subsequently passed through a second Ni-NTA column, and further purified on a Superdex 75 size exclusion column equilibrated in 20 mM Tris, pH 8.5, 150 mM NaCl, 2 mM DTT.

6.2.6.4 CCHFV OTU$_{169}$ and CCHFV OTU$_{185}$

Plasmids encoding the CCHFV OTU domain residues 1-169 (pGEX-*CCHFV OTU$_{169}$)* and residues 1-185 (pET49b-*CCHFV OTU$_{185}$*) fused with a GST tag and an HRV3c protease cleavage site were used for the expression and purification of the CCHFV OTU domain as described previously (102,105). Briefly, *E. coli* BL21-Gold (DE3) cells transformed with either of the plasmids were grown to an OD_{600} of 0.9-1.0 at 37˚C with shaking, and protein expression was induced with a final concentration of 1 mM IPTG at 30˚C for 19-21 hrs. Cells were resuspended in 25 ml of lysis buffer (50mM Tris-Cl pH 7.2, 200 mM NaCl, 5 mM EDTA, 5 mM DTT) and lysed via French Press. The lysate was clarified by centrifugation at 48,298 x g for 30-40 min. The supernatant was loaded onto GST-Bind resin (VWR) in a gravity column pre-equilibrated with the lysis buffer, and proteins were eluted in 50 mM Tris-Cl pH 7.2, 500 mM NaCl, 5 mM EDTA, 5 mM DTT and 15 mM reduced glutathione. The GST tag was cleaved by addition of GST-tagged HRV 3c protease during overnight dialysis against 50 mM Tris pH 7.4, 150 mM NaCl, 1 mM EDTA, 1 mM DTT. Cleaved CCHF-vOTU proteins were collected as flow-through by passing the digest through a recharged GST-Bind column, concentrated and loaded onto the Superdex-75 column (GE Healthcare). Purified proteins, eluted in 20 mM Tris pH 7.2, 150 mM NaCl and 1mM DTT, were then used for further analyses.

6.2.7 Protein crystallization

6.2.7.1 MERS-CoV PL_{pro}-ME.2 and -ME.4 complexes

To form the non-covalent MERS-CoV PL^{pro}-UbV complexes, a 4-fold molar excess of ME.4 or ME.2 was incubated with MERS-CoV PL^{pro} overnight at 4°C. The excess, unbound UbVs were removed from the sample using a Superdex 75 size exclusion column and fractions containing the MERS-CoV PL^{pro}-UbV complex were pooled and concentrated to 10 mg/mL. The MERS-CoV PL^{pro}-ME.4 complex was found to crystallize under similar conditions to those previously reported for the MERS-CoV PL^{pro}-Ub complex (93), with optimal crystals appearing in 0.1 M trisodium citrate pH 5.6, 20% (w/v) polyethylene glycol (PEG) 4000 and 20% (v/v) isopropanol. Crystals of the MERS-CoV PL^{pro}-ME.2 complex were grown in 0.1 M trisodium citrate pH 5.6, 19% (w/v) PEG 4000 and 19% (v/v) 1,2-isopropanediol. Crystals were grown by mixing PL^{pro}-UbV (10 mg/mL and 9 mg/mL for PL^{pro}-ME.4 and PL^{pro}-ME.2, respectively) with crystallization solution at a 1:1 volumetric ratio (2 μL MERS-CoV PL^{pro}-UbV + 2 μL well solution). Immediately prior to mixing, 1 M DTT was added to the MERS-CoV PL^{pro}-UbV complexes to a final concentration of 10 mM to prevent oxidation of the sample.

6.2.7.2 CCHFV OTU_{169}-CC.2 and CCHFV OTU_{185}-CC.4 complexes

Purified CCHFV OTU was pooled with 2-3-fold molar excess of purified UbV and dialyzed overnight against 50 mM Tris pH 8.0, 150 mM NaCl and 2 mM DTT. Protein complexes were concentrated and loaded onto a Superdex 75 size exclusion column and eluted in 50 mM Tris, 150 mM NaCl and 2 mM DTT. For all samples, a single peak corresponding to the respective complex was observed in the gel filtration profile and two bands corresponding to the CCHFV OTU and respective UbV were observed by SDS-PAGE, indicating the high purity of

the complexes. The CCHFV OTU_{169}-CC.2 complex was concentrated to 12 mg/ml for crystallization trials, and initial crystals and crystalline material obtained from preliminary screens were used to prepare seed stocks for microseed matrix screening (353,354), which was set up for the hanging drop vapor diffusion method in 48-well VDX plates (Hampton Research) and carried out using conventional screens (Qiagen) at 4°C, with and without heterogeneous nucleation using 0.3-0.4 cm strands of human hair (355). Total drop volume was 2 µl containing equal volumes of the protein complex and the well solution. Crystals of the CCHFV OTU_{169}-CC.2 complex were grown in 30% (w/v) PEG 4000, 0.2 M $CaCl_2$ and 0.1 M HEPES pH 7.5 and appeared after 5-8 days.

The CCHFV OTU_{185}-CC.4 complex was concentrated to 23 mg/ml and initial leads were observed with a combinatorial approach using microseed matrix screening with crystallization screens (Qiagen) along with the Silver Bullets screen (Hampton Research) and micro-seeding using crystals of a CCHFV OTU_{185}-CC.5 (a weaker binding variant selected by phage display) complex. Using the hanging drop vapor diffusion method and 48-well VDX trays (Hampton Research), screens were set up at 20°C with a reservoir volume of 150 µl, and a drop size of 3.5 µl, which comprised of 1.5 µl of the protein complex, 1 µl of the reservoir solution and 1 µl of Silver Bullet additive, added in this order. Crystals were obtained with 25% (w/v) PEG 3350, 0.1 M Tris pH 7.0 and 0.2 M sodium chloride. The Silver Bullet formulation in the drop was as follows: 0.16% (w/v) each of 5-Sulfosalicylic acid dehydrate, dodecanedioic acid, hippuric acid, mellitic acid, oxalacetic acid, suberic acid and 0.02 M HEPES sodium pH 6.8.

6.2.8 X-ray data collection

6.2.8.1 MERS-CoV PL_{pro}-ME.2 and -ME.4 complexes

Crystals were harvested by sweeping through a cryoprotectant solution containing 0.1 M trisodium citrate pH 5.6, 22% (w/v) PEG 4000, 21% (v/v) 1,2-propanediol (PL^{pro}-ME.4), or harvested directly from the crystallization solution (PL^{pro}-ME.2) and flash-cooled in LN_2. X-ray diffraction data for PL^{pro}-ME.4 crystals were collected using a Rigaku 007HF MicroFocus X-ray generator and R-AXIS IV++ detector. PL^{pro}-ME.2 data collection was carried out at the Canadian Light Source on beamline 08B1-1. Diffraction data for the PL^{pro}-ME.4 and –ME.2 crystals were integrated and scaled using XDS (305), followed by merging using Aimless within the CCP4 software suite. Initial phase estimates were determined via molecular replacement (MR) within phenix.phaser using the previously determined MERS-CoV PL^{pro} domain (PDB ID: 4RF0) and a polyAla Ub model (PDB ID: 4RF0) as independent search models (307). Model building and refinement were performed using Coot and phenix.refine, respectively (309,310). Coordinate files and structure factors for MERS-CoV PL^{pro}-ME.2 and –ME.4 have been deposited to the Protein Data Bank under accession numbers 5V6A and 5V69, respectively.

6.2.8.2 CCHFV OTU_{169}-CC.2 and CCHFV OTU_{185}-CC.4 complexes

Single crystals of the CCHFV OTU_{169}-CC.2 and CCHFV OTU_{185}-CC.4 complexes were swept through cryoprotectant containing well solution supplemented with 20-30% ethylene glycol, and X-ray diffraction data were collected at the Canadian Light Source on beamline 08ID-1 at 100K. X-ray diffraction data were indexed and scaled using XDS (305) and merged with Aimless (356). Initial phases for the CCHFV OTU_{169}-CC.2 and CCHFV OTU_{185}-CC.4 complexes were determined by MR within phenix.phaser (307) using the previously reported

CCHFV OTU domain bound to Ub (PDB 3PT2) (105) as a search model. The structures of CC.2 and CC.4 bound to CCHFV OTU were subsequently modelled and refined into the MR maps using Coot (309) and phenix.refine, respectively (310). Coordinate files and structure factors for CCHFV OTU-CC.2 and –CC.4 have been deposited to the Protein Data Bank under accession numbers 5V5H and 5V5G, respectively.

6.2.9 Plasmids used for cell culture work

The following plasmids were described elsewhere or provided by others: pcDNA3.1-MERS-CoV-PL^{pro} WT and active site mutant C1592A (93), pCAGGS-HA-nsp3C-4-V5 (93), pcDNA-eGFP (99), pCAGGS- MAVS (provided by N. Frias-Staheli), pLuc-IFN-β (277) and pRL-TK (Promega). pcDNA3-HA-Ub was generated by cloning PCR-amplified Ub (using pCMV-FLAG-Ub (279) as a template) in pcDNA3.1(-) (Invitrogen) in frame with an N-terminal HA tag. Codon optimized SARS-CoV-PL^{pro} (amino acids 1541-1855 of the SARS-CoV pp1a/pp1ab (NCBI ID: AY291315.1)) with removed potential splice sites and polyadenylation signals (IDT) was cloned into pcDNA3.1(-) in frame with a C-terminal V5-tag generating pcDNA3.1(-)-SARS-CoV-PL^{pro}-V5. pcDNA3.1(-)-SARS-CoV-PL^{pro}-V5 was used as template for site-directed mutagenesis using the QuikChange^{TM} strategy (Stratagene using Accuzyme DNA polymerase from Bioline) to mutate the active site cysteine to alanine (Cys1651Ala).

In the UbV-containing pDONR-221 vectors (Thermo Fisher Scientific) a methionine was introduced before the already present N-terminal FLAG tag using the QuikChange^{TM} strategy. In pDONR-221-FLAG-Ub substitutions Gly75Ala+Gly76Ala were introduced in Ub to generate pDONR-221-FLAG-Ub.AA. FLAG-UbVs were cloned in destination vectors pcDNA3.1-DEST or pLenti6.3/TO/V5-DEST (Thermo Fisher Scientific) using the Gateway technology (Thermo Fisher Scientific). Primer sequences are available upon request.

6.2.10 Cell culture and antibodies

HEK293T were grown in Dulbecco's DMEM supplemented with 10% FCS (Bodinco BV), 100 units/ml penicillin, 100 units/ml streptomycin and 2 mM L-glutamine. Vero cells (Erasmus Medical Center) and MRC5 cells (ATCC CCL-171) were cultured in EMEM with 8% FCS, 100 units/ml penicillin and streptomycin, 2 mM L-glutamine and non-essential amino acids (PAA). HuH-7 cells were maintained in DMEM containing 8% FCS, antibiotics and non-essential amino acids. DMEM, EMEM and supplements were obtained from Lonza.

Proteins on Western blot were visualized using the following primary antibodies: mouse anti-FLAG (F3165; Sigma-Aldrich), mouse anti-V5 (37-7500; Invitrogen), mouse anti-HA (ab18181; Abcam), rabbit anti-GFP (99), rabbit anti-SARS-CoV nsp4 (357), rabbit anti-MERS-CoV p4b (358) and mouse anti-actin (A5316; Sigma-Aldrich). Primary antibodies were detected with HRP-conjugated secondary antibodies (P0447 and P0217; Dako). In an indirect immunofluorescence assay primary antibody mouse anti-FLAG (F3165; Sigma-Aldrich) and secondary antibody Alexa488-conjugated goat anti-mouse immunoglobulin G (IgG) antibody (A-11001; Thermo Fisher Scientific) were used.

6.2.11 Immunofluorescence detection of UbVs

HEK293T cells were transfected with FLAG-ME.1-4 using the calcium phosphate transfection method described previously (*5*), and fixed in 3% paraformaldehyde. Cells were then washed in phosphate buffered saline (PBS) + 10mM glycine, followed by incubation in PBS + 0.2% Triton X-100. Cells were then incubated for 1hr at RT with mouse anti-FLAG diluted in PBS + 5% BSA (1:1000), washed in PBS and incubated with donkey anti-mouse-Cy3 secondary antibody (1:1000) for 1hr at RT. Hoechst stain was used at a 1:100 dilution in order to visualize cellular nuclei.

6.2.12 Protease activity assays in cell culture

Protease activity assays as described in Bailey-Elkin et al. (93) were performed with slight modifications. Briefly, to assess the DUB activity of MERS-CoV PL^{pro} in the presence of UbVs, HEK293T cells were co-transfected using the calcium phosphate transfection method with plasmids encoding HA-tagged Ub (0.25 μg), MERS-CoV-PL^{pro}-V5 (0.2 μg), FLAG-tagged UbVs (0.5; 0.75 or 1 μg, as indicated) and GFP (0.25 μg). In order to establish whether the MERS-CoV-directed UbVs target SARS-CoV PL^{pro}, DUB assays were also performed with SARS-CoV-PL^{pro}-V5 (0.2 μg) instead of MERS-CoV-PL^{pro}-V5. The *in trans* cleavage activity of MERS-CoV PL^{pro} in the presence of UbVs was determined by co-expressing HA-nsp3C-4-V5 (0.2 μg), MERS-CoV-PL^{pro}-V5 (0.15 μg), FLAG-tagged UbVs (0.5; 0.75 or 1 μg) and GFP (0.25 μg) in HEK293T cells. Empty pcDNA vector was added to supplement to a total of 2 μg of plasmid DNA transfected per well of a 12-wells cluster. At 18 h post transfection, cells were lysed in 2xLSB containing 25 mM NEM (Sigma). Proteins were separated in an SDS-PAGE gel, blotted onto Hybond-P (0,45 μm pore size, GE-Heathcare) and visualized after antibody incubation steps using Pierce ECL 2 Western blotting substrate (Thermo Fisher Scientific). To visualize FLAG-tagged UbVs the proteins separated in an SDS-page gel were blotted onto 0,2 μm polyvinylidene fluoride (PVDF) membranes (GE-Heathcare). The membranes were blocked with dried milk powder in PBS containing 0,05% Tween-20 followed by antibody incubation steps.

6.2.13 Luciferase-based IFN-β reporter assay

In a luciferase-based IFN-β reporter assay the effect of the UbVs on the suppression of IFN-β promoter activity by viral PL^{pro}s was investigated. HEK293T cells grown to 80%

confluency in a 24-wells plate were co-transfected with a combination of plasmids encoding the firefly luciferase reporter gene under control of the IFN-β promoter (25 ng), *Renilla* luciferase (5 ng), innate immune inducer mitochondrial antiviral signalling protein (MAVS; 25 ng), MERS-CoV PL^{pro}-V5 (250 ng) and FLAG-tagged UbVs (250, 500, 750 ng). Alternatively, SARS-CoV PL^{pro}-V5 (100 ng) and FLAG-tagged UbVs (750 ng) were co-expressed with firefly luciferase under control of the IFN-β promoter, *Renilla* luciferase and MAVS. Total amounts of transfected DNA were equalized by the addition of empty pcDNA vector. Both firefly and *Renilla* luciferase activities were measured (Mithras LB 940 multimode reader; Berthold Technologies) using the Dual-Luciferase reporter assay system (Promega) 16 h post transfection. After normalizing the firefly luciferase activity to *Renilla* luciferase activity, an unpaired two-tailed Student's t test was performed and p values <0.05 were considered statistically significant. Firefly and *Renilla* luciferase activities were measured in triplicate and assays were repeated independently at least three times.

6.3 Results

6.3.1 Potent and selective UbV inhibitors of MERS-CoV and CCHFV vDUBs

The UbV library (193) was screened against the MERS-CoV PL^{pro} domain (MERS-CoV PL^{pro}) and the CCHFV OTU domain (CCHFV OTU). Within three weeks, UbVs were identified that bound with high affinity to either MERS-CoV PL^{pro} (ME.1 to ME.4) or CCHFV OTU (CC.1 to CC.5) (**Figure 6.1 A**). To confirm the specificity of the UbVs towards their cognate vDUBs, the phage-displayed UbVs were challenged against a diverse panel of 11 DUBs from several species representing distinct DUB families (USP, OTU, and UCH). All UbVs bound to their cognate viral proteins but not to any of the 11 additional DUBs (**Figure 6.1 B**). To determine the

binding affinity of each UbV, phage enzyme-linked immunosorbent assays (**Figure 6.2**) and Bio-Layer Interferometry (BLI) measurements were performed (**Table 6.1**). Each UbV was found to bind its cognate vDUB with affinities in the low to sub-nanomolar range, whereas wild-type Ub (Ub.wt) showed binding to MERS-CoV or CCHFV vDUBs only in the high micromolar range (**Figure 6.2 B**). Consistent with the high affinities observed for the UbVs toward their respective vDUBs, each UbV also potently inhibited the deubiquitinating and deISGylating activities of MERS-CoV PL^{pro} or CCHFV OTU as measured using the fluorogenic substrates Ub-AMC or ISG15-AMC, respectively (**Figure 6.1 C** and **Figure 6.3**). The most potent inhibitors of MERS-CoV PL^{pro} and CCHFV OTU were ME.4 (deubiquitination IC_{50} = 0.8 nM and deISGlyation IC_{50} = 1.2 nM) and CC.4 (deubiquitination IC_{50} = 3.3 nM and deISGlyation IC_{50} = 11 nM), respectively. Furthermore, the UbVs were confirmed to inhibit processing of Lys48- and Lys63-linked tetra-Ub substrates by their respective vDUBs (**Figure 6.1 D**).

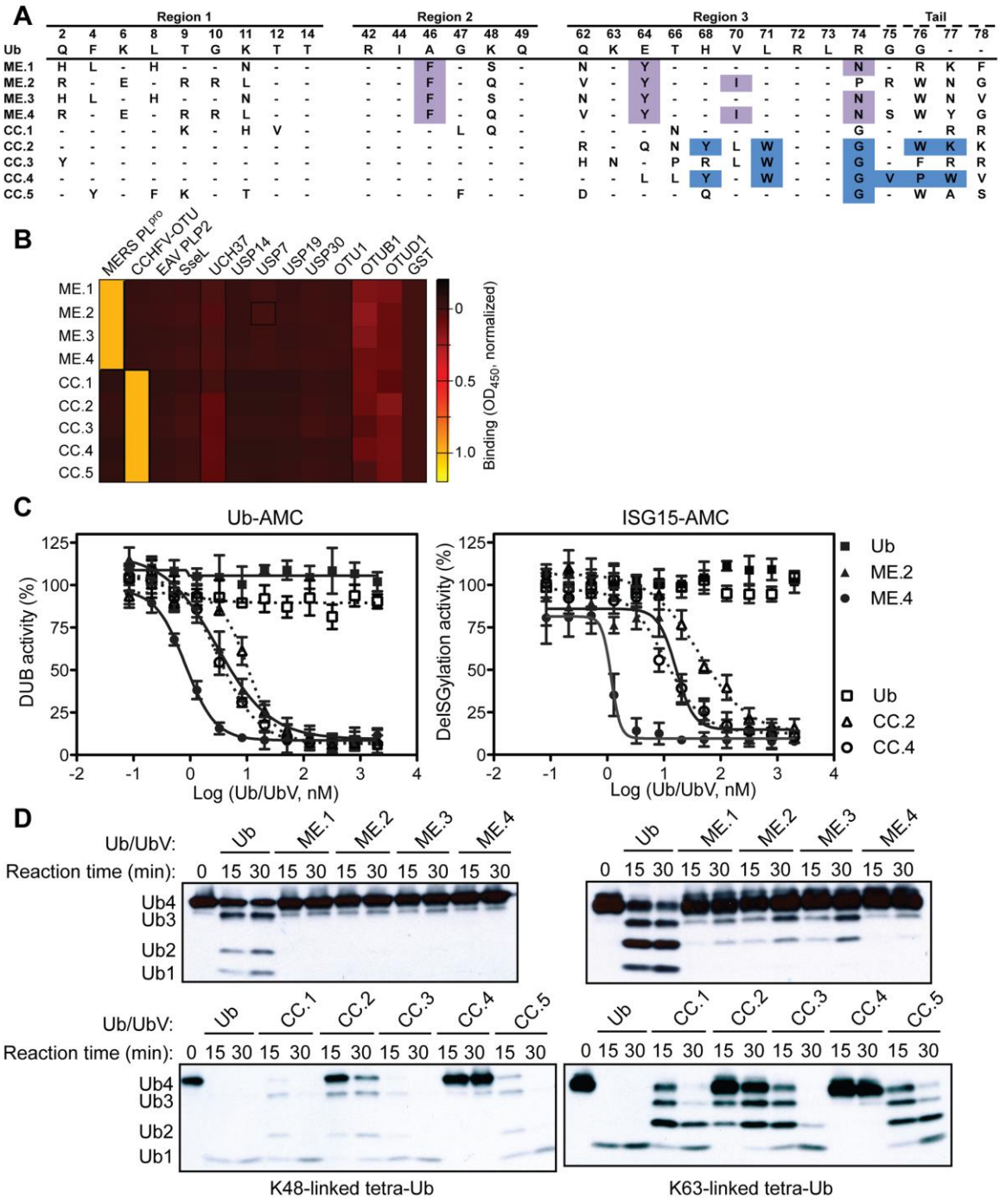

Figure 6.1 UbVs inhibit activity of MERS-CoV PL^{pro} and CCHFV OTU *in vitro*.
(A) Sequences of UbVs that bind MERS-CoV or CCHFV vDUBs. Only regions subjected to diversification relative to Ub.wt in the phage-displayed library are shown. Amino acids discussed in the text are highlighted. (B) The binding specificities of phage-displayed UbVs *(y-axis*) are shown across a group of 12 DUBs *(x-axis),* as assessed by phage ELISA. Sub-saturating concentrations of phage were added to immobilized proteins as indicated. Bound phages were

detected by the addition of anti-M13-HRP and colorimetric development of TMB peroxidase substrate. The mean value of absorbance at 450 nm is shaded in a black-red-yellow gradient. (C) Inhibition of MERS-CoV PL^{pro} (solid lines) or CCHFV OTU (dashed lines) by the cognate UbVs shown as dose-response curves using Ub-AMC (*left*) or ISG15-AMC (*right*) as a substrate. The IC_{50} value was determined as the concentration of UbV that reduced proteolytic activity by 50%. The Ub.wt data obtained in the deISGylation assay cannot be fitted by GraphPad Prism so no lines are shown. (D) Effects of UbV inhibitors on vDUB activity against Lys48/Lys63 tetra-Ub substrates. Purified MERS-CoV PL^{pro} (*top panels*) or CCHFV OTU (*bottom panels*) was incubated with the indicated UbV or Ub.wt (negative control) and biotinylated tetra-Ub at 37°C for a time course of 30 minutes. Western blots were probed with ExtrAvidin-HRP (EA-HRP) to detect biotin-Ub. Inhibition of proteolysis was shown by a delay of appearance of the digestion products tri-Ub (Ub3), di-Ub (Ub2) and mono-Ub (Ub1).

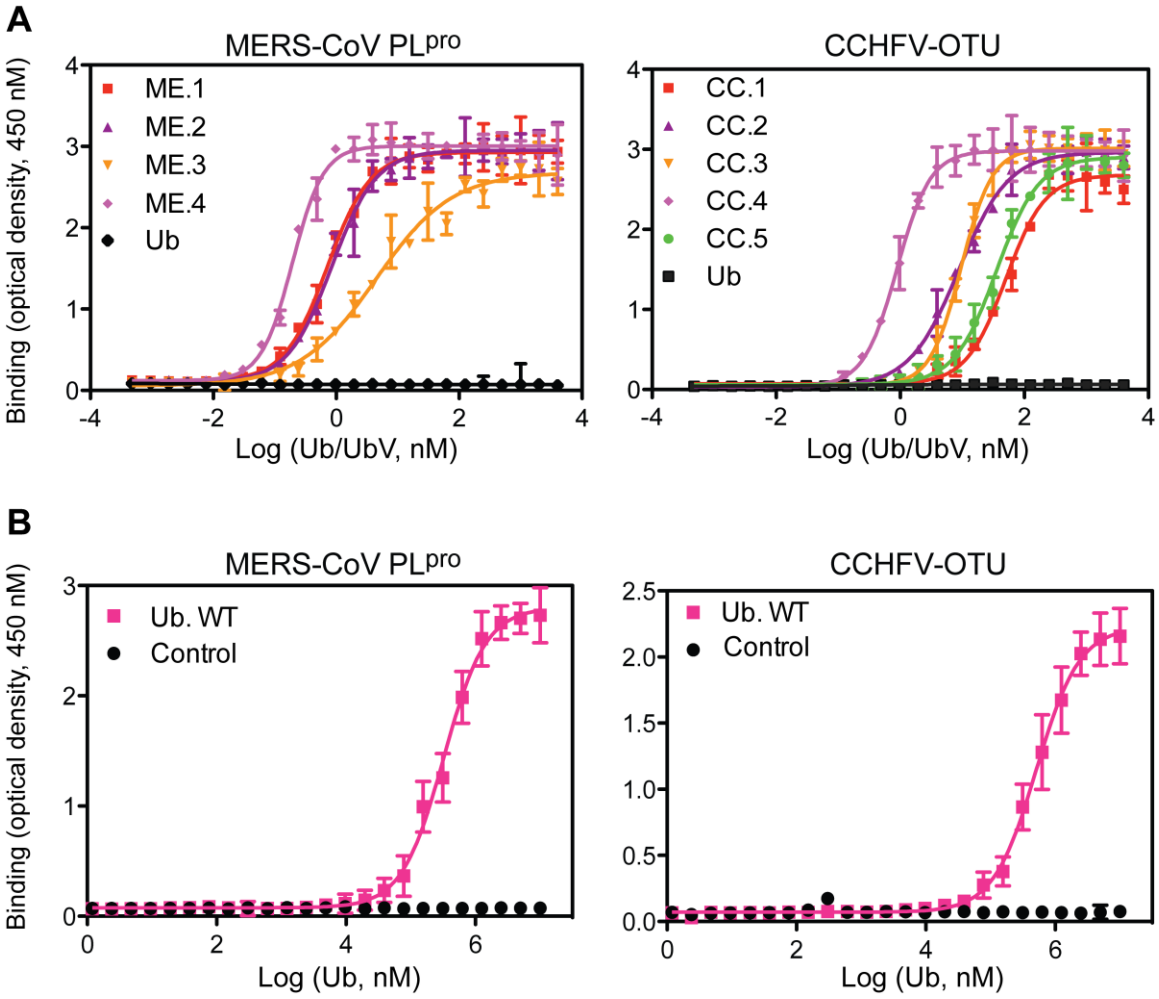

Figure 6.2 UbVs bound with high affinity to MERS-CoV PL^{pro} and CCHFV OTU.
(A) Binding curves of UbVs to the cognate viral proteases (left panel: MERS-CoV PL^{pro}; right panel: CCHFV OTU), measured by ELISA. The half maximal binding concentrations (EC_{50}) of UbVs to indicated vDUBs were determined by established methods (191). Viral proteases (1 μM) were immobilized in microtiter plates. Serial dilutions of FLAG-tagged UbV or Ub (up to 4 μM, 24 points) were added and incubated for 20 min at room temperature. Wells were washed and bound UbV/Ub was detected by anti-FLAG-HRP conjugate antibody and colorimetric development of TMB peroxidase substrate. The absorbance at 450 nm (y-axis) was plotted against Log (UbV/Ub concentration, nM) (x-axis). Data were presented as the mean ± SD (N = 3). (B) Binding curves of wild type Ub (Ub.wt) to MERS-CoV PL^{pro} (left) and CCHFV OTU (right). Experiments were performed as described in (A) except the concentration of Ub was increased (up to 10 mM, 24 serial dilutions). Data were presented as the mean ± SD (N = 3).

Table 6.1 Binding affinities of viral DUBs and UbVs evaluated by Bio-Layer Interferometry (BLI).

Ligands	Analytes	K_D
CCHFV-OTU	CC.1	463 ± 44.3 nM
	CC.2	158 ± 11.2 nM
	CC.3	453 ± 17.2 nM
	CC.4	9.0 ± 0.4 nM
	CC.5	10.4 ± 0.7 nM
	CC.4.4	no binding
	CC.4.5	no binding
MERS-CoV PLpro	ME.1	19.4 ± 0.7 nM
	ME.2	53.2 ± 2.2 nM
	ME.3	15.6 ± 0.4 nM
	ME.4	35.9 ± 1.6 nM
	ME.4.1	1030 ± 297 nM

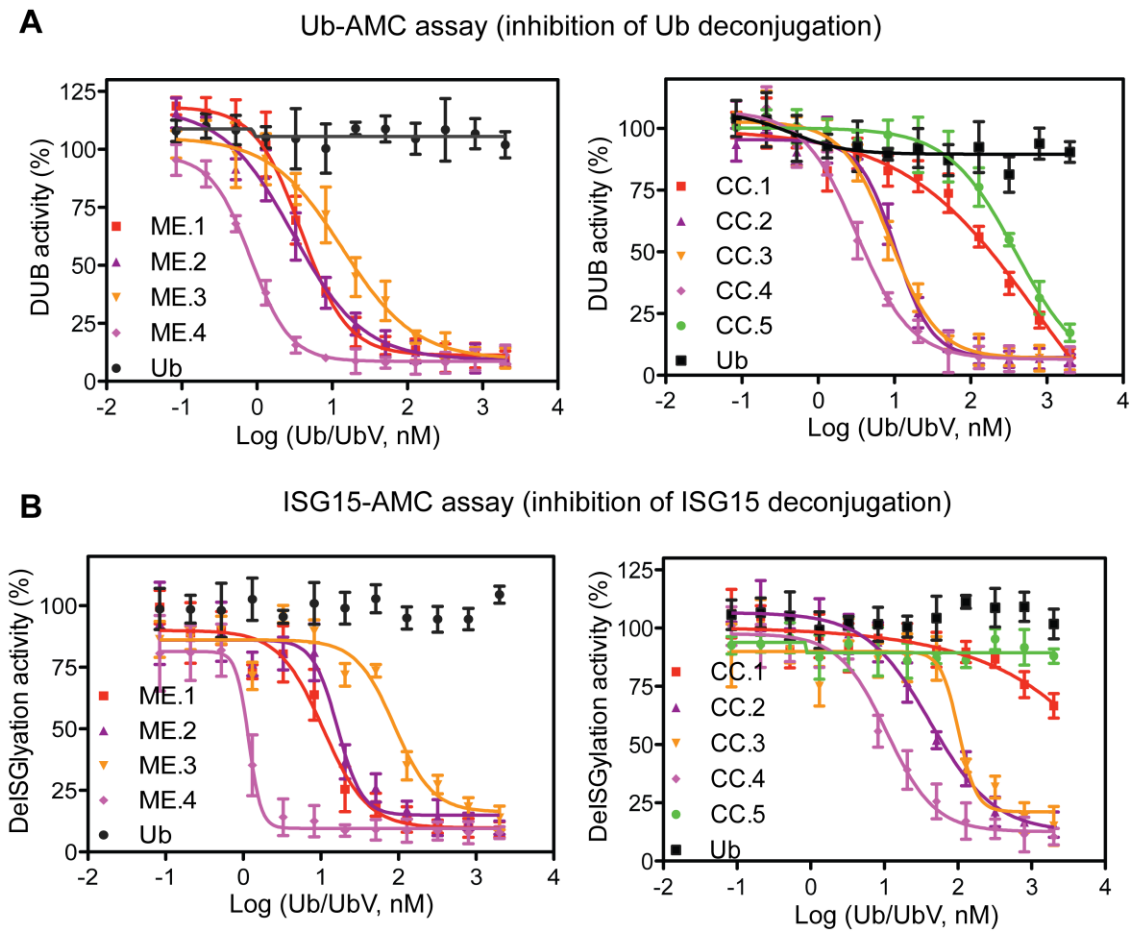

Figure 6.3 MERS-CoV PL^{pro} and CCHFV OTU are inhibited by UbVs in vitro.
(A-B) Inhibition of MERS-CoV PL^{pro} (left) or CCHFV OTU (right) by the cognate UbVs shown as dose-response curves using Ub-AMC (A) or ISG15-AMC (B) as a substrate. The IC_{50} values were determined as the concentrations of UbVs that reduced deubiquitination or deISGylation activity by 50%. The wt Ub data obtained in the deISGylation assay can not be fitted by GraphPad Prism so no lines were shown.

6.3.2 Structural basis for vDUB inhibition by UbVs

To reveal the molecular basis for the inhibition of MERS-CoV PL^{pro} by UbVs, crystal structures of the enzyme were determined bound to ME.2 or ME.4 (Figure 6.4 A,B and **Table 6.2**). Both UbVs bound in nearly identical orientations as Ub.wt (**Figure 6.4 C** and **Figure 6.5 A**) with interface surface areas of ~1000 $Å^2$ (93,359). Substitutions common to both ME.4 and ME.2 at positions 46, 64 and 70 (**Figure 6.1 A**) were found to promote more favorable hydrophobic interactions with the enzyme relative to Ub.wt. In comparison to Ub.wt residue Val70, UbV residue Ile70 extends further into a hydrophobic pocket of PL^{pro} formed by residues Thr1730* and Val1691* (*asterisks* denote amino acid numbering of MERS-CoV polyprotein) (**Figure 6.4 D**). UbV residue Phe46 inserts into a hydrophobic pocket formed by PL^{pro} residues Trp1668*, Glu1670*, Val1680*, Leu1682*, Tyr1690* and Tyr1705*, and forms a cation-π interaction with Arg1715* (**Figure 6.4 E**). These extensive interactions are not formed at the PL^{pro}-Ub.wt interface with the Ub.wt residue Ala46. In addition, UbV residue Tyr64 makes more extensive hydrophobic interactions with Val1706* and Gly1710*, compared to Ub.wt residue Glu64 **(Figure 6.4 F**). The UbVs also differ in their C-terminal residues at positions 74, 75 and 77 (**Figure 6.1 A**). In ME.4, Asn74 extends into the active site and forms a hydrogen bonding network with Asp1645* and Gly1758* (**Figure 6.4 G**), which mimics hydrogen bonds formed by the same region of MERS-CoV PL^{pro} with Ub.wt residues Arg74, Gly75 and Gly76 (**Figure 6.4 H**). In ME.2, Pro74 cannot form an analogous hydrogen bonding network, which likely contributes to the decreased inhibitory potency of ME.2 compared to ME.4 (**Figure 6.1 D** and **Figure 6.3 A,B**). Instead, Pro74 and the C-terminal tail are excluded from the active site and the main-chains interact through a hydrogen bond formed between the main-chain amide nitrogen of Arg75 and the backbone carbonyl of Glu1754* (**Figure 6.4 I**). A structural comparison of the C-

terminal regions of ME.2 and ME.4 near the PL^{pro} active site is shown in **Figure 6.6**. Additional substitutions in the N-terminal region of ME.4 and ME.2 (**Figure 6.1 A**, region 1) do not make favourable contacts with MERS-CoV PL^{pro}, and in fact, residues 8-10 and 7-10 of ME.4 and ME.2, respectively, failed to resolve in electron density maps (**Figure 6.7**). Taken together, our structural analyses revealed that a small subset of substitutions is sufficient to enhance hydrophobic packing and hydrogen bond networks to endow ME.4 and ME.2 with highly potent and specific inhibitory activity against MERS-CoV PL^{pro}.

Table 6.2 Crystallographic and refinement statistics for MERS CoV PL^{pro} bound to ubiquitin variants

Crystal	MERS-CoV PL^{pro}-ME.4	MERS-CoV PL^{pro}-ME.2
X-ray source	Rigaku R-AXIS IV++	CLS 08B1-1
Crystal geometry		
Space group	$C222_1$	$C222_1$
Unit cell (Å)	*a*=48.21 *b*=110.96 *c*=185.90; α=β=γ=90°	*a*=47.07 *b*=109.78 *c*=183.96; α=β=γ=90°
Crystallographic data		
Wavelength (Å)	1.5419	1.2811
Resolution range (Å)	47.64-2.55 (2.64-2.55) *	45.97-2.70 (2.80-2.70)
Total observations	53264 (5257)	57650 (5719)
Unique reflections	16565 (1629)	13337 (1291)
Multiplicity	3.2 (3.2)	4.3 (4.4)
Completeness (%)	99.0 (100)	98.7 (97.6)
R_{merge}	0.11 (0.63)	0.073 (0.68)
CC1/2	0.99 (0.68)	0.99 (0.88)
I/σI	10.9 (1.80)	16.69 (2.34)
Wilson B-factor ($Å^2$)	37.21	54.23
Refinement statistics		
Reflections in test set	1656 (163)	1267 (99)
Protein atoms	3042	2976
Zinc atoms	1	1
Solvent molecules	97	20
R_{work}/R_{free}	0.1972 / 0.2455	0.2169 / 0.2732
RMSDs		
Bond lengths/angles (Å/°)	0.002/0.49	0.001/0.41
Ramachandran plot		
Favored/allowed (%)	96/4	95/4.1
Average B factor ($Å^2$)	38.16	57.52
Macromolecules	38.22	57.36
Solvent	36.74	52.53

*Values in parentheses refer to the highest resolution shell

Table 6.3 Crystallographic and refinement statistics for CCHFV OTU bound to ubiquitin variants

Crystal	CCHFV OTU-CC.4	CCHFV OTU-CC.2
X-ray source	CLS 08ID-1	CLS 08ID-1
Crystal geometry		
Space group	$P4_32_12$	C2
Unit cell (Å)	$a=b=64.31$	$a=101.4$, $b=33.60$
	c=277.58	$c=71.25$
	α=β=γ=90°	$a=c=90°$, $\beta=96.51°$
Crystallographic data		
Wavelength (Å)	0.979	0.979
Resolution range (Å)	47.17-2.10 (2.10-2.16)	43.43-1.50 (1.53-1.50)
Total observations	209641 (17075)	141907 (6821)
Unique reflections	34979 (2828)	38017 (1876)
Multiplicity	6.0 (6.0)	3.7 (3.6)
Completeness (%)	99.5 (99.8)	98.7 (96.6)
R_{merge}	0.084 (0.89)	0.03 (0.62)
CC1/2	0.998 (0.926)	0.99 (0.79)
I/σI	12.2 (2.2)	18.7 (2.1)
Wilson B-factor ($Å^2$)	33.96	18.63
Refinement statistics		
Reflections in test set	1998 (197)	1999 (195)
Protein atoms	3878	1926
Zinc atoms		
Solvent molecules	212	223
R_{work}/R_{free}	0.1743 / 0.2291	0.1563 / 0.1775
RMSDs		
Bond lengths/angles (Å/°)	0.010/1.04	0.008/0.97
Ramachandran plot		
Favored/allowed (%)	98/2	100/0
Average B factor ($Å^2$)	40.59	28.27
Macromolecules	40.44	26.98
Solvent	43.57	38.29

*Values in parentheses refer to the highest resolution shell

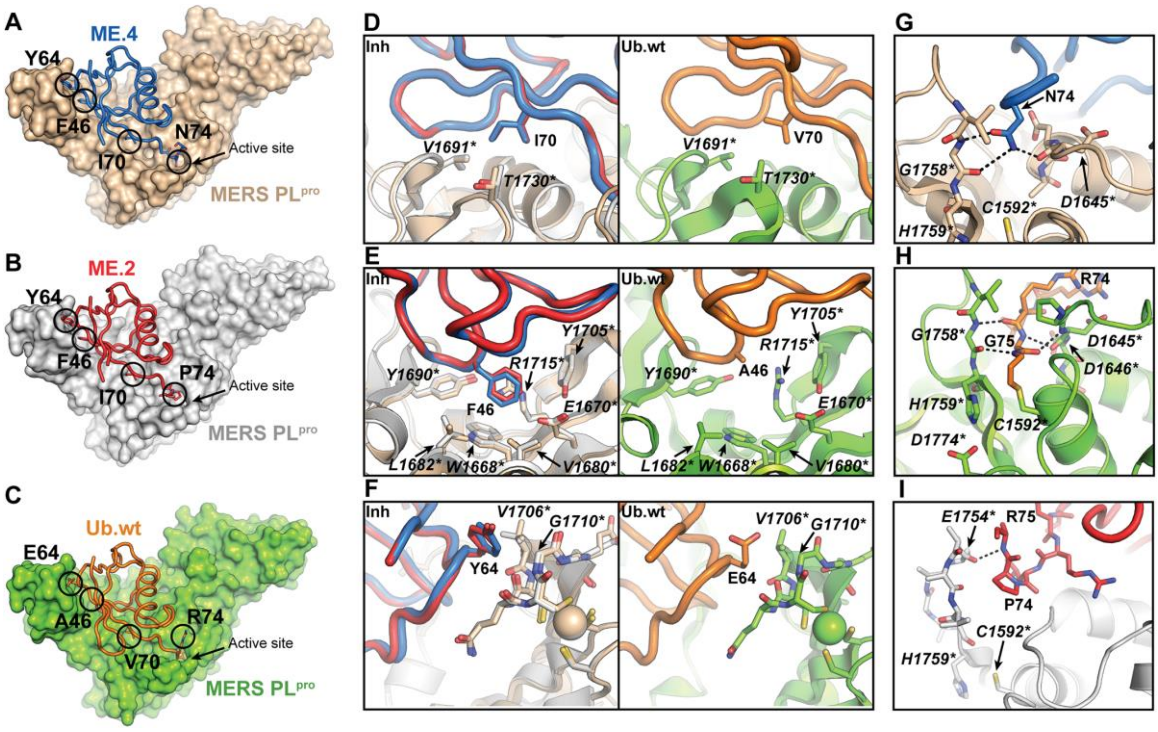

Figure 6.4 Structural basis for UbV inhibition of MERS-CoV PL^{pro}.
(A-C) Crystal structure of (A) the MERS-CoV PL^{pro}-ME.4 complex, (B) the MERS-CoV PL^{pro}-ME.2 complex, and (C) the MERS-CoV PL^{pro}-Ub.wt complex (PDB ID: 4RF0). PL^{pro} domains are shown as surface representations, and coloured in wheat, gray and chartreuse for the PL^{pro}-ME.4, -ME.2 and –Ub.wt complexes, respectively. ME.4, ME.2 and Ub.wt are shown as tubes and coloured in marine, red and orange, respectively. (D) Close up of a superposition of the MERS-CoV PL^{pro}-ME.4 and -ME.2 complexes (left panel) showing detailed interactions between PL^{pro} and residue Ile70 of ME.4 or ME.2, and a comparison (right panel) of the same region in the PL^{pro}-Ub.wt complex. PL^{pro} residues are shown as sticks and labelled with in italics with asterisks. (E) Close up of the MERS-CoV PL^{pro}-ME.4 and -ME.2 complexes (left panel) showing detailed interactions between PL^{pro} and residue Phe46 of ME.4 or ME.2, and a comparison (right panel) of the same region in the PL^{pro}-Ub.wt complex. (F) Close up of the MERS-CoV PL^{pro}-ME.4 and -ME.2 complexes (left panel) showing detailed interactions between PL^{pro} and residue Tyr64 of ME.4 or ME.2, and a comparison (right panel) of the same region in the PL^{pro}-Ub.wt complex. (G) Close up of ME.4 residue Asn74 bound near the active site of PL^{pro}. Hydrogen bonds are represented by dashed black lines. (H) Close up of the C-terminus of Ub.wt covalently bound in the active site of PL^{pro}. (I) Close up of ME.2 residue Pro^{74} bound near the active site of PL^{pro}. Figures were generated using PyMOL (16).

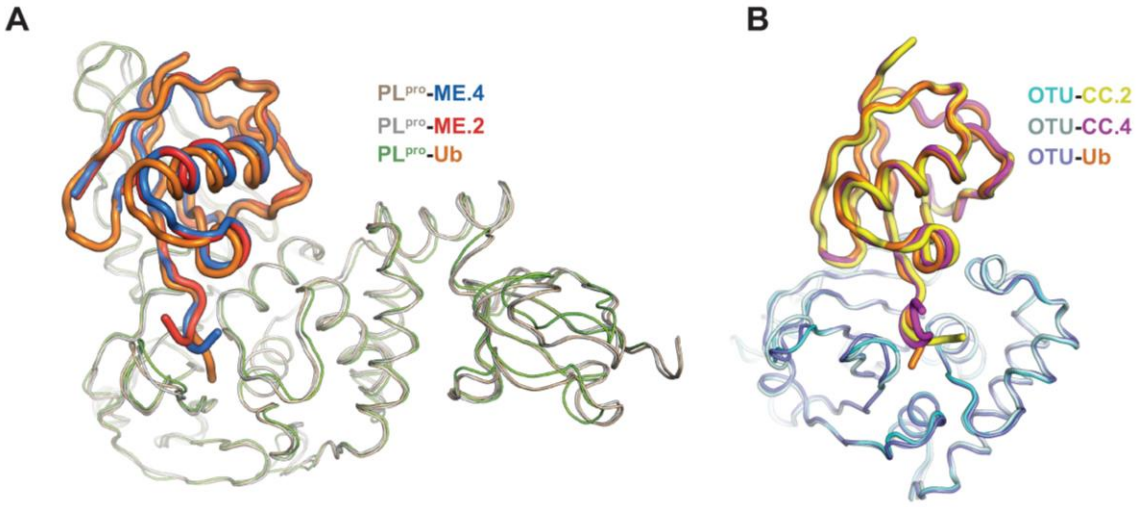

Figure 6.5 MERS-CoV- and CCHFV-specific UbVs bind their cognate DUBs in comparable orientations to Ub.wt.
(A) Superposition of the MERS-CoV PL^{pro}-Ub.wt, -ME.2 and -ME.4 complexes. PL^{pro} is displayed as ribbons, and coloured in chartreuse, gray and wheat in the PL^{pro}-Ub.wt, -ME.2 and -ME.4 structures, respectively. The Ub and UbV structures are displayed as tubes, and coloured in orange, red and marine in the PL^{pro}-Ub.wt, -ME.2 and -ME.4 structures, respectively. (B) Superposition of the CCHFV OTU-Ub.wt, -CC.2 and CC.4 complexes. CCHFV OTU is displayed as ribbons, and coloured in slate, cyan and pale cyan in the CCHFV OTU-Ub.wt, -CC.2 and -CC.4 structures, respectively. The Ub and UbV structures are displayed as tubes, and coloured in orange, yellow and magenta in the CCHFV OTU-Ub.wt, -CC.2 and -CC.4 structures, respectively. Structures were aligned within PyMOL (16).

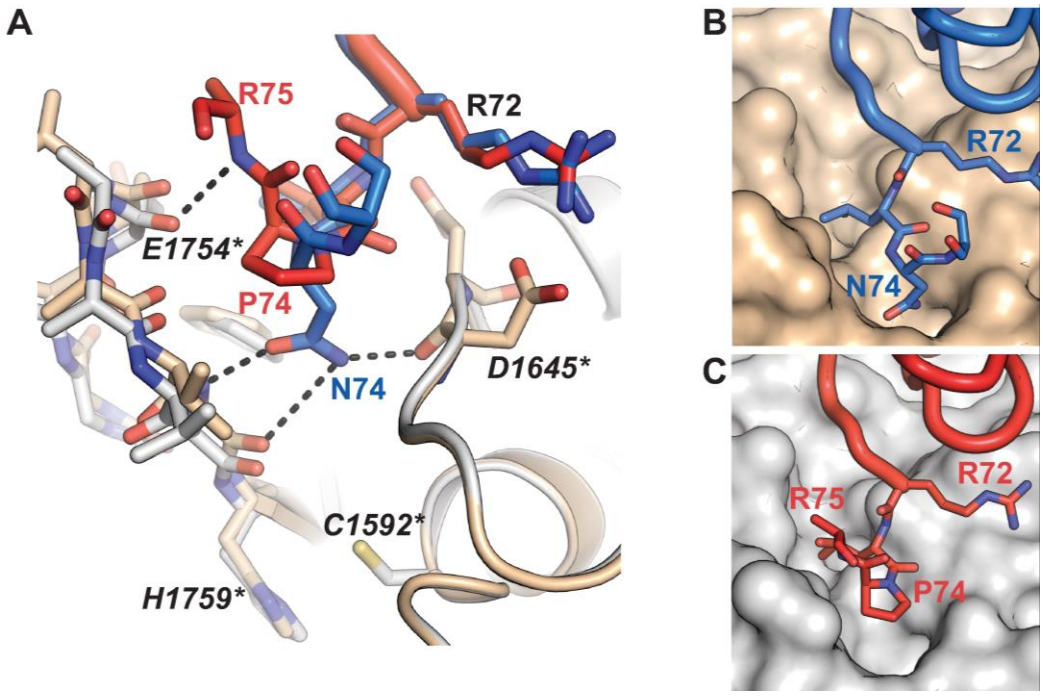

Figure 6.6 Comparison of the C-terminal regions of ME.2 and ME.4 in the active site of MERS-CoV PL^{pro}.

(A) Superposition of the C-terminal regions of the MERS-CoV PL^{pro}-ME.2 and –ME.4 structures. PL^{pro} is coloured in gray and wheat in the MERS-CoV PL^{pro}-ME.2 and –ME.4 structures, and ME.2 and ME.4 are coloured in red and marine, respectively. PL^{pro} active site residues His1759 and Cys1592 are shown as sticks, along with additional PL^{pro}, ME.2 and ME.4 residues involved in binding. (B) Close up of the C-terminus of ME.4 in the MERS-CoV PL^{pro}-ME.4 complex, with PL^{pro} depicted in a surface representation. (C) Close up of the C-terminus of ME.2 in the MERS-CoV PL^{pro}-ME.2 complex, with PL^{pro} depicted in a surface representation.

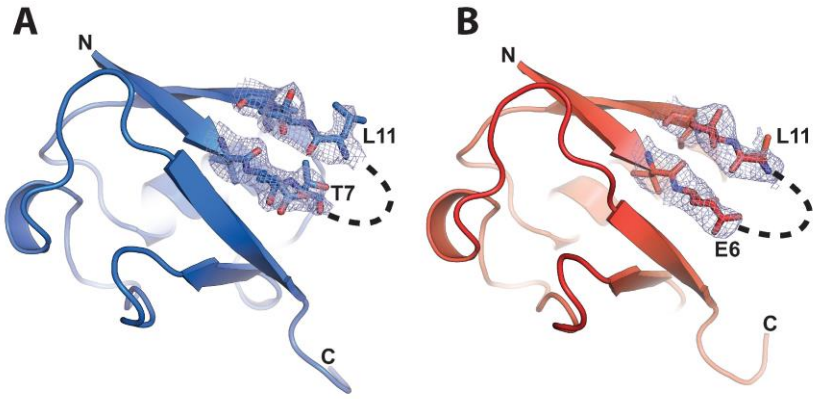

Figure 6.7 Residues in the N-terminal β-hairpin of ME.4 and ME.2 are disordered.
(A) Cartoon representation of ME.4 (marine). Dashed line indicates missing residues 8-10 which were not resolved in the electron density maps. A $2F_o$-F_c electron density map is displayed as blue mesh and contoured at 1.0 RMSD. (B) Cartoon representation of ME.2 (red). Dashed line indicates missing residues 7-10. Figure generated with PyMOL (16).

Similarly, crystal structures of CCHFV OTU were determined bound to CC.2 or CC.4 to gain insight into how they selectively block the DUB and deISGylating activities of the viral protease (**Figure 6.8 A,B** and **Table 6.3**). CC.2 and CC.4 were bound in the same orientation as Ub.wt with similar buried surface areas of ~1000 $Å^2$ (**Figure 6.8 C** and **Figure 6.5 B**) (105,106). Interestingly, substitutions in these UbVs were concentrated in the C-terminal region (**Figure 6.1 A**) and only substitutions at position 68 and downstream were found to interact with the enzyme. In both UbVs, Tyr68 improves hydrophobic packing with Thr10*, Val12* and Val18* (*asterisks* denote amino acid numbering of the large segment-encoded protein of CCHFV), relative to His68 in Ub.wt (**Figure 6.8 D**). In CC.2, residue Leu70 projects further into a hydrophobic cavity in CCHFV OTU formed by residues Val12*, Ile14*, Val18* and Ile131*, than does the equivalent Ub.wt residue Val70 (**Figure 6.8 E**). The conformational freedom of a Gly substitution at position 74 enables the C-terminal tail of each UbV to form numerous favorable interactions with the enzyme. Residues Gly75 and Val75 of CC.2 and CC.4, respectively, occupy space on the CCHFV OTU surface, which in the case of Ub.wt is occupied by the side-chain of Arg74 (**Figure 6.8 E-G**). This alternative conformation permitted by Gly74 in CC.2 and CC.4 allows the side-chain of Trp76 or Trp77 of CC.2 or CC.4, respectively, to pack within different adjacent grooves near the CCHFV OTU active site, with Trp76 of CC.2 forming a cation-π interaction with Arg92* (**Figure 6.8 E**), and the amide nitrogen group of CC.4 residue Trp77 forming a hydrogen bond with the side chain of Gln149* (**Figure 6.8 F**). Conversely, Trp71 in both CC.2 and CC.4 does not interact with CCHFV OTU, but instead packs into a hydrophobic cavity within each UbV (**Figure 6.8 E,F**). Differences between the orientations of the C-terminal tails of CC.2 and CC.4 arise from the variation at positions 75 and 76. In CC.4, residue Val75 packs against CCHFV OTU residue Trp99*, and Pro76 appears to restrict conformational

freedom and enable hydrophobic interactions with Trp99* and Thr150* (**Figure 6.8 F**). Together with the packing orientation of Trp77, these additional contacts likely account for the high binding affinity of CC.4 for CCHFV OTU (**Table 6.1**).

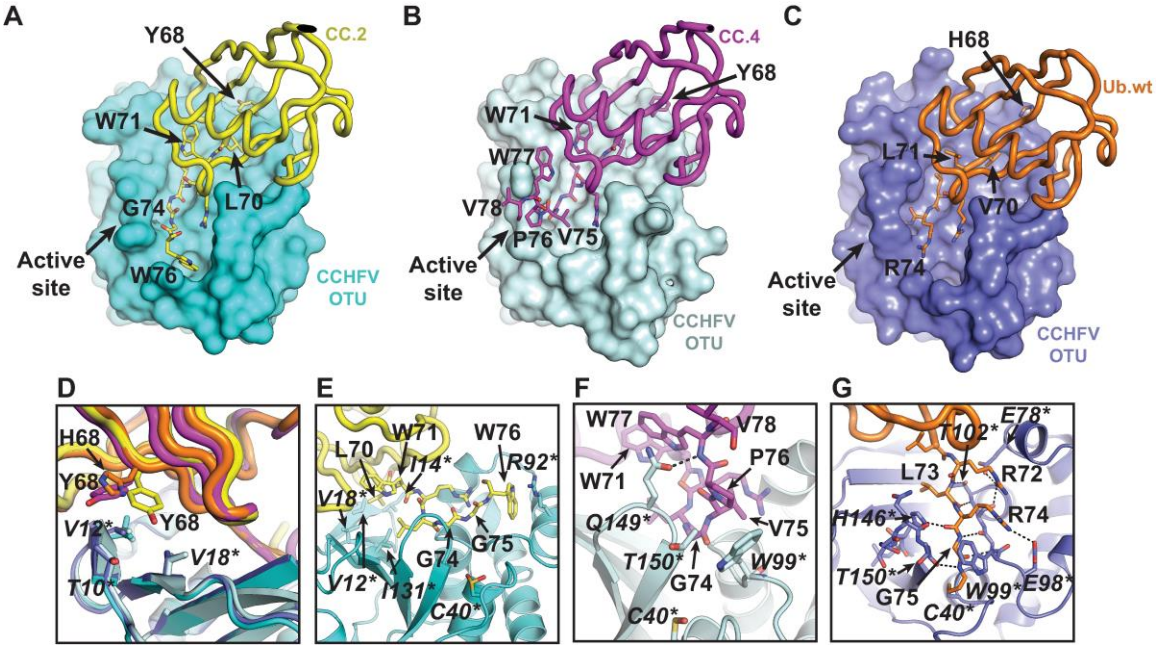

Figure 6.8 Structural basis for UbV inhibition of CCHFV OTU.
(A-C) Crystal structure of (A) the CCHFV OTU-CC.2 complex, (B) the CCHFV OTU-CC.4 complex, and (C) the CCHFV OTU-Ub.wt complex (PDB ID: 3PT2). OTU domains are shown as surface representations, and coloured in cyan, light cyan and slate for the OTU-CC.2, -CC.4 and –Ub.wt complexes, respectively. CC.2, CC.4 and Ub.wt are shown as tubes and coloured in yellow, magenta and orange, respectively. (D) Overlay of the CCHFV OTU-CC.2, CC.4 and –Ub.wt structures showing interactions between CCHFV OTU and CC.2 or CC.4 residue Tyr68 or Ub.wt residue His^{68}. UbV and Ub.wt residues are shown as sticks and labelled in regular font. CCHFV OTU residues are shown as sticks and labelled in italics with asterisks. (E) Close up of interactions between the C-terminus of CC.2 and CCHFV OTU. (F) Close up of interactions between the C-terminus of CC.4 and CCHFV OTU. (G) Close up of interactions between the C-terminus of Ub.wt and the active site of CCHFV OTU. Figures were generated using PyMOL (16).

6.3.3 UbVs inhibit MERS-CoV PL^{pro} activity in cell culture assays

During my visit at the LUMC with the help of Robert Knaap, we generated the preliminary results showing that the UbVs expressed in cell culture (**Figure 6.9**), and that ME.1 and ME.4 inhibited global DUB activity of MERS-CoV PL^{pro}, but did not inhibit the DUB activity of EAV PLP2 (**Figure 6.10**). Further, we demonstrated that ME.1 and ME.4 inhibited IFN-β promoter activity in a dose-dependent manner (**Figure 6.11**). These preliminary findings provided proof-of-principal for the feasibility of inhibiting the DUB activity of PL^{pro} in cell culture using MERS-CoV-specific UbVs. The assays were subsequently optimized and repeated by Robert Knaap as described in the following paragraph. These results appear in **Figure 6.12**.

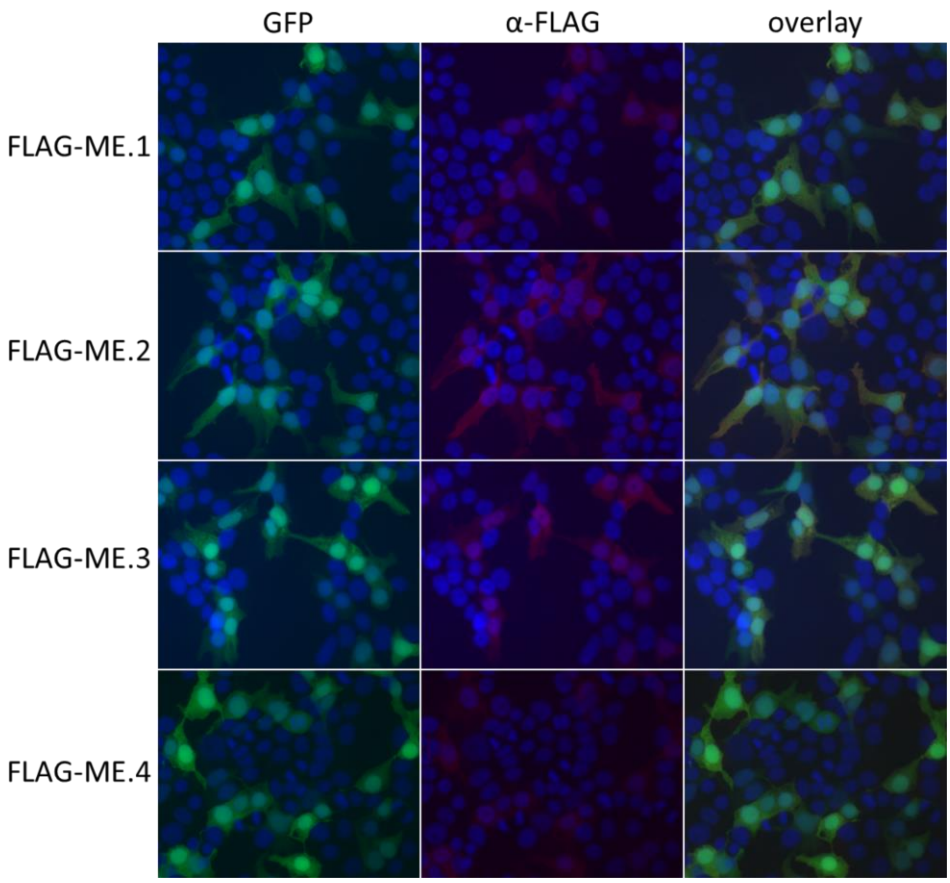

Figure 6.9 Immunofluorescence detection of MERS-CoV PL^{pro} UbVs in HEK293T cells. FLAG-tagged UbVs were stained with α-FLAG-Cy3 conjugated antibody following transfection with plasmid pCMV encoding the indicated UbVs, and visualized via confocal microscopy using a Cy3 filter.

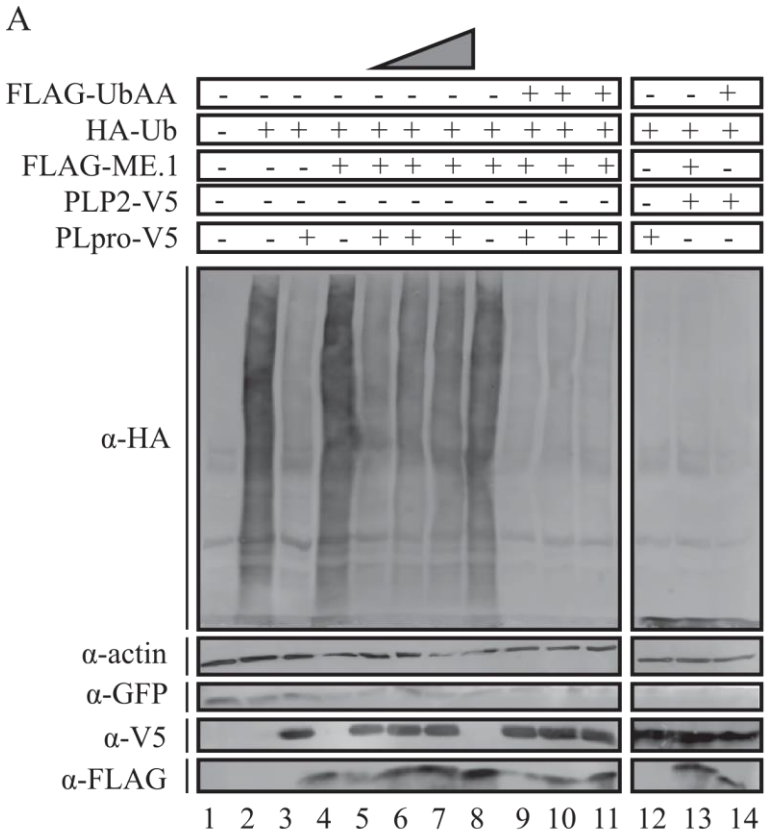
A
FLAG-UbAA
HA-Ub
FLAG-ME.1
PLP2-V5
PLpro-V5
α-HA
α-actin
α-GFP
α-V5
α-FLAG
1 2 3 4 5 6 7 8 9 10 11 12 13 14

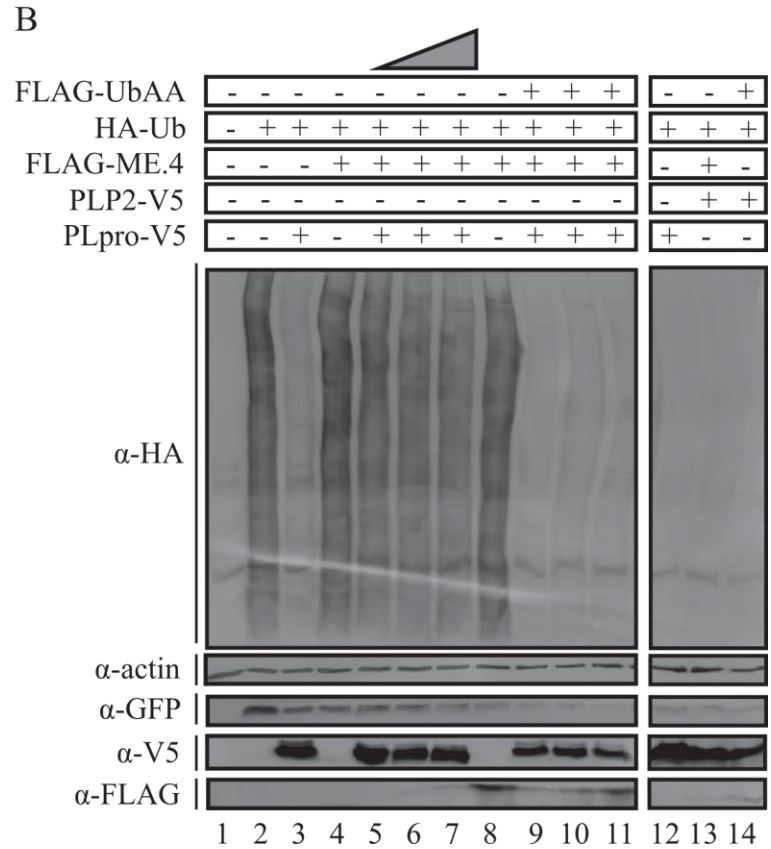
B
FLAG-UbAA
HA-Ub
FLAG-ME.4
PLP2-V5
PLpro-V5
α-HA
α-actin
α-GFP
α-V5
α-FLAG
1 2 3 4 5 6 7 8 9 10 11 12 13 14

Figure 6.10 PL^{pro}-specific UbVs ME.1 and ME.4 inhibit deubiquitination of cellular proteins. (A) Western blot analysis of MERS-CoV PL^{pro} DUB activity in the presence of ME.1. HEK293T cells were transfected with plasmids encoding the indicated constructs. Increasing concentrations plasmid encoding either ME.1 (lanes 5-7) or UbAA (lanes 9-11) are indicated (500, 1000 and 1500 ng). ME.1 was transfected in the presence of EAV PLP2 (lane 13). Global cellular conjugates of HA-tagged Ub are visualized as a smear. (B) Western blot analysis of MERS-CoV PL^{pro} DUB activity in the presence of ME.4.

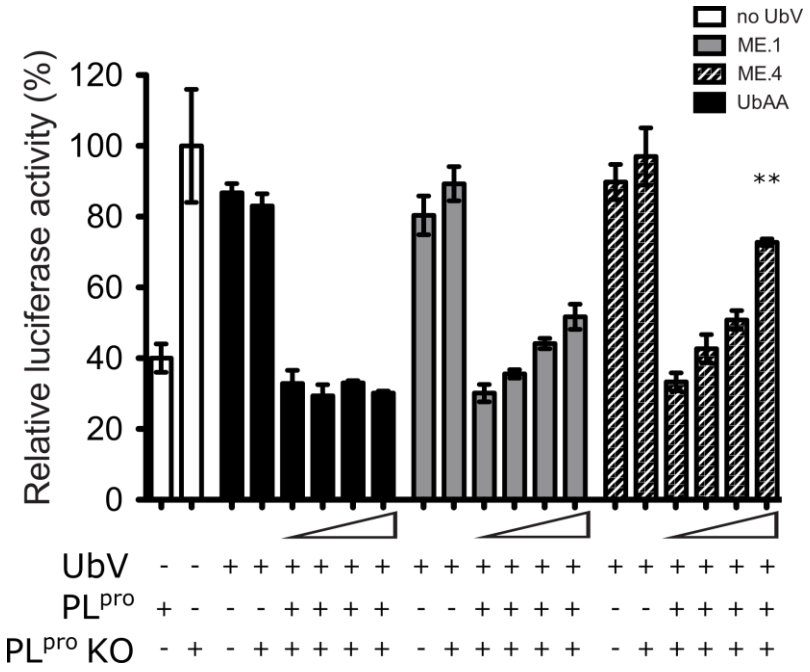

Figure 6.11 IFN-β promoter activity in HEK293T cells in the presence of MERS-CoV PL^{pro} and increasing concentrations of ME.1 and ME.4.
Cells were transfected with plasmid encoding the firefly luciferase gene under control of the IFN-β promoter, MERS-CoV PL^{pro} and varying concentrations of plasmid encoding ME.1 or ME.4. Innate immune response signaling was induced with plasmid encoding constitutively active MAVS. PL^{pro} KO indicates the Cys1592Ala catalytic knockout. Significance relative to wild-type without expression of a UbV was calculated using an unpaired two-tailed Student's *t* test and significant values are indicated: ** $p < 0.01$. *Bars* represent mean and *error bars* represent S.D. Luciferase activity was calculated relative to PL^{pro} KO, which was taken as 100%.

To explore the effects of UbVs on MERS-CoV PL^{pro} activity in cells, deubiquitination assays were performed by transfecting cells with combinations of plasmids encoding the following proteins: HA-tagged Ub (which becomes conjugated to cellular proteins), MERS-CoV PL^{pro}, and UbVs (which are unconjugatable due to substitutions in the C-terminal di-Gly motif). A clear decrease of cellular HA-Ub conjugates was observed during co-expression of MERS-CoV PL^{pro}, while there was no effect upon expression of a catalytically inactive mutant (**Figure 6.12 A,** compare lanes 3 and 4). The co-expression of increasing doses of different UbVs attenuated MERS-CoV PL^{pro} DUB activity to varying degrees (**Figure 6.12 A** and **Figure 6.13 A**). In a dose-dependent manner, ME.4 co-expression resulted in severe inhibition of HA-Ub deconjugation mediated by MERS-CoV PL^{pro}, whereas co-expression of an unconjugatable form of Ub.wt as a negative control (Ub.AA, which contains Gly75Ala and Gly76Ala substitutions) had no effect on the DUB activity of MERS-CoV PL^{pro} at any dose (**Figure 6.12 A,** compare lanes 5-7 to 8-10). Like ME.4, ME.2 had a strong effect resulting in near complete inhibition of MERS-CoV PL^{pro} DUB activity at the lowest UbV dose, whereas the inhibitory effect of ME.1 and ME.3 was apparent only at higher UbV doses (**Figure 6.13 A**). Notably, none of the UbVs inhibited the DUB activity of the closely related SARS-CoV PL^{pro}, highlighting their specificity for MERS-CoV PL^{pro} (**Figure 6.14 A**). A superposition of ME.4 onto the Ub domain of a previously determined SARS-CoV-Ub complex suggests that Phe^{46} and Ile^{70} of ME.4 clash with Val^{188*} and Met^{209*} of SARS-CoV PL^{pro}, respectively, and offers a plausible explanation for the specificity of ME.2 and ME.4 toward MERS-COV PL^{pro} (**Figure 6.15**).

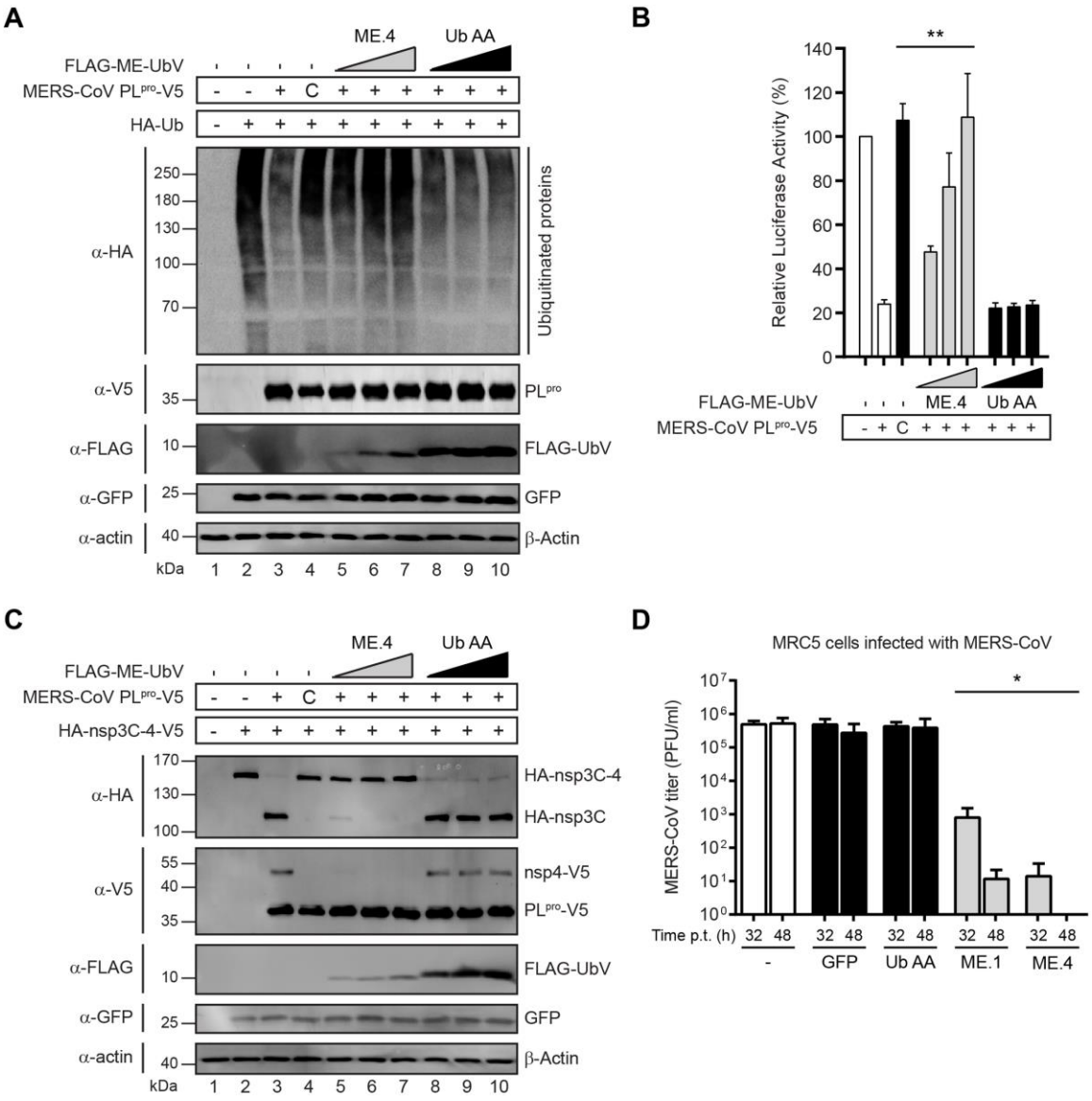

Figure 6.12 UbVs inhibit proteolytic activity of MERS-CoV PL^{pro} in cell culture and affect MERS-CoV replication.

(A) The effects of UbVs on the DUB activity of MERS-CoV PL^{pro} was determined by co-transfecting HEK293T cells with plasmids encoding HA-Ub, MERS-CoV PL^{pro}-V5 (wild type or the active site mutant Cys1592Ala annotated as "C" throughout the rest of the figure), FLAG-ME-UbV as indicated (in increasing dose) and GFP (as a transfection control). Cells were lysed 18 hours post transfection and expressed proteins were analyzed by western blotting. DUB activity of MERS-CoV PL^{pro} was visualized by the deconjugation of HA-Ub from cellular proteins. (B) Assessment of the inhibitory effects of UbVs on the suppression of the IFN-β promoter by MERS-CoV PL^{pro}. HEK293T cells were transfected with plasmids encoding firefly luciferase reporter gene under control of the IFN-β promoter, *Renilla* luciferase, innate immune

response inducer mitochondrial antiviral signaling protein (MAVS), MERS-CoV PL^{pro}-V5 (wild type or the active site mutant C) and FLAG-tagged UbVs (in increasing dose). Cells were lysed 16 hours post transfection and both firefly and *Renilla* luciferase activities were measured. Results represent at least three independent experiments. Significance relative to wild-type without expression of a UbV was calculated using an unpaired two-tailed Student's *t* test and significant values were indicated: ** $p < 0.01$. *Bars* represent mean and *error bars* represent S.D. (C) Proteolytic cleavage capability of MERS-CoV PL^{pro} was assessed in the presence of the UbVs. N-terminally HA-tagged and C-terminally V5-tagged nsp3C-4 (excluding the PL^{pro} domain) was co-expressed with V5-tagged MERS-CoV PL^{pro}-V5 (wild type or the active site mutant C), FLAG-ME-UbV (with increasing doses) and GFP (as a transfection control). Cells were lysed 18 hours post transfection and proteolytic cleavage activity was assessed by western blotting to detect generation of N-terminal HA-tagged nsp3C and C-terminal V5-tagged nsp4 cleavage products. (D) MERS-CoV titers of collected supernatants from lentivirus transduced and, subsequently, MERS-CoV infected MRC5 cells. MRC-5 cells were transduced with lentiviruses encoding FLAG-UbVs, FLAG-Ub.AA or GFP (latter two as controls) and, either 32 hours or 48 hours post-transduction, the cells were infected with MERS-CoV at a multiplicity of infection of 0.01. After another 32 hours, culture supernatants were harvested and MERS-CoV titers were determined by plaque assays on Vero cells. Significant difference relative to MERS-CoV titers from lentivirus transduced MRC5 cells expressing Ub.AA is indicated: * $p < 0.05$. *Bars* represent mean and *error bars* represent S.D.

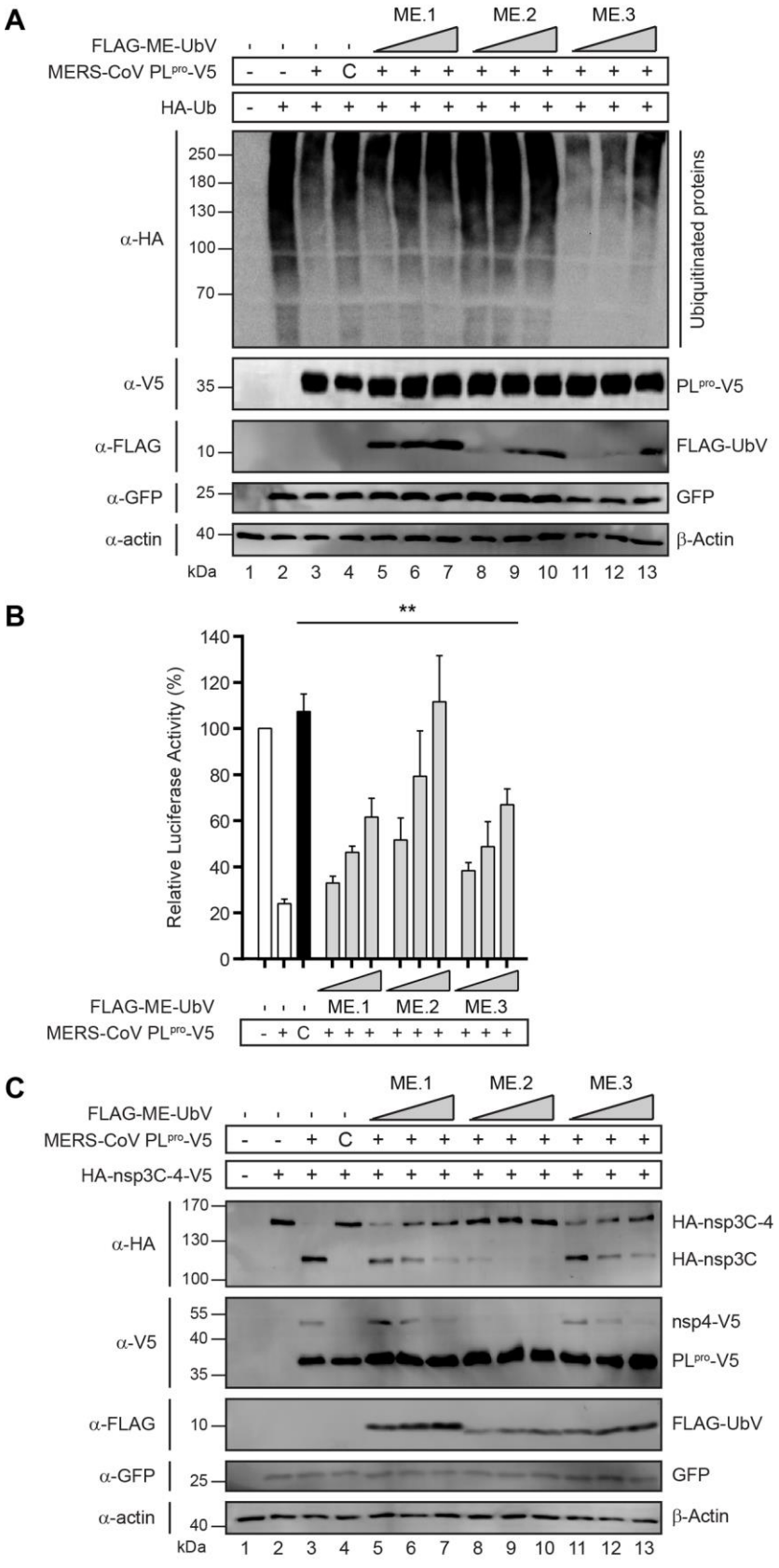
A
ME.1
ME.2
ME.3
FLAG-ME-UbV
MERS-CoV PLpro-V5
HA-Ub
α-HA
Ubiquitinated proteins
α-V5
PLpro-V5
α-FLAG
FLAG-UbV
α-GFP
GFP
α-actin
β-Actin
kDa
B
**
Relative Luciferase Activity (%)
C
HA-nsp3C-4-V5
HA-nsp3C-4
HA-nsp3C
nsp4-V5

Figure 6.13 Proteolytic activity of MERS-CoV PL^{pro} is inhibited by UbVs.
(A) Inhibition of MERS-CoV PL^{pro} DUB activity by ME.1, ME.2 and ME.3 was determined by expressing HA-Ub, MERS-CoV PL^{pro}-V5 (wild type or the active site mutant Cys1592Ala designated as C), FLAG-ME-UbV (500, 750 or 1000 ng of the appropriate plasmid) and GFP (as a transfection control) in HEK293T cells. After obtaining protein lysates the expressed proteins were separated on a SDS-PAGE gel, blotted and visualized after antibody incubations. (B) Suppression of the IFN-β promoter activity by MERS-CoV PL^{pro} in the presence of UbVs was assessed by transfecting plasmids encoding firefly luciferase reporter gene under control of the IFN-β promoter, *Renilla* luciferase, MAVS, MERS-CoV PL^{pro}-V5 (wild type or the active site mutant C) and FLAG-tagged UbVs (250, 500 or 750 ng). Firefly and *Renilla* luciferase activities were measured 16 h post transfection and significance relative to wild-type without expression of a UbV was calculated using an unpaired two-tailed Student's *t* test. Significant values were indicated: ** $p < 0.01$. *Bars* represent mean and *error bars* represent S.D (N=3). (C) Proteolytic cleavage capability of MERS-CoV PL^{pro} was assessed in the presence of the UbVs. N-terminally HA-tagged and C-terminally V5-tagged nsp3C-4 (a polyprotein fragment excluding PL^{pro}) was co-expressed with MERS-CoV PL^{pro}-V5 (wild type or the active site mutant C), FLAG-ME-UbV (at increasing concentrations) and GFP (as a transfection control). Cells were lysed 18 h post-transfection and expressed proteins were analyzed by Western blotting.

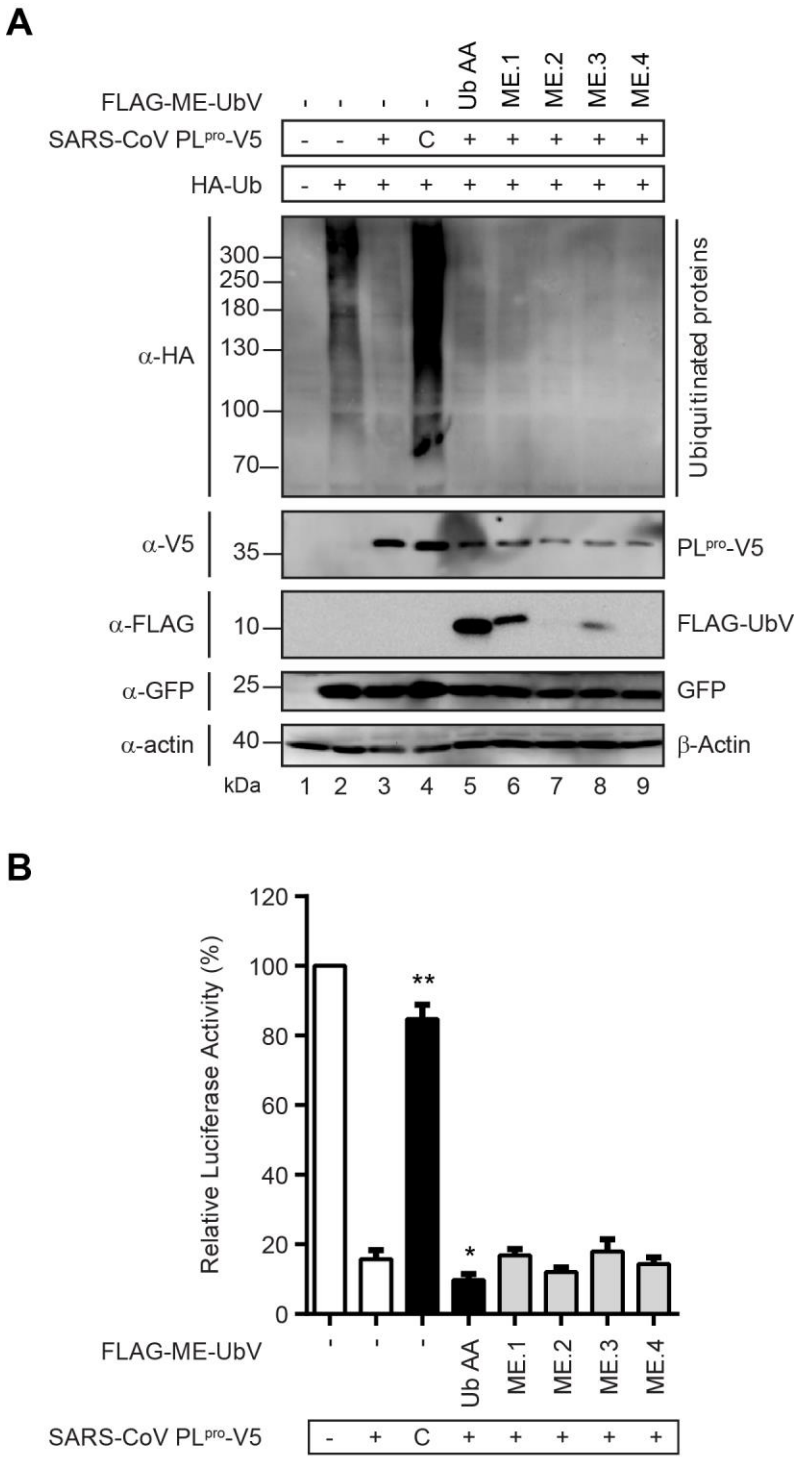

Figure 6.14 MERS-CoV-directed UbVs do not inhibit the DUB activity of SARS-CoV PL^{pro}. (A) SARS-CoV PL^{pro}'s DUB activity in the presence of UbVs was determined by co-transfecting HEK293T cells with plasmids encoding HA-Ub, SARS-CoV PL^{pro}-V5 (wild type or the active site mutant Cys1651Ala designated as C), FLAG-ME-UbV (1000 ng) and GFP (as a transfection control). 18 h post-transfection cells were lysed and deconjugation of HA-tagged Ub by SARS-

CoV PL^{pro} was visualized via Western blotting. (B) HEK293T cells were transfected with plasmids encoding firefly luciferase reporter gene under control of the IFN-β promoter, *Renilla* luciferase, MAVS, SARS-CoV PL^{pro}-V5 (wild type or the active site mutant C; 100 ng) and FLAG-tagged UbVs (750 ng). Cells were lysed 16 h post-transfection and both firefly and *Renilla* luciferase activities were measured. Significance relative to wild-type without expression of a UbV was measured using an unpaired two-tailed Student's *t* test; significant values were indicated: ** $p < 0.01$. *Bars* represent mean and *error bars* represent S.D (N=3).

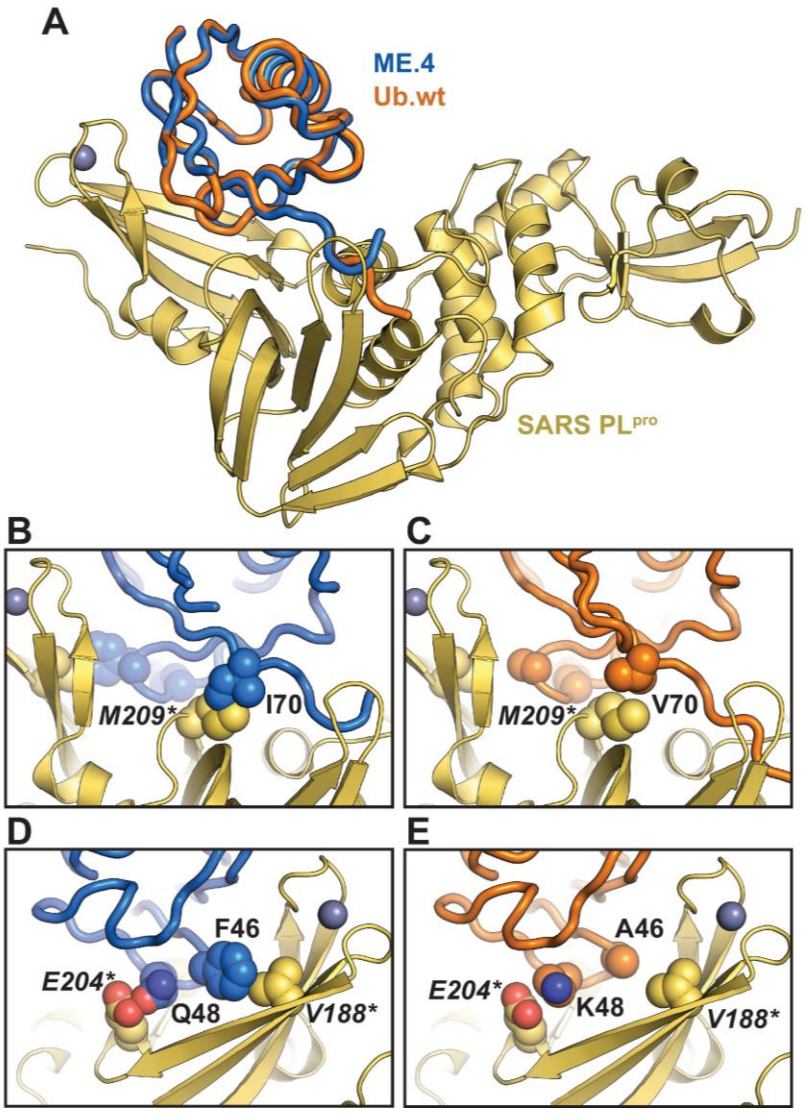

Figure 6.15 Structural model of the SARS-CoV PL^{pro} domain bound to the MERS-CoV PL^{pro}-specific ME.4.
(A) The SARS-CoV PL^{pro} domain is shown as a cartoon representation (yellow-orange). ME.4 and Ub.wt are shown in tubes (marine and orange, respectively). The ME.4 structure determined herein was superposed over Ub bound to the SARS-CoV PL^{pro} domain (4M0W (166)) (B) Close-up of residue clashes occurring between SARS-CoV PL^{pro} and ME.4. Residues are shown as spheres, with SARS-CoV PL^{pro} residues indicated with asterisks and in italics. SARS-CoV PL^{pro} residue Met209 clashed with ME.4 residue Ile70, compared with Ub residue Val70 (C). (D) SARS-CoV PL^{pro} residues Glu204 and Val188 clash with ME.4 residues Gln48 and Val188, respectively, compared to Ub.wt residues Lys48 and Ala46 (E). Figure generated in PyMOL (16).

We previously found that the DUB activity of MERS-CoV PL^{pro} suppresses IFN-β promoter activity upon activation of cellular innate immune signaling (93). In a luciferase-based IFN-β reporter assay we show that ectopically expressed UbVs competed with endogenous Ub for binding to MERS-CoV PL^{pro} resulting in an alleviated suppression of the IFN-β promoter activity (**Figure 6.12 B** and **Figure 6.13 B**). Consistent with described binding and inhibition data, ME.2 and ME.4 were more potent than ME.1 and ME.3 at blocking the ability of MERS-CoV PL^{pro} to suppress IFN-β promoter activation, whereas none of the UbVs were able to block suppression of the IFN-β promoter activity by SARS-CoV PL^{pro} (**Figure 6.14 B**). The UbVs thus prevented MERS-CoV PL^{pro}-mediated suppression of cellular anti-viral innate immune responses, and in a remarkably selective, virus-specific manner.A critical step in the replication cycle of MERS-CoV is the processing of viral polyproteins into functional non-structural proteins (nsps) that is accomplished in part by the protease activity of PL^{pro}, which cleaves the nsp1↓2, nsp2↓3, and nsp3↓4 junctions (183). In order to assess the ability of UbVs to inhibit MERS-CoV PL^{pro}-mediated polyprotein processing activity, an *in trans* cleavage assay was performed (93). FLAG-tagged UbVs and V5-tagged MERS-CoV PL^{pro} were co-expressed with N-terminally HA-tagged and C-terminally V5-tagged nsp3C-4 (HA-nsp3C-4-V5), a fragment of the viral polyprotein encompassing the C-terminal part of nsp3 (excluding the PL^{pro} domain) and nsp4. *In trans* cleavage of the nsp3↓4 junction is indicative of proteolytic activity of PL^{pro} during infection (93). MERS-CoV PL^{pro} efficiently cleaved HA-nsp3C-4-V5 into HA-nsp3C and nsp4-V5 products, whereas the active site mutant did not (**Figure 6.12 C,** compare lanes 3 and 4). The cleavage of the nsp3↓4 site was not affected upon expression of the negative control Ub.AA, whereas only a fraction of HA-nsp3C-4-V5 was cleaved upon expression of ME.4 or ME.2 at the lowest dose, and cleavage was completely blocked at higher UbV doses (**Figure 6.12 C** compare

lanes 5-7 to 8-10, **Figure 6.13 C**). Increasing doses of ME.1 and ME.3 also resulted in reduced cleavage as gradually more HA-nsp3C-4-V5 precursor was observed (**Figure 6.13 C**).

6.3.4 UbVs block MERS-CoV replication in cells

To directly asses the ability of UbVs to inhibit MERS-CoV replication, MERS-CoV PL^{pro}-specific UbVs were ectopically expressed in cell culture, and cells were subsequently infected with MERS-CoV. MRC5 and HuH-7 cell lines were transduced with lentiviruses encoding FLAG-tagged UbVs, Ub.AA, or GFP. Efficient expression of FLAG-ME.1 and GFP in these cells was confirmed by fluorescence microscopy and by western blotting (**Figure 6.16**). Either 32 or 48 hours post-transduction, cells were infected with MERS-CoV at a m.o.i. of 0.01, and MERS-CoV titers were determined from supernatants harvested 32 hours post infection (**Figure 6.12 D**). In MRC5 cells, ME.1 and ME.4 expression resulted in significantly lower virus titers as these dropped from 5×10^5 plaque forming units (PFU)/ml recovered from control cells to 1,000 or 10 PFU/ml, respectively, when the MERS-CoV infection was started 32 hours post-transduction (**Figure 6.12 D**). The effect of the UbVs was even more pronounced in MRC5 cells that were infected with MERS-CoV 48 hours post-transduction, as virus titers dropped below 10 PFU/ml upon expression of ME.4, which represented a reduction in infectious progeny titers of more than four orders of magnitude (**Figure 6.12 D**) and correlated with higher expression of the UbVs at this time point (**Figure 6.16** and **Figure 6.17**). In HuH-7 cells the expression of GFP or Ub.AA did not affect MERS-CoV titers compared to the non-transduced cells, whereas ME.1 expression led to a two orders of magnitude reduction in virus titer, and an even greater reduction of more than three orders of magnitude was observed upon ME.4 expression (**Figure 6.18**). The effect of UbVs on MERS-CoV progeny titers was more severe in MRC5 cells compared to HuH-7 cells, which might be due to generally higher expression of UbVs in MRC5

cells than in HuH-7 cells (**Figure 6.12 D**, **Figure 6.16 B** and **Figure 6.18**). Taken together, these studies show that UbVs readily inhibit the proteolytic activities of MERS-CoV PL^{pro} in cells and provide extremely effective protection from MERS-CoV infection.

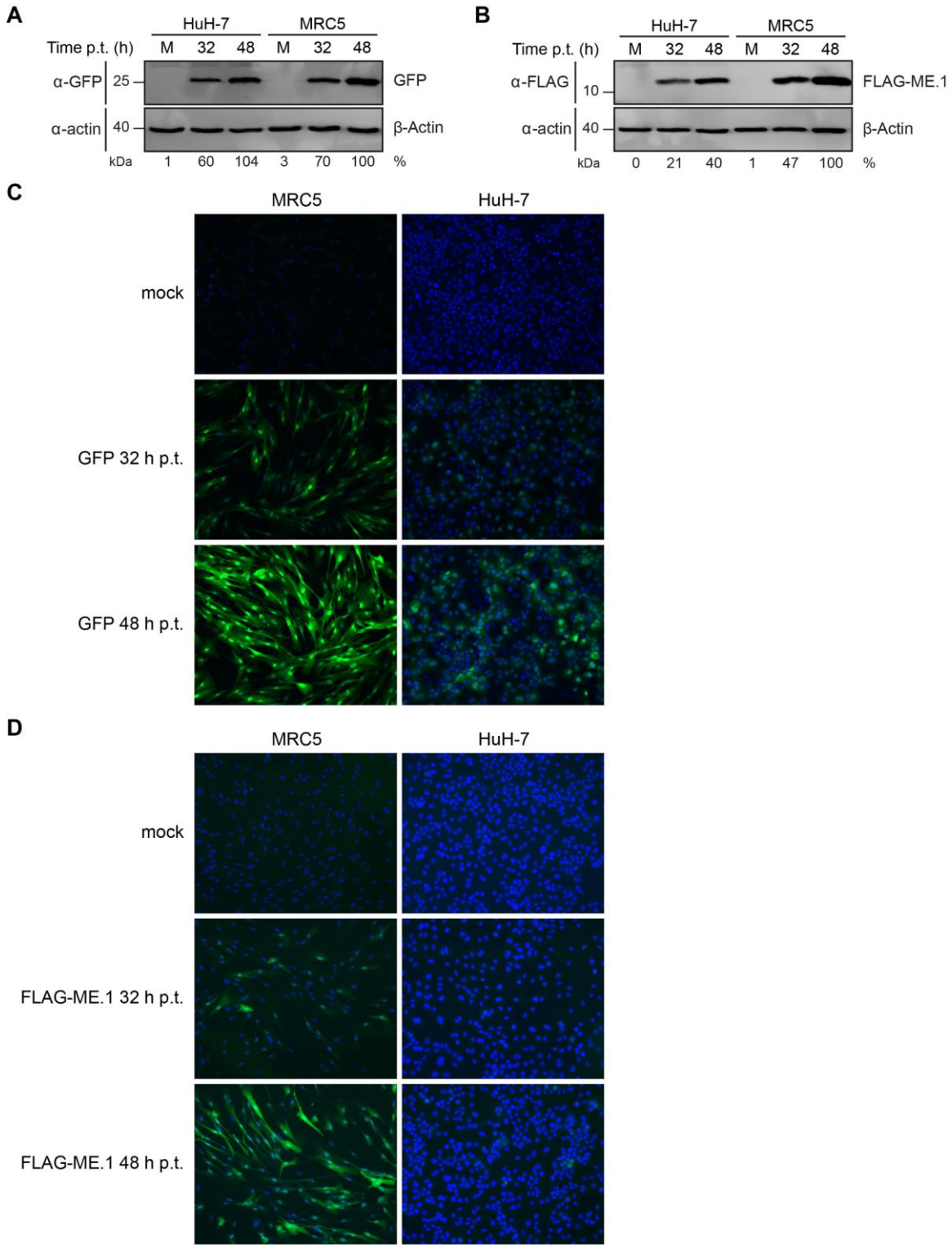

Figure 6.16 Analysis of lentivirus transduction of MRC5 and HuH-7 cells.
(A, B) Western blot analysis of transduced MRC5 and HuH-7 cells with lentiviruses encoding GFP (A) or FLAG-ME.1 (B) both 32 h and 48 h pt. As a control cells were mock transduced

(designated as M). Relative expression of GFP and FLAG-ME.1 was quantified and normalized to actin and expression levels in MRC5 cells 48 h p.t. were set at 100%. (C) GFP transduced MRC5 and HuH-7 cells were fixed 32 h or 48 h p.t. and nuclear DNA was stained using Hoechst. Images were taken using fixed exposure times for both the GFP and Hoechst signal. (D) Immunofluorescence assay of FLAG-ME.1-transduced MRC5 and HuH-7 cells that were fixed 32 h or 48 h p.t. Cells were labelled with a mouse monoclonal antibody recognizing FLAG followed by labelling with a secondary Alexa488-conjugated goat anti-mouse antibody. Exposure times were kept the same for each image.

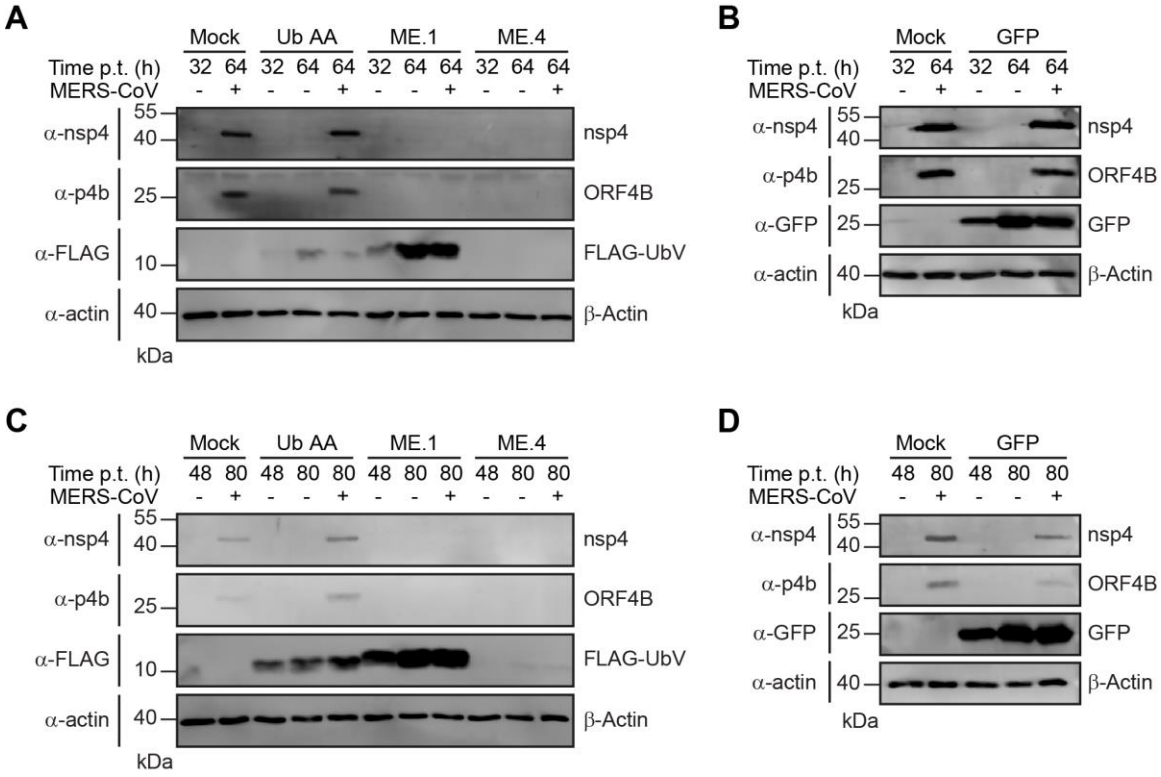

Figure 6.17 Western blot analysis of MERS-CoV infection on transduced MRC5 cells shows decreased viral protein production as a result of UbV expression.
Upon collection of supernatants after MERS-CoV infection of transduced MRC5 cells protein lysates were obtained. Expression of two viral proteins was analyzed by Western blotting, MERS-CoV nsp4 (using cross-reacting SARS-CoV nsp4 antiserum), and MERS-CoV ORF4B. Lentivirus-induced expression of FLAG-UbVs or GFP was confirmed and actin was used as a loading control. Representative Western blots are shown for transduced MRC5 cells that were infected with MERS-CoV at a multiplicity of infection of 0.01 either 32 h p.t. (A, B) or 48 h p.t. (C, D).

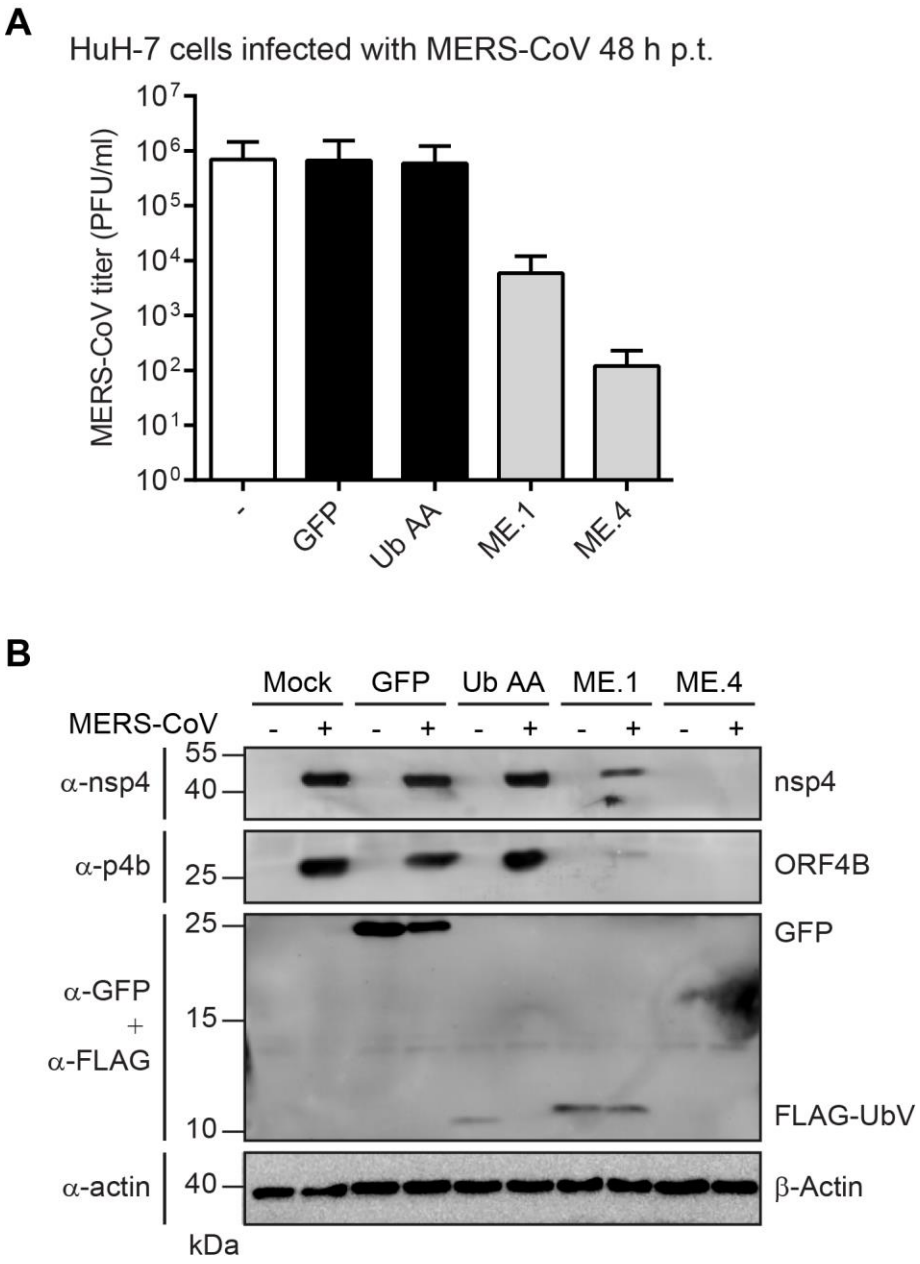

Figure 6.18 Titers of MERS-CoV progeny decreased upon infection of HuH-7 cells expressing UbVs.

(A) HuH-7 cells were transduced with lentiviruses encoding FLAG-UbVs or GFP (as control) respectively and 48 h pt these cells were infected with MERS-CoV at a multiplicity of infection of 0.01. Culture supernatants were collected 32 h post MERS-CoV infection and infectious progeny titers were determined by plaque assays. (B) Lentivirus transduced and MERS-CoV infected HuH-7 cells were 32 h post MERS-CoV infection lysed and expression of MERS-CoV nsp4, MERS-CoV ORF4B as well as expression of FLAG-UbVs or GFP was visualized via Western blotting.

6.4 Discussion

The continued introduction of viruses from zoonotic sources into human populations poses a serious and constant threat to human health (360). In the case of coronavirus infection, therapeutic options are limited, and vaccine development remains in progress (360,361). Here, we describe a unique protein engineering platform that can be used to rapidly generate UbVs to selectively block the activity of vDUBs from a range of evolutionarily distinct viral lineages. Indeed, UbVs generated against MERS-CoV almost completely abolished the replication of this virus in host cells. Meanwhile, none of the UbVs generated in this study likely cross-reacted with human DUBs as no toxicity was observed upon expression of UbVs, demonstrating their potential therapeutic safety.

Targeting intracellular targets with protein-based inhibitors is currently not a therapeutic option due to the practical limitations of immunogenicity and the lack of efficient means for delivering proteins in to cells *in vivo*. However, progress continues to be made on methods for intracellular delivery of mRNA or proteins (362-364), and strategies to reduce immunogenicity, including the use of mirror-image proteins (365), have been developed. Thus, in the future, we are hopeful that UbVs may become bona fide drug candidates, but at present, they are best viewed as tool compounds that can enable drug discovery. For example, while the interface between the UbVs and vDUBs is large, we have recently used combinatorial mutagenesis to reveal a smaller site on human USPs within the UbV interaction interface, which may be amenable as a target for small-molecule inhibitor design (352). Indeed, while the design of small molecules that target protein-protein interfaces remains challenging, there are successful examples where polypeptide-based tools have facilitated design and screening of small molecule inhibitors (366).

A plethora of viruses causing human disease encode for vDUBs implicated in replication and/or pathogenesis, emphasizing the potential clinical importance of vDUBs as therapeutic targets (73,82,83,89,93,158,367). The UbV development platform can also be readily extended to target viruses that infect plants and animals of economic importance, including PRRSV, EAV bovine CoV, TGEV, PEDV and TYMV, all of which encode vDUBs that are essential for virus replication (26). In contrast, some vDUBs, like the CCHFV OTU protease, do not appear to process viral polyproteins and are instead dedicated to increasing viral pathogenicity by suppressing cellular innate immunity (102,293). Interestingly, the CCHFV OTU protease comprises a domain on the viral polymerase, and targeting it with a UbV may not only suppress viral pathogenicity but RNA replication as well, since it has been found that viral OTU DUB activity can suppress proteasome-dependent viral polymerase degradation (253). Additionally, the strong binding of UbV to the viral polymerase could cause steric hindrance and in this way affect polymerase function.

With current transgenic technologies (368), livestock and plant crops expressing virus-specific UbVs could be readily engineered to generate virus-resistant organisms. Significant progress has also been made towards the development of animal models of MERS-CoV infection ((369-371) and reviewed in (372)), which includes a CRISPR-Cas9-edited mouse model used in concert with a mouse-adapted MERS-CoV strain, together mimicking MERS-CoV pathology observed in humans (373). These technologies will provide attractive platforms to assess the efficacy of UbV delivery systems to treat MERS-CoV infection *in vivo*.

The utilization of the Ub scaffold as a template for vDUB inhibitor development exploits the large Ub-binding interface to provide a high degree of specificity in comparison to small molecule-based approaches, since the latter usually rely on targeting the active site of the viral

protease, thereby invoking the risk of cross-reactivity with cellular proteases. The amino acid substitutions in UbVs that confer potent inhibition of vDUBs are distributed across relatively large binding interfaces, and we speculate that resistance to UbVs is less likely to develop in comparison to small-molecule inhibitors. The larger binding surface and the much tighter binding affinities of UbVs (low to sub-nanomolar, **Figure 6.1 C**) compared to reported micromolar affinities for small-molecule inhibitors of MERS-CoV PL^{pro} (188) imply that rather extensive mutations in the viral protease will be necessary to efficiently repel the UbV. Since development of resistance mutations requires virus replication, the extreme reduction in MERS-CoV progeny titers upon expression of UbVs during infection is therefore expected to severely delay occurrence of resistance. Additionally, if a resistant virus happens to be already present in the quasi species it is likely that mutations to repel the UbV from the vDUB will concomitantly lead to less optimal binding of the viral protease to Ub/ISG15 itself and maybe even the virus replicase polyproteins. Therefore, the resistant virus is expected to be attenuated and to have at least reduced deubiquitinating/deISGylating activity that is important for the virus' capacity to suppress innate immune response (93,211). This idea is supported by described escape mutants for MHV to a broad-spectrum CoV 3C-like protease inhibitor where the inhibitor-resistant virus was attenuated in mice, highlighting that the mutant was generated at the cost of replicative fitness (374). In future experiments we will experimentally assess the development of UbV resistance during infection in cell culture and mouse models, which will show whether our speculations are correct.

Ultimately, in the event that resistant strains do emerge in a clinical setting, new UbVs targeting these strains can also be generated rapidly. Most importantly, unlike small-molecule approaches that can take years to implement and often fail, phage display yields potent and

selective viral inhibitors in weeks, a rate that could allow therapeutic development to keep pace with the continued emergence of pathogenic viruses and limit their pandemic potential. Together, these findings make further exploration of UbVs as potent and rapidly developed antiviral agents an exciting and promising venture.

Chapter 7
Structural insights into substrate recognition by MERS-CoV PL^{pro}

Contributions statement

The Lys48-linked diUb activity-based probe was provided by Monique Mulder and Huib Ovaa (LUMC). I performed the MERS-CoV PL^{pro} expression, purification and coupling reactions, as well as the crystallization, data collection, structural determination and structural analysis. This work is to be published.

7.1 Introduction

The importance of viral counter-measures targeting cellular Ub-dependent signalling pathways during infection is becoming increasingly more evident as we continue to discover viral enzymes capable of disrupting these processes. Considerable progress has been made with respect to Coronavirus DUBs in particular, as evidenced by several reports describing the interactions between SARS- and MERS-CoV PL^{pro}s in complex with Ub (93,166), diUb (168) and portions of ISG15 (167). It is clear that the interaction between DUBs and their cognate substrates can be dependent on multiple subsites within a protease, which can determine the specific isopeptide bonds and Ub chain linkages which are recognized. This is particularly evident in the case of the SARS-CoV PL^{pro} domain, which has been found to recognize Lys48-linked diUb molecules with particularly high affinity, cleaving polyUb chains in a di-distributive manner (90,168). Although the specific ubiquitinated cellular targets of SARS-CoV PL^{pro} are unknown, signaling molecules including IκBα require modification by Lys48-linked Ub chains to elicit their pro-inflammatory function. The substrate preference for viral DUBs is thus likely to play a role in the specific innate immune and pro-inflammatory pathways which are affected during infection. With respect to MERS-CoV PL^{pro}, there is no apparent preference when comparing Lys48 and Lys63 (91,93) polyUb linkage types, suggesting that either MERS-CoV PL^{pro} recognizes different linkage types specifically though either S2 or S1' subsites, or that there is little or no structural discrimination by PL^{pro}, with recognition occurring primarily through interaction with monoUb at the S1 site as previously described (93).

Here, the crystal structure of MERS-CoV PL^{pro} in covalent complex with Lys48-linked diUb is described. An activity based-probe (ABP) was used containing a cysteine-reactive electrophile at the isopeptide bond, thus enabling the capture of PL^{pro} in complex with a substrate

spanning the active site. Consistent with reported *in vitro* data, PL^{pro} does not appear to have a distinct S1' site, with the majority of substrate contacts occurring at the S1 site between PL^{pro} and the distal Ub moiety. With respect to ISG15 binding, previous reports have structurally characterized the interactions between PL^{pro} and ISG15 using a truncated form of the substrate containing only the C-terminal UBL (375). In order to further explore the structural requirements for ISG15 recognition by PL^{pro}, the crystal structure of PL^{pro} in complex with full-length ISG15 to 2.4 Å was determined. As has been suggested (167), MERS-CoV PL^{pro} does not appear to explicitly recognize the N-terminal UBL of ISG15, and instead relies on interactions between the C-terminal UBL at the S1 site to mediate substrate recognition.

*7.2 **Methods***

7.2.1 Expression and purification of MERS-CoV PLpro

MERS-CoV PL^{pro} was expressed and purified as described in section 5.2.4. Following removal of the His_6-SUMO tag, tagless PL^{pro} was used for all coupling reactions described below.

7.2.2 Generation of the ISG15-3Br expression construct, and generation of the ISG153Br suicide substrate.

In order to generate the ISG15 expression construct, ISG15 was amplified from the previously reported pTYB2-ISG15(Cys78Ser) plasmid (105), which contains a Cys78Ser mutation in order to prevent aggregation (304). Amplification of ISG15 (residues 1- 156) was performed using primers containing NdeI and BspQI restriction sites at the 5' and 3' ends, respectively, in order to allow for directional cloning into plasmid pTXB1. Insertion into pTXB1 placed ISG15Cys78Ser in-frame with a C-terminal intein domain, followed by a chitin binding

domain in order to allow for self-cleavage and chemical modification of the C-terminus of ISG15. The plasmid was transformed into BL21 (DE3) Gold cells (New England Biolabs) in order to allow for T7 polymerase-driven, IPTG-inducible protein expression. Expression, purification and modification of $ISG15_{(Cys78Ser)}$ to $ISG153Br_{(Cys78Ser)}$ was performed in the same manner as Ub3Br, and is described in section 2.2.2.

7.2.3 Generation of the MERS-CoV PL^{pro}-ISG15 complex

MERS-CoV PL^{pro} and $ISG153Br_{(Cys78Ser)}$ were mixed together at final concentrations of 1.2 and 2.5 µM, respectively, and incubated for 1 hr at RT, with end-over-end mixing. Following coupling the PL^{pro}-ISG15 complex was dialyzed against buffer A (20 mM Bis-Tris pH 6.0, 40 mM NaCl, 2mM DTT) in preparation for cation exchange. The next day, PL^{pro}-ISG15 was loaded onto a Source 15S cation exchange column (GE Healthcare) and washed with 5 CV buffer A. The PLpro-ISG15 complex was eluted by running a linear gradient of buffer B (20 mM Bis-Tris pH 6.0, 100 mM NaCl, 2mM DTT), from 0-100% B over 200 mL (20 CV) at a flowrate of 2 mL/min. The PLpro-ISG15 complex eluted as a single peak, which was subsequently pooled and dialyzed against 20 mM Tris pH 8.5, 150 mM NaCl, 2 mM DTT in preparation for crystallization.

7.2.4 Crystallization of the MERS-CoV PL^{pro}-ISG15 complex

Crystals of the PL^{pro}-ISG15 complex were grown by hanging drop vapour diffusion by mixing 2 µL of PL^{pro}-ISG15 (19 mg/mL) with 2 µL of crystallization solution composed of 21% 1,2 – isopropanediol, 20% PEG 4000, 0.1M trisodium citrate pH 5.6. Crystals were grown at 20°C in a 48-well VDX48 plate (Hampton Research). Prior to freezing, crystals of PL^{pro}-ISG15

were swept through a cryoprotectant solution of 21% 1,2 – isopropanediol, 22% PEG 4000, 0.1M trisodium citrate pH 5.6.

7.2.5 Data collection and structural determination of the MERS-CoV PL^{pro}-ISG15 complex

X-ray diffraction images were collected at the Canadian Light Source on beamline 08B1-1. Images were integrated using iMosflm (376), and scaled and merged using Aimless (356) within the CCP4i2 software suite. Initial phase estimates were obtained by successive molecular replacement experiments within MOLREP (377). First, PL^{pro} lacking the N-terminal UBL (residues 1541-1801; 4RF0) was placed, followed by placement of the N-terminal UBL domain (residues 1482-1540; 4RF0). Subsequently, the C-terminal UBL of ISG15 (residues 77-154; 1Z2M) was placed, followed by placement of a polyalanine model of the N-terminal UBL molecule (residues 3-76; 1Z2M). Subsequent model building and refinement was carried out using Coot (309) and REFMAC (378), respectively. Crystallographic and refinement statistics for the MERS-CoV PL^{pro}-ISG15 complex are reported in **Table 7.1**.

Table 7.1 Crystallographic and refinement statistics for the MERS-CoV PL^{pro}-ISG15 structure.

Crystal	MERS-CoV PL^{pro}-ISG15
X-ray source	CLS 08B1-1
Crystal geometry	
Space group	I4
Unit cell (Å)	*a*=130.62 *b*=130.62 *c*=61.88; α=β=γ=90°
Crystallographic data	
Wavelength (Å)	1.2822
Resolution range (Å)	92.36-2.40 (8.98-2.40)
Total observations	130146 (13580)
Unique reflections	20593 (2169)
Multiplicity	6.3 (6.3)
Completeness (%)	100 (100)
R_{merge}	0.073 (0.71)
CC1/2	0.99 (0.79)
I/σI	14.2 (2.6)
Wilson B-factor (Å^2)	49.81
Refinement statistics	
Reflections in test set	(1054)
Protein atoms	3548
Zinc atoms	1
Solvent molecules	71
R_{work}/R_{free}	0.2246 / 0.2850
RMSDs	
Bond lengths/angles (Å/°)	0.015/1.679
Ramachandran plot	
Favored/allowed (%)	95.63/3.49
Average B factor (Å^2)	
Macromolecules	81.70
Solvent	53.72

*Values in parentheses refer to the highest resolution shell

7.2.6 MERS-CoV PL^{pro}-Lys48diUb complex formation and crystallization

The Lys48diUb activity-based probe (Lys48diUb-ABP) was provided by Dr. Huib Ovaa, and is described in (257). Tagless PL^{pro} and Lys48diUb-ABP were mixed at final concentrations of 5 µM and 20 µM, respectively, and incubated at 37°C for 1 hr. The PL^{pro}-Lys48diUb complex was then purified *via* size exclusion chromatography using a Superdex 75 (GE Healthcare) column, and eluted in 20 mM HEPES pH 7.5, 150 mM NaCl, 5 mM DTT. The PL^{pro}-Lys48diUb complex crystallized in 100 mM HEPES sodium salt pH 7.5, 10% (v/v) isopropanol, 20% (w/v) PEG 4000. Crystallization was performed *via* hanging drop vapour diffusion, where 2 µL of PL^{pro}-Lys48diUb (8 mg/mL) was mixed with 2 µL of well solution, and equilibrated against 25 µL of well solution in a 48-well VDX48 plate (Hampton Research) at 20°C.

7.2.7 Structural determination of the MERS-CoV PL^{pro}-Lys48diUb complex

X-ray diffraction images for the PL^{pro}-Lys48diUb complex were collected at the Canadian Light Source on beamline 08B1-1. Images were integrated using iMosflm, and data reduction was performed using Aimless (356) within in the CCP4i2 suite (379). In order to determine initial phases, a series of molecular replacement experiments were carried out within MOLREP (377). First, PL^{pro} lacking the N-terminal Ubl (residues 1541-1801; 4RF0) was placed, followed by placement of the N-terminal Ubl (residues 1482-1540; 4RF0). Subsequently, the distal Ub (1UBQ) was placed, followed by placement of the proximal Ub molecule using a polyalanine Ub search model. Subsequent model building and refinement was carried out using Coot (309) and REFMAC (378), respectively. Crystallographic and refinement statistics are reported in **Table 7.2**.

Table 7.2 Crystallographic and refinement statistics for the MERS-CoV PL^{pro}-Lys48diUb structure.

Crystal	MERS-CoV PL^{pro}-Lys48diUb
X-ray source	CLS 08B1-1
Crystal geometry	
Space group	I4
Unit cell (Å)	*a*=130.49 *b*=130.49 *c*=60.97; α=β=γ=90°
Crystallographic data	
Wavelength (Å)	1.2817
Resolution range (Å)	35.41-2.60 (9.01-2.50)
Total observations	74940 (8359)
Unique reflections	17773 (1970)
Multiplicity	4.2 (4.2)
Completeness (%)	99.1 (98.3)
R_{merge}	0.068 (0.76)
CC1/2	0.99 (0.66)
I/σI	14.6 (2.2)
Wilson B-factor (Å^2)	49.80
Refinement statistics	
Reflections in test set	(898)
Protein atoms	3469
Zinc atoms	1
Solvent molecules	54
R_{work}/R_{free}	0.2218 / 0.2706
RMSDs	
Bond lengths/angles (Å/°)	0.010/1.056
Ramachandran plot	
Favored/allowed (%)	95.63/3.49
Average B factor (Å^2)	
Macromolecules	71.28
Solvent	51.40

*Values in parentheses refer to the highest resolution shell

7.3 Results

7.3.1 PL^{pro} interacts primarily with the C-terminal UBL of ISG15

The crystal structure of MERS-CoV PL^{pro} in complex with full-length ISG15 shows that the enzyme primarily recognizes the C-terminal UBL of ISG15 ($ISG15_{C\text{-}term}$), interacting with the fold in a similar manner to that seen in the PL^{pro}-Ub structure (Section 5.3.2.2; **Figure 7.1 A**). Relatively few contacts occur between PL^{pro} and $ISG15_{N\text{-}term}$, and further, regions of the electron density maps corresponding the $ISG15_{N\text{-}term}$ are significantly weaker than those corresponding to the PL^{pro}-bound $ISG15_{C\text{-}term}$ (**Figure 7.1 B, C**), indicating substantial mobility of the domain within the crystal. Taken together, it appears as though the primary sites of interaction between PL^{pro} are localized to the S1 site of PL^{pro}, and there does not appear to be a distinct S2 site present to interact with $ISG15_{N\text{-}term}$.

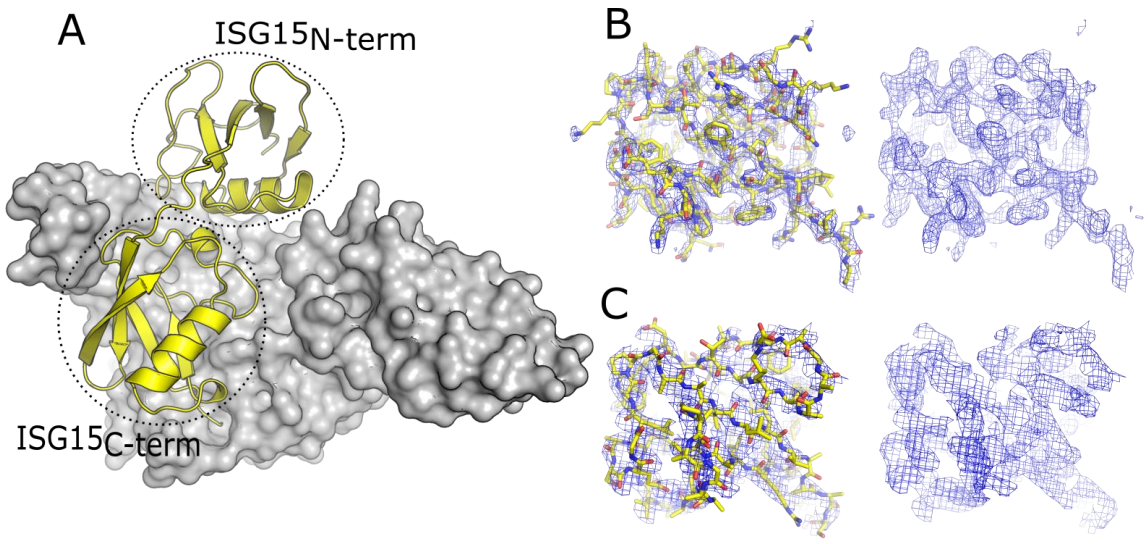

Figure 7.1 Crystal structure of the MERS-CoV PL^{pro}-ISG15 complex.
(A) PLpro (gray surface) is shown bound to ISG15 (yellow cartoon). The N- and C-terminal UBL domains are labeled and indicated with dashed circles. (B) Electron density maps corresponding to $ISG15_{C\text{-}term}$. The right panel shown $ISG15_{C\text{-}term}$ as yellow sticks, with the electron density map displayed as blue mesh. The left panel shows only the electron density map. (C) Electron density maps corresponding to $ISG15_{N\text{-}term}$. The right panel shows $ISG15_{N\text{-}term}$ as yellow sticks, with the electron density map displayed as blue mesh. The left panel shows only the electron density map. Electron density maps in B and C are $2F_o$-F_c maps contoured at 1.0σ.

The specific interactions we observed between PL^{pro} and $ISG15_{C\text{-}term}$ are in general consistent with those previously reported in the crystal structure of MERS-CoV PL^{pro} in complex with the C-terminal UBL of ISG15 (375). These include hydrogen bonding interactions between the backbone carbonyl groups of PL^{pro} residues Lys1686 and Cys1689, and the sidechain of ISG15 residue Lys129 (**Figure 7.2 A**), as well as a salt bridge formed between PL^{pro} residue Lys1657 and ISG15 residue Glu132 (**Figure 7.2 B**). A mainchain hydrogen bond is also seen between the backbone amide of PL^{pro} residue Val1691 and ISG15 residue Gly128. (**Figure 7.2 C**) The interface is also stabilized by hydrophobic interactions, with ISG15 residue Trp123 extending into a hydrophobic pocket formed by PL^{pro} residues Arg1649, His1652 and Val1691 (**Figure 7.2 D**), and ISG15 residue Pro130 interacting with PL^{pro} residues Thr1653 and His1652 (**Figure 7.2 E**). Interestingly, our crystal structure also captures an electrostatic interaction between PL^{pro} residue Asn1638 and ISG15 residue Gln134, which is not present in the previously reported structure (375) (**Figure 7.2 F**). In addition to interactions between PL^{pro} and $ISG15_{C\text{-}term}$, a hydrogen bonding interaction was observed between PL^{pro} and $ISG15_{N\text{-}term}$, between the backbone carbonyl group of PL^{pro} (**Figure 7.2 G**), as well as a hydrogen bonding interaction between the backbone amine of ISG15 residue Arg57 and the backbone carbonyl of PL^{pro} residue Val1681 (**Figure 7.2 H**). It is worth noting however, that given the quality of the electron density maps corresponding to $ISG15_{N\text{-}term}$, caution should be observed when interpreting specific interactions between sidechains of this domain with PL^{pro}. Interactions between the C-terminal RLRGG motif of ISG15 and PL^{pro} mimic those observed in the PL^{pro}-Ub complex (Section 5.3.2.3).

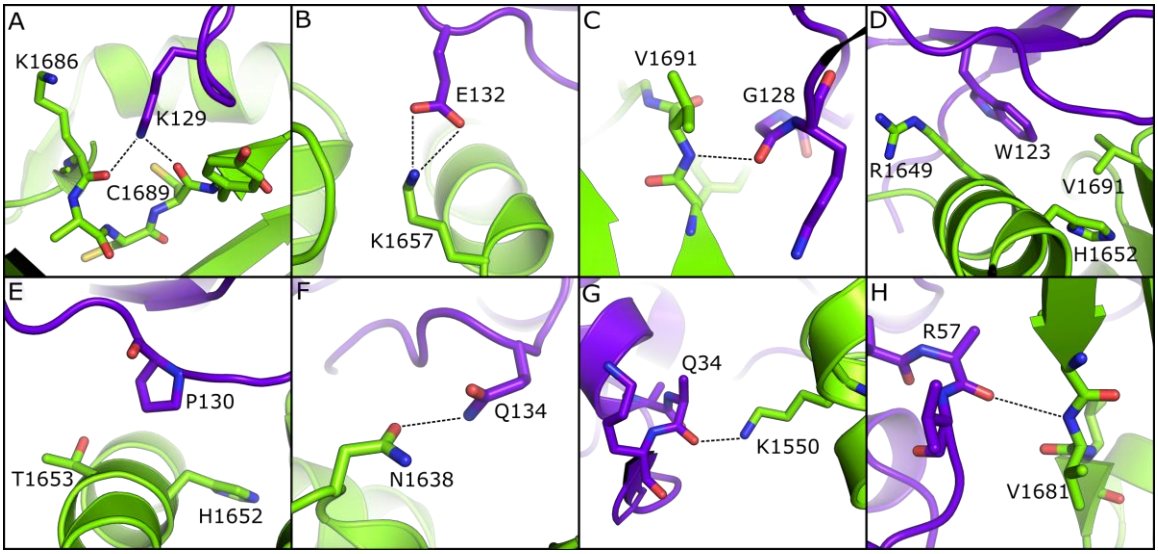

Figure 7.2 Specific interactions between MERS-CoV PL^{pro} and ISG15.
(A, B) Hydrogen bonding and electrostatic interactions observed in at the PL^{pro}-$ISG15_{C\text{-}term}$ interface. PL^{pro} is shown in green, and ISG15 is shown in purple. Relevant residues are shown as sticks and labelled, and hydrogen bonds are depicted as dashed lines. (D, E) Hydrophobic interactions at the PL^{pro}-$ISG15_{C\text{-}term}$ interface. (F) Unique hydrogen bonding interaction observed in this study. (G, H) Hydrogen bonding interactions observed at the PL^{pro}-$ISG15_{N\text{-}term}$ interface.

7.3.2 PL^{pro} does not possess a clear S1' binding site with respect to Lys48diUb binding

The crystal structure of PL^{pro} in complex with Lys48diUb captures the enzyme in a state with a diUb substrate spanning the active site, mimicking substrate binding during hydrolysis *via* an "exo" type mechanism, whereby the terminal distal Ub monomer (Ub_{dist}) is removed from an existing polyUb chain. Unsurprisingly, Ub_{dist} is bound in the same orientation as was observed for the previously determined PL^{pro}-Ub structure (Section 5.3.2.2), and engages Ub in an identical manner. PL^{pro} also appears to adopt the same conformation as was observed in the "closed" PL^{pro}-Ub structure, with the fingers domain engaging the distal Ub moiety.

While a complex of PL^{pro}-Lys48diUb was able to be captured and crystallized (**Figure 7.3**), there does not appear to be a distinct S1' site present to accommodate the proximal Ub (Ub_{prox}) of Lys48diUb, with Ub_{prox} also associated with significantly higher *B*-factor values compared to those refined for PL^{pro} and Ub_{dist} (**Figure 7.4 A**). In addition, while the electron density maps representing the Ub_{dist} are easily interpretable, those representing Ub_{prox} are poorly resolved (**Figure 7.4 B, C**), as was seen in the case of the PL^{pro}-ISG15 structure, and indicating significant mobility within the Ub_{prox}, and the covalent link at the PL^{pro} was not resolved in the density maps. These observations support the apparent lack of specificity displayed by PL^{pro} toward Lys48 and Lys63 polyUb molecules. Despite the absence of an obvious S1' site for Ub_{prox}, there are two hydrogen bonding interactions observed at the PLpro-Ub_{prox} interface, and a single hydrophobic interaction. The backbone amide of PL^{pro} residue Val1757 (located on the BL2 loop) hydrogen bonds with the backbone carbonyl of Ub_{prox} residue Asp58 (**Figure 7.3**), and the side chain of PL^{pro} residue Asn1590 hydrogen bonds with Ub_{prox} residue Glu51 (**Figure 7.3**). In addition, Tyr59 of Ub_{prox} packs against Val1757 of PL^{pro} (**Figure 7.3**).

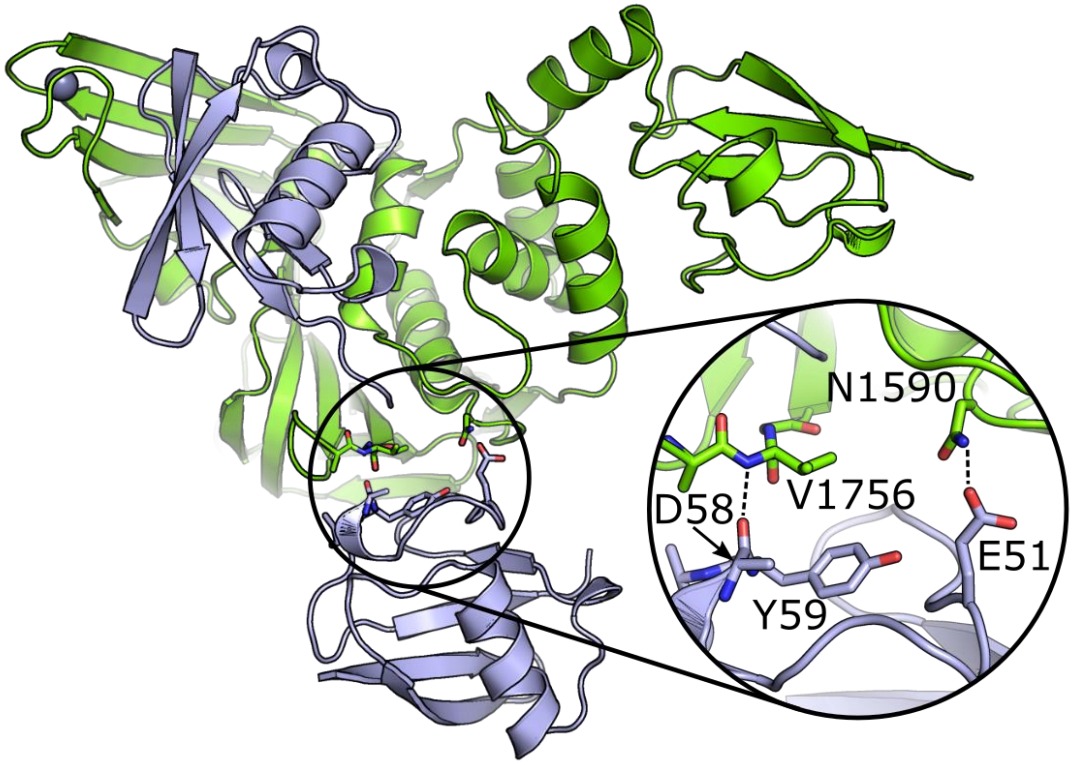

Figure 7.3 Crystal structure of the MERS-CoV PL^{pro}-diUb48 complex.
Cartoon representation of the PL^{pro}-Lys48diUb complex. A close-up of interactions between PL^{pro} (green) and Ub_{prox} (light blue) are shown inset, with relevant residues drawn as sticks and labelled. Hydrogen bonds are represented by a dashed line.

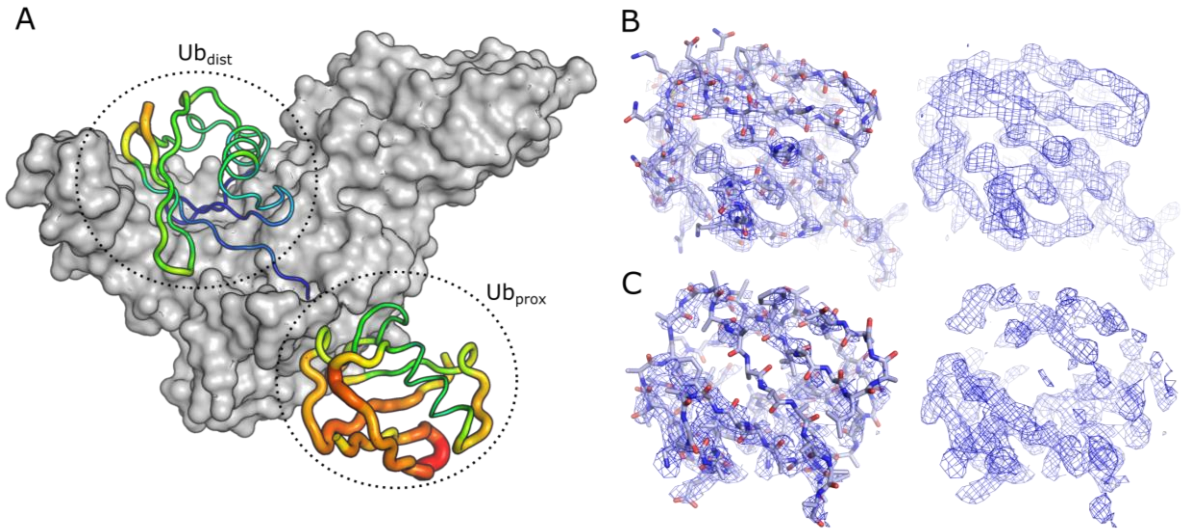

Figure 7.4 The proximal Ub moiety of Lys48-linked diUb bound to MERS-CoV PL^{pro} is mobile. (A) Crystal structure of the PL^{pro}-Lys48diUb complex, with PL^{pro} shown as a gray surface representation, and Lys48diUb displayed as *B*-factor putty. Temperature factors are coloured as a gradient from blue (low) to high (red). (B) Electron density maps corresponding to Ub$_{dist}$. The left panel shows Ub$_{dist}$ as light blue sticks, with the electron density map displayed as blue mesh. The right panel shows only the electron density map. (C) Electron density maps corresponding to Ub$_{prox}$. The left panel shows Ub$_{prox}$ as light blue sticks, with the electron density map displayed as blue mesh. The right panel shows only the electron density map. Electron density maps in B and C are $2F_o$-F_c maps contoured at 1.0σ.

Canonically, Lys48-linked diUb is considered to exist in solution in compact conformations with interactions occurring between hydrophobic patches of Ub moieties (**Figure 1.1 B**), however it is important to note that while the predominant form of Lys48-linked polyUb chains in solution may be relatively compact, polyUb chains can exist in equilibrium with more "open" and accessible structures, and indeed DUBs select for a particular conformation of polyUb in order to catalyze their hydrolysis (380). Notably, the cellular USP21 binds a more extended conformation of Lys48-linked diUb present in low concentrations at equilibrium (380), and a crystal structure of SARS-CoV PL^{pro} in complex with Lys48-linked diUb also binds an extended conformation of the substrate (168). Similar to USP21 and SARS-CoV PL^{pro}, MERS-CoV PL^{pro} also binds Lys48-linked diUb in an extended conformation, with few contacts occurring between the Ub molecules bound across the active site.

7.4 Discussion

7.4.1 Engagement of full-length ISG15 by MERS-CoV PL^{pro}

While there have been several studies investigating the structural basis for ISG15 recognition by viral DUBs (103-106,167,229,375), the work described here provides the first structure of a viral USP in complex with full-length ISG15, comprising of both UBL domains. Corroborating earlier evidence pertaining to the energetics of ISG15 binding by MERS-CoV PL^{pro}, there appear to be few contacts made between the N-terminal UBL of ISG15 and the viral DUB. This sits in contrast to the evidence relating to ISG15 binding by SARS-CoV PL^{pro}, which has been shown to have a higher affinity for full-length ISG15 compared to a truncated ISG15 substrate lacking the N-terminal UBL (167), which suggests that SARS-CoV PL^{pro} may specifically engage the N-terminal UBL of ISG15.

7.4.2 Recognition of Lys48-linked diUb by MERS-CoV PL^{pro}

The importance of developing a clear picture of the specific mechanisms used by DUBs to recognize polyUb substrates should not be underemphasized. As discussed in Chapter 1, many viral enzymes utilise DUBs to counteract cellular antiviral mechanisms and promote replication. Further, numerous Ub-dependent cellular processes are carefully regulated by DUBs, and have been identified as candidates for therapeutic intervention (381,382). Understanding the precise interactions and molecular requirements for substrate interaction can help guide the generation of specific therapeutics targeted toward these enzymes. As the substrates for DUBs often exist in the form of polyUb chains, individual Ub moieties within a chain have been demonstrated to interact *via* specific sites on a cognate protease, with these sites exploiting the unique structural environment presented by polyUb chains of different linkage types. The cellular USP DUBs USP30 and CYLD for example, have been shown to interact with proximal Ub moieties *via* a defined S1' site (383,384).

Interestingly, we demonstrate here that MERS-CoV PL^{pro} does not appear to specifically accommodate Lys48-linked diUb using an obivous S1' site. This mechanism of polyUb binding has been demonstrated with USP7 and USP21, which showed similar kinetics toward monoUb as they did toward most diUbs, and suggested discrimination of certain linkage types by steric interference of a proximal Ub for sub-optimal linkage types, rather than specific, favorable interactions with optimal substrates. It is however worth noting that while USP7, USP21 and MERS-CoV PL^{pro} do not appear to recognize a proximal Ub domain it is possible that specific recognition of polyUb chains may occur *via* an S2 site, specifically interacting with a Ub molecule distal to that bound at the S1 site. Indeed, this has been demonstrated to be the case for

both USP21 and SARS-CoV PL^{pro}, which have been shown crystallographically to specifically recognize Met1- and Lys48-linked diUb, respectively via defined S2 sites (168,345).

Structural investigation into the possibility of a MERS-CoV PL^{pro} diUb-specific S2 site would require the use of a diUb probe possessing a reactive group at the C-terminus of the proximal Ub molecule, and a non-hydrolysable bond between the distal and proximal Ub moieties, as has been implemented in the study of the SARS-CoV PL^{pro} domain (168). Further, while this work and others suggest that MERS-CoV PL^{pro} may have a relaxed specificity for polyUb chains, the existing reports focus primarily on Lys48 and Lys63 Ub linkage types, and we therefore cannot rule out the possibility that PL^{pro} may engage alternate linkage types through specific interactions. Additionally, as MERS-CoV PL^{pro} is only a single domain within the larger nsp3, it is possible that polyUb chain recognition could be facilitated by additional domains present within the full-length viral protein. The cellular DUBs MINDY-1 and TRABID, for example use a motif interacting with Ub (MIU) and ankyrin-repeat (Ank) Ub-binding domains, respectively, to associate with and process polyUb chains of specific linkage types (385,386).

Chapter 8
Conclusions

My studies into the structural biology of viral deubiquitinating enzymes began with the structural determination of the EAV PLP2 domain. Earlier efforts had implicated this dual-function viral enzyme in the inhibition of cellular innate immune responses by way of its DUB activity. The structural data described herein provided the first look at a unique, compact Zn-finger-containing viral DUB and polyprotein processing enzyme in complex with a Ub substrate. Prior to the understanding of the molecular interactions occurring at the interface of PLP2 and Ub, it was difficult to assess the role of PLP2 with respect to its DUB activity. The simple introduction of catalytically inactive PLP2 into recombinant virus prevents viral replication by way of disrupting polyprotein cleavage activity, thus complicating these studies. Further, in these cases we cannot rule out the possibility that cellular processes deemed to be influenced by PLP2 DUB activity are a result of non-specific (or Ub-independent) proteolytic processes carried out by PLP2. The crystal structure of EAV PLP2 in complex with Ub thus allowed for the specific disruption of DUB activity, without affecting the proteolytic ability of the enzyme, permitting us to study directly their role with respect to DUB activity. Through the introduction of specific structure-guided mutations in PLP2, these studies demonstrated directly that the DUB activity of PLP2 was responsible for the inhibition of RIG-I-mediated inhibition of IFN-β transcription. This provided the means to develop using reverse-genetics recombinant EAV deficient in DUB activity in order to study this function directly, and also for the potential application as an attenuated live-virus vaccine. Continuing works carried out by our collaborators demonstrated that the DUB-negative virus offered a similar level of protection with respect to the vaccine

strain from which it was derived (212). Further structural investigation uncovered the molecular basis for the recognition of a second cellular protein by EAV PLP2, eISG15. These findings not only provided structural evidence for this second antiviral mechanism, but also produced the first structure of equine ISG15, a molecule of previously unknown structure.

During the course of this research, a novel Coronavirus emerged into human populations, and the previous structural studies of EAV PLP2 prompted investigation into the PL^{pro} domain of MERS-CoV PL^{pro}, also involved in polyprotein processing and deubiquitination. We determined by X-ray crystallography the atomic structure of MERS-CoV PL^{pro} both in complex with Ub, and in its apo form. These structures revealed significant structural mobility within the PL^{pro} fingers subdomain, as well as the structural rational behind its ability to recognize and process Ub. Using these structures, the DUB activity of PL^{pro} was selectively deactivated, and its role in the downregulation of cellular innate immune responses was assessed, establishing its ability to inhibit MAVS-mediated IFN-β induction. This structural work was further complemented by the structural determination of PL^{pro} in complex with two additional PL^{pro} substrates: full-length ISG15 and Lys48-linked diUb. Elements of each substrate, Ub_{prox} and $ISG15_{N\text{-}term}$, were both found to bind to poorly defined structural elements onto PL^{pro}, suggesting a relatively promiscuous substrate selectivity for PL^{pro} outside of the S1 site, and provided the first efforts toward the definition of structural elements within PL^{pro} involved in substrate interaction outside of the well-defined S1 binding site.

Currently, there are no approved MERS-CoV-specific therapeutics available as treatment. The importance of PL^{pro} DUB and protease activity with respect to viral infection and replication, along with its divergent sequence with respect to eukaryotic DUBs, showcases the enzyme as a viable candidate for specific therapeutic intervention. The PL^{pro}-specific Ub-based

therapeutics described herein effectively inhibited viral replication in cell culture through the competitive inhibition of both polyprotein processing and deubiquitinating activities. The structural investigation into the increased affinity of the UbVs with respect to PL^{pro} binding revealed the formation of several novel hydrophobic and hydrogen-bonding interactions exploited at the PL^{pro}-UbV interface. The development of these potent inhibitors will be furthered by the investigation into potential protein delivery methods, and the assessment of these therapies in established MERS-CoV animal models.

Many of the studies described in this thesis have focused on applying structural biology in order to elucidate precisely which cellular pathways are targeted by Nidovirus DUBs, however it is only the first step towards defining how these enzymes engage the environment of their hosts. Both EAV PLP2 and MERS-CoV PL^{pro} contain transmembrane domains as part of the full nsp expressed during infection. Naturally, these domains could greatly influence cellular localization and substrate availability. These factors could be further influenced in the context of a live virus, where additional viral products could influence substrate specificity. Ideally, studies pertaining to the activities of viral DUBs would be able to establish directly which cellular products are being targeted for deubiquitination, and which polyUb linkage types are being processed. These interactions could be probed even further, in order to establish the temporal regulation of these processes, and the kinetics of DUB activity during infection. Recently, proteomics methods have been developed aimed at addressing these questions, permitting for the quantitative measurement of ubiquitinated substrates under varying experimental conditions, and the determination of polyUb linkage types present on a substrate of interest. The generation of DUB-deficient EAV PLP2 and MERS-CoV PL^{pro} permit the development of DUB-negative

virus strains, which could now be used to probe the specific cellular targets, and specific polyUb linkage types processed by these DUBs during infection.

This work has focused primarily on the investigation into the DUB activity of EAV PLP2 and MERS-CoV PL^{pro}, however this is only one of the functions carried out by these viral enzymes. Indeed, PLP2 and PL^{pro} play critical roles in the maturation of the viral polyprotein, by cleaving one or more sites within the polyprotein in order to release functional nsps. While a number of studies have probed the structural elements of Ub-binding by viral DUBs, there is currently little structural evidence for how these proteases recognize their cognate polyprotein sites. It is unknown whether these proteases require the presence of specific folds within the viral polyprotein in order to bind and carry out hydrolysis, or if the recognition is limited to a consensus sequence of a few or several amino acids. This area of study could potentially uncover novel protease sites for therapeutic targeting, and provide further insight into the structural biology behind viral polyprotein maturation.

References

1. Komander, D., and Rape, M. (2012) The ubiquitin code. *Annu. Rev. Biochem.* **81**, 203-229

2. Dikic, I., Wakatsuki, S., and Walters, K. J. (2009) Ubiquitin-binding domains - from structures to functions. *Nat. Rev. Mol. Cell Biol.* **10**, 659-671

3. Husnjak, K., and Dikic, I. (2012) Ubiquitin-binding proteins: decoders of ubiquitin-mediated cellular functions. *Annu. Rev. Biochem.* **81**, 291-322

4. Akutsu, M., Dikic, I., and Bremm, A. (2016) Ubiquitin chain diversity at a glance. *J. Cell Sci.* **129**, 875-880

5. Kulathu, Y., and Komander, D. (2012) Atypical ubiquitylation - the unexplored world of polyubiquitin beyond Lys48 and Lys63 linkages. *Nat. Rev. Mol. Cell Biol.* **13**, 508-523

6. Yau, R., and Rape, M. (2016) The increasing complexity of the ubiquitin code. *Nat. Cell Biol.* **18**, 579-586

7. Davis, M. E., and Gack, M. U. (2015) Ubiquitination in the antiviral immune response. *Virology* **479-480**, 52-65

8. Heaton, S. M., Borg, N. A., and Dixit, V. M. (2016) Ubiquitin in the activation and attenuation of innate antiviral immunity. *J. Exp. Med.* **213**, 1-13

9. Hochstrasser, M. (2009) Origin and function of ubiquitin-like proteins. *Nature* **458**, 422-429

10. Cappadocia, L., and Lima, C. D. (2018) Ubiquitin-like Protein Conjugation: Structures, Chemistry, and Mechanism. *Chem. Rev.* **118**, 889-918

11. van der Veen, A. G., and Ploegh, H. L. (2012) Ubiquitin-like proteins. *Annu. Rev. Biochem.* **81**, 323-357

12. Morales, D. J., and Lenschow, D. J. (2013) The antiviral activities of ISG15. *J. Mol. Biol.* **425**, 4995-5008

13. Hermann, M., and Bogunovic, D. (2017) ISG15: In Sickness and in Health. *Trends Immunol.* **38**, 79-93

14. Bogunovic, D., Byun, M., Durfee, L. A., Abhyankar, A., Sanal, O., Mansouri, D., Salem, S., Radovanovic, I., Grant, A. V., Adimi, P., Mansouri, N., Okada, S., Bryant, V. L., Kong, X. F., Kreins, A., Velez, M. M., Boisson, B., Khalilzadeh, S., Ozcelik, U., Darazam, I. A., Schoggins, J. W., Rice, C. M., Al-Muhsen, S., Behr, M., Vogt, G., Puel, A., Bustamante, J., Gros, P., Huibregtse, J. M., Abel, L., Boisson-Dupuis, S., and

Casanova, J. L. (2012) Mycobacterial disease and impaired IFN-gamma immunity in humans with inherited ISG15 deficiency. *Science* **337**, 1684-1688

15. Zhang, X., Bogunovic, D., Payelle-Brogard, B., Francois-Newton, V., Speer, S. D., Yuan, C., Volpi, S., Li, Z., Sanal, O., Mansouri, D., Tezcan, I., Rice, G. I., Chen, C., Mansouri, N., Mahdaviani, S. A., Itan, Y., Boisson, B., Okada, S., Zeng, L., Wang, X., Jiang, H., Liu, W., Han, T., Liu, D., Ma, T., Wang, B., Liu, M., Liu, J. Y., Wang, Q. K., Yalnizoglu, D., Radoshevich, L., Uze, G., Gros, P., Rozenberg, F., Zhang, S. Y., Jouanguy, E., Bustamante, J., Garcia-Sastre, A., Abel, L., Lebon, P., Notarangelo, L. D., Crow, Y. J., Boisson-Dupuis, S., Casanova, J. L., and Pellegrini, S. (2015) Human intracellular ISG15 prevents interferon-alpha/beta over-amplification and auto-inflammation. *Nature* **517**, 89-93

16. Schrodinger, LLC. (2015) The PyMOL Molecular Graphics System, Version 1.8.

17. Komander, D., Clague, M. J., and Urbe, S. (2009) Breaking the chains: structure and function of the deubiquitinases. *Nat. Rev. Mol. Cell Biol.* **10**, 550-563

18. Fraile, J. M., Quesada, V., Rodriguez, D., Freije, J. M., and Lopez-Otin, C. (2012) Deubiquitinases in cancer: new functions and therapeutic options. *Oncogene* **31**, 2373-2388

19. Faesen, A. C., Luna-Vargas, M. P., Geurink, P. P., Clerici, M., Merkx, R., van Dijk, W. J., Hameed, D. S., El Oualid, F., Ovaa, H., and Sixma, T. K. (2011) The differential modulation of USP activity by internal regulatory domains, interactors and eight ubiquitin chain types. *Chem. Biol.* **18**, 1550-1561

20. Mevissen, T. E., Hospenthal, M. K., Geurink, P. P., Elliott, P. R., Akutsu, M., Arnaudo, N., Ekkebus, R., Kulathu, Y., Wauer, T., El Oualid, F., Freund, S. M., Ovaa, H., and Komander, D. (2013) OTU deubiquitinases reveal mechanisms of linkage specificity and enable ubiquitin chain restriction analysis. *Cell* **154**, 169-184

21. Gan, J., Qiao, N., Strahan, R., Zhu, C., Liu, L., Verma, S. C., Wei, F., and Cai, Q. (2016) Manipulation of ubiquitin/SUMO pathways in human herpesviruses infection. *Rev. Med. Virol.* **26**, 435-445

22. Luo, H. (2016) Interplay between the virus and the ubiquitin-proteasome system: molecular mechanism of viral pathogenesis. *Curr. Opin. Virol.* **17**, 1-10

23. Wimmer, P., and Schreiner, S. (2015) Viral Mimicry to Usurp Ubiquitin and SUMO Host Pathways. *Viruses* **7**, 4854-4872

24. Minor, M. M., and Slagle, B. L. (2014) Hepatitis B virus HBx protein interactions with the ubiquitin proteasome system. *Viruses* **6**, 4683-4702

25. Wilson, V. G. (2014) The role of ubiquitin and ubiquitin-like modification systems in papillomavirus biology. *Viruses* **6**, 3584-3611

26. Calistri, A., Munegato, D., Carli, I., Parolin, C., and Palu, G. (2014) The ubiquitin-conjugating system: multiple roles in viral replication and infection. *Cells* **3**, 386-417

27. Mattoscio, D., Segre, C. V., and Chiocca, S. (2013) Viral manipulation of cellular protein conjugation pathways: The SUMO lesson. *World J Virol* **2**, 79-90

28. Everett, R. D., Boutell, C., and Hale, B. G. (2013) Interplay between viruses and host sumoylation pathways. *Nat. Rev. Microbiol.* **11**, 400-411

29. Rajsbaum, R., and Garcia-Sastre, A. (2013) Viral evasion mechanisms of early antiviral responses involving regulation of ubiquitin pathways. *Trends Microbiol.* **21**, 421-429

30. Schulz, K. S., and Mossman, K. L. (2016) Viral Evasion Strategies in Type I IFN Signaling – A Summary of Recent Developments. *Front. Immunol.* **7**

31. Ivashkiv, L. B., and Donlin, L. T. (2014) Regulation of type I interferon responses. *Nat. Rev. Immunol.* **14**, 36-49

32. Schneider, W. M., Chevillotte, M. D., and Rice, C. M. (2014) Interferon-stimulated genes: a complex web of host defenses. *Annu. Rev. Immunol.* **32**, 513-545

33. Smith, S., and Jefferies, C. (2014) Role of DNA/RNA sensors and contribution to autoimmunity. *Cytokine Growth Factor Rev.* **25**, 745-757

34. Hu, H., and Sun, S. C. (2016) Ubiquitin signaling in immune responses. *Cell Res.* **26**, 457-483

35. Jiang, X., and Chen, Z. J. (2011) The role of ubiquitylation in immune defence and pathogen evasion. *Nat. Rev. Immunol.* **12**, 35-48

36. Chiang, C., and Gack, M. U. (2017) Post-translational Control of Intracellular Pathogen Sensing Pathways. *Trends Immunol.* **38**, 39-52

37. Sparrer, K. M., and Gack, M. U. (2015) Intracellular detection of viral nucleic acids. *Curr. Opin. Microbiol.* **26**, 1-9

38. McFadden, M. J., Gokhale, N. S., and Horner, S. M. (2017) Protect this house: cytosolic sensing of viruses. *Curr. Opin. Virol.* **22**, 36-43

39. Chen, Q., Sun, L., and Chen, Z. J. (2016) Regulation and function of the cGAS-STING pathway of cytosolic DNA sensing. *Nat. Immunol.* **17**, 1142-1149

40. Rajsbaum, R., Garcia-Sastre, A., and Versteeg, G. A. (2014) TRIMmunity: the roles of the TRIM E3-ubiquitin ligase family in innate antiviral immunity. *J. Mol. Biol.* **426**, 1265-1284

41. May, M. J., and Ghosh, S. (1998) Signal transduction through NF-κB. *Immunol. Today* **19**, 80-88

42. Wang, Q., Liu, X., Cui, Y., Tang, Y., Chen, W., Li, S., Yu, H., Pan, Y., and Wang, C. (2014) The E3 Ubiquitin Ligase AMFR and INSIG1 Bridge the Activation of TBK1 Kinase by Modifying the Adaptor STING. *Immunity* **41**, 919-933

43. Malynn, B. A., and Ma, A. (2010) Ubiquitin makes its mark on immune regulation. *Immunity* **33**, 843-852

44. Jiang, X., Kinch, L. N., Brautigam, C. A., Chen, X., Du, F., Grishin, N. V., and Chen, Z. J. (2012) Ubiquitin-induced oligomerization of the RNA sensors RIG-I and MDA5 activates antiviral innate immune response. *Immunity* **36**, 959-973

45. Reikine, S., Nguyen, J. B., and Modis, Y. (2014) Pattern Recognition and Signaling Mechanisms of RIG-I and MDA5. *Front. Immunol.* **5**, 342

46. Chen, J., and Chen, Z. J. (2013) Regulation of NF-kappaB by ubiquitination. *Curr. Opin. Immunol.* **25**, 4-12

47. Chattopadhyay, S., Kuzmanovic, T., Zhang, Y., Wetzel, J. L., and Sen, G. C. (2016) Ubiquitination of the Transcription Factor IRF-3 Activates RIPA, the Apoptotic Pathway that Protects Mice from Viral Pathogenesis. *Immunity* **44**, 1151-1161

48. Zhao, X., Zhu, H., Yu, J., Li, H., Ge, J., and Chen, W. (2016) c-Cbl-mediated ubiquitination of IRF3 negatively regulates IFN-beta production and cellular antiviral response. *Cell. Signal.* **28**, 1683-1693

49. Zinngrebe, J., Montinaro, A., Peltzer, N., and Walczak, H. (2014) Ubiquitin in the immune system. *EMBO Rep.* **15**, 28-45

50. Friedman, C. S., O'Donnell, M. A., Legarda-Addison, D., Ng, A., Cardenas, W. B., Yount, J. S., Moran, T. M., Basler, C. F., Komuro, A., Horvath, C. M., Xavier, R., and Ting, A. T. (2008) The tumour suppressor CYLD is a negative regulator of RIG-I-mediated antiviral response. *EMBO Rep.* **9**, 930-936

51. Kayagaki, N., Phung, Q., Chan, S., Chaudhari, R., Quan, C., O'Rourke, K. M., Eby, M., Pietras, E., Cheng, G., Bazan, J. F., Zhang, Z., Arnott, D., and Dixit, V. M. (2007) DUBA: a deubiquitinase that regulates type I interferon production. *Science* **318**, 1628-1632

52. Wertz, I. E., O'Rourke, K. M., Zhou, H., Eby, M., Aravind, L., Seshagiri, S., Wu, P., Wiesmann, C., Baker, R., Boone, D. L., Ma, A., Koonin, E. V., and Dixit, V. M. (2004) De-ubiquitination and ubiquitin ligase domains of A20 downregulate NF-kappaB signalling. *Nature* **430**, 694-699

53. Ma, A., and Malynn, B. A. (2012) A20: linking a complex regulator of ubiquitylation to immunity and human disease. *Nat. Rev. Immunol.* **12**, 774-785

54. Parvatiyar, K., Barber, G. N., and Harhaj, E. W. (2010) TAX1BP1 and A20 inhibit antiviral signaling by targeting TBK1-IKKi kinases. *J. Biol. Chem.* **285**, 14999-15009

55. Shembade, N., Ma, A., and Harhaj, E. W. (2010) Inhibition of NF-kappaB signaling by A20 through disruption of ubiquitin enzyme complexes. *Science* **327**, 1135-1139

56. Lopez-Castejon, G., and Edelmann, M. J. (2016) Deubiquitinases: Novel Therapeutic Targets in Immune Surveillance? *Mediators Inflamm.* **2016**, 3481371

57. Elliott, P. R., and Komander, D. (2016) Regulation of Met1-linked polyubiquitin signalling by the deubiquitinase OTULIN. *FEBS J.* **283**, 39-53

58. Sun, S. C. (2008) Deubiquitylation and regulation of the immune response. *Nat. Rev. Immunol.* **8**, 501-511

59. Sun, H., Zhang, Q., Jing, Y. Y., Zhang, M., Wang, H. Y., Cai, Z., Liuyu, T., Zhang, Z. D., Xiong, T. C., Wu, Y., Zhu, Q. Y., Yao, J., Shu, H. B., Lin, D., and Zhong, B. (2017) USP13 negatively regulates antiviral responses by deubiquitinating STING. *Nat. Commun.* **8**, 15534

60. Mathis, B. J., Lai, Y., Qu, C., Janicki, J. S., and Cui, T. (2015) CYLD-mediated signaling and diseases. *Curr. Drug Targets* **16**, 284-294

61. Catrysse, L., Vereecke, L., Beyaert, R., and van Loo, G. (2014) A20 in inflammation and autoimmunity. *Trends Immunol.* **35**, 22-31

62. tenOever, B. R. (2016) The Evolution of Antiviral Defense Systems. *Cell Host Microbe* **19**, 142-149

63. Lauring, A. S., Frydman, J., and Andino, R. (2013) The role of mutational robustness in RNA virus evolution. *Nat. Rev. Microbiol.* **11**, 327-336

64. Koonin, E. V., Dolja, V. V., and Krupovic, M. (2015) Origins and evolution of viruses of eukaryotes: The ultimate modularity. *Virology* **479-480**, 2-25

65. Chan, Y. K., and Gack, M. U. (2016) Viral evasion of intracellular DNA and RNA sensing. *Nat. Rev. Microbiol.* **14**, 360-373

66. Beachboard, D. C., and Horner, S. M. (2016) Innate immune evasion strategies of DNA and RNA viruses. *Curr. Opin. Microbiol.* **32**, 113-119

67. Isaacson, M. K., and Ploegh, H. L. (2009) Ubiquitination, ubiquitin-like modifiers, and deubiquitination in viral infection. *Cell Host Microbe* **5**, 559-570

68. Randow, F., and Lehner, P. J. (2009) Viral avoidance and exploitation of the ubiquitin system. *Nat. Cell Biol.* **11**, 527-534

69. Gu, Z., and Shi, W. (2016) Manipulation of viral infection by deubiquitinating enzymes: new players in host-virus interactions. *Future Microbiol.* **11**, 1435-1446

70. Balakirev, M. Y., Jaquinod, M., Haas, A. L., and Chroboczek, J. (2002) Deubiquitinating function of adenovirus proteinase. *J. Virol.* **76**, 6323-6331

71. Kattenhorn, L. M., Korbel, G. A., Kessler, B. M., Spooner, E., and Ploegh, H. L. (2005) A deubiquitinating enzyme encoded by HSV-1 belongs to a family of cysteine proteases that is conserved across the family Herpesviridae. *Mol. Cell* **19**, 547-557

72. Kim, E. T., Oh, S. E., Lee, Y. O., Gibson, W., and Ahn, J. H. (2009) Cleavage specificity of the UL48 deubiquitinating protease activity of human cytomegalovirus and the growth of an active-site mutant virus in cultured cells. *J. Virol.* **83**, 12046-12056

73. Wang, S., Wang, K., Li, J., and Zheng, C. (2013) Herpes simplex virus 1 ubiquitin-specific protease UL36 inhibits beta interferon production by deubiquitinating TRAF3. *J. Virol.* **87**, 11851-11860

74. Ye, R., Su, C., Xu, H., and Zheng, C. (2017) Herpes Simplex Virus 1 Ubiquitin-Specific Protease UL36 Abrogates NF-kappaB Activation in DNA Sensing Signal Pathway. *J. Virol.* **91**

75. Schlieker, C., Weihofen, W. A., Frijns, E., Kattenhorn, L. M., Gaudet, R., and Ploegh, H. L. (2007) Structure of a herpesvirus-encoded cysteine protease reveals a unique class of deubiquitinating enzymes. *Mol. Cell* **25**, 677-687

76. Whitehurst, C. B., Ning, S., Bentz, G. L., Dufour, F., Gershburg, E., Shackelford, J., Langelier, Y., and Pagano, J. S. (2009) The Epstein-Barr virus (EBV) deubiquitinating enzyme BPLF1 reduces EBV ribonucleotide reductase activity. *J. Virol.* **83**, 4345-4353

77. Gastaldello, S., Hildebrand, S., Faridani, O., Callegari, S., Palmkvist, M., Di Guglielmo, C., and Masucci, M. G. (2010) A deneddylase encoded by Epstein-Barr virus promotes viral DNA replication by regulating the activity of cullin-RING ligases. *Nat. Cell Biol.* **12**, 351-361

78. Whitehurst, C. B., Vaziri, C., Shackelford, J., and Pagano, J. S. (2012) Epstein-Barr virus BPLF1 deubiquitinates PCNA and attenuates polymerase eta recruitment to DNA damage sites. *J. Virol.* **86**, 8097-8106

79. Saito, S., Murata, T., Kanda, T., Isomura, H., Narita, Y., Sugimoto, A., Kawashima, D., and Tsurumi, T. (2013) Epstein-Barr virus deubiquitinase downregulates TRAF6-mediated NF-kappaB signaling during productive replication. *J. Virol.* **87**, 4060-4070

80. van Gent, M., Braem, S. G., de Jong, A., Delagic, N., Peeters, J. G., Boer, I. G., Moynagh, P. N., Kremmer, E., Wiertz, E. J., Ovaa, H., Griffin, B. D., and Ressing, M. E. (2014) Epstein-Barr virus large tegument protein BPLF1 contributes to innate immune evasion through interference with toll-like receptor signaling. *PLoS Pathog.* **10**, e1003960

81. Gonzalez, C. M., Wang, L., and Damania, B. (2009) Kaposi's sarcoma-associated herpesvirus encodes a viral deubiquitinase. *J. Virol.* **83**, 10224-10233

82. Inn, K. S., Lee, S. H., Rathbun, J. Y., Wong, L. Y., Toth, Z., Machida, K., Ou, J. H., and Jung, J. U. (2011) Inhibition of RIG-I-mediated signaling by Kaposi's sarcoma-associated herpesvirus-encoded deubiquitinase ORF64. *J. Virol.* **85**, 10899-10904

83. Chen, Z., Wang, Y., Ratia, K., Mesecar, A. D., Wilkinson, K. D., and Baker, S. C. (2007) Proteolytic processing and deubiquitinating activity of papain-like proteases of human coronavirus NL63. *J. Virol.* **81**, 6007-6018

84. Clementz, M. A., Chen, Z., Banach, B. S., Wang, Y., Sun, L., Ratia, K., Baez-Santos, Y. M., Wang, J., Takayama, J., Ghosh, A. K., Li, K., Mesecar, A. D., and Baker, S. C. (2010) Deubiquitinating and interferon antagonism activities of coronavirus papain-like proteases. *J. Virol.* **84**, 4619-4629

85. Nicholson, B., Leach, C. A., Goldenberg, S. J., Francis, D. M., Kodrasov, M. P., Tian, X., Shanks, J., Sterner, D. E., Bernal, A., Mattern, M. R., Wilkinson, K. D., and Butt, T. R. (2008) Characterization of ubiquitin and ubiquitin-like-protein isopeptidase activities. *Protein Sci.* **17**, 1035-1043

86. Sun, L., Xing, Y., Chen, X., Zheng, Y., Yang, Y., Nichols, D. B., Clementz, M. A., Banach, B. S., Li, K., Baker, S. C., and Chen, Z. (2012) Coronavirus papain-like proteases negatively regulate antiviral innate immune response through disruption of STING-mediated signaling. *PLoS One* **7**, e30802

87. Xing, Y., Chen, J., Tu, J., Zhang, B., Chen, X., Shi, H., Baker, S. C., Feng, L., and Chen, Z. (2013) The papain-like protease of porcine epidemic diarrhea virus negatively regulates type I interferon pathway by acting as a viral deubiquitinase. *J. Gen. Virol.* **94**, 1554-1567

88. Wojdyla, J. A., Manolaridis, I., van Kasteren, P. B., Kikkert, M., Snijder, E. J., Gorbalenya, A. E., and Tucker, P. A. (2010) Papain-like protease 1 from transmissible gastroenteritis virus: crystal structure and enzymatic activity toward viral and cellular substrates. *J. Virol.* **84**, 10063-10073

89. Lindner, H. A., Fotouhi-Ardakani, N., Lytvyn, V., Lachance, P., Sulea, T., and Menard, R. (2005) The papain-like protease from the severe acute respiratory syndrome coronavirus is a deubiquitinating enzyme. *J. Virol.* **79**, 15199-15208

90. Bekes, M., Rut, W., Kasperkiewicz, P., Mulder, M. P., Ovaa, H., Drag, M., Lima, C. D., and Huang, T. T. (2015) SARS hCoV papain-like protease is a unique Lys48 linkage-specific di-distributive deubiquitinating enzyme. *Biochem. J.* **468**, 215-226

91. Baez-Santos, Y. M., Mielech, A. M., Deng, X., Baker, S., and Mesecar, A. D. (2014) Catalytic function and substrate specificity of the papain-like protease domain of nsp3 from the Middle East respiratory syndrome coronavirus. *J. Virol.* **88**, 12511-12527

92. Chen, X., Yang, X., Zheng, Y., Yang, Y., Xing, Y., and Chen, Z. (2014) SARS coronavirus papain-like protease inhibits the type I interferon signaling pathway through interaction with the STING-TRAF3-TBK1 complex. *Protein Cell* **5**, 369-381

93. Bailey-Elkin, B. A., Knaap, R. C., Johnson, G. G., Dalebout, T. J., Ninaber, D. K., van Kasteren, P. B., Bredenbeek, P. J., Snijder, E. J., Kikkert, M., and Mark, B. L. (2014) Crystal structure of the Middle East respiratory syndrome coronavirus (MERS-CoV) papain-like protease bound to ubiquitin facilitates targeted disruption of deubiquitinating activity to demonstrate its role in innate immune suppression. *J. Biol. Chem.* **289**, 34667-34682

94. Chen, Y., Savinov, S. N., Mielech, A. M., Cao, T., Baker, S. C., and Mesecar, A. D. (2015) X-ray Structural and Functional Studies of the Three Tandemly Linked Domains of Non-structural Protein 3 (nsp3) from Murine Hepatitis Virus Reveal Conserved Functions. *J. Biol. Chem.* **290**, 25293-25306

95. Zheng, D., Chen, G., Guo, B., Cheng, G., and Tang, H. (2008) PLP2, a potent deubiquitinase from murine hepatitis virus, strongly inhibits cellular type I interferon production. *Cell Res.* **18**, 1105-1113

96. Wang, G., Chen, G., Zheng, D., Cheng, G., and Tang, H. (2011) PLP2 of mouse hepatitis virus A59 (MHV-A59) targets TBK1 to negatively regulate cellular type I interferon signaling pathway. *PLoS One* **6**, e17192

97. Yu, L., Zhang, X., Wu, T., Wang, Y., Meng, J., Liu, Q., Niu, X., and Wu, Y. (2017) The papain-like protease of avian infectious bronchitis virus has deubiquitinating activity. *Arch. Virol.* **162**, 1943-1950

98. Kong, L., Shaw, N., Yan, L., Lou, Z., and Rao, Z. (2015) Structural View and Substrate Specificity of Papain-like Protease from Avian Infectious Bronchitis Virus. *J. Biol. Chem.* **290**, 7160-7168

99. van Kasteren, P. B., Beugeling, C., Ninaber, D. K., Frias-Staheli, N., van Boheemen, S., Garcia-Sastre, A., Snijder, E. J., and Kikkert, M. (2012) Arterivirus and Nairovirus Ovarian Tumor Domain-Containing Deubiquitinases Target Activated RIG-I To Control Innate Immune Signaling. *J. Virol.* **86**, 773-785

100. Deaton, M. K., Spear, A., Faaberg, K. S., and Pegan, S. D. (2014) The vOTU domain of highly-pathogenic porcine reproductive and respiratory syndrome virus displays a differential substrate preference. *Virology* **454-455**, 247-253

101. Sun, Z., Chen, Z., Lawson, S. R., and Fang, Y. (2010) The cysteine protease domain of porcine reproductive and respiratory syndrome virus nonstructural protein 2 possesses deubiquitinating and interferon antagonism functions. *J. Virol.* **84**, 7832-7846

102. Frias-Staheli, N., Giannakopoulos, N. V., Kikkert, M., Taylor, S. L., Bridgen, A., Paragas, J., Richt, J. A., Rowland, R. R., Schmaljohn, C. S., Lenschow, D. J., Snijder, E. J., Garcia-Sastre, A., and Virgin, H. W. t. (2007) Ovarian tumor domain-containing viral proteases evade ubiquitin- and ISG15-dependent innate immune responses. *Cell Host Microbe* **2**, 404-416

103. Capodagli, G. C., McKercher, M. A., Baker, E. A., Masters, E. M., Brunzelle, J. S., and Pegan, S. D. (2011) Structural analysis of a viral ovarian tumor domain protease from the Crimean-Congo hemorrhagic fever virus in complex with covalently bonded ubiquitin. *J. Virol.* **85**, 3621-3630

104. Capodagli, G. C., Deaton, M. K., Baker, E. A., Lumpkin, R. J., and Pegan, S. D. (2013) Diversity of ubiquitin and ISG15 specificity among nairoviruses' viral ovarian tumor domain proteases. *J. Virol.* **87**, 3815-3827

105. James, T. W., Frias-Staheli, N., Bacik, J. P., Levingston Macleod, J. M., Khajehpour, M., Garcia-Sastre, A., and Mark, B. L. (2011) Structural basis for the removal of ubiquitin and interferon-stimulated gene 15 by a viral ovarian tumor domain-containing protease. *Proc. Natl. Acad. Sci. U. S. A.* **108**, 2222-2227

106. Akutsu, M., Ye, Y., Virdee, S., Chin, J. W., and Komander, D. (2011) Molecular basis for ubiquitin and ISG15 cross-reactivity in viral ovarian tumor domains. *Proc. Natl. Acad. Sci. U. S. A.* **108**, 2228-2233

107. Wang, D., Fang, L., Li, P., Sun, L., Fan, J., Zhang, Q., Luo, R., Liu, X., Li, K., Chen, H., Chen, Z., and Xiao, S. (2011) The leader proteinase of foot-and-mouth disease virus negatively regulates the type I interferon pathway by acting as a viral deubiquitinase. *J. Virol.* **85**, 3758-3766

108. Shang, P., Misra, S., Hause, B., and Fang, Y. (2017) A naturally occurring recombinant enterovirus expresses a torovirus deubiquitinase. *J. Virol.* **91**, e00450-00417

109. Chenon, M., Camborde, L., Cheminant, S., and Jupin, I. (2012) A viral deubiquitylating enzyme targets viral RNA-dependent RNA polymerase and affects viral infectivity. *EMBO J.* **31**, 741-753

110. Zhang, C., and Zhou, D. (2016) Adenoviral vector-based strategies against infectious disease and cancer. *Hum. Vaccin. Immunother.* **12**, 2064-2074

111. Knipe, D. M., and Howley, P. M. (2013) *Fields virology*, 6th ed., Wolters Kluwer/Lippincott Williams & Wilkins Health, Philadelphia, PA

112. Weber, J. (1976) Genetic analysis of adenovirus type 2 III. Temperature sensitivity of processing viral proteins. *J. Virol.* **17**, 462-471

113. Webster, A., Russell, S., Talbot, P., Russell, W. C., and Kemp, G. D. (1989) Characterization of the adenovirus proteinase: substrate specificity. *J. Gen. Virol.* **70 (Pt 12)**, 3225-3234

114. Mangel, W. F., McGrath, W. J., Toledo, D. L., and Anderson, C. W. (1993) Viral DNA and a viral peptide can act as cofactors of adenovirus virion proteinase activity. *Nature* **361**, 274-275

115. Ding, J., McGrath, W. J., Sweet, R. M., and Mangel, W. F. (1996) Crystal structure of the human adenovirus proteinase with its 11 amino acid cofactor. *EMBO J.* **15**, 1778-1783

116. Kamphuis, I. G., Kalk, K. H., Swarte, M. B., and Drenth, J. (1984) Structure of papain refined at 1.65 A resolution. *J. Mol. Biol.* **179**, 233-256

117. Baniecki, M. L., McGrath, W. J., and Mangel, W. F. (2013) Regulation of a viral proteinase by a peptide and DNA in one-dimensional space: III. atomic resolution structure of the nascent form of the adenovirus proteinase. *J. Biol. Chem.* **288**, 2081-2091

118. Rawlings, N. D., Barrett, A. J., and Finn, R. (2016) Twenty years of the MEROPS database of proteolytic enzymes, their substrates and inhibitors. *Nucleic Acids Res.* **44**, D343-350

119. Gupta, S., Mangel, W. F., McGrath, W. J., Perek, J. L., Lee, D. W., Takamoto, K., and Chance, M. R. (2004) DNA binding provides a molecular strap activating the adenovirus proteinase. *Mol. Cell. Proteomics* **3**, 950-959

120. Brown, P., Pullan, W., Yang, Y., and Zhou, Y. (2016) Fast and accurate non-sequential protein structure alignment using a new asymmetric linear sum assignment heuristic. *Bioinformatics* **32**, 370-377

121. Roizman, B., and Whitley, R. J. (2013) An inquiry into the molecular basis of HSV latency and reactivation. *Annu. Rev. Microbiol.* **67**, 355-374

122. Jha, H. C., Pei, Y., and Robertson, E. S. (2016) Epstein-Barr Virus: Diseases Linked to Infection and Transformation. *Front. Microbiol.* **7**, 1602

123. Sompallae, R., Gastaldello, S., Hildebrand, S., Zinin, N., Hassink, G., Lindsten, K., Haas, J., Persson, B., and Masucci, M. G. (2008) Epstein-barr virus encodes three bona fide ubiquitin-specific proteases. *J. Virol.* **82**, 10477-10486

124. Borodovsky, A., Ovaa, H., Kolli, N., Gan-Erdene, T., Wilkinson, K. D., Ploegh, H. L., and Kessler, B. M. (2002) Chemistry-based functional proteomics reveals novel members of the deubiquitinating enzyme family. *Chem. Biol.* **9**, 1149-1159

125. Borodovsky, A., Kessler, B. M., Casagrande, R., Overkleeft, H. S., Wilkinson, K. D., and Ploegh, H. L. (2001) A novel active site-directed probe specific for deubiquitylating enzymes reveals proteasome association of USP14. *EMBO J.* **20**, 5187-5196

126. Paludan, S. R., Bowie, A. G., Horan, K. A., and Fitzgerald, K. A. (2011) Recognition of herpesviruses by the innate immune system. *Nat. Rev. Immunol.* **11**, 143-154

127. Schlieker, C., Korbel, G. A., Kattenhorn, L. M., and Ploegh, H. L. (2005) A deubiquitinating activity is conserved in the large tegument protein of the herpesviridae. *J. Virol.* **79**, 15582-15585

128. Hilterbrand, A. T., Boutz, D. R., Marcotte, E. M., and Upton, J. W. (2017) Murine Cytomegalovirus Deubiquitinase Regulates Viral Chemokine Levels To Control Inflammation and Pathogenesis. *MBio* **8**, e01864-01816

129. Calderwood, M. A., Venkatesan, K., Xing, L., Chase, M. R., Vazquez, A., Holthaus, A. M., Ewence, A. E., Li, N., Hirozane-Kishikawa, T., Hill, D. E., Vidal, M., Kieff, E., and Johannsen, E. (2007) Epstein-Barr virus and virus human protein interaction maps. *Proc. Natl. Acad. Sci. U. S. A.* **104**, 7606-7611

130. Duda, D. M., Scott, D. C., Calabrese, M. F., Zimmerman, E. S., Zheng, N., and Schulman, B. A. (2011) Structural regulation of cullin-RING ubiquitin ligase complexes. *Curr. Opin. Struct. Biol.* **21**, 257-264

131. Whitehurst, C. B., Li, G., Montgomery, S. A., Montgomery, N. D., Su, L., and Pagano, J. S. (2015) Knockout of Epstein-Barr virus BPLF1 retards B-cell transformation and lymphoma formation in humanized mice. *MBio* **6**, e01574-01515

132. Wang, J., Loveland, A. N., Kattenhorn, L. M., Ploegh, H. L., and Gibson, W. (2006) High-molecular-weight protein (pUL48) of human cytomegalovirus is a competent deubiquitinating protease: mutant viruses altered in its active-site cysteine or histidine are viable. *J. Virol.* **80**, 6003-6012

133. Gredmark, S., Schlieker, C., Quesada, V., Spooner, E., and Ploegh, H. L. (2007) A functional ubiquitin-specific protease embedded in the large tegument protein (ORF64) of murine gammaherpesvirus 68 is active during the course of infection. *J. Virol.* **81**, 10300-10309

134. Jarosinski, K., Kattenhorn, L., Kaufer, B., Ploegh, H., and Osterrieder, N. (2007) A herpesvirus ubiquitin-specific protease is critical for efficient T cell lymphoma formation. *Proc. Natl. Acad. Sci. U. S. A.* **104**, 20025-20030

135. Bottcher, S., Maresch, C., Granzow, H., Klupp, B. G., Teifke, J. P., and Mettenleiter, T. C. (2008) Mutagenesis of the active-site cysteine in the ubiquitin-specific protease contained in large tegument protein pUL36 of pseudorabies virus impairs viral replication in vitro and neuroinvasion in vivo. *J. Virol.* **82**, 6009-6016

136. Huffmaster, N. J., Sollars, P. J., Richards, A. L., Pickard, G. E., and Smith, G. A. (2015) Dynamic ubiquitination drives herpesvirus neuroinvasion. *Proc. Natl. Acad. Sci. U. S. A.* **112**, 12818-12823

137. Zhong, N. S., Zheng, B. J., Li, Y. M., Poon, Xie, Z. H., Chan, K. H., Li, P. H., Tan, S. Y., Chang, Q., Xie, J. P., Liu, X. Q., Xu, J., Li, D. X., Yuen, K. Y., Peiris, and Guan, Y. (2003) Epidemiology and cause of severe acute respiratory syndrome (SARS) in Guangdong, People's Republic of China, in February, 2003. *Lancet* **362**, 1353-1358

138. Drosten, C., Gunther, S., Preiser, W., van der Werf, S., Brodt, H. R., Becker, S., Rabenau, H., Panning, M., Kolesnikova, L., Fouchier, R. A., Berger, A., Burguiere, A. M., Cinatl, J., Eickmann, M., Escriou, N., Grywna, K., Kramme, S., Manuguerra, J. C., Muller, S., Rickerts, V., Sturmer, M., Vieth, S., Klenk, H. D., Osterhaus, A. D., Schmitz, H., and Doerr, H. W. (2003) Identification of a novel coronavirus in patients with severe acute respiratory syndrome. *N. Engl. J. Med.* **348**, 1967-1976

139. Ksiazek, T. G., Erdman, D., Goldsmith, C. S., Zaki, S. R., Peret, T., Emery, S., Tong, S., Urbani, C., Comer, J. A., Lim, W., Rollin, P. E., Dowell, S. F., Ling, A. E., Humphrey, C. D., Shieh, W. J., Guarner, J., Paddock, C. D., Rota, P., Fields, B., DeRisi, J., Yang, J. Y., Cox, N., Hughes, J. M., LeDuc, J. W., Bellini, W. J., Anderson, L. J., and Group, S. W. (2003) A novel coronavirus associated with severe acute respiratory syndrome. *N. Engl. J. Med.* **348**, 1953-1966

140. Peiris, J. S., Lai, S. T., Poon, L. L., Guan, Y., Yam, L. Y., Lim, W., Nicholls, J., Yee, W. K., Yan, W. W., Cheung, M. T., Cheng, V. C., Chan, K. H., Tsang, D. N., Yung, R. W., Ng, T. K., Yuen, K. Y., and group, S. s. (2003) Coronavirus as a possible cause of severe acute respiratory syndrome. *Lancet* **361**, 1319-1325

141. Zaki, A. M., van Boheemen, S., Bestebroer, T. M., Osterhaus, A. D., and Fouchier, R. A. (2012) Isolation of a novel coronavirus from a man with pneumonia in Saudi Arabia. *N. Engl. J. Med.* **367**, 1814-1820

142. WHO. Middle East respiratory syndrome coronavirus (MERS-CoV) – Saudi Arabia.

143. Raj, V. S., Farag, E. A., Reusken, C. B., Lamers, M. M., Pas, S. D., Voermans, J., Smits, S. L., Osterhaus, A. D., Al-Mawlawi, N., Al-Romaihi, H. E., AlHajri, M. M., El-Sayed, A. M., Mohran, K. A., Ghobashy, H., Alhajri, F., Al-Thani, M., Al-Marri, S. A., El-Maghraby, M. M., Koopmans, M. P., and Haagmans, B. L. (2014) Isolation of MERS coronavirus from a dromedary camel, Qatar, 2014. *Emerg. Infect. Dis.* **20**, 1339-1342

144. Guan, Y., Zheng, B. J., He, Y. Q., Liu, X. L., Zhuang, Z. X., Cheung, C. L., Luo, S. W., Li, P. H., Zhang, L. J., Guan, Y. J., Butt, K. M., Wong, K. L., Chan, K. W., Lim, W.,

Shortridge, K. F., Yuen, K. Y., Peiris, J. S., and Poon, L. L. (2003) Isolation and characterization of viruses related to the SARS coronavirus from animals in southern China. *Science* **302**, 276-278

145. van der Hoek, L., Pyrc, K., Jebbink, M. F., Vermeulen-Oost, W., Berkhout, R. J., Wolthers, K. C., Wertheim-van Dillen, P. M., Kaandorp, J., Spaargaren, J., and Berkhout, B. (2004) Identification of a new human coronavirus. *Nat. Med.* **10**, 368-373

146. Hamre, D., and Procknow, J. J. (1966) A new virus isolated from the human respiratory tract. *Proc. Soc. Exp. Biol. Med.* **121**, 190-193

147. van der Hoek, L., Sure, K., Ihorst, G., Stang, A., Pyrc, K., Jebbink, M. F., Petersen, G., Forster, J., Berkhout, B., and Uberla, K. (2005) Croup is associated with the novel coronavirus NL63. *PLoS Med.* **2**, e240

148. Lane, T. E., and Hosking, M. P. (2010) The pathogenesis of murine coronavirus infection of the central nervous system. *Crit. Rev. Immunol.* **30**, 119-130

149. Lee, C. (2015) Porcine epidemic diarrhea virus: An emerging and re-emerging epizootic swine virus. *Virol. J.* **12**, 193

150. Perlman, S., and Netland, J. (2009) Coronaviruses post-SARS: update on replication and pathogenesis. *Nat. Rev. Microbiol.* **7**, 439-450

151. Rota, P. A., Oberste, M. S., Monroe, S. S., Nix, W. A., Campagnoli, R., Icenogle, J. P., Penaranda, S., Bankamp, B., Maher, K., Chen, M. H., Tong, S., Tamin, A., Lowe, L., Frace, M., DeRisi, J. L., Chen, Q., Wang, D., Erdman, D. D., Peret, T. C., Burns, C., Ksiazek, T. G., Rollin, P. E., Sanchez, A., Liffick, S., Holloway, B., Limor, J., McCaustland, K., Olsen-Rasmussen, M., Fouchier, R., Gunther, S., Osterhaus, A. D., Drosten, C., Pallansch, M. A., Anderson, L. J., and Bellini, W. J. (2003) Characterization of a novel coronavirus associated with severe acute respiratory syndrome. *Science* **300**, 1394-1399

152. Marra, M. A., Jones, S. J., Astell, C. R., Holt, R. A., Brooks-Wilson, A., Butterfield, Y. S., Khattra, J., Asano, J. K., Barber, S. A., Chan, S. Y., Cloutier, A., Coughlin, S. M., Freeman, D., Girn, N., Griffith, O. L., Leach, S. R., Mayo, M., McDonald, H., Montgomery, S. B., Pandoh, P. K., Petrescu, A. S., Robertson, A. G., Schein, J. E., Siddiqui, A., Smailus, D. E., Stott, J. M., Yang, G. S., Plummer, F., Andonov, A., Artsob, H., Bastien, N., Bernard, K., Booth, T. F., Bowness, D., Czub, M., Drebot, M., Fernando, L., Flick, R., Garbutt, M., Gray, M., Grolla, A., Jones, S., Feldmann, H., Meyers, A., Kabani, A., Li, Y., Normand, S., Stroher, U., Tipples, G. A., Tyler, S., Vogrig, R., Ward, D., Watson, B., Brunham, R. C., Krajden, M., Petric, M., Skowronski, D. M., Upton, C., and Roper, R. L. (2003) The Genome sequence of the SARS-associated coronavirus. *Science* **300**, 1399-1404

153. Ruan, Y. J., Wei, C. L., Ee, A. L., Vega, V. B., Thoreau, H., Su, S. T., Chia, J. M., Ng, P., Chiu, K. P., Lim, L., Zhang, T., Peng, C. K., Lin, E. O., Lee, N. M., Yee, S. L., Ng, L.

F., Chee, R. E., Stanton, L. W., Long, P. M., and Liu, E. T. (2003) Comparative full-length genome sequence analysis of 14 SARS coronavirus isolates and common mutations associated with putative origins of infection. *Lancet* **361**, 1779-1785

154. Snijder, E. J., Bredenbeek, P. J., Dobbe, J. C., Thiel, V., Ziebuhr, J., Poon, L. L., Guan, Y., Rozanov, M., Spaan, W. J., and Gorbalenya, A. E. (2003) Unique and conserved features of genome and proteome of SARS-coronavirus, an early split-off from the coronavirus group 2 lineage. *J. Mol. Biol.* **331**, 991-1004

155. Thiel, V., Ivanov, K. A., Putics, A., Hertzig, T., Schelle, B., Bayer, S., Weissbrich, B., Snijder, E. J., Rabenau, H., Doerr, H. W., Gorbalenya, A. E., and Ziebuhr, J. (2003) Mechanisms and enzymes involved in SARS coronavirus genome expression. *J. Gen. Virol.* **84**, 2305-2315

156. Harcourt, B. H., Jukneliene, D., Kanjanahaluethai, A., Bechill, J., Severson, K. M., Smith, C. M., Rota, P. A., and Baker, S. C. (2004) Identification of severe acute respiratory syndrome coronavirus replicase products and characterization of papain-like protease activity. *J. Virol.* **78**, 13600-13612

157. Sulea, T., Lindner, H. A., Purisima, E. O., and Menard, R. (2005) Deubiquitination, a new function of the severe acute respiratory syndrome coronavirus papain-like protease? *J. Virol.* **79**, 4550-4551

158. Barretto, N., Jukneliene, D., Ratia, K., Chen, Z., Mesecar, A. D., and Baker, S. C. (2005) The papain-like protease of severe acute respiratory syndrome coronavirus has deubiquitinating activity. *J. Virol.* **79**, 15189-15198

159. Devaraj, S. G., Wang, N., Chen, Z., Chen, Z., Tseng, M., Barretto, N., Lin, R., Peters, C. J., Tseng, C. T., Baker, S. C., and Li, K. (2007) Regulation of IRF-3-dependent innate immunity by the papain-like protease domain of the severe acute respiratory syndrome coronavirus. *J. Biol. Chem.* **282**, 32208-32221

160. Spiegel, M., Pichlmair, A., Martinez-Sobrido, L., Cros, J., Garcia-Sastre, A., Haller, O., and Weber, F. (2005) Inhibition of Beta interferon induction by severe acute respiratory syndrome coronavirus suggests a two-step model for activation of interferon regulatory factor 3. *J. Virol.* **79**, 2079-2086

161. Frieman, M., Ratia, K., Johnston, R. E., Mesecar, A. D., and Baric, R. S. (2009) Severe acute respiratory syndrome coronavirus papain-like protease ubiquitin-like domain and catalytic domain regulate antagonism of IRF3 and NF-kappaB signaling. *J. Virol.* **83**, 6689-6705

162. Matthews, K., Schafer, A., Pham, A., and Frieman, M. (2014) The SARS coronavirus papain like protease can inhibit IRF3 at a post activation step that requires deubiquitination activity. *Virol. J.* **11**, 209

163. Ratia, K., Saikatendu, K. S., Santarsiero, B. D., Barretto, N., Baker, S. C., Stevens, R. C., and Mesecar, A. D. (2006) Severe acute respiratory syndrome coronavirus papain-like protease: structure of a viral deubiquitinating enzyme. *Proc. Natl. Acad. Sci. U. S. A.* **103**, 5717-5722

164. Hu, M., Li, P., Li, M., Li, W., Yao, T., Wu, J. W., Gu, W., Cohen, R. E., and Shi, Y. (2002) Crystal structure of a UBP-family deubiquitinating enzyme in isolation and in complex with ubiquitin aldehyde. *Cell* **111**, 1041-1054

165. Chaudhuri, R., Tang, S., Zhao, G., Lu, H., Case, D. A., and Johnson, M. E. (2011) Comparison of SARS and NL63 papain-like protease binding sites and binding site dynamics: inhibitor design implications. *J. Mol. Biol.* **414**, 272-288

166. Chou, C. Y., Lai, H. Y., Chen, H. Y., Cheng, S. C., Cheng, K. W., and Chou, Y. W. (2014) Structural basis for catalysis and ubiquitin recognition by the severe acute respiratory syndrome coronavirus papain-like protease. *Acta Crystallogr. D Biol. Crystallogr.* **70**, 572-581

167. Daczkowski, C. M., Dzimianski, J. V., Clasman, J. R., Goodwin, O., Mesecar, A. D., and Pegan, S. D. (2017) Structural insights into the interaction of coronavirus papain-like proteases and interferon-stimulated gene product 15 from different species. *J. Mol. Biol.* **429**, 1661-1683

168. Bekes, M., van der Heden van Noort, G. J., Ekkebus, R., Ovaa, H., Huang, T. T., and Lima, C. D. (2016) Recognition of Lys48-Linked Di-ubiquitin and Deubiquitinating Activities of the SARS Coronavirus Papain-like Protease. *Mol. Cell* **62**, 572-585

169. Eletr, Z. M., and Wilkinson, K. D. (2014) Regulation of proteolysis by human deubiquitinating enzymes. *Biochim. Biophys. Acta* **1843**, 114-128

170. Ratia, K., Kilianski, A., Baez-Santos, Y. M., Baker, S. C., and Mesecar, A. (2014) Structural Basis for the Ubiquitin-Linkage Specificity and deISGylating activity of SARS-CoV papain-like protease. *PLoS Pathog.* **10**, e1004113

171. Drag, M., Mikolajczyk, J., Bekes, M., Reyes-Turcu, F. E., Ellman, J. A., Wilkinson, K. D., and Salvesen, G. S. (2008) Positional-scanning fluorigenic substrate libraries reveal unexpected specificity determinants of DUBs (deubiquitinating enzymes). *Biochem. J.* **415**, 367-375

172. Han, Y. S., Chang, G. G., Juo, C. G., Lee, H. J., Yeh, S. H., Hsu, J. T., and Chen, X. (2005) Papain-like protease 2 (PLP2) from severe acute respiratory syndrome coronavirus (SARS-CoV): expression, purification, characterization, and inhibition. *Biochemistry* **44**, 10349-10359

173. Chou, C. Y., Chien, C. H., Han, Y. S., Prebanda, M. T., Hsieh, H. P., Turk, B., Chang, G. G., and Chen, X. (2008) Thiopurine analogues inhibit papain-like protease of severe acute respiratory syndrome coronavirus. *Biochem. Pharmacol.* **75**, 1601-1609

174. Ratia, K., Pegan, S., Takayama, J., Sleeman, K., Coughlin, M., Baliji, S., Chaudhuri, R., Fu, W., Prabhakar, B. S., Johnson, M. E., Baker, S. C., Ghosh, A. K., and Mesecar, A. D. (2008) A noncovalent class of papain-like protease/deubiquitinase inhibitors blocks SARS virus replication. *Proc. Natl. Acad. Sci. U. S. A.* **105**, 16119-16124

175. Chen, X., Chou, C. Y., and Chang, G. G. (2009) Thiopurine analogue inhibitors of severe acute respiratory syndrome-coronavirus papain-like protease, a deubiquitinating and deISGylating enzyme. *Antivir. Chem. Chemother.* **19**, 151-156

176. Ghosh, A. K., Takayama, J., Aubin, Y., Ratia, K., Chaudhuri, R., Baez, Y., Sleeman, K., Coughlin, M., Nichols, D. B., Mulhearn, D. C., Prabhakar, B. S., Baker, S. C., Johnson, M. E., and Mesecar, A. D. (2009) Structure-based design, synthesis, and biological evaluation of a series of novel and reversible inhibitors for the severe acute respiratory syndrome-coronavirus papain-like protease. *J. Med. Chem.* **52**, 5228-5240

177. Ghosh, A. K., Takayama, J., Rao, K. V., Ratia, K., Chaudhuri, R., Mulhearn, D. C., Lee, H., Nichols, D. B., Baliji, S., Baker, S. C., Johnson, M. E., and Mesecar, A. D. (2010) Severe acute respiratory syndrome coronavirus papain-like novel protease inhibitors: design, synthesis, protein-ligand X-ray structure and biological evaluation. *J. Med. Chem.* **53**, 4968-4979

178. Lee, H., Cao, S., Hevener, K. E., Truong, L., Gatuz, J. L., Patel, K., Ghosh, A. K., and Johnson, M. E. (2013) Synergistic inhibitor binding to the papain-like protease of human SARS coronavirus: mechanistic and inhibitor design implications. *ChemMedChem* **8**, 1361-1372

179. Baez-Santos, Y. M., Barraza, S. J., Wilson, M. W., Agius, M. P., Mielech, A. M., Davis, N. M., Baker, S. C., Larsen, S. D., and Mesecar, A. D. (2014) X-ray structural and biological evaluation of a series of potent and highly selective inhibitors of human coronavirus papain-like proteases. *J. Med. Chem.* **57**, 2393-2412

180. Baez-Santos, Y. M., St John, S. E., and Mesecar, A. D. (2015) The SARS-coronavirus papain-like protease: structure, function and inhibition by designed antiviral compounds. *Antiviral Res.* **115**, 21-38

181. van Boheemen, S., de Graaf, M., Lauber, C., Bestebroer, T. M., Raj, V. S., Zaki, A. M., Osterhaus, A. D., Haagmans, B. L., Gorbalenya, A. E., Snijder, E. J., and Fouchier, R. A. (2012) Genomic characterization of a newly discovered coronavirus associated with acute respiratory distress syndrome in humans. *MBio* **3**, e00473-00412

182. Kilianski, A., Mielech, A. M., Deng, X., and Baker, S. C. (2013) Assessing activity and inhibition of Middle East respiratory syndrome coronavirus papain-like and 3C-like proteases using luciferase-based biosensors. *J. Virol.* **87**, 11955-11962

183. Yang, X., Chen, X., Bian, G., Tu, J., Xing, Y., Wang, Y., and Chen, Z. (2014) Proteolytic processing, deubiquitinase and interferon antagonist activities of Middle East respiratory syndrome coronavirus papain-like protease. *J. Gen. Virol.* **95**, 614-626

184. Lei, J., Mesters, J. R., Drosten, C., Anemuller, S., Ma, Q., and Hilgenfeld, R. (2014) Crystal structure of the papain-like protease of MERS coronavirus reveals unusual, potentially druggable active-site features. *Antiviral Res.* **109**, 72-82

185. Lin, M. H., Chuang, S. J., Chen, C. C., Cheng, S. C., Cheng, K. W., Lin, C. H., Sun, C. Y., and Chou, C. Y. (2014) Structural and functional characterization of MERS coronavirus papain-like protease. *J. Biomed. Sci.* **21**, 54

186. Lei, J., and Hilgenfeld, R. (2016) Structural and mutational analysis of the interaction between the Middle-East respiratory syndrome coronavirus (MERS-CoV) papain-like protease and human ubiquitin. *Virol. Sin.* **31**, 288-299

187. Mielech, A. M., Kilianski, A., Baez-Santos, Y. M., Mesecar, A. D., and Baker, S. C. (2014) MERS-CoV papain-like protease has deISGylating and deubiquitinating activities. *Virology* **450-451**, 64-70

188. Lee, H., Lei, H., Santarsiero, B. D., Gatuz, J. L., Cao, S., Rice, A. J., Patel, K., Szypulinski, M. Z., Ojeda, I., Ghosh, A. K., and Johnson, M. E. (2015) Inhibitor recognition specificity of MERS-CoV papain-like protease may differ from that of SARS-CoV. *ACS Chem. Biol.* **10**, 1456-1465

189. Hilgenfeld, R. (2014) From SARS to MERS: crystallographic studies on coronaviral proteases enable antiviral drug design. *FEBS J.* **281**, 4085-4096

190. Clasman, J. R., Baez-Santos, Y. M., Mettelman, R. C., O'Brien, A., Baker, S. C., and Mesecar, A. D. (2017) X-ray Structure and Enzymatic Activity Profile of a Core Papain-like Protease of MERS Coronavirus with utility for structure-based drug design. *Sci. Rep.* **7**, 40292

191. Zhang, W., Wu, K. P., Sartori, M. A., Kamadurai, H. B., Ordureau, A., Jiang, C., Mercredi, P. Y., Murchie, R., Hu, J., Persaud, A., Mukherjee, M., Li, N., Doye, A., Walker, J. R., Sheng, Y., Hao, Z., Li, Y., Brown, K. R., Lemichez, E., Chen, J., Tong, Y., Harper, J. W., Moffat, J., Rotin, D., Schulman, B. A., and Sidhu, S. S. (2016) System-Wide Modulation of HECT E3 Ligases with Selective Ubiquitin Variant Probes. *Mol. Cell* **62**, 121-136

192. Gorelik, M., Orlicky, S., Sartori, M. A., Tang, X., Marcon, E., Kurinov, I., Greenblatt, J. F., Tyers, M., Moffat, J., Sicheri, F., and Sidhu, S. S. (2016) Inhibition of SCF ubiquitin ligases by engineered ubiquitin variants that target the Cul1 binding site on the Skp1-F-box interface. *Proc. Natl. Acad. Sci. U. S. A.* **113**, 3527-3532

193. Ernst, A., Avvakumov, G., Tong, J., Fan, Y., Zhao, Y., Alberts, P., Persaud, A., Walker, J. R., Neculai, A. M., Neculai, D., Vorobyov, A., Garg, P., Beatty, L., Chan, P. K., Juang, Y. C., Landry, M. C., Yeh, C., Zeqiraj, E., Karamboulas, K., Allali-Hassani, A., Vedadi, M., Tyers, M., Moffat, J., Sicheri, F., Pelletier, L., Durocher, D., Raught, B., Rotin, D., Yang, J., Moran, M. F., Dhe-Paganon, S., and Sidhu, S. S. (2013) A strategy for modulation of enzymes in the ubiquitin system. *Science* **339**, 590-595

194. Manczyk, N., Yates, B. P., Veggiani, G., Ernst, A., Sicheri, F., and Sidhu, S. S. (2017) Structural and functional characterization of a ubiquitin variant engineered for tight and specific binding to an alpha-helical ubiquitin interacting motif. *Protein Sci.* **26**, 1060-1069

195. Zhang, W., Bailey-Elkin, B. A., Knaap, R. C. M., Khare, B., Dalebout, T. J., Johnson, G. G., van Kasteren, P. B., McLeish, N. J., Gu, J., He, W., Kikkert, M., Mark, B. L., and Sidhu, S. S. (2017) Potent and selective inhibition of pathogenic viruses by engineered ubiquitin variants. *PLoS Pathog.* **13**, e1006372

196. Lee, H. J., Shieh, C. K., Gorbalenya, A. E., Koonin, E. V., La Monica, N., Tuler, J., Bagdzhadzhyan, A., and Lai, M. M. (1991) The complete sequence (22 kilobases) of murine coronavirus gene 1 encoding the putative proteases and RNA polymerase. *Virology* **180**, 567-582

197. Kanjanahaluethai, A., and Baker, S. C. (2000) Identification of mouse hepatitis virus papain-like proteinase 2 activity. *J. Virol.* **74**, 7911-7921

198. Mielech, A. M., Deng, X., Chen, Y., Kindler, E., Wheeler, D. L., Mesecar, A. D., Thiel, V., Perlman, S., and Baker, S. C. (2015) Murine coronavirus ubiquitin-like domain is important for papain-like protease stability and viral pathogenesis. *J. Virol.* **89**, 4907-4917

199. Putics, A., Gorbalenya, A. E., and Ziebuhr, J. (2006) Identification of protease and ADP-ribose 1"-monophosphatase activities associated with transmissible gastroenteritis virus non-structural protein 3. *J. Gen. Virol.* **87**, 651-656

200. Liu, D. X., Tibbles, K. W., Cavanagh, D., Brown, T. D., and Brierley, I. (1995) Identification, expression, and processing of an 87-kDa polypeptide encoded by ORF 1a of the coronavirus infectious bronchitis virus. *Virology* **208**, 48-57

201. Lim, K. P., and Liu, D. X. (1998) Characterization of the two overlapping papain-like proteinase domains encoded in gene 1 of the coronavirus infectious bronchitis virus and determination of the C-terminal cleavage site of an 87-kDa protein. *Virology* **245**, 303-312

202. Lim, K. P., and Liu, D. X. (1998) Characterisation of a papain-like proteinase domain encoded by ORF1a of the coronavirus IBV and determination of the C-terminal cleavage site of an 87 kDa protein. *Adv. Exp. Med. Biol.* **440**, 173-184

203. Lim, K. P., Ng, L. F., and Liu, D. X. (2000) Identification of a novel cleavage activity of the first papain-like proteinase domain encoded by open reading frame 1a of the coronavirus Avian infectious bronchitis virus and characterization of the cleavage products. *J. Virol.* **74**, 1674-1685

204. Lauber, C., Goeman, J. J., Parquet Mdel, C., Nga, P. T., Snijder, E. J., Morita, K., and Gorbalenya, A. E. (2013) The footprint of genome architecture in the largest genome expansion in RNA viruses. *PLoS Pathog.* **9**, e1003500

205. Snijder, E. J., Kikkert, M., and Fang, Y. (2013) Arterivirus molecular biology and pathogenesis. *J. Gen. Virol.* **94**, 2141-2163

206. Neumann, E. J., Kliebenstein, J. B., Johnson, C. D., Mabry, J. W., Bush, E. J., Seitzinger, A. H., Green, A. L., and Zimmerman, J. J. (2005) Assessment of the economic impact of porcine reproductive and respiratory syndrome on swine production in the United States. *J. Am. Vet. Med. Assoc.* **227**, 385-392

207. Holtkamp, D. J., Kliebenstein, J. B., Neumann, E. J., Zimmerman, J. J., Rotto, H. F., Yoder, T. K., Wang, C., Yeske, P. E., Mowrer, C. L., and Haley, C. A. (2013) Assessment of the economic impact of porcine reproductive and respiratory syndrome virus on United States pork producers. *J. Swine. Health. Prod.* **21**, 72-84

208. Vatter, H. A., Di, H., Donaldson, E. F., Radu, G. U., Maines, T. R., and Brinton, M. A. (2014) Functional analyses of the three simian hemorrhagic fever virus nonstructural protein 1 papain-like proteases. *J. Virol.* **88**, 9129-9140

209. Snijder, E. J., Wassenaar, A. L., Spaan, W. J., and Gorbalenya, A. E. (1995) The arterivirus Nsp2 protease. An unusual cysteine protease with primary structure similarities to both papain-like and chymotrypsin-like proteases. *J. Biol. Chem.* **270**, 16671-16676

210. Makarova, K. S., Aravind, L., and Koonin, E. V. (2000) A novel superfamily of predicted cysteine proteases from eukaryotes, viruses and Chlamydia pneumoniae. *Trends Biochem. Sci.* **25**, 50-52

211. van Kasteren, P. B., Bailey-Elkin, B. A., James, T. W., Ninaber, D. K., Beugeling, C., Khajehpour, M., Snijder, E. J., Mark, B. L., and Kikkert, M. (2013) Deubiquitinase function of arterivirus papain-like protease 2 suppresses the innate immune response in infected host cells. *Proc. Natl. Acad. Sci. U. S. A.* **110**, E838-847

212. van Kasteren, P. B., Knaap, R. C., van den Elzen, P., Snijder, E. J., Balasuriya, U. B., van den Born, E., and Kikkert, M. (2015) In vivo assessment of equine arteritis virus vaccine improvement by disabling the deubiquitinase activity of papain-like protease 2. *Vet. Microbiol.* **178**, 132-137

213. Han, J., Rutherford, M. S., and Faaberg, K. S. (2009) The porcine reproductive and respiratory syndrome virus nsp2 cysteine protease domain possesses both trans- and cis-cleavage activities. *J. Virol.* **83**, 9449-9463

214. Han, J., Rutherford, M. S., and Faaberg, K. S. (2010) Proteolytic products of the porcine reproductive and respiratory syndrome virus nsp2 replicase protein. *J. Virol.* **84**, 10102-10112

215. Fang, Y., Treffers, E. E., Li, Y., Tas, A., Sun, Z., van der Meer, Y., de Ru, A. H., van Veelen, P. A., Atkins, J. F., Snijder, E. J., and Firth, A. E. (2012) Efficient -2 frameshifting by mammalian ribosomes to synthesize an additional arterivirus protein. *Proc. Natl. Acad. Sci. U. S. A.* **109**, E2920-2928

216. Li, Y., Treffers, E. E., Napthine, S., Tas, A., Zhu, L., Sun, Z., Bell, S., Mark, B. L., van Veelen, P. A., van Hemert, M. J., Firth, A. E., Brierley, I., Snijder, E. J., and Fang, Y. (2014) Transactivation of programmed ribosomal frameshifting by a viral protein. *Proc. Natl. Acad. Sci. U. S. A.* **111**, E2172-2181

217. Kappes, M. A., Miller, C. L., and Faaberg, K. S. (2013) Highly divergent strains of porcine reproductive and respiratory syndrome virus incorporate multiple isoforms of nonstructural protein 2 into virions. *J. Virol.* **87**, 13456-13465

218. Sun, Z., Li, Y., Ransburgh, R., Snijder, E. J., and Fang, Y. (2012) Nonstructural protein 2 of porcine reproductive and respiratory syndrome virus inhibits the antiviral function of interferon-stimulated gene 15. *J. Virol.* **86**, 3839–3850

219. Bente, D. A., Forrester, N. L., Watts, D. M., McAuley, A. J., Whitehouse, C. A., and Bray, M. (2013) Crimean-Congo hemorrhagic fever: history, epidemiology, pathogenesis, clinical syndrome and genetic diversity. *Antiviral Res.* **100**, 159-189

220. Treib, J., Dobler, G., Haass, A., von Blohn, W., Strittmatter, M., Pindur, G., Froesner, G., and Schimrigk, K. (1998) Thunderclap headache caused by Erve virus? *Neurology* **50**, 509-511

221. Woessner, R., Grauer, M. T., Langenbach, J., Dobler, G., Kroeger, J., Mielke, H. G., Mueller, P., Haass, A., and Treib, J. (2000) The Erve virus: possible mode of transmission and reservoir. *Infection* **28**, 164-166

222. Kinsella, E., Martin, S. G., Grolla, A., Czub, M., Feldmann, H., and Flick, R. (2004) Sequence determination of the Crimean-Congo hemorrhagic fever virus L segment. *Virology* **321**, 23-28

223. Honig, J. E., Osborne, J. C., and Nichol, S. T. (2004) Crimean-Congo hemorrhagic fever virus genome L RNA segment and encoded protein. *Virology* **321**, 29-35

224. Evans, P. C., Ovaa, H., Hamon, M., Kilshaw, P. J., Hamm, S., Bauer, S., Ploegh, H. L., and Smith, T. S. (2004) Zinc-finger protein A20, a regulator of inflammation and cell survival, has de-ubiquitinating activity. *Biochem. J.* **378**, 727-734

225. Boone, D. L., Turer, E. E., Lee, E. G., Ahmad, R. C., Wheeler, M. T., Tsui, C., Hurley, P., Chien, M., Chai, S., Hitotsumatsu, O., McNally, E., Pickart, C., and Ma, A. (2004) The ubiquitin-modifying enzyme A20 is required for termination of Toll-like receptor responses. *Nat. Immunol.* **5**, 1052-1060

226. Messick, T. E., Russell, N. S., Iwata, A. J., Sarachan, K. L., Shiekhattar, R., Shanks, J. R., Reyes-Turcu, F. E., Wilkinson, K. D., and Marmorstein, R. (2008) Structural basis for ubiquitin recognition by the Otu1 ovarian tumor domain protein. *J. Biol. Chem.* **283**, 11038-11049

227. Bergeron, E., Zivcec, M., Chakrabarti, A. K., Nichol, S. T., Albarino, C. G., and Spiropoulou, C. F. (2015) Recovery of Recombinant Crimean Congo Hemorrhagic Fever Virus Reveals a Function for Non-structural Glycoproteins Cleavage by Furin. *PLoS Pathog.* **11**, e1004879

228. Bakshi, S., Holzer, B., Bridgen, A., McMullan, G., Quinn, D. G., and Baron, M. D. (2013) Dugbe virus ovarian tumour domain interferes with ubiquitin/ISG15-regulated innate immune cell signalling. *J. Gen. Virol.* **94**, 298-307

229. Deaton, M. K., Dzimianski, J. V., Daczkowski, C. M., Whitney, G. K., Mank, N. J., Parham, M. M., Bergeron, E., and Pegan, S. D. (2016) Biochemical and Structural Insights into the Preference of Nairoviral DeISGylases for Interferon-Stimulated Gene Product 15 Originating from Certain Species. *J. Virol.* **90**, 8314-8327

230. Holzer, B., Bakshi, S., Bridgen, A., and Baron, M. D. (2011) Inhibition of interferon induction and action by the nairovirus Nairobi sheep disease virus/Ganjam virus. *PLoS One* **6**, e28594

231. Burroughs, J. N., Sangar, D. V., Clarke, B. E., Rowlands, D. J., Billiau, A., and Collen, D. (1984) Multiple proteases in foot-and-mouth disease virus replication. *J. Virol.* **50**, 878-883

232. Strebel, K., and Beck, E. (1986) A second protease of foot-and-mouth disease virus. *J. Virol.* **58**, 893-899

233. Kirchweger, R., Ziegler, E., Lamphear, B. J., Waters, D., Liebig, H. D., Sommergruber, W., Sobrino, F., Hohenadl, C., Blaas, D., Rhoads, R. E., and et al. (1994) Foot-and-mouth disease virus leader proteinase: purification of the Lb form and determination of its cleavage site on eIF-4 gamma. *J. Virol.* **68**, 5677-5684

234. Piccone, M. E., Rieder, E., Mason, P. W., and Grubman, M. J. (1995) The foot-and-mouth disease virus leader proteinase gene is not required for viral replication. *J. Virol.* **69**, 5376-5382

235. de Los Santos, T., de Avila Botton, S., Weiblen, R., and Grubman, M. J. (2006) The leader proteinase of foot-and-mouth disease virus inhibits the induction of beta interferon mRNA and blocks the host innate immune response. *J. Virol.* **80**, 1906-1914

236. Chinsangaram, J., Koster, M., and Grubman, M. J. (2001) Inhibition of L-deleted foot-and-mouth disease virus replication by alpha/beta interferon involves double-stranded RNA-dependent protein kinase. *J. Virol.* **75**, 5498-5503

237. Chinsangaram, J., Piccone, M. E., and Grubman, M. J. (1999) Ability of foot-and-mouth disease virus to form plaques in cell culture is associated with suppression of alpha/beta interferon. *J. Virol.* **73**, 9891-9898

238. de Los Santos, T., Diaz-San Segundo, F., and Grubman, M. J. (2007) Degradation of nuclear factor kappa B during foot-and-mouth disease virus infection. *J. Virol.* **81**, 12803-12815

239. de los Santos, T., Segundo, F. D., Zhu, J., Koster, M., Dias, C. C., and Grubman, M. J. (2009) A conserved domain in the leader proteinase of foot-and-mouth disease virus is required for proper subcellular localization and function. *J. Virol.* **83**, 1800-1810

240. Gorbalenya, A. E., Koonin, E. V., and Lai, M. M. (1991) Putative papain-related thiol proteases of positive-strand RNA viruses. Identification of rubi- and aphthovirus proteases and delineation of a novel conserved domain associated with proteases of rubi-, alpha- and coronaviruses. *FEBS Lett.* **288**, 201-205

241. Guarne, A., Tormo, J., Kirchweger, R., Pfistermueller, D., Fita, I., and Skern, T. (1998) Structure of the foot-and-mouth disease virus leader protease: a papain-like fold adapted for self-processing and eIF4G recognition. *EMBO J.* **17**, 7469-7479

242. Gorbalenya, A. E., and Koonin, E. V. (1991) Endonuclease (R) subunits of type-I and type-III restriction-modification enzymes contain a helicase-like domain. *FEBS Lett.* **291**, 277-281

243. Cencic, R., Mayer, C., Juliano, M. A., Juliano, L., Konrat, R., Kontaxis, G., and Skern, T. (2007) Investigating the substrate specificity and oligomerisation of the leader protease of foot and mouth disease virus using NMR. *J. Mol. Biol.* **373**, 1071-1087

244. Santos, J. A., Gouvea, I. E., Judice, W. A., Izidoro, M. A., Alves, F. M., Melo, R. L., Juliano, M. A., Skern, T., and Juliano, L. (2009) Hydrolytic properties and substrate specificity of the foot-and-mouth disease leader protease. *Biochemistry* **48**, 7948-7958

245. Nogueira Santos, J. A., Assis, D. M., Gouvea, I. E., Judice, W. A., Izidoro, M. A., Juliano, M. A., Skern, T., and Juliano, L. (2012) Foot and mouth disease leader protease (Lbpro): Investigation of prime side specificity allows the synthesis of a potent inhibitor. *Biochimie* **94**, 711-718

246. Steinberger, J., Grishkovskaya, I., Cencic, R., Juliano, L., Juliano, M. A., and Skern, T. (2014) Foot-and-mouth disease virus leader proteinase: structural insights into the mechanism of intermolecular cleavage. *Virology* **468-470**, 397-408

247. Morch, M. D., Boyer, J. C., and Haenni, A. L. (1988) Overlapping open reading frames revealed by complete nucleotide sequencing of turnip yellow mosaic virus genomic RNA. *Nucleic Acids Res.* **16**, 6157-6173

248. Bransom, K. L., Weiland, J. J., and Dreher, T. W. (1991) Proteolytic maturation of the 206-kDa nonstructural protein encoded by turnip yellow mosaic virus RNA. *Virology* **184**, 351-358

249. Bransom, K. L., and Dreher, T. W. (1994) Identification of the essential cysteine and histidine residues of the turnip yellow mosaic virus protease. *Virology* **198**, 148-154

250. Rozanov, M. N., Drugeon, G., and Haenni, A. L. (1995) Papain-like proteinase of turnip yellow mosaic virus: a prototype of a new viral proteinase group. *Arch. Virol.* **140**, 273-288

251. Jakubiec, A., Drugeon, G., Camborde, L., and Jupin, I. (2007) Proteolytic processing of turnip yellow mosaic virus replication proteins and functional impact on infectivity. *J. Virol.* **81**, 11402-11412

252. Camborde, L., Planchais, S., Tournier, V., Jakubiec, A., Drugeon, G., Lacassagne, E., Pflieger, S., Chenon, M., and Jupin, I. (2010) The ubiquitin-proteasome system regulates the accumulation of Turnip yellow mosaic virus RNA-dependent RNA polymerase during viral infection. *Plant Cell* **22**, 3142-3152

253. Lombardi, C., Ayach, M., Beaurepaire, L., Chenon, M., Andreani, J., Guerois, R., Jupin, I., and Bressanelli, S. (2013) A Compact Viral Processing Proteinase/Ubiquitin Hydrolase from the OTU Family. *PLoS Pathog.* **9**, e1003560

254. Bailey-Elkin, B. A., van Kasteren, P. B., Snijder, E. J., Kikkert, M., and Mark, B. L. (2014) Viral OTU deubiquitinases: a structural and functional comparison. *PLoS Pathog.* **10**, e1003894

255. Ordureau, A., Munch, C., and Harper, J. W. (2015) Quantifying ubiquitin signaling. *Mol. Cell* **58**, 660-676

256. Flierman, D., van der Heden van Noort, G. J., Ekkebus, R., Geurink, P. P., Mevissen, T. E., Hospenthal, M. K., Komander, D., and Ovaa, H. (2016) Non-hydrolyzable Diubiquitin Probes Reveal Linkage-Specific Reactivity of Deubiquitylating Enzymes Mediated by S2 Pockets. *Cell Chem. Biol.* **23**, 472-482

257. Mulder, M. P., El Oualid, F., ter Beek, J., and Ovaa, H. (2014) A native chemical ligation handle that enables the synthesis of advanced activity-based probes: diubiquitin as a case study. *ChemBioChem* **15**, 946-949

258. Pruneda, J. N., Durkin, C. H., Geurink, P. P., Ovaa, H., Santhanam, B., Holden, D. W., and Komander, D. (2016) The Molecular Basis for Ubiquitin and Ubiquitin-like Specificities in Bacterial Effector Proteases. *Mol. Cell* **63**, 261-276

259. Firth, A. E., and Brierley, I. (2012) Non-canonical translation in RNA viruses. *J. Gen. Virol.* **93**, 1385-1409

260. Dougherty, W. G., and Semler, B. L. (1993) Expression of virus-encoded proteinases: functional and structural similarities with cellular enzymes. *Microbiol. Rev.* **57**, 781-822

261. Gorbalenya, A. E., Donchenko, A. P., Blinov, V. M., and Koonin, E. V. (1989) Cysteine proteases of positive strand RNA viruses and chymotrypsin-like serine proteases. A distinct protein superfamily with a common structural fold. *FEBS Lett.* **243**, 103-114

262. Hellen, C. U., Krausslich, H. G., and Wimmer, E. (1989) Proteolytic processing of polyproteins in the replication of RNA viruses. *Biochemistry* **28**, 9881-9890

263. Etchison, D., Milburn, S. C., Edery, I., Sonenberg, N., and Hershey, J. W. (1982) Inhibition of HeLa cell protein synthesis following poliovirus infection correlates with the proteolysis of a 220,000-dalton polypeptide associated with eucaryotic initiation factor 3 and a cap binding protein complex. *J. Biol. Chem.* **257**, 14806-14810

264. Krausslich, H. G., Nicklin, M. J., Toyoda, H., Etchison, D., and Wimmer, E. (1987) Poliovirus proteinase 2A induces cleavage of eucaryotic initiation factor 4F polypeptide p220. *J. Virol.* **61**, 2711-2718

265. Li, X. D., Sun, L., Seth, R. B., Pineda, G., and Chen, Z. J. (2005) Hepatitis C virus protease NS3/4A cleaves mitochondrial antiviral signaling protein off the mitochondria to evade innate immunity. *Proc. Natl. Acad. Sci. U. S. A.* **102**, 17717-17722

266. Meylan, E., Curran, J., Hofmann, K., Moradpour, D., Binder, M., Bartenschlager, R., and Tschopp, J. (2005) Cardif is an adaptor protein in the RIG-I antiviral pathway and is targeted by hepatitis C virus. *Nature* **437**, 1167-1172

267. Ventoso, I., MacMillan, S. E., Hershey, J. W., and Carrasco, L. (1998) Poliovirus 2A proteinase cleaves directly the eIF-4G subunit of eIF-4F complex. *FEBS Lett.* **435**, 79-83

268. Gohara, D. W., Ha, C. S., Kumar, S., Ghosh, B., Arnold, J. J., Wisniewski, T. J., and Cameron, C. E. (1999) Production of "authentic" poliovirus RNA-dependent RNA polymerase (3D(pol)) by ubiquitin-protease-mediated cleavage in Escherichia coli. *Protein Expr. Purif.* **17**, 128-138

269. Collaborative Computational Project Number 4. (1994) The CCP4 Suite: Programs for Protein Crystallography. in *Acta Crystallogr. D Biol. Crystallogr.*

270. Adams, P. D., Afonine, P. V., Bunkoczi, G., Chen, V. B., Davis, I. W., Echols, N., Headd, J. J., Hung, L.-W., Kapral, G. J., Grosse-Kunstleve, R. W., McCoy, A. J., Moriarty, N. W., Oeffner, R., Read, R. J., Richardson, D. C., Richardson, J. S., Terwilliger, T. C., and Zwart, P. H. (2010) PHENIX: a comprehensive Python-based system for macromolecular structure solution. *Acta Crystallogr. D Biol. Crystallogr.* **66**, 213-221

271. Brunger, A. T. (1992) Free R-Value - a Novel Statistical Quantity for Assessing the Accuracy of Crystal-Structures. *Nature* **355**, 472-475

272. Emsley, P., and Cowtan, K. (2004) Coot: model-building tools for molecular graphics. *Acta Crystallogr. D Biol. Crystallogr.* **60**, 2126-2132

273. Posthuma, C. C., Pedersen, K. W., Lu, Z., Joosten, R. G., Roos, N., Zevenhoven-Dobbe, J. C., and Snijder, E. J. (2008) Formation of the arterivirus replication/transcription complex: a key role for nonstructural protein 3 in the remodeling of intracellular membranes. *J. Virol.* **82**, 4480-4491

274. van Dinten, L. C., den Boon, J. A., Wassenaar, A. L., Spaan, W. J., and Snijder, E. J. (1997) An infectious arterivirus cDNA clone: identification of a replicase point mutation that abolishes discontinuous mRNA transcription. *Proc. Natl. Acad. Sci. U. S. A.* **94**, 991-996

275. Nedialkova, D. D., Gorbalenya, A. E., and Snijder, E. J. (2010) Arterivirus Nsp1 modulates the accumulation of minus-strand templates to control the relative abundance of viral mRNAs. *PLoS Pathog.* **6**, e1000772

276. Rozen, S., and Skaletsky, H. J. (1998) Primer3. *Methods Mol. Biol.* **132**

277. Fitzgerald, K. A., McWhirter, S. M., Faia, K. L., Rowe, D. C., Latz, E., Golenbock, D. T., Coyle, A. J., Liao, S. M., and Maniatis, T. (2003) IKKepsilon and TBK1 are essential components of the IRF3 signaling pathway. *Nat. Immunol.* **4**, 491-496

278. Gack, M. U., Shin, Y. C., Joo, C. H., Urano, T., Liang, C., Sun, L., Takeuchi, O., Akira, S., Chen, Z., Inoue, S., and Jung, J. U. (2007) TRIM25 RING-finger E3 ubiquitin ligase is essential for RIG-I-mediated antiviral activity. *Nature* **446**, 916-920

279. Gack, M. U., Albrecht, R. A., Urano, T., Inn, K. S., Huang, I. C., Carnero, E., Farzan, M., Inoue, S., Jung, J. U., and Garcia-Sastre, A. (2009) Influenza A virus NS1 targets the ubiquitin ligase TRIM25 to evade recognition by the host viral RNA sensor RIG-I. *Cell Host Microbe* **5**, 439-449

280. Versteeg, G. A., Hale, B. G., van Boheemen, S., Wolff, T., Lenschow, D. J., and Garcia-Sastre, A. (2010) Species-specific antagonism of host ISGylation by the influenza B virus NS1 protein. *J. Virol.* **84**, 5423-5430

281. MacLachlan, N. J., Balasuriya, U. B., Hedges, J. F., Schweidler, T. M., McCollum, W. H., Timoney, P. J., Hullinger, P. J., and Patton, J. F. (1998) Serologic response of horses to the structural proteins of equine arteritis virus. *J. Vet. Diagn. Invest.* **10**, 229-236

282. Malakhov, M. P., Kim, K. I., Malakhova, O. A., Jacobs, B. S., Borden, E. C., and Zhang, D. E. (2003) High-throughput immunoblotting. Ubiquitin-like protein ISG15 modifies key regulators of signal transduction. *J. Biol. Chem.* **278**, 16608-16613

283. DeLano, W. L. (2002) The PyMOL Molecular Graphics System. DeLano Scientific, Palo Alto, CA, USA.

284. Andreini, C., Bertini, I., and Cavallaro, G. (2011) Minimal Functional Sites Allow a Classification of Zinc Sites in Proteins. *PLoS One* **6**, e26325

285. Holm, L., and Rosenström, P. (2010) Dali server: conservation mapping in 3D. *Nucleic Acids Res.* **38**, W545-W549

286. Juang, Y.-C., Landry, M.-C., Sanches, M., Vittal, V., Leung, C. C. Y., Ceccarelli, Derek F., Mateo, A.-Rachele F., Pruneda, Jonathan N., Mao, D. Y. L., Szilard, Rachel K., Orlicky, S., Munro, M., Brzovic, Peter S., Klevit, Rachel E., Sicheri, F., and Durocher, D. (2012) OTUB1 Co-opts Lys48-Linked Ubiquitin Recognition to Suppress E2 Enzyme Function. *Mol. Cell* **45**, 384-397

287. Wiener, R., Zhang, X., Wang, T., and Wolberger, C. (2012) The mechanism of OTUB1-mediated inhibition of ubiquitination. *Nature* **483**, 618-622

288. Huang, O. W., Ma, X., Yin, J., Flinders, J., Maurer, T., Kayagaki, N., Phung, Q., Bosanac, I., Arnott, D., Dixit, V. M., Hymowitz, S. G., Starovasnik, M. A., and Cochran, A. G. (2012) Phosphorylation-dependent activity of the deubiquitinase DUBA. *Nat. Struct. Mol. Biol.* **19**, 171-175

289. Durfee, L. A., Lyon, N., Seo, K., and Huibregtse, J. M. (2010) The ISG15 conjugation system broadly targets newly synthesized proteins: implications for the antiviral function of ISG15. *Mol. Cell* **38**, 722-732

290. Morrison, J. M., and Racaniello, V. R. (2009) Proteinase 2Apro is essential for enterovirus replication in type I interferon-treated cells. *J. Virol.* **83**, 4412-4422

291. Ventoso, I., and Carrasco, L. (1995) A poliovirus 2A(pro) mutant unable to cleave 3CD shows inefficient viral protein synthesis and transactivation defects. *J. Virol.* **69**, 6280-6288

292. Yu, S. F., and Lloyd, R. E. (1991) Identification of essential amino acid residues in the functional activity of poliovirus 2A protease. *Virology* **182**, 615-625

293. Bergeron, E., Albarino, C. G., Khristova, M. L., and Nichol, S. T. (2010) Crimean-Congo hemorrhagic fever virus-encoded ovarian tumor protease activity is dispensable for virus RNA polymerase function. *J. Virol.* **84**, 216-226

294. Bosanac, I., Wertz, I. E., Pan, B., Yu, C., Kusam, S., Lam, C., Phu, L., Phung, Q., Maurer, B., Arnott, D., Kirkpatrick, D. S., Dixit, V. M., and Hymowitz, S. G. (2010) Ubiquitin Binding to A20 ZnF4 Is Required for Modulation of NF-κB Signaling. *Mol. Cell* **40**, 548-557

295. Zhang, J., Timoney, P. J., Shuck, K. M., Seoul, G., Go, Y. Y., Lu, Z., Powell, D. G., Meade, B. J., and Balasuriya, U. B. (2010) Molecular epidemiology and genetic characterization of equine arteritis virus isolates associated with the 2006-2007 multi-state disease occurrence in the USA. *J. Gen. Virol.* **91**, 2286-2301

296. Holyoak, G. R., Balasuriya, U. B., Broaddus, C. C., and Timoney, P. J. (2008) Equine viral arteritis: current status and prevention. *Theriogenology* **70**, 403-414

297. Tong, G. Z., Zhou, Y. J., Hao, X. F., Tian, Z. J., An, T. Q., and Qiu, H. J. (2007) Highly pathogenic porcine reproductive and respiratory syndrome, China. *Emerg. Infect. Dis.* **13**, 1434-1436

298. Li, Y., Wang, X., Bo, K., Tang, B., Yang, B., Jiang, W., and Jiang, P. (2007) Emergence of a highly pathogenic porcine reproductive and respiratory syndrome virus in the Mid-Eastern region of China. *Vet. J.* **174**, 577-584

299. Tian, K., Yu, X., Zhao, T., Feng, Y., Cao, Z., Wang, C., Hu, Y., Chen, X., Hu, D., Tian, X., Liu, D., Zhang, S., Deng, X., Ding, Y., Yang, L., Zhang, Y., Xiao, H., Qiao, M., Wang, B., Hou, L., Wang, X., Yang, X., Kang, L., Sun, M., Jin, P., Wang, S., Kitamura, Y., Yan, J., and Gao, G. F. (2007) Emergence of fatal PRRSV variants: unparalleled outbreaks of atypical PRRS in China and molecular dissection of the unique hallmark. *PLoS One* **2**, e526

300. Chen, Z., Lawson, S., Sun, Z., Zhou, X., Guan, X., Christopher-Hennings, J., Nelson, E. A., and Fang, Y. (2010) Identification of two auto-cleavage products of nonstructural protein 1 (nsp1) in porcine reproductive and respiratory syndrome virus infected cells: nsp1 function as interferon antagonist. *Virology* **398**, 87-97

301. Beura, L. K., Sarkar, S. N., Kwon, B., Subramaniam, S., Jones, C., Pattnaik, A. K., and Osorio, F. A. (2010) Porcine reproductive and respiratory syndrome virus nonstructural protein 1beta modulates host innate immune response by antagonizing IRF3 activation. *J. Virol.* **84**, 1574-1584

302. Richt, J. A., and Garcia-Sastre, A. (2009) Attenuated influenza virus vaccines with modified NS1 proteins. *Curr. Top. Microbiol. Immunol.* **333**, 177-195

303. Jensen, S., and Thomsen, A. R. (2012) Sensing of RNA viruses: a review of innate immune receptors involved in recognizing RNA virus invasion. *J. Virol.* **86**, 2900-2910

304. Narasimhan, J., Wang, M., Fu, Z., Klein, J. M., Haas, A. L., and Kim, J. J. (2005) Crystal structure of the interferon-induced ubiquitin-like protein ISG15. *J. Biol. Chem.* **280**, 27356-27365

305. Kabsch, W. (2010) XDS. *Acta Crystallogr. D Biol. Crystallogr.* **66**, 125-132

306. Evans, P. (2006) Scaling and assessment of data quality. *Acta Crystallogr. D Biol. Crystallogr.* **62**, 72-82

307. McCoy, A. J., Grosse-Kunstleve, R. W., Adams, P. D., Winn, M. D., Storoni, L. C., and Read, R. J. (2007) Phaser crystallographic software. *J. Appl. Crystallogr.* **40**, 658-674

308. Terwilliger, T. C., Grosse-Kunstleve, R. W., Afonine, P. V., Moriarty, N. W., Zwart, P. H., Hung, L. W., Read, R. J., and Adams, P. D. (2008) Iterative model building, structure refinement and density modification with the PHENIX AutoBuild wizard. *Acta Crystallogr. D Biol. Crystallogr.* **64**, 61-69

309. Emsley, P., Lohkamp, B., Scott, W. G., and Cowtan, K. (2010) Features and development of Coot. *Acta Crystallogr. D Biol. Crystallogr.* **66**, 486-501

310. Afonine, P. V., Grosse-Kunstleve, R. W., Echols, N., Headd, J. J., Moriarty, N. W., Mustyakimov, M., Terwilliger, T. C., Urzhumtsev, A., Zwart, P. H., and Adams, P. D. (2012) Towards automated crystallographic structure refinement with phenix.refine. *Acta Crystallogr. D Biol. Crystallogr.* **68**, 352-367

311. Waterhouse, A. M., Procter, J. B., Martin, D. M., Clamp, M., and Barton, G. J. (2009) Jalview Version 2--a multiple sequence alignment editor and analysis workbench. *Bioinformatics* **25**, 1189-1191

312. Basters, A., Geurink, P. P., Rocker, A., Witting, K. F., Tadayon, R., Hess, S., Semrau, M. S., Storici, P., Ovaa, H., Knobeloch, K. P., and Fritz, G. (2017) Structural basis of the specificity of USP18 toward ISG15. *Nat. Struct. Mol. Biol.* **24**, 270-278

313. Uddin, M. J., Suen, W. W., Bosco-Lauth, A., Hartwig, A. E., Hall, R. A., Bowen, R. A., and Bielefeldt-Ohmann, H. (2016) Kinetics of the West Nile virus induced transcripts of selected cytokines and Toll-like receptors in equine peripheral blood mononuclear cells. *Vet. Res.* **47**, 61

314. Scholte, F. E. M., Zivcec, M., Dzimianski, J. V., Deaton, M. K., Spengler, J. R., Welch, S. R., Nichol, S. T., Pegan, S. D., Spiropoulou, C. F., and Bergeron, E. (2017) Crimean-Congo Hemorrhagic Fever Virus Suppresses Innate Immune Responses via a Ubiquitin and ISG15 Specific Protease. *Cell Rep.* **20**, 2396-2407

315. Huang, T. T., and D'Andrea, A. D. (2006) Regulation of DNA repair by ubiquitylation. *Nat. Rev. Mol. Cell Biol.* **7**, 323-334

316. Clague, M. J., and Urbe, S. (2010) Ubiquitin: same molecule, different degradation pathways. *Cell* **143**, 682-685

317. Oudshoorn, D., Versteeg, G. A., and Kikkert, M. (2012) Regulation of the innate immune system by ubiquitin and ubiquitin-like modifiers. *Cytokine Growth Factor Rev.* **23**, 273-282

318. Nijman, S. M., Luna-Vargas, M. P., Velds, A., Brummelkamp, T. R., Dirac, A. M., Sixma, T. K., and Bernards, R. (2005) A genomic and functional inventory of deubiquitinating enzymes. *Cell* **123**, 773-786

319. Jiang, J., and Tang, H. (2010) Mechanism of inhibiting type I interferon induction by hepatitis B virus X protein. *Protein Cell* **1**, 1106-1117

320. Robin, C., Beaurepaire, L., Chenon, M., Jupin, I., and Bressanelli, S. (2012) In praise of impurity: 30S ribosomal S15 protein-assisted crystallization of turnip yellow mosaic virus proteinase. *Acta Crystallogr. Sect. F Struct. Biol. Cryst. Commun.* **68**, 486-490

321. Schrodinger, LLC. (2010) The PyMOL Molecular Graphics System, Version 1.3r1.

322. Wassenaar, A. L., Spaan, W. J., Gorbalenya, A. E., and Snijder, E. J. (1997) Alternative proteolytic processing of the arterivirus replicase ORF1a polyprotein: evidence that NSP2 acts as a cofactor for the NSP4 serine protease. *J. Virol.* **71**, 9313-9322

323. Ziebuhr, J., Snijder, E. J., and Gorbalenya, A. E. (2000) Virus-encoded proteinases and proteolytic processing in the Nidovirales. *J. Gen. Virol.* **81**, 853-879

324. Holm, L., Kaariainen, S., Rosenstrom, P., and Schenkel, A. (2008) Searching protein structure databases with DaliLite v.3. *Bioinformatics* **24**, 2780-2781

325. Krissinel, E., and Henrick, K. (2004) Secondary-structure matching (SSM), a new tool for fast protein structure alignment in three dimensions. *Acta Crystallogr. D Biol. Crystallogr.* **60**, 2256-2268

326. Martelli, G. P., Adams, M. J., Kreuze, J. F., and Dolja, V. V. (2007) Family Flexiviridae: a case study in virion and genome plasticity. *Annu. Rev. Phytopathol.* **45**, 73-100

327. Mielech, A. M., Chen, Y., Mesecar, A. D., and Baker, S. C. (2014) Nidovirus papain-like proteases: Multifunctional enzymes with protease, deubiquitinating and deISGylating activities. *Virus Res.* **194**, 184-190

328. Spiegel, M., and Weber, F. (2006) Inhibition of cytokine gene expression and induction of chemokine genes in non-lymphatic cells infected with SARS coronavirus. *Virol. J.* **3**, 17-17

329. Cheung, C. Y., Poon, L. L. M., Ng, I. H. Y., Luk, W., Sia, S.-F., Wu, M. H. S., Chan, K.-H., Yuen, K.-Y., Gordon, S., Guan, Y., and Peiris, J. S. M. (2005) Cytokine responses in severe acute respiratory syndrome coronavirus-infected macrophages in vitro: possible relevance to pathogenesis. *J. Virol.* **79**, 7819-7826

330. Chu, H., Zhou, J., Ho-Yin Wong, B., Li, C., Cheng, Z.-S., Lin, X., Kwok-Man Poon, V., Sun, T., Choi-Yi Lau, C., Fuk-Woo Chan, J., Kai-Wang To, K., Chan, K.-H., Lu, L., Zheng, B.-J., and Yuen, K.-Y. (2014) Productive replication of Middle East respiratory syndrome coronavirus in monocyte-derived dendritic cells modulates innate immune response. *Virology* **454-455**, 197-205

331. Chan, R. W. Y., Chan, M. C. W., Agnihothram, S., Chan, L. L. Y., Kuok, D. I. T., Fong, J. H. M., Guan, Y., Poon, L. L. M., Baric, R. S., Nicholls, J. M., and Peiris, J. S. M. (2013) Tropism of and innate immune responses to the novel human betacoronavirus lineage C virus in human ex vivo respiratory organ cultures. *J. Virol.* **87**, 6604-6614

332. Lau, S. K., Lau, C. C., Chan, K. H., Li, C. P., Chen, H., Jin, D. Y., Chan, J. F., Woo, P. C., and Yuen, K. Y. (2013) Delayed induction of proinflammatory cytokines and suppression of innate antiviral response by the novel Middle East respiratory syndrome coronavirus: implications for pathogenesis and treatment. *J. Gen. Virol.* **94**, 2679-2690

333. te Velthuis, A. J., Arnold, J. J., Cameron, C. E., van den Worm, S. H., and Snijder, E. J. (2010) The RNA polymerase activity of SARS-coronavirus nsp12 is primer dependent. *Nucleic Acids Res.* **38**, 203-214

334. Seth, R. B., Sun, L., Ea, C. K., and Chen, Z. J. (2005) Identification and characterization of MAVS, a mitochondrial antiviral signaling protein that activates NF-kappaB and IRF 3. *Cell* **122**, 669-682

335. Lin, R., Heylbroeck, C., Pitha, P. M., and Hiscott, J. (1998) Virus-dependent phosphorylation of the IRF-3 transcription factor regulates nuclear translocation, transactivation potential, and proteasome-mediated degradation. *Mol. Cell. Biol.* **18**, 2986-2996

336. Grosse-Kunstleve, R. W., and Adams, P. D. (2003) Substructure search procedures for macromolecular structures. *Acta Crystallogr. D Biol. Crystallogr.* **59**, 1966-1973

337. Terwilliger, T. C. (2000) Maximum-likelihood density modification. *Acta Crystallogr. D Biol. Crystallogr.* **56**, 965-972

338. Terwilliger, T. C., Adams, P. D., Read, R. J., McCoy, A. J., Moriarty, N. W., Grosse-Kunstleve, R. W., Afonine, P. V., Zwart, P. H., and Hung, L. W. (2009) Decision-making in structure solution using Bayesian estimates of map quality: the PHENIX AutoSol wizard. *Acta Crystallogr. D Biol. Crystallogr.* **65**, 582-601

339. Graham, F. L., and van der Eb, A. J. (1973) A new technique for the assay of infectivity of human adenovirus 5 DNA. *Virology* **52**, 456-467

340. Hadari, T., Warms, J. V., Rose, I. A., and Hershko, A. (1992) A ubiquitin C-terminal isopeptidase that acts on polyubiquitin chains. Role in protein degradation. *J. Biol. Chem.* **267**, 719-727

341. Faesen, A. C., Luna-Vargas, M. P., and Sixma, T. K. (2012) The role of UBL domains in ubiquitin-specific proteases. *Biochem. Soc. Trans.* **40**, 539-545

342. Rawlings, N. D., Waller, M., Barrett, A. J., and Bateman, A. (2014) MEROPS: the database of proteolytic enzymes, their substrates and inhibitors. *Nucleic Acids Res.* **42**, D503-509

343. Krishna, S. S., Majumdar, I., and Grishin, N. V. (2003) Structural classification of zinc fingers: survey and summary. *Nucleic Acids Res.* **31**, 532-550

344. Renatus, M., Parrado, S. G., D'Arcy, A., Eidhoff, U., Gerhartz, B., Hassiepen, U., Pierrat, B., Riedl, R., Vinzenz, D., Worpenberg, S., and Kroemer, M. (2006) Structural basis of ubiquitin recognition by the deubiquitinating protease USP2. *Structure* **14**, 1293-1302

345. Ye, Y., Akutsu, M., Reyes-Turcu, F., Enchev, R. I., Wilkinson, K. D., and Komander, D. (2011) Polyubiquitin binding and cross-reactivity in the USP domain deubiquitinase USP21. *EMBO Rep.* **12**, 350-357

346. Hu, M., Li, P., Song, L., Jeffrey, P. D., Chenova, T. A., Wilkinson, K. D., Cohen, R. E., and Shi, Y. (2005) Structure and mechanisms of the proteasome-associated deubiquitinating enzyme USP14. *EMBO J.* **24**, 3747-3756

347. Heideker, J., and Wertz, I. E. (2015) DUBs, the regulation of cell identity and disease. *Biochem. J.* **465**, 1-26

348. Kemp, M. (2016) Recent Advances in the Discovery of Deubiquitinating Enzyme Inhibitors. *Prog. Med. Chem.* **55**, 149-192

349. Tonikian, R., Zhang, Y., Boone, C., and Sidhu, S. S. (2007) Identifying specificity profiles for peptide recognition modules from phage-displayed peptide libraries. *Nat. Protoc.* **2**, 1368-1386

350. Carlotti, F., Bazuine, M., Kekarainen, T., Seppen, J., Pognonec, P., Maassen, J. A., and Hoeben, R. C. (2004) Lentiviral vectors efficiently transduce quiescent mature 3T3-L1 adipocytes. *Mol. Ther.* **9**, 209-217

351. van den Worm, S. H., Eriksson, K. K., Zevenhoven, J. C., Weber, F., Zust, R., Kuri, T., Dijkman, R., Chang, G., Siddell, S. G., Snijder, E. J., Thiel, V., and Davidson, A. D. (2012) Reverse genetics of SARS-related coronavirus using vaccinia virus-based recombination. *PLoS One* **7**, e32857

352. Leung, I., Dekel, A., Shifman, J. M., and Sidhu, S. S. (2016) Saturation scanning of ubiquitin variants reveals a common hot spot for binding to USP2 and USP21. *Proc. Natl. Acad. Sci. U. S. A.* **113**, 8710

353. D'Arcy, A., Villard, F., and Marsh, M. (2007) An automated microseed matrix-screening method for protein crystallization. *Acta Crystallogr. D Biol. Crystallogr.* **63**, 550-554

354. Ireton, G. C., and Stoddard, B. L. (2004) Microseed matrix screening to improve crystals of yeast cytosine deaminase. *Acta Crystallogr. D Biol. Crystallogr.* **60**, 601-605

355. Georgieva, D. G., Kuil, M. E., Oosterkamp, T. H., Zandbergen, H. W., and Abrahams, J. P. (2007) Heterogeneous nucleation of three-dimensional protein nanocrystals. *Acta Crystallogr. D Biol. Crystallogr.* **63**, 564-570

356. Evans, P. R. (2011) An introduction to data reduction: space-group determination, scaling and intensity statistics. *Acta Crystallogr. D Biol. Crystallogr.* **67**, 282-292

357. van Hemert, M. J., van den Worm, S. H., Knoops, K., Mommaas, A. M., Gorbalenya, A. E., and Snijder, E. J. (2008) SARS-coronavirus replication/transcription complexes are membrane-protected and need a host factor for activity in vitro. *PLoS Pathog.* **4**, e1000054

358. Matthews, K. L., Coleman, C. M., van der Meer, Y., Snijder, E. J., and Frieman, M. B. (2014) The ORF4b-encoded accessory proteins of Middle East respiratory syndrome coronavirus and two related bat coronaviruses localize to the nucleus and inhibit innate immune signalling. *J. Gen. Virol.* **95**, 874-882

359. Krissinel, E., and Henrick, K. (2007) Inference of macromolecular assemblies from crystalline state. *J. Mol. Biol.* **372**, 774-797

360. de Wit, E., van Doremalen, N., Falzarano, D., and Munster, V. J. (2016) SARS and MERS: recent insights into emerging coronaviruses. *Nat. Rev. Microbiol.* **14**, 523-534

361. Haagmans, B. L., van den Brand, J. M., Raj, V. S., Volz, A., Wohlsein, P., Smits, S. L., Schipper, D., Bestebroer, T. M., Okba, N., Fux, R., Bensaid, A., Solanes Foz, D., Kuiken, T., Baumgartner, W., Segales, J., Sutter, G., and Osterhaus, A. D. (2016) An orthopoxvirus-based vaccine reduces virus excretion after MERS-CoV infection in dromedary camels. *Science* **351**, 77-81

362. Auger, A., Park, M., Nitschke, F., Minassian, L. M., Beilhartz, G. L., Minassian, B. A., and Melnyk, R. A. (2015) Efficient Delivery of Structurally Diverse Protein Cargo into Mammalian Cells by a Bacterial Toxin. *Mol. Pharm.* **12**, 2962-2971

363. D'Astolfo, D. S., Pagliero, R. J., Pras, A., Karthaus, W. R., Clevers, H., Prasad, V., Lebbink, R. J., Rehmann, H., and Geijsen, N. (2015) Efficient intracellular delivery of native proteins. *Cell* **161**, 674-690

364. Gaj, T., Liu, J., Anderson, K. E., Sirk, S. J., and Barbas, C. F., 3rd. (2014) Protein delivery using Cys2-His2 zinc-finger domains. *ACS Chem. Biol.* **9**, 1662-1667

365. Uppalapati, M., Lee, D. J., Mandal, K., Li, H., Miranda, L. P., Lowitz, J., Kenney, J., Adams, J. J., Ault-Riche, D., Kent, S. B., and Sidhu, S. S. (2016) A Potent d-Protein Antagonist of VEGF-A is Nonimmunogenic, Metabolically Stable, and Longer-Circulating in Vivo. *ACS Chem. Biol.* **11**, 1058-1065

366. Arkin, M. R., Tang, Y., and Wells, J. A. (2014) Small-molecule inhibitors of protein-protein interactions: progressing toward the reality. *Chem. Biol.* **21**, 1102-1114

367. Ziebuhr, J., Schelle, B., Karl, N., Minskaia, E., Bayer, S., Siddell, S. G., Gorbalenya, A. E., and Thiel, V. (2007) Human coronavirus 229E papain-like proteases have overlapping specificities but distinct functions in viral replication. *J. Virol.* **81**, 3922-3932

368. Miao, X. (2013) Recent advances in the development of new transgenic animal technology. *Cell. Mol. Life Sci.* **70**, 815-828

369. Agrawal, A. S., Garron, T., Tao, X., Peng, B. H., Wakamiya, M., Chan, T. S., Couch, R. B., and Tseng, C. T. (2015) Generation of a transgenic mouse model of Middle East respiratory syndrome coronavirus infection and disease. *J. Virol.* **89**, 3659-3670

370. Pascal, K. E., Coleman, C. M., Mujica, A. O., Kamat, V., Badithe, A., Fairhurst, J., Hunt, C., Strein, J., Berrebi, A., Sisk, J. M., Matthews, K. L., Babb, R., Chen, G., Lai, K. M., Huang, T. T., Olson, W., Yancopoulos, G. D., Stahl, N., Frieman, M. B., and Kyratsous, C. A. (2015) Pre- and postexposure efficacy of fully human antibodies against Spike protein in a novel humanized mouse model of MERS-CoV infection. *Proc. Natl. Acad. Sci. U. S. A.* **112**, 8738-8743

371. Zhao, J., Li, K., Wohlford-Lenane, C., Agnihothram, S. S., Fett, C., Zhao, J., Gale, M. J., Jr., Baric, R. S., Enjuanes, L., Gallagher, T., McCray, P. B., Jr., and Perlman, S. (2014) Rapid generation of a mouse model for Middle East respiratory syndrome. *Proc. Natl. Acad. Sci. U. S. A.* **111**, 4970-4975

372. van Doremalen, N., and Munster, V. J. (2015) Animal models of Middle East respiratory syndrome coronavirus infection. *Antiviral Res.* **122**, 28-38

373. Cockrell, A. S., Yount, B. L., Scobey, T., Jensen, K., Douglas, M., Beall, A., Tang, X. C., Marasco, W. A., Heise, M. T., and Baric, R. S. (2016) A mouse model for MERS coronavirus-induced acute respiratory distress syndrome. *Nat. Microbiol.* **2**, 16226

374. Deng, X., StJohn, S. E., Osswald, H. L., O'Brien, A., Banach, B. S., Sleeman, K., Ghosh, A. K., Mesecar, A. D., and Baker, S. C. (2014) Coronaviruses resistant to a 3C-like protease inhibitor are attenuated for replication and pathogenesis, revealing a low genetic barrier but high fitness cost of resistance. *J. Virol.* **88**, 11886-11898

375. Daczkowski, C. M., Goodwin, O. Y., Dzimianski, J. V., Farhat, J. J., and Pegan, S. D. (2017) Structurally Guided Removal of DeISGylase Biochemical Activity from Papain-Like Protease Originating from Middle East Respiratory Syndrome Coronavirus. *J. Virol.* **91**, JVI.01067-01017

376. Powell, H. R., Battye, T. G. G., Kontogiannis, L., Johnson, O., and Leslie, A. G. W. (2017) Integrating macromolecular X-ray diffraction data with the graphical user interface iMosflm. *Nat. Protoc.* **12**, 1310-1325

377. Vagin, A., and Teplyakov, A. (2010) Molecular replacement with MOLREP. *Acta Crystallogr. D Biol. Crystallogr.* **66**, 22-25

378. Murshudov, G. N., Vagin, A. A., and Dodson, E. J. (1997) Refinement of macromolecular structures by the maximum-likelihood method. *Acta Crystallogr. D Biol. Crystallogr.* **53**, 240-255

379. Winn, M. D., Ballard, C. C., Cowtan, K. D., Dodson, E. J., Emsley, P., Evans, P. R., Keegan, R. M., Krissinel, E. B., Leslie, A. G., McCoy, A., McNicholas, S. J., Murshudov, G. N., Pannu, N. S., Potterton, E. A., Powell, H. R., Read, R. J., Vagin, A.,

and Wilson, K. S. (2011) Overview of the CCP4 suite and current developments. *Acta Crystallogr. D Biol. Crystallogr.* **67**, 235-242

380. Ye, Y., Blaser, G., Horrocks, M. H., Ruedas-Rama, M. J., Ibrahim, S., Zhukov, A. A., Orte, A., Klenerman, D., Jackson, S. E., and Komander, D. (2012) Ubiquitin chain conformation regulates recognition and activity of interacting proteins. *Nature* **492**, 266-270

381. Turnbull, A. P., Ioannidis, S., Krajewski, W. W., Pinto-Fernandez, A., Heride, C., Martin, A. C. L., Tonkin, L. M., Townsend, E. C., Buker, S. M., Lancia, D. R., Caravella, J. A., Toms, A. V., Charlton, T. M., Lahdenranta, J., Wilker, E., Follows, B. C., Evans, N. J., Stead, L., Alli, C., Zarayskiy, V. V., Talbot, A. C., Buckmelter, A. J., Wang, M., McKinnon, C. L., Saab, F., McGouran, J. F., Century, H., Gersch, M., Pittman, M. S., Marshall, C. G., Raynham, T. M., Simcox, M., Stewart, L. M. D., McLoughlin, S. B., Escobedo, J. A., Bair, K. W., Dinsmore, C. J., Hammonds, T. R., Kim, S., Urbe, S., Clague, M. J., Kessler, B. M., and Komander, D. (2017) Molecular basis of USP7 inhibition by selective small-molecule inhibitors. *Nature* **550**, 481-486

382. Kategaya, L., Di Lello, P., Rouge, L., Pastor, R., Clark, K. R., Drummond, J., Kleinheinz, T., Lin, E., Upton, J. P., Prakash, S., Heideker, J., McCleland, M., Ritorto, M. S., Alessi, D. R., Trost, M., Bainbridge, T. W., Kwok, M. C. M., Ma, T. P., Stiffler, Z., Brasher, B., Tang, Y., Jaishankar, P., Hearn, B. R., Renslo, A. R., Arkin, M. R., Cohen, F., Yu, K., Peale, F., Gnad, F., Chang, M. T., Klijn, C., Blackwood, E., Martin, S. E., Forrest, W. F., Ernst, J. A., Ndubaku, C., Wang, X., Beresini, M. H., Tsui, V., Schwerdtfeger, C., Blake, R. A., Murray, J., Maurer, T., and Wertz, I. E. (2017) USP7 small-molecule inhibitors interfere with ubiquitin binding. *Nature* **550**, 534-538

383. Sato, Y., Goto, E., Shibata, Y., Kubota, Y., Yamagata, A., Goto-Ito, S., Kubota, K., Inoue, J., Takekawa, M., Tokunaga, F., and Fukai, S. (2015) Structures of CYLD USP with Met1- or Lys63-linked diubiquitin reveal mechanisms for dual specificity. *Nat. Struct. Mol. Biol.* **22**, 222-229

384. Sato, Y., Okatsu, K., Saeki, Y., Yamano, K., Matsuda, N., Kaiho, A., Yamagata, A., Goto-Ito, S., Ishikawa, M., Hashimoto, Y., Tanaka, K., and Fukai, S. (2017) Structural basis for specific cleavage of Lys6-linked polyubiquitin chains by USP30. *Nat. Struct. Mol. Biol.* **24**, 911-919

385. Kristariyanto, Y. A., Abdul Rehman, S. A., Weidlich, S., Knebel, A., and Kulathu, Y. (2017) A single MIU motif of MINDY-1 recognizes K48-linked polyubiquitin chains. *EMBO Rep.* **18**, 392-402

386. Licchesi, J. D., Mieszczanek, J., Mevissen, T. E., Rutherford, T. J., Akutsu, M., Virdee, S., El Oualid, F., Chin, J. W., Ovaa, H., Bienz, M., and Komander, D. (2011) An ankyrin-repeat ubiquitin-binding domain determines TRABID's specificity for atypical ubiquitin chains. *Nat. Struct. Mol. Biol.* **19**, 62-71